Growth-Adapted Tensegrity Structures: A New Calculus for the Space Economy

Anthony Longman and R.E. Skelton

July 14, 2014

Contents

List of Figures

Chapter 1

Executive Summary

1.1 Goal: Enable Evolutionary Growth of Space Habitats

- The objective, achieved in this report, is to create a feasible, well-organized growth concept for a torus-shaped space habitat, based on scientific methods and design procedures, starting from an initial scale capable of deployment on 2 or 3 rocket launches, and with all subsequent construction using space-based materials.
- Defining a torus by two radii (R, r), the range of the intended growth capability is to be from $(R = 10m, r = 5m)$ to $(R = 1000m, r = 500m)$.

Figure 1.1: Evolvable Space Habitat Development - the Goal
Peter Rubin's artwork (p.rubin@ironroosterstudios.com) depicts a 16km diameter torus pressure hull habitat. Our research shows a feasible pathway towards engineered habitats at this scale.

- These objectives will be achieved by new efficient structural engineering methods called Tensegrity Engineering.

1.1.1 Subordinate Objectives

The proposal for Phase 1 specified a series of objectives toward the pursuit of deploying a growth capable tensegrity-based space habitat. We summarize here a brief outline of these objectives, and the progress made in our Phase 1 efforts.

1. Objective: Document and illustrate a workable strategy for growth in space of an operationally loaded tensegrity torus pressure hull system.

   Result: Achieved (see § 5.3.5).

2. Objective: Document a feasible approach for automated tensegrity fabrication in space.

   Result: In full communication with our technical monitors, we deferred the automation task until after the habitat design was matured. The nominal design, the growth, and the shielding study dominated our priorities in Phase 1. During the process of developing the design, different methods of fabrication emerged and will be a focus in Phase 2. The design of the pressure hull evolved to became predominantly an inflatable structure with distributed compression elements for application of moment forces to counter precession. Given the separation of the shielding function into a separate unpressurized structure, the issue of appropriate fabrication methods for this remain to be addressed, once the design of that structure has been resolved under Phase II.

3. Objective: Document and illustrate key system parameters and potential growth rates through time of the chosen habitat configuration, based on optimal geometry.

   Result: The direction of evolution of the design in Phase I will require to be matured in Phase II, and appropriate fabrication techniques developed. Once this research is in place, estimation of the mining requirements and feasible rate of acquisition of materials can be made, as this is likely to be a determining factor in the rate of growth of the habitat. Additional insights into this question will come from study of real estate development scenarios on earth.

4. Demonstrate feasibility of a tensegrity habitat concept. The report provides the following conclusions. Operating at 1-g and using UHMWPE material for cables and a 1mm hull, the structural mass required to build the habitat of size $(R, r) = (10m, 5m)$ is $1,576$ kg. The structural mass required to build the habitat of size $(R, r) = (405m, 130m)$ is $83,516,117$ kg. The structural mass required to build the habitat of size $(R, r) = (830m, 65m)$ is $19,567,582$ kg (eight times less mass than required to build the 1-g, same sized Stanford Torus of the 1970s). Appendices A and B provide other designs using the DHT topology, yielding masses: 1.6?103 kg for $(R, r) = (10, 5)$, and 1.4?$10^1$0 kg for $(R, r) = (1000m, 500m)$. The DHT topology provides much greater structural stiffness. The control laws developed in Phase II will determine the required stiffness and stability properties, and the amount of control energy required to meet the control performance objectives (minimal control energy, reasonably fast response to correct displacement errors or spin rate errors). While much work remains to be done, this report documents the proof of concept.

5. Evaluate growth related interactions of frame with i) access system ii) shielding system iii) hull system iv) thermal management, illumination and power systems.

Result: i) Access system. (See § 5.2.5.) ii) Shielding system. (See § 5.4.) iii) Hull system. (See § 6.33.) iv) Thermal management. (See § 5.5.2.) v) Illumination. (See § 5.2.3.) vi) Power systems. (See § 5.5.3.)

6. Characterize necessary feedback and control strategies for a.) spin about two axes (for gravity and sunlight), b.) gyroscopic control forces to control precession, and c.) control systems to maintain stable configurations during structural growth.

   Result: Achieved. See § 6.1, § 6.10.

7. Evaluate strategies for growing integrally deployed water bag hull and shielding while maintaining hull closure and characterize a feasible pathway for this.

   Result: Design evolution has separated the water bag shielding into a distinct structure separate from the pressure hull. Strategies for growth of this shield structure have been evaluated, and a preferred choice selected. Evaluation of strategy for growing a separate shield structure has been achieved. (See § 5.4.)

8. Evaluate double/multi-hull offering air-lock function for repairs/growth.

   Result: Achieved. (See § 5.3.2.)

9. Automated Fabrication and Assembly. Analyze and compare the requirements of our configurations against the range of demonstrated capability in the robotics field to determine whether any radical new capability is required. Outline robotic means for deployment of new structural and hull elements.

   Result: Achieved. The general pace of advances in the robotics field, specific current research on tensegrity robotic systems being conducted by the Department of Mechanical and Aerospace Engineering, University of California San Diego, [2, 3, 4] and the capabilities illustrated in NASA's DEXTRE robot on the ISS, persuade us that the necessary robotic capability to carry out the tasks required for realization of our concept may be safely assumed for the time being, until our research on other tasks has progressed further and the actual needs are more closely defined.

10. Space environment interaction, power, means of access. Define viable schematic design for these elements. a.) Solar Orientation - achieved b.) Solar energy, light distribution to the interior - achieved c.) Overall estimated power requirements d.) Waste Heat Management e.) Accessing the Habitat.

    Result: a.) Achieved. (See § 5.5.1.) b.) Achieved. (See § 5.2.3.) c.) Overall estimated power requirements. Due to the evolution of the design to a separate shield structure this task is deferred until Phase II. d.) Achieved. (See § 5.5.2.) e.) Achieved. (See § 5.2.5.)

11. Capability for Ecosystem Development. We made no specific claims in this regard, but this overall objective has guided our thought processes. We have demonstrated the feasibility of sustained pressure hull expansion, and a feasible overall system architecture. We have shown a strategy for the deployment of a separate shield structure with sufficient water bag thickness. Feasibility of the systems as a whole appears to be demonstrable, and an attainable goal. Following deployment, a research program will be required to study how the constituent species of potential candidate ecosystems adapt to the levels of exposure to GCR/SPE type radiation encountered on the habitat. Ground based installations that simulate the habitat environment with soil processed from simulated regolith and supporting microbial, plant and

animal populations in enclosure type testbed environments can be set up and run in advance of the habitat deployment to provide a head start on ecosystem deployment and development within the habitat.

12. Demonstrate by calculation that a distributed momentum control system is adequate. Optimize the location and number of these units in the structure.

    Result: Appendices C and D show how to control the precession of the habitat using momentum exchange control laws. On the basis of this study we chose to spin the habitat about an axis perpendicular to the ecliptic plane. The optimization of the number and location of the momentum wheels will occur in Phase II. This optimization will guarantee a specified error bound on the displacement errors, the spin rate errors, and spin direction errors, while maximizing the energy stored from solar arrays into momentum wheels..

13. Objective: Develop a new momentum exchange control actuator concept.

    Result: by moving mass around in a controlled way, it is possible to use momentum control concepts to control the habitat torus. Thrusters (ion engines, solar pressure, or propellants) will likely be needed for translating the mirror and shield structure to maintain proper displacements relative to the torus. A new momentum exchange actuator concept is a preexisting invention of Skelton. We elected to defer that discussion for now, since the same feasibility can be demonstrated using standard rigid momentum wheels, strategically placed. (see § 6.10.3.)

1.2 Comparisons with Previous Space Habitat Proposals

We provide here a brief review of three notable precursors to our concept – the Stanford Torus, Gerard O'Neill's Island One design, and the International Space Station – to aid the reader in evaluating the merits of our work.

1.2.1 1975 Stanford Torus

The Stanford Torus, proposed during the 1975 NASA Summer Study [5], conducted at Stanford University, is the most fully developed precursor concept that parallels our own, and allows instructive numerical comparisons to be drawn.

- Although our proposed deployment involves very different torus proportions, simplified calculations in Chapter 7 provide a head-to-head comparison of our structural approach with the Stanford approach, using the same radius figures of 830m and 65m contained in the report of the Stanford study. These calculations show that our UHMWPE tensegrity technology would support the same projected surface area while using only 6% of the mass of the Stanford Torus alumnum hull.

- The Stanford design has inadequate shielding coverage. A static regolith shield was to be positioned at the sides and beneath, to supplement the aluminum hull, but no such protection was provided overhead, beyond the minimal 1-inch aluminum shielding built into the chevron mirror system. The intent of this mirror system was to admit light, and impede the passage of ionizing particle radiation, a task for which it was inadequate as conceived. Although the geometric principles of the system are correct its implementation was inappropriate in terms of scale and materials and was therefore incapable of providing a meaningful degree

of shielding. This left the habitat interior substantially lacking in overhead shielding, in consequence of which, the occupants would have faced severe exposure to GCR over time with negative health consequences for the population. In contrast, our approach applies the mirror logic with the correct materials at the appropriate scale, providing complete coverage from all directions and with fully customizable shielding levels.

- The Stanford torus has no growth capability.
- In terms of realizability, our approach allows the deployment of an initial configuration offering startup life-support and shielding using only 2 to 3 launches and the in space acquisition costs of 50,000 tons of water. By contrast, the Stanford study was predicated on large investments of time and capital for the development of industrial infrastructure on the lunar surface as a precondition for commencing construction activities for the habitat itself, whose mass it is estimated would have approached 10 million tons when completed.

Our approach offers radical improvements in efficiency, economy of means and feasibility of capitalization over the Stanford Torus.

1.2.2 Island Three (O'Neill Cylinder)

Gerard O'Neill's iconic Cylinder concept was for a pair of massive counter-rotating rigid cylindrical habitats, each 5 miles in diameter and 20 miles long. This concept was proposed by O'Neill in his 1976 book "The High Frontier: Human Colonies in Space" and has proved to be an enduring source of inspiration since that time. In reality, there are a number of difficulties with the idea as proposed by O'Neill. A few examples will serve to illustrate:

- Operating the very large movable rotating angled mirror panels, the ends of which would be subject to multiple g forces, would have required the repeated expenditure of very large amounts of energy.
- The sun-pointing axis would have subjected the required linkages between the pairs of contra-rotating cylinders to very large tension and compression loads, and the cylinder walls to high shear forces, due to the twisting action of precession forces within the cylinders.
- Spin of the cylinder about the axis of minimum inertia (the longitudinal axis) is an unstable motion, as demonstrated by America's first satellite, Explorer 1.
- The working hypothesis was that the atmosphere and the structural hull would suffice for shielding purposes. Given that 50% of the hull surface was to be transparent to sunlight, and that a half pressure atmosphere was to be employed, the assertion that this would provide adequate shielding is doubtful at best, in light of current estimates of the severity of the challenge poised by galactic cosmic radiation and solar proton events..
- The economic model was for the large upfront construction costs to be offset by the subsequent labor of colonists in the construction of massive space based solar power stations, the revenue from which would eventually defray these very large initial costs. This model combined very high initial outlay of capital with very long payback time and very high levels of technical uncertainty and risk of failure.
- Island Three has no structural growth capability.

By contrast to the monumental scale of plans for the construction of Island Three, our approach of enabling habitat growth from a small initial size has the clear advantage that it can be developed and applied in a short period of time for a fraction of the initial investment required in the Island Three scenario. OUr habitat can then be grown in response to demonstrated demand and profitability, in the process demonstrating a mechanism that can jumpstart a new phase of development in the space economy.

1.2.3 International Space Station (ISS)

The ISS has been built and thus offers a concrete benchmark for comparisons.

- The ISS offers no gravity effect.
- The ISS offers little in the way of shielding beyond an emergency shelter, since it benefits from location within earth's magnetosphere.
- Construction is ongoing, and has to date required 40 launches to support a maximum permanent crew of six.
- Construction is modular, and growth requires assembly by astronauts in spacesuits.
- The cost of construction through 2015 was estimated by Claude Lafleur in the March 8, 2010 issue of The Space Review, at $150 billion.
- NASA website* lists the mass of the ISS as 419,455kg, and the pressurized volume as 916 cubic meters at 1 atmosphere. Deducting 1,000kg for the solar array mass, gives a structural mass of 418,455kg, and a mass efficiency ratio of 457kg per cubic meter of enclosed habitable volume.

*www.nasa.gov/mission pages/station/main/onthestation/facts_and_figures.html#.U7SbIhYW3EM

1.2.4 The Evolvable Growth Capable Habitat Concept

By contrast our initial deployed 1 atmosphere pressure hull structure weighs around 1600kg and encloses 4,935 cubic meters of volume, giving an initial mass efficiency of 0.32kg per cubic meter, **an improvement of over 1400 times compared to the ISS, while accommodating 1-g operational loading.**

Other features of our habitat design include:

- Growth capability (as measured by area) in excess of three orders of magnitude.
- Our concept offers a secure mechanism for pressure hull expansion.
- Population range – from 10 to 10,000+ at Biosphere II space standards, or from 28 to 28,000+ using the Stanford Torus metric.
- Initial deployment from earth with 2-3 launches.
- Fully customizable omni-directional shielding equivalent to that afforded at sea level on earth.
- Supports – and requires – development of space mining.

- Maximum theoretically attainable structural and material efficiency, with desired safety factor.
- Affords – and requires – naturalistic ecosystem deployment in space for CELSS.
- Allows emulation of solar diurnal cycle.
- Large shielded vacuum industrial zone (exceeding habitable floor area).
- Protected axial zero-g 'space garage'.
- Designed for robotic in vacuum construction.

Chapter 2

Motivation

2.1 Making the Solar System Accessible to Human Use

We live at a remarkable point in time. Among the profusion of possibilities that present themselves is the potential for the first human settlements beyond planet earth.

A common presumption is that this will occur on the planet Mars. There is little doubt that humans will walk on the surface of Mars, and perhaps maintain permanent bases there, as we have done in Antarctica. Overcoming the challenges in doing this will require great ingenuity. Such difficulties, however, are mere shadows of the difficulty of sustaining viable long-term human settlement – including birthing and raising healthy children – on the Martian surface.

The conclusions within this research paper point to a parallel possibility: that humans in the near future will live on constructed earth-grade real estate in space, either orbiting above Mars, or at any of the myriad potential locations in the solar system offering desirable strategic benefits. The technology for doing this is the subject of this research paper.

There are two reasons for believing that this will occur:

First is the simple fact that in environmental terms, biology is destiny. Along with other life on earth, humans are exquisitely adapted and evolved to live, and thrive, in the specific set of environmental conditions that prevail at or near the surface of planet earth. Even the environment of earth, of course, is not uniformly benign and supportive of life. The mismatch between human biology and the environment at the surface of Mars, however, is such that humans must either remake the planet, and themselves, through large scale terraforming and the attempted human adaptation to 35% earth standard gravity, or live inside artificial environments, possibly including large centrifuges to simulate earth gravity, or all of the above, for such a colonization effort to have a chance of success.

Compared to the challenges raised by such proposals, developing the space habitat technology we describe is a simple task, and as this paper will show, the technology required for construction of the physical and geometric infrastructure for human habitation in space is today within our grasp.

The capacity to engineer life support systems in space, seen from this perspective, will be the capacity to recreate in microcosm the environment of earth in space, including the provision of artificial gravity effect through rotation, and of sufficient levels of shielding from the DNA-shredding impact of galactic cosmic radiation and solar proton events.

Once the feasibility of building life support infrastructure of this kind is established, it becomes natural to think in terms of furnishing such accommodations in the manner that is most pleasing and supportive of life, in the largest sense.

In such a scenario, we would choose to take with us into space everything that supports and

nourishes life, creating jewel-like island worlds – shrines to the beauty and richness of earth's biosphere.

The technological capability to accomplish this will owe much of its inspiration to the vision of Gerard K. O'Neill in the 1970's [5]. O'Neill's concept was significantly ahead of its time, however, and no economically feasible pathway was found to attain the immense structures envisaged. While the concept has gained wide currency in the realm of science fiction, its realization is still generally considered to lie in the distant future.

The second reason why the time may now be ripe for the space habitat concept to be realized is the coincidence of two new and fruitful ideas. The first of these ideas is an entirely new development in the mathematics of structural engineering theory – the creation of rigorous mathematics for the engineering of tensegrity structures. This mathematics underlies and makes possible the second idea, that of growing a very large space habitat structure from a small seed structure, compact enough to be launched from earth, and to do this using chiefly space based materials.

In the following chapters we will outline the relevance of tensegrity engineering in this context, and its application to such structures through our research.

Chapter 3

Background

3.1 The Development of Access to Space

From a systems engineering perspective, the history of man's approach to access space involved these evolutionary steps:

1. During the 1960s, the entire system was designed *a priori* and constructed on earth in its full operational size, and launched from earth. This required expensive launches to insert into space the larger volume and mass of the operational configuration of the manned or unmanned space hardware system.

2. During the late 60s and early 70s, launch volume was reduced by deploying selected components after access to space. The first efforts involved man in the deployment process.

3. During the 1970s robotic arms helped deploy the satellites from the shuttle bay.

4. The next logical step toward economy was to launch large sus-systems for assembly in space, as demonstrated in the International Space Station (ISS).

5. A logical further evolutionary step may involve launching only raw material (e.g a roll of cable and a box of bars) for in-situ fabrication of structural systems in space.

6. The final step in structural terms of this evolutionary sequence will be the ability to launch only a set of tools to mine asteroids or the moon and use space material rather than earth materials to fabricate the structural system. Such capability would be foundational for a general capability for space settlement. Development of this capability will not be intrinsically hard, once the motivation to bring it into being exists.

7. For manned systems and habitats, the final grand challenge is to create a technology that allows one to *grow* habitat structures from one operational configuration to another, while enabling more capabilities and more humans with each growth cycle.

It is evident that a permanent presence of man in space (including birthing and growing children) will require a 1g habitat. Such a habitat technology will be economical only to the degree that the above grand challenges are solved. Our research focuses on the final grand challenge listed above. Several innovations and revolutionary technologies will be required to do this economically. The first requirement will be to develop engineering technology to grow a space structure. The second requirement will be to develop engineering technology to support the ambient loads

of the operational system with the smallest possible mass (resources from expensive mining or earth launches), and preserving the structural integrity in the presence of these loads (including atmospheric pressure) during growth cycles. Hence the growth must be a controlled process, not a jack-in-the-box type of deployment.

Successful space research has always led the way to improved science and engineering in non-space technologies. We expect the same revolutionary contributions to improve the design and manufacturing of earth-based structures. The book "Tensegrity Systems" [1] provides the evidence that Tensegrity Engineering (a major research component of this study) can revolutionize the kinds of structures we build and the methods we use to build them.

3.2 Tensegrity Engineering, a Revolutionary Approach to Structure Design: An Enabler for Space Habitats

A habitat in space will require the most efficient use of material possible. This will require revolutionary approaches to:

1. design material
2. fabricate material
3. find the most efficient topology for structure.
4. form the material into structure
5. Control the structure

The history of engineering made giant strides as engineers and scientists were able to advance the design criteria. These advances loosely followed in this sequence:

1. Designing structures just to support static gravity loads (e.g Stonehenge)
2. Designing structures to survive a variety of static and dynamic loads (e.g. wind, earthquakes)
3. Designing structures that could be dynamically controlled (e.g. aircraft, spacecraft)

Engineers inherited myopic vision as we moved from one of these advancements to another, by thinking of these problems as *additive*, where one simply *adds* a new technology, say dynamic or control analysis, to the existing structure design methods. More engineers are beginning to understand now that one cannot integrate two disciplines by starting at the state of the art of either one. (e.g. structure design and control design). For example, one cannot know what dynamic features are best to model (or manufacture) for control design, because the control is typically designed *after* the structure is designed and the dynamics are modeled. Control design relies on the given model, and yet the control will add dynamics of its own possibly exciting some unmodeled features of the structure itself. This demonstrates the interdependence between the disciplines of structure design and control design. Yet universities tend to treat them as separate subjects.

It has been said that in the first half of the 20th century physics drove and enabled new technology, and that engineering was the enabler in the last half of that century. But engineering has left us with many component technologies (e.g. materials, structure, dynamics, controls, signal processing) without providing rules how to integrate the design of components to get a coordinated system design. There is still no generally accepted solution to this dilemma, but we will present

strong evidence that the *tensegrity paradigm* for structures provides the best analytical tools to integrate structure design, control design, and signal processing. These are critical steps to enable a mission of the scale of a 1g habitat in space, and these advancements will serve as enablers of many *non-space* applications of structure design.

One may loosely define tensegrity as a prestressable structure whose structural elements are axially loaded. This means that the compressive members (e.g. bars, pipes) are not subject to bending moments (except from inertial forces). This saves mass since the member diameter does not have to be sized to support bending moments. In tensegrity the overall structure can bend, but no members bend.

These are the properties of tensegrity that underpin all of engineering mechanics and efficient structure design:

- Instead of designing the control system to work against the structural equilibrium (e.g. to modify shape or stiffness), the tensegrity control commands actually modify the structure itself in such a way that it is always in equilibrium (e.g. at each new required shape).
- Tensegrity can change its stiffness without changing its external shape (by changing equilibria of internal configurations).
- Tensegrity can change its shape without changing its stiffness (by changing equilibria of internal configurations).
- The most efficient structure (minimal mass) for supporting compressive loads is a tensegrity structure.
- The most efficient structure (minimal mass) for supporting cantilevered bending loads is a tensegrity structure.
- The most efficient structure (minimal mass) for supporting simply-supported bending loads is a tensegrity structure.
- The most efficient structure (minimal mass) for supporting torsion loads is a tensegrity structure.

Since every structure has components experiencing at least one of these kinds of loads, we have shown in published works that the understanding of tensegrity is fundamental to the insights for structure design, and that the analytical tools developed for this tensegrity paradigm will allow tensegrity engineering to advance the design of unlimited applications and technologies. These are widespread contributions that can be a profound byproduct of the habitat research.

Chapter 4

An Illustrative Mission Concept

4.1 Habitat Growth Capability as the Enabler of Economic Development

To illustrate its potential to create value we describe the application of this technology to an expandable space/life sciences research platform located at one of the Earth-Moon libration points, (to be determined). Starting from a highly compact initial state, the platform will be capable of progressive increases in size and functionality, using processed regolith for feedstock material, and in-situ manufacturing and fabrication techniques to transform this into structural components. The mission scenario begins with the launch and self-deployment of a compact lightweight, tensegrity based, core structural system, comprising the skin and bones, muscles and tendons for a pressure hull and shield structure, accompanied by a separate deployable primary mirror. Following deployment, pre-positioned bulk water-shielding acquired from asteroidal (or lunar) sources is installed, sufficient to achieve a baseline minimum level of protection from radiation. With required onboard supporting equipment, this will comprise a fully functional life support platform capable of repeated growth iterations subject to availability of raw materials. With an initial major radius of 10m and minor radius of 5.5m the structure supports approx. 700 sq.m of projected area. With a rotation period of 11 seconds a 1/3 g gravity effect is produced, offering a physiologically feasible set of initial conditions, capable of evolution in the directions determined to be most desirable.

Using the population density figure from the 1975 Stanford Torus study [5] of 67 sq.m per person, the habitat will support a crew of 10, with a scientific functionality comparable to the ISS on steroids – massively more space available for appropriate research, 2 year-stay initial shielding levels and partial gravity effect, plus long-haul capability to operate in deep space. The habitat will have unique value as a platform for fundamental space/life sciences research, and specifically into the nurture and development of long-term life support ecosystems, a primary goal being to develop and evaluate robust candidate systems and monitor indicators of ecosystem health.

The facility will support research in space horticulture, space medicine, space manufacturing, lunar surface scientific research, and early stage commercial and lunar tourism operations. Maximum length of stay for occupants will progress with the growth in thickness of shielding.

As a point of reference on the growth characteristics, allowing for boundary effects of the expansion mechanism, a sequence of 11 feasible growth events (each doubling the previous projected surface area) would result in an increase of projected area of 950 times.

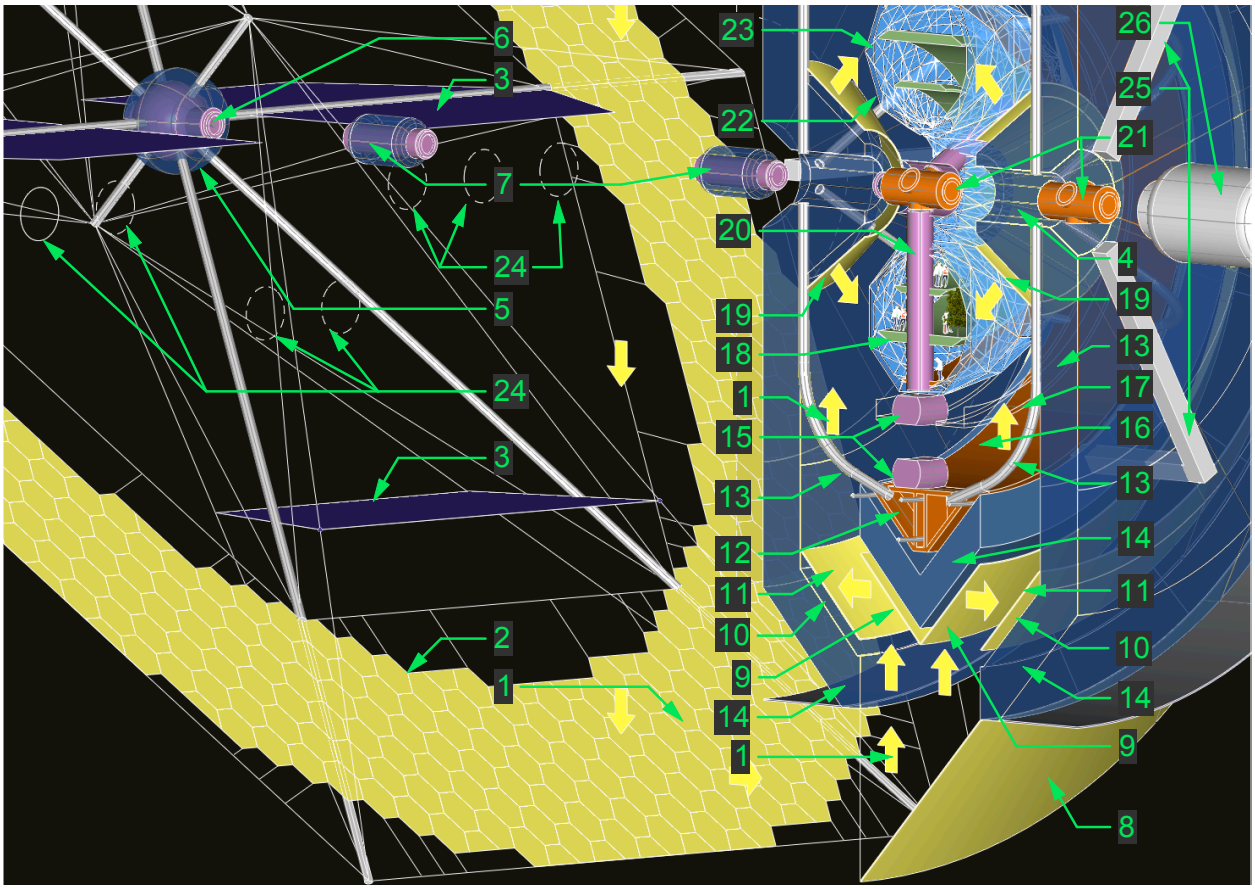

Figure 4.1: 3D Cutaway – Initial Size Habitat as Deployed

This is a schematic closeup 3DCAD image showing one limb of a single primary mirror initial habitat deployment after acquisition of sufficient water to provide 4m of shielding. The image shows schematic details for the structure of a tensegrity primary mirror. Numbered key: 1.) Direction of light rays, 2.) Modular primary mirror, 3.) Solar panel arrays, 4.) External docking port, 5.) Primary mirror hub, pressurized and shielded, 6.) Shuttle docking port, 7.) Shuttle, 8.) Mirror #2, 9.) Mirror #3, 10.) Machine service cavity, typical for all mirrors., 11.) Mirror #4, 12.) Bulk material storage bin, 13.) Bulk material loading chute 14.) Water shielding shown at 4m thick, 15.) Rotational transit system, 16.) Workshop floor, 17.) Lightweight disassembly deck with guard rail, 18.) Habitable interior, 19.) Mirror #5, 20.) Elevator shaft, 21.) Docking taxi with airlocks, 22.) First generation deployed pressure hull, 23.) Second generation expandable pressure hull in pre-deployment position inside existing hull, 24.) Microwave power transmission dish provisional locations (rectenna not shown). 25.) Freight elevator shafts, 26.) Visiting spacecraft

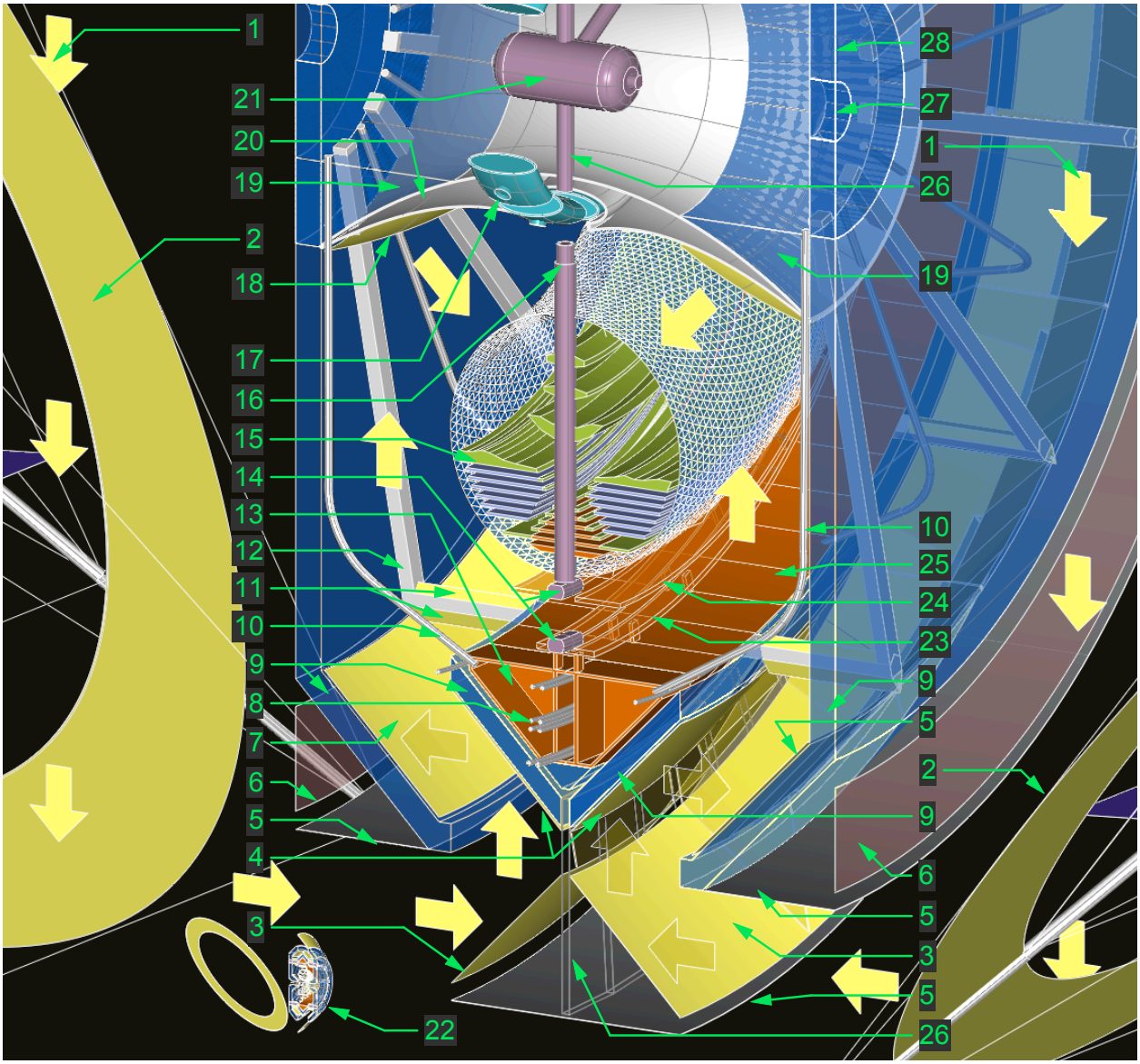

Figure 4.2: 3D Cutaway – Mature Size Habitat After Multiple Growth Iterations

This composite closeup 3DCAD image shows one limb of a dual primary mirror habitat after its projected area has been expanded approximately 950 times from initial deployment size (shown in single primary mirror version to scale at bottom left.) The image shows schematic interior details and the dual primary mirrors in the left background and bottom right foreground. Numbered key: 1.) Direction of light rays, 2.) Dual primary mirrors, 3.) Mirror #2, 4.) Mirror #3, 5.) Solar panels, 6.) Possible location of microwave power transmission rectenna, 7.) Mirror #4, 8.) Schematic suspension cables (not to scale), 9.) 31m thick water shielding, 10.) Bulk material loading chute, 11.) Deflecting mirrors, 12.) Freight elevator shaft, 13.) Bulk material storage and process bin, 14.) Rotational transit system, 15.) Pressurized habitable interior, 16.) Elevator shaft with retractable/extendable uplink airlock, 17.) Ring shuttle with airlocks, 18.) Mirror #5, 19.) Water storage reservoir, 20.) Tensegrity diaphragm, 21.) Pressurized hub with docking ports doubles as lifeboat in emergency, 22.) Initial deployment habitat size to scale, 23.) Raised platform deck for rotational transit system (RTS), 24.) Disassembly deck, 25.) Workshop floor, 26.) Tensegrity structural support spine, 27.) Small diameter docking portal, 28.) Large diameter docking portal.

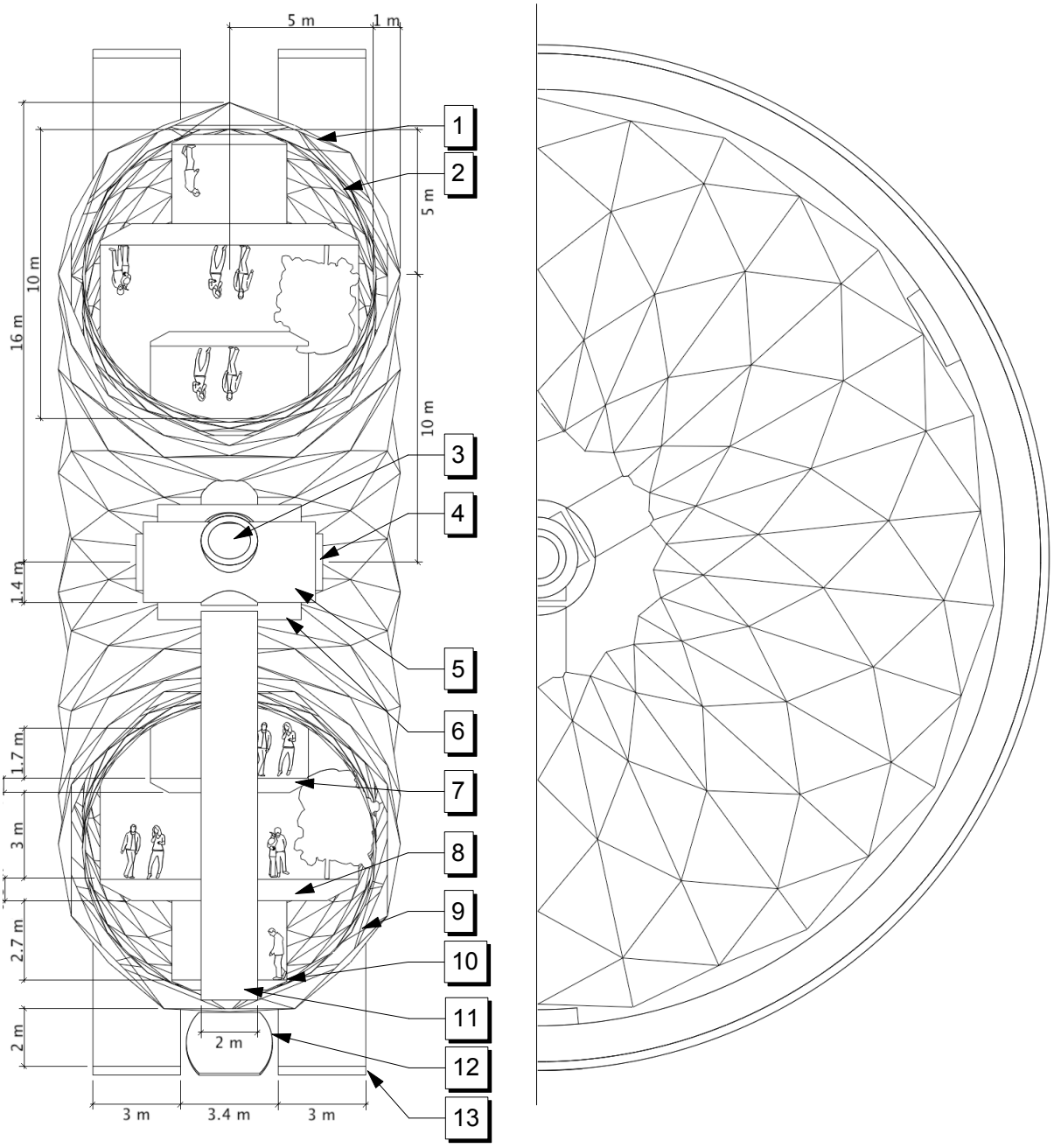

Figure 4.3: Section and Elevation of Pressure Hull Prior to first Growth Iteration

This figure shows section and elevation line drawings of the habitat pressure hull. Numbered key: 1.) Pressure hull as deployed from earth, 2.) New pressure hull ready for expansion, 3.) Side airlock of docking taxi, 4.) End airlock of docking taxi, 5.) Docking taxi pressure hull, 6.) Hub docking port, 7.) Attic deck structure, 8.) Ground surface deck structure, 9.) Cavity space between existing and new pressure hulls, 10.) Basement deck structure, 11.) Base of elevator column, 12.) Rotational transit cab, 13.) Disassembly platform.

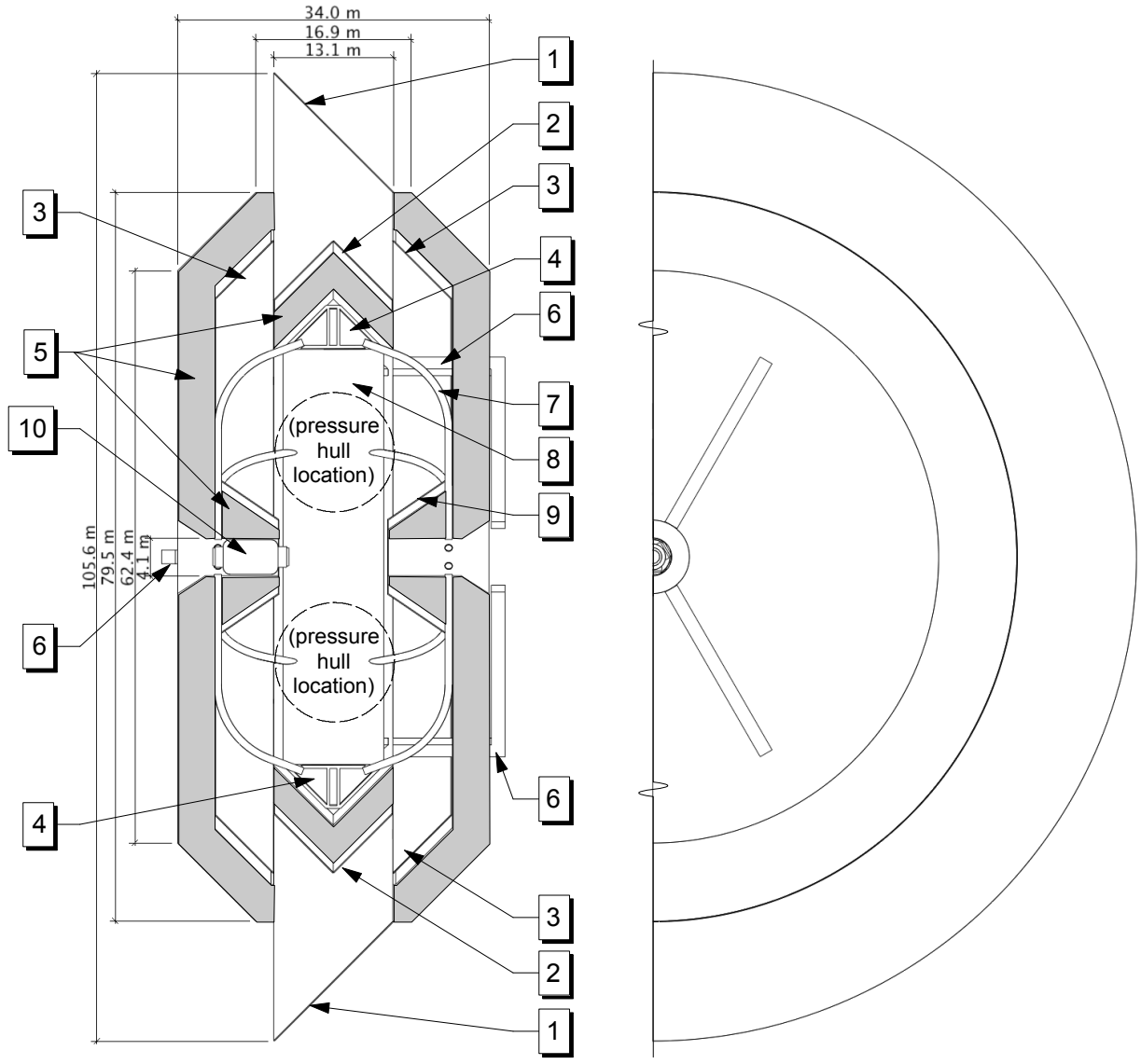

Figure 4.4: Section and Elevation of Shield Structure as prepared for first Growth Iteration
This figure shows section and elevation line drawings of the habitat shield structure and associated workshop floor/service deck. Numbered key: 1.) Mirror #2, 2.) Mirror #3 with V-shaped shielding baffle behind, 3.) Mirror #4, 4.) Bulk material storage bin, 5.) Water shielding, 6.) Freight elevator/bridge, 7.) Bulk material chute, 8.) Workshop floor/service deck, 9.) Mirror#5, 10.) Primary mirror access shuttle in berth.

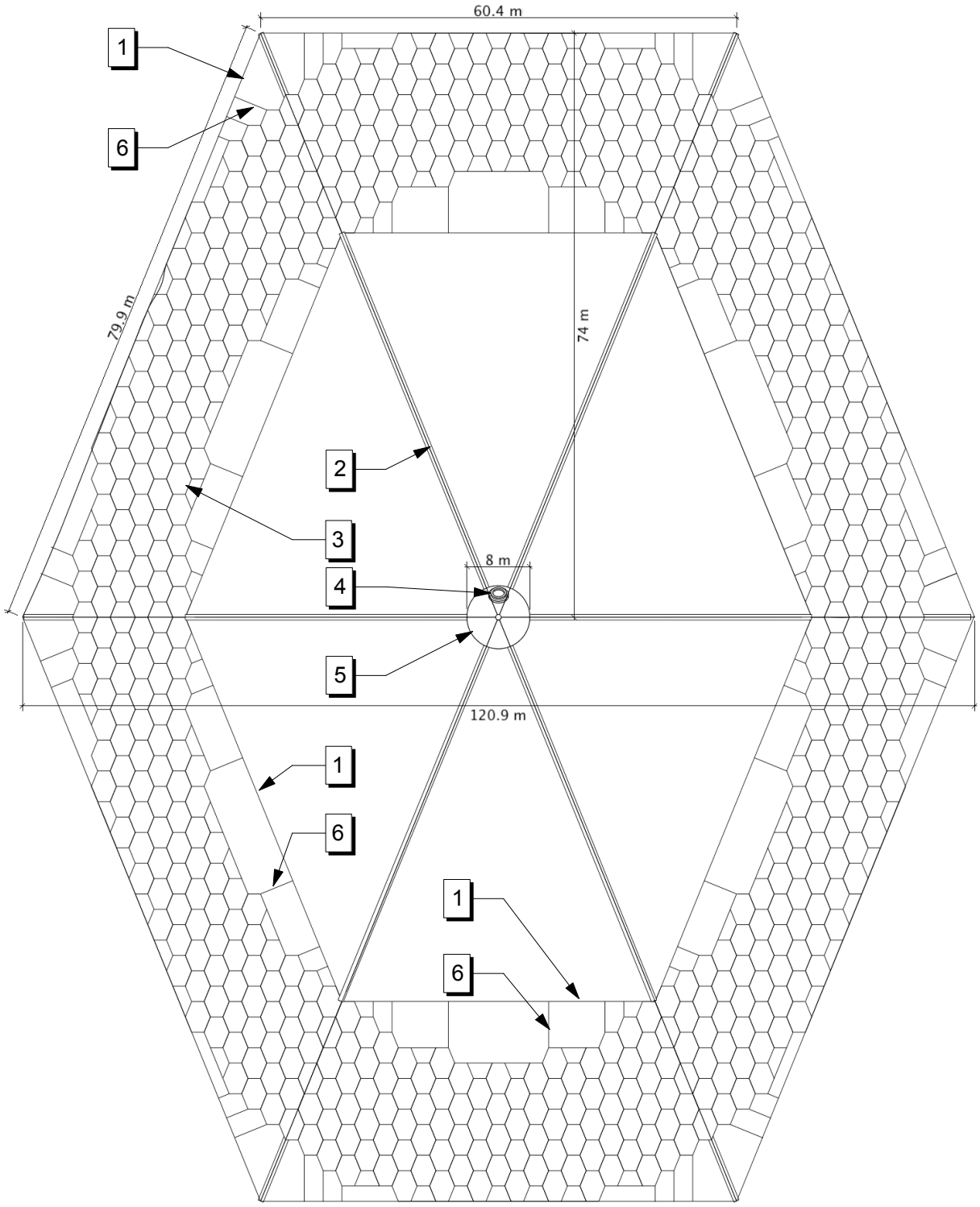

Figure 4.5: Orthogonal Elevation of Primary Mirror at Initial deployment (PV Arrays omitted)
This figure shows a plan view of the primary mirror viewed perpendicular to the mirror surface. Numbered key: 1.) Primary suspension cables, 2.) Primary compression strut, 3.) Modular mirror panel, 4.) Docking port, 5.) Primary mirror hub, 6.) Secondary suspension cables.

Chapter 5

Design Principles and Functional Drivers

5.1 Safety and Evolvability as Strategic Principles

The scale of operation enabled by this concept implies

a time frame spanning many decades. Prudence requires dividing the problem into smaller steps, and showing that the long-term goal is feasible through repeating these steps using today's technology. This approach based on the premise of periodic renewability of structure, allows for the routine incorporation of improved technology as this becomes available.

In our analysis to determine the key functional drivers and dominant form factors for growth of a pressurized habitat in space this strategy of dividing the overall objective into a series of smaller repeated growth iterations also has the benefit of allowing the repeated use of essentially similar procedures, building on lessons learned at each cycle, in addition to allowing the adoption of new materials and techniques.

5.2 Articulation of Functional Drivers

In commencing our research we sought to stirke the most logical and fruitful balance between dominion form factors, and develop growth enabling geometry from this basis. A functional geometry has emerged, with a well articulated separation of functions with demanding space requirements.

5.2.1 Structural Principles

The following observations are foundational:

1. Minimum mass
   For any given objective, mass is to be minimized through tensegrity engineering. The following observations are predicated on the use of tensegrity engineering:

2. Cables: Growth by Extension
   Tensegrity structures are dominated by cables. In growing a tensegrity structure the length of cables may be increased by unwinding a reeled cable or by adding links to a cable comprised of links.

3. Cables: Growth by Multiplication
   Capacity of the cable system to carry load may be increased by replacing a cable with a thicker cable, by adding multiple cables along a given line, or by increasing the frequency of cables in a cable grid.

4. Struts: Growth by Extension
   As tensegrity structures are dominated by tensile members, the importance of individual strut is increased. A given strut may be replaced by a more mass efficient tensegrity compound strut, the appropriate level of regression being a function of economics. All references to posts or struts should be understood as including the option for equivalent tensegrity elements where this is economically desirable. The habitat will employ many tensegrity compression struts, and many will include a built-in expansion capability across a given range. Absent other factors, the extent of expansion for a given instance will be determined by the extent of the current overall growth cycle.

5. Struts: Growth by Multiplication
   In the habitat torus, where the structure is overwhelmingly dominated by tension forces – atmospheric pressure providing the compressive counterbalance – rigid compression elements are required for the application of control moments to counter precession and for stability control. This is accomplished by means of a system of multiple widely distributed momentum wheels mounted on rigid struts. As the pressure hull grows in size additional units will be added to maintain the required control moments.

5.2.2 Evolvability, and Limits of Growth

1. Shielding against GCR – for now, More is Better
   At our present level of ignorance in regard to what constitutes sufficient shielding against GCR in deep space, we have chosen an open ended strategy to develop long-term shielding capability for the habitat by providing the capacity to add shielding until experimental data show that a point of sufficiency has been reached. Given that the habitat is infrastructure and not primarily a vehicle requiring rapid acceleration, a mass based passive shielding system is the logical choice. Shielding thickness will be developed as rapidly as possible, enabling progressively longer periods of residence on the habitat before rotation back to earth. The rate of availability of water in the quantities required, and the cost and timescale involved in its acquisition, will be a major determinant of the growth arc through time. Recent reports that the asteroid 3225 Don Quixote, which orbits between Jupiter and Earth, is in fact a comet containing an estimated 100 billion tons of water, are indicative the the needed resources will become available when there is a demand for them.

2. Limits on Growth
   There are advantages to size and there are costs to size. If the advantages outweigh the costs, growth is desirable and this system will allow the growth to occur. A law of increasing costs applies in that each expansion of the structure requires more mass per unit of projected surface area to support it (basically this means the cost per square foot of the maximum width ground plane for the habitat increases each time the structure grows). There are ultimate physical size omits for rotating structures where the mass required to restraint centrifugal force goes to infinity. IN the case of our structural system this limit is at around a 300 km radius.

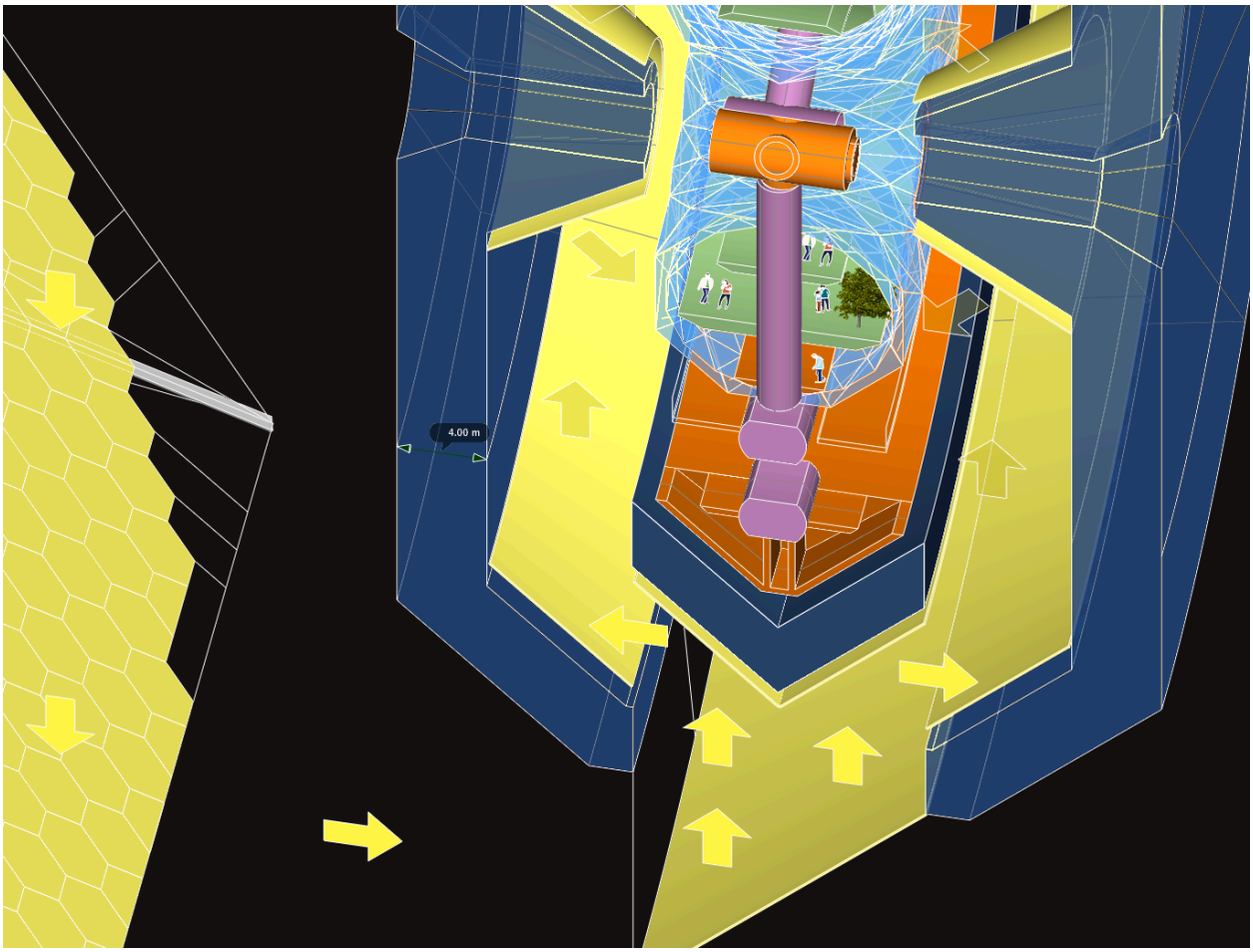

Figure 5.1: Relationship of Mirror and Shielding Systems

This illustration shows the relationship between the requirements of the mirror system to admit light and the water shielding to prevent line of sight penetration of GCR and SPE. Initial goal for water shielding of the deployed habitat is 4m as shown here. Mirror surfaces are yellow.

5.2.3 Sunlight vs. Shielding

The requirement to admit light to the habitat while excluding harmful radiation is a powerful shaping influence on the form of the habitat structure.

1. Strategy for Shielding and Light
   Due to the thickness of water shielding required and the rapid reduction in transmission of light with increasing depth, it is not practical to get sufficient quantities of light directly through the depth of shielding required to approximate conditions found on earth, even at high altitudes, let alone at sea level. Therefore a break must be introduced in the shielding perimeter and am offset pathway with mirrors employed to bring light to the interior.

2. Separation of Shielding from Pressure Hull
   Due to the required thickness of water shielding against GCR, this shielding must be separated from the pressure hull, as a completely independent structure. This allows for a much reduced rotation rate and reduced loads from the shielding. (A small rotation is preferable to none, as it allows for the exercise of control and the use of the gyroscopic effect for stabilization.)

3. Integration of Light, Shielding Geometry
   The geometry of the shield structure and the geometry of the mirror system have been integrated to a high degree, resulting in an efficient shared structure.

5.2.4 Raw Materials: Handling Storing and Processing

A growing structure requires feedstock materials. Handling and processing these flows has exerted a shaping influence on the form of the habitat.

1. Bonus Low-g Workshop and Service Deck and Storage
   Supporting large scale structural growth requires handling a large flow of materials into the habitat. An incidental result of the mirror and shielding geometry is the availability directly below (outboard from) the pressure hull of a substantial unpressurized volume at low-g, suitable for storage of raw asteroidal/lunar or other bulk materials. This offers potentially high value as a shielded low-g industrial processing and fabrication zone with large below deck capacity, where bulk robotic processing of materials may be carried out.

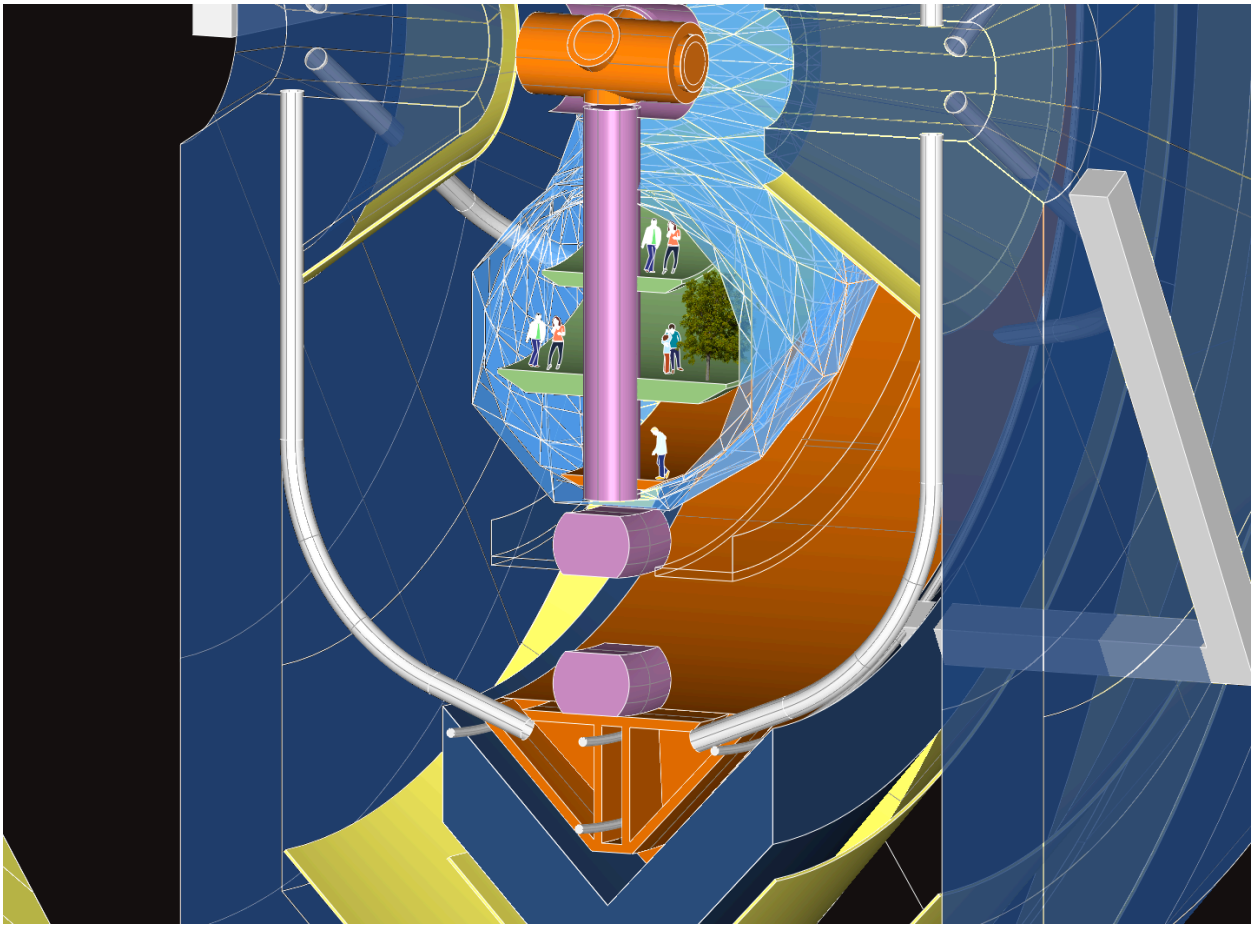

Figure 5.2: Service Deck
The Service Deck (orange) is outboard from the pressure hull (blue) and encloses material storage bins and fabrication shops. Freight elevators and bulk material chutes (white) deliver material from the hub docking ports.

2. Bulk Material Loading Shafts
   Shafts to deliver materials and cargo from the central docking port to the storage bins below the Workshop Floor are required. Some of these may be enclosed chutes taking advantage of centrifugal force to deliver unprocessed regolith. Others will be elevator shafts on the inside of the main shield structure wall, with bridges across the light shafts through which sunlight flows to the torus interior. The bridges can be covered with mirror surface panels, above and below, and arranged so that light striking the underside of one bridge will be directed laterally towards the upper surfaces of each adjacent bridge, minimizing loss of light and rendering them effectively invisible from the interior of the torus.

5.2.5 Internal Access – Rotational Transit Systems

Differential rotation of the major structural elements requires dedicated transit systems to provide direct access between these elements.

1. Pressure Hull / Workshop Floor

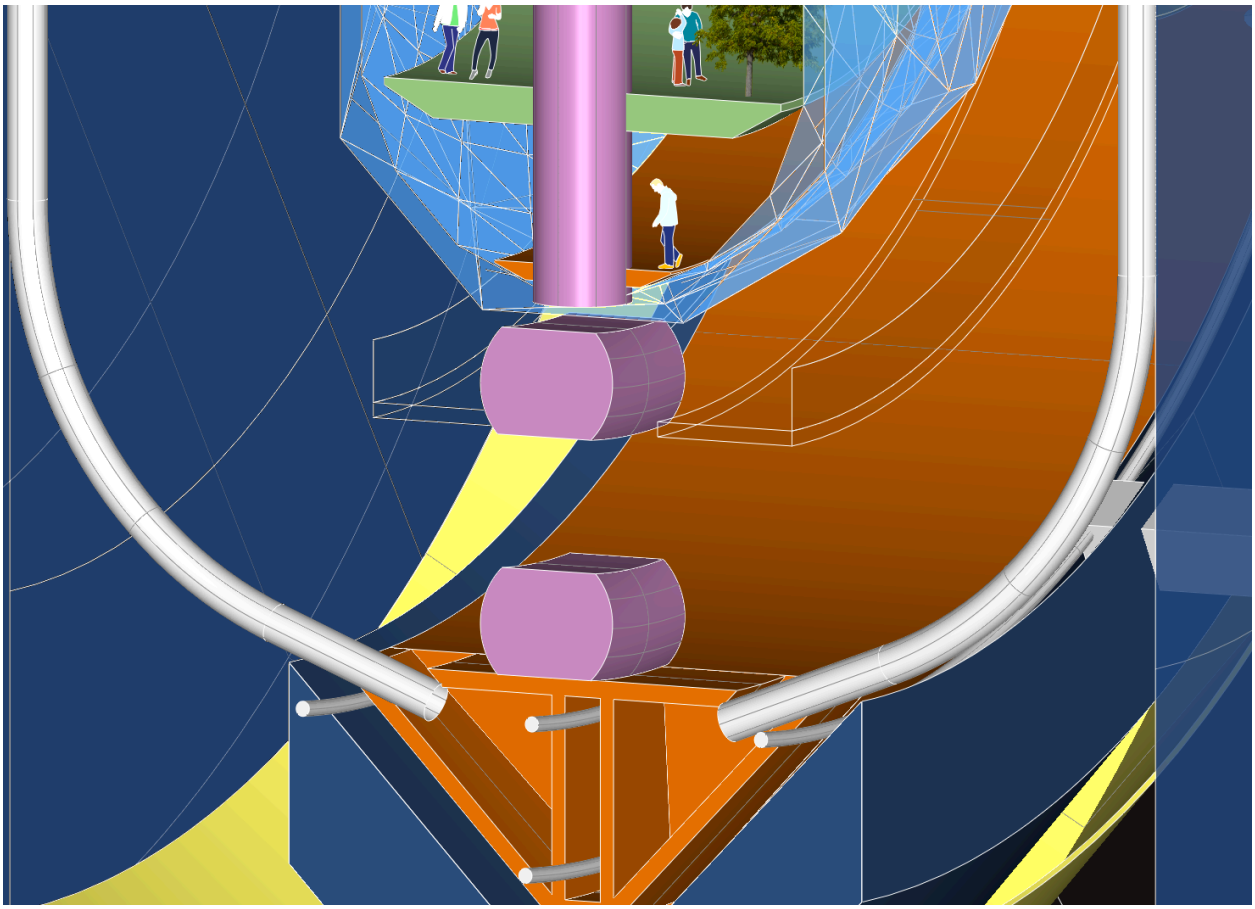

Figure 5.3: Rotational Transit System
The Rotational Transit System (purple) is a gondola-style suspended vehicle. It is released from or captured by an inclined rail suspended from the spinning torus (not shown) – and rolls on its undercarriage system along the Service Deck. It enables access between the bottom of the elevator column and

To bring inside all the components for construction of the new hull and to safely decommission and remove all the elements of the old hull it will be essential to have a means for direct access between the pressurized torus lower level and the workshop and service deck below, capable of accommodating to their different rotation rates.

To accomplish this, the elevator columns connecting the habitat to the central hub would be extended down to open through the floor of the pressure hull. A pair of deployable / retractable suspended inclined rails would face in ram and wake directions. These would allow ascent and descent of a bogey suspended gondola with wheeled undercarriage to the service deck below. Hardware providing capability analogous to this already exists in cable car gondola systems.

2. Evolution of Hub Access and Emergency (Lifeboat) Systems

   While a simple unconnected coaxial hub geometry for the Pressure Hull and Shield Structure will suffice at the beginning, it will become desirable to have a more sophisticated geometry to deal with the stability and alignment needs of the two structures, as scale increases. The elevator shafts to the central hub would be interrupted by a circular subway-train type articulated system of structurally linked – but separately pressurized – compartments, each with its own airlock capability. This would be located above the pressure hull close to the central axis where relative rotational velocities are reduced. This flexible jointed ring structure would have a passive magnetic suspension and be able to speed up or slow down its rotation rate, to match both the pressure hull and the shield structure in turn. The elevator shafts up from the pressure hull would terminate directly below this system with retractable and extendable segments fitted with docking airlocks. The central hub in this configuration would thus be continuous with the Shield Structure, not the Pressure Hull. The great advantage of this system is that the ring shuttle is small relative to the pressure hull and to the shield structure, and can be engineered to be maneuvered relatively easily to accommodate each of these in turn in the event of any relative alignment issues. In addition a very large central garage space is opened up. In this mature state, the central hub becomes a fully capable

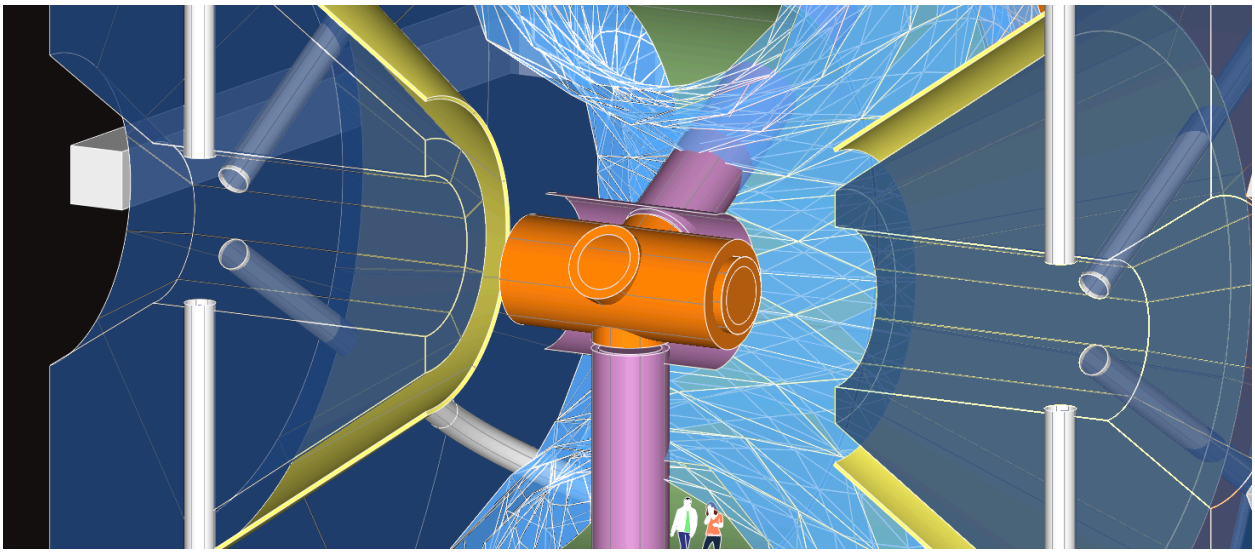

Figure 5.4: Docking Taxi
The initial state of the docking hub, with Docking Taxi / Lifeboat shown at the center in orange.

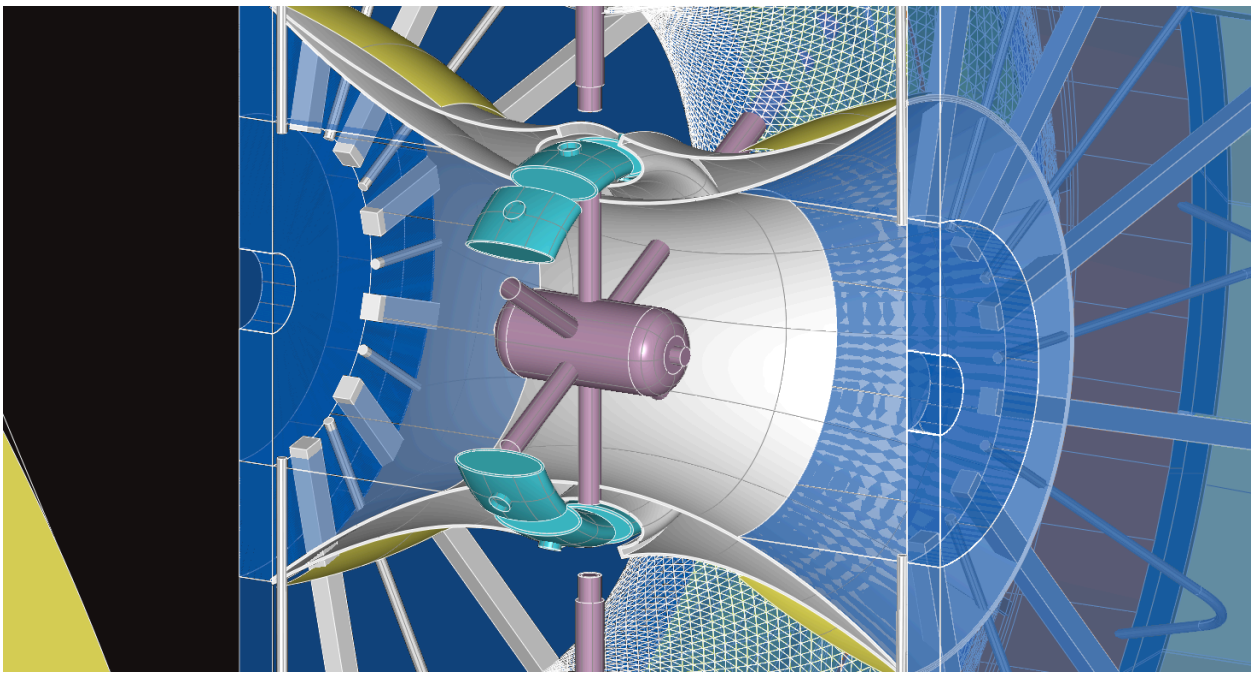

Figure 5.5: Mature Docking Hub
The mature state of the docking hub, with Ring Shuttle and central Docking Hub / Lifeboat.

emergency evacuation spacecraft in the event of emergency.

5.3 Development of the Expandable Hull Concept

The concept of multi-hull protection for the pressure hull has been a continuous thread through our work.

5.3.1 Self-Renewing Hull Systems

One of our earliest studies was of a perpetually self-renewing cycling hull concept. This goal was abandoned after it became clear that the requirements of shielding against GCR and SPE would necessitate separating the shield in form the pressure hull and greatly increasing its depth over time, rendering the concept of a separate cycling outer hull surface obsolete. The desirable concept of recyclability of an outer shield structure was retained however, and is embodied in the water shield structure of our present concept.

5.3.2 Multi-layer Hulls

Another manifestation of the same impulse was in our investigation of multi-hull structures. There are obvious desirable qualities in this concept, and we do not therefore discount its future application in this field, although a word of caution is in order regarding the reduction in light transmission that results from increasing net thickness of hull material. However we conclude that adding a second hull will be most appropriate when a habitat structure has already accomplished the anticipated needs for expansion, as our investigation shows that such multi-hull structures will be costly and difficult to grow, in comparison to single hull structures. Significantly, as detailed in

the next section, our preferred growth strategy for the pressure hull utilizes a temporary dual hull configuration as a key step in ensuring success in the growth iteration.

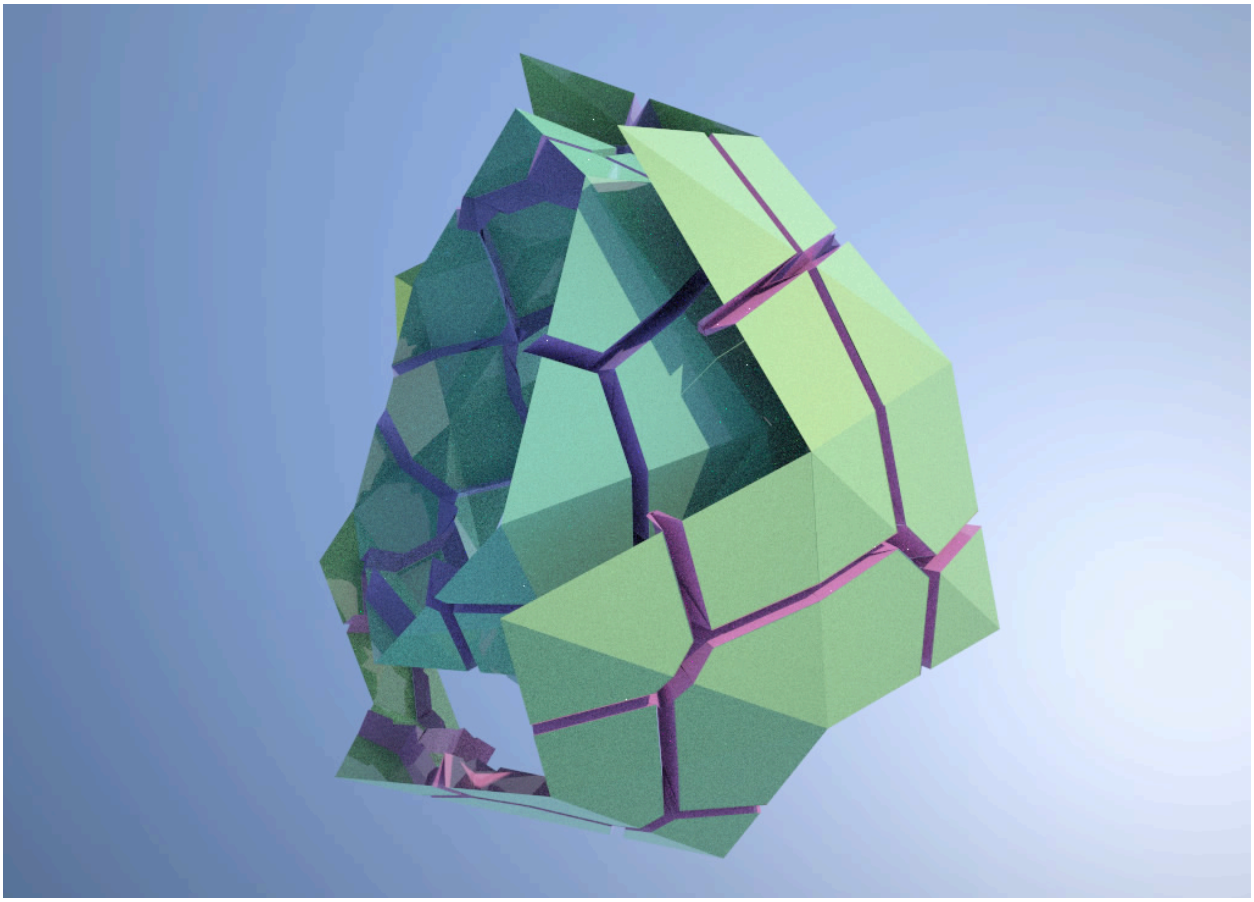

Figure 5.6: Double Hull Growth Geometry

The image shows component segments of a double hull geometry in a partially expanded state, illustrating the typical arrangement of growth seams with folded hull material. This approach represents only a partial solution of the problem and was abandoned in favor of the 'inside out' approach. A typical progression of the seam alignments in relation to the triangular panel edges may be observed.

5.3.3 Overall Folding Protocols

In addressing the design of the hull expansion mechanisms, several precursor questions needed to be studied and answered before the main challenge of formulating an expansion protocol could be addressed. Among these were:

- What goals should be set regarding the long-term proportions of the pressure hull?
- What is the effect of a particular growth mechanism on the evolution through time of the habitat proportions?
- Which growth mechanisms have the most desirable growth characteristics over time?

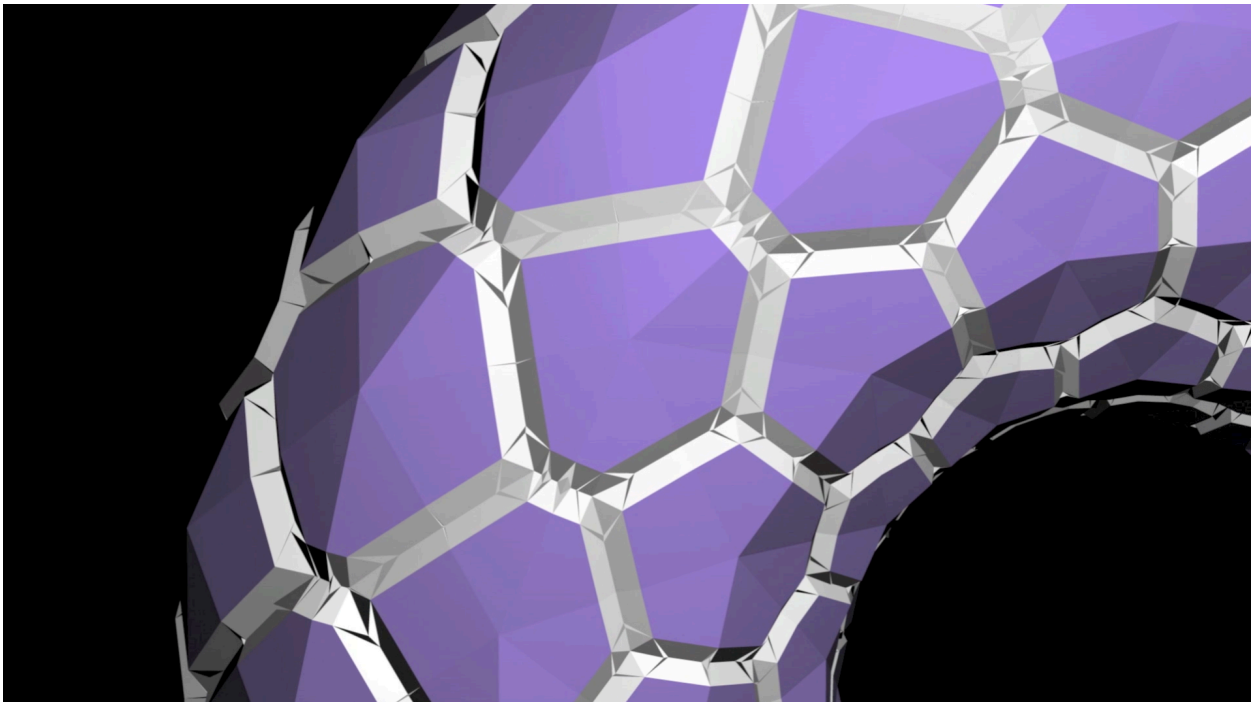

Figure 5.7: Typical Hull Folding Protocol
This image illustrates a typical application of the folding protocols we developed. There are sometimes more than one set of folds possible to achieve a given end result. The geometry is most readily understood at the half expanded state as shown here.

We decided that it would be desirable as far as possible to maintain a constant set of proportions over time so that desirable functional attributes mediated by geometry would more easily be preserved without major interventions. We decided therefore to exclude from consideration the various potential growth mechanisms that substantially altered the proportions of the torus pressure hull through time. As a result of this we decided to aim for a growth paradigm that involved growing both the major and minor radius of the torus in parallel, with the goal of maintaining the desirable fat proportions of the torus over time, and to a great degree this goal was achieved. This decision to grow the entire surface of the torus equally, translates to the need to enlarge every facet of the torus at the same time. This led directly to an origami-like configuration where pre-folded material is unfolded across all the faces of the hull in parallel, and then to study of the exact geometric protocols that would define a workable folding system.

5.3.4 Torus Hull Expansion Mechanical Strategy Options

There are three potential pathways to hull expansion that might prove feasible to pursue.

All of them depend on precisely arranged origami-style folded panels of hull material, that are attached to either the exterior or interior surface of the new hull along a network of precisely oriented growth seams.

These seams are arranged between two fundamental alignments with respect to the hull panel edges. The first is perpendicular to the edges, for simplicity in handling the planar change from one panel to the next. The second is along the edge shared by two adjacent hull panels.

A progressive transition occurs between these orientations from the outward facing portions of

the torus to the mid-section and through to the inward facing portions. Halfway round from the outer portion of the torus to the inner portion, the growth seams align perpendicularly at the panel edges dividing them into three 4-sided facets, and the location of the meeting point of these three dividing seams occurs near the centroid of the triangular panel. Elsewhere, however, continuity of the growth seam segues this division to result in one 5-sided panel and two 3-sided panels, due to the progressively shifting proportions of the hull panels from outside to outside across the torus surface.

5.3.5 Option A. Inside Out Expansion (our choice)

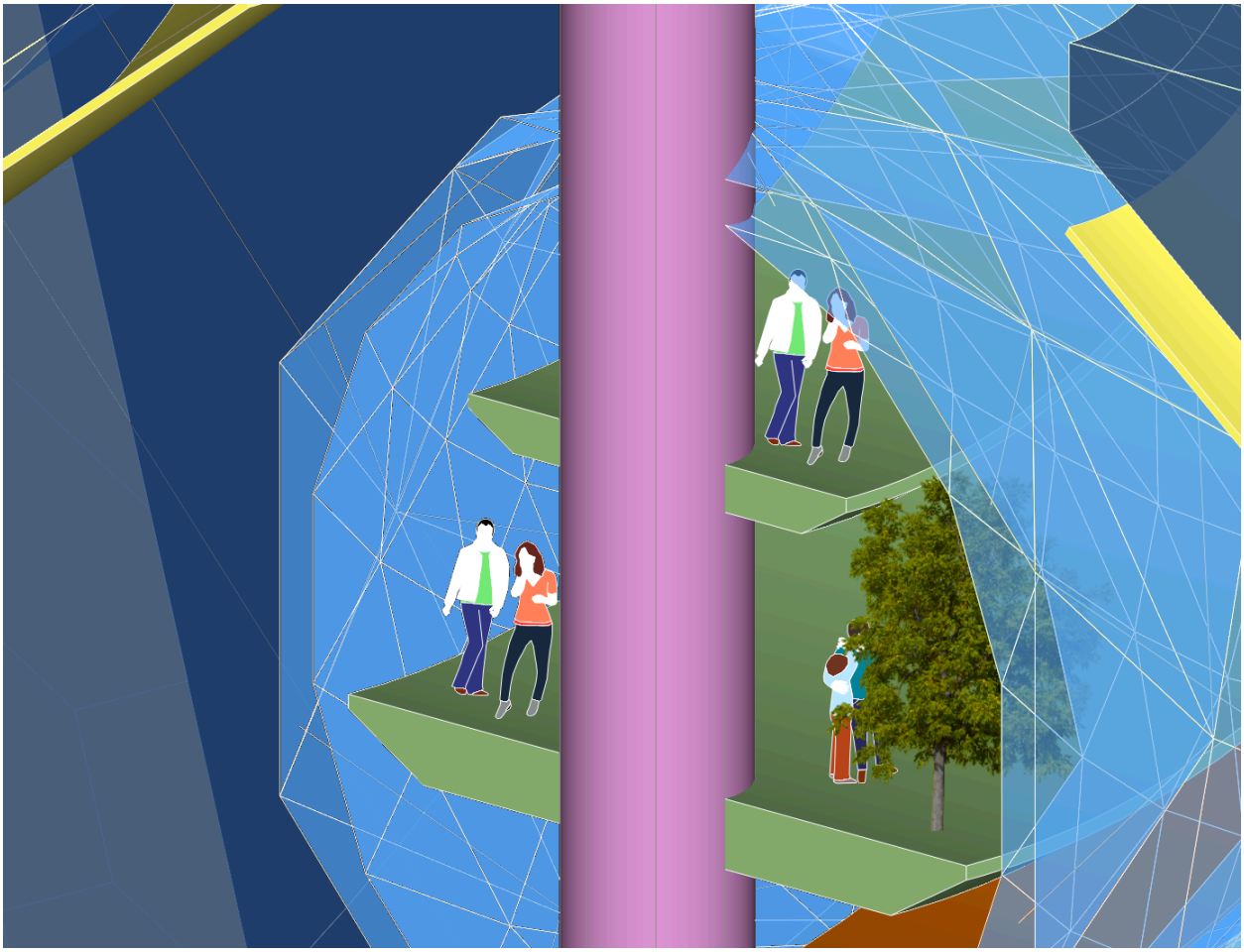

Figure 5.8: "Inside Out" Hull Growth Setup
The new hull to is built just inside the existing hull with pre-folded expansion seams on the outside, and the hull tensegrity cables attached to the hull material at the inside surface. Since the new hull will expand to nearly twice its initial size it must have a greater number of panels to keep the material span within constant.

This approach is based on the counter intuitive idea of constructing a new hull with built-in expansion capacity *inside* the existing hull, pressure testing it before the decision is made to commit to disassembling the obsolete outer hull and then finally expanding the new hull. This method requires the folded material to point outward, and the hull load bearing cables to be

attached to the inside face of the hull. While this adds an extra attachment requirement, it assures continuous access to the cables for maintenance and inspection from the inside, an immense plus in our view.

The benefit of this increased safety is purchased at the cost of the investment in expenditure of energy and processing and fabrication of materials. The significance of this in automatic ongoing maintenance to the degree that the structure is continually rebuilt at each growth event ensuring additionally that technical advances can be incorporated along with the benefit from lessons learned along the way.

5.3.6 Option A. Detailed Folding Protocols

Given the desirability of compactness under this strategy, we have demonstrated feasibility of a quadruply folded growth seam intersection, reducing the space occupied by projection of the folded material by 75%. This ensures that the desirable 'fat' ratio of minor radius to major radius is not aggressively impacted during the initial expansion events under Option A.

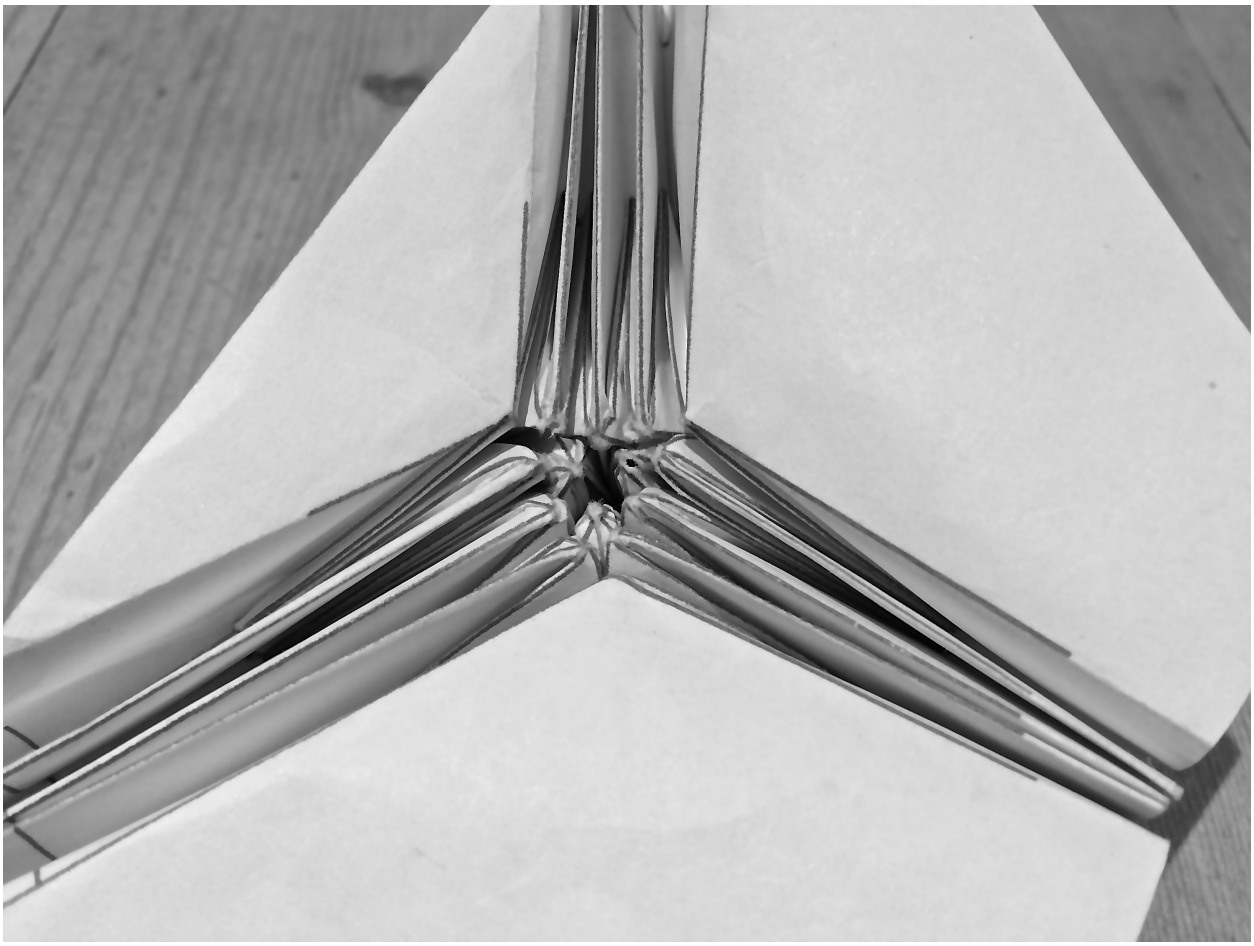

Figure 5.9: Hull Growth Seam Quadruple Fold Intersection
The illustration shows an initial proof of concept for quadruple folding regime for hull material at a 3-way growth seam intersection, as viewed from hull panel face side

5.3.7 Option B. Direct Extrusion of Hull Material Through a Folded Pathway

The second pathway starts from the same folded panel geometry but takes this as the basis for in-situ extrusion of a dual stream of new hull material injected along the interior edge comprising the centerline of the folded panel geometry. The pathway through the mold follows these folded surfaces.

Four qualifications for this method must be noted.

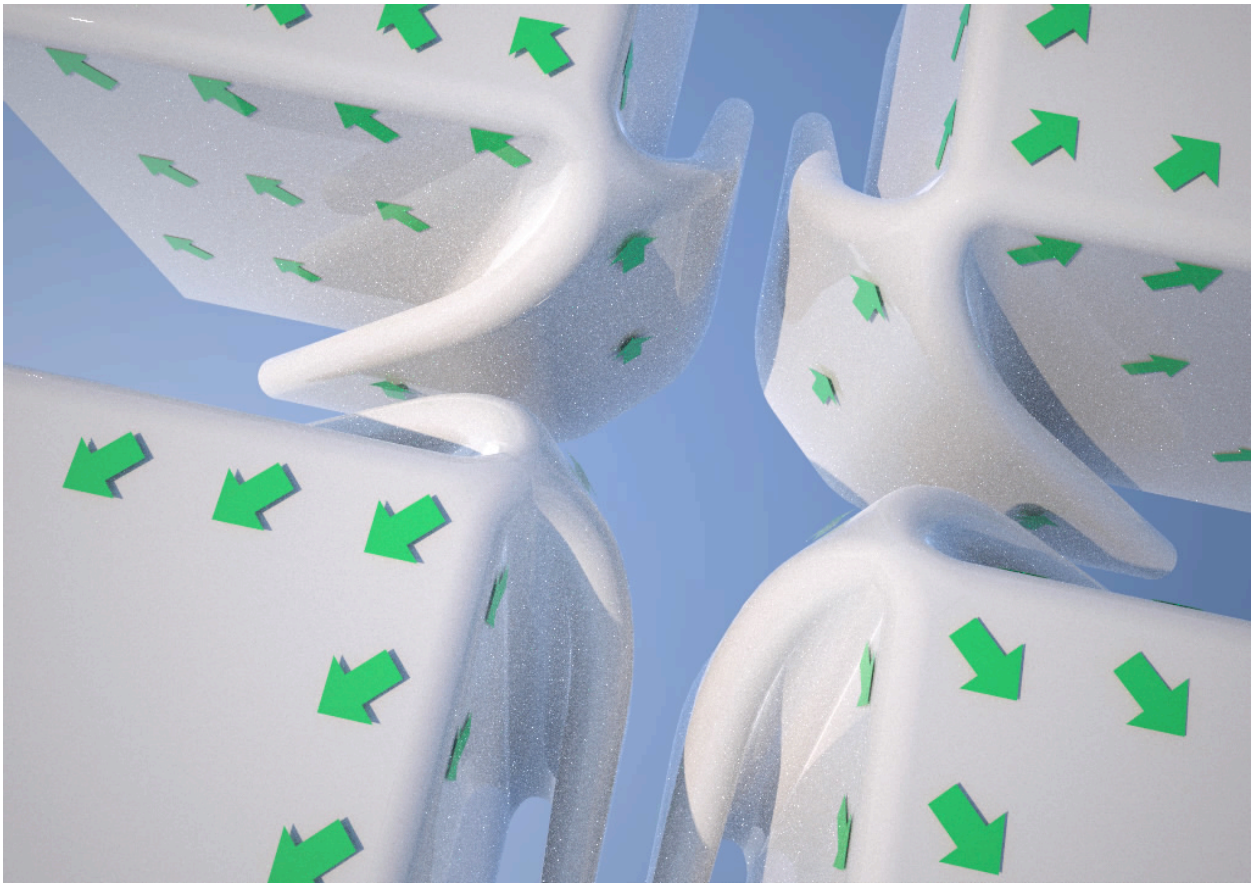

Figure 5.10: Schematic of 4-way Intersection for Extruded Hull Growth Seams
Schematic 4-way junction of growth seams showing pathway of extruded hull surface through the extrusion mullions (not shown). The direction of flow of the extruded material surface is indicated by the green arrows. The space between the material surfaces would be occupied by the extrusion mullion profile, leaving only the four horizontal quadrant panels visible and exposed to the vacuum. The folded pathway ensures even flow distribution and provides the extruding mullion with a better grip on the extruding material.

1. First, in order for the material in the mold to be able to flow around the folds, the radius of the folded edges must be increased to a suitably larger radius curved transition surface. This is in principle feasible, as for instance when any thick material such as carpet is folded, this is the configuration that results, with radius folds rather than sharp edge folds. (The same transitions can be seen in the transitional curved edge folding seen in stacks of basket style paper coffee filters.)

2. The second qualification to be noted is that the folding solution required for the habitat hull resolves into three distinct conditions, i.) intersections where three fold lines meet, ii.) transitional folds accommodating the change in planar alignment at the boundary between adjacent hull panels, and iii.) straight sections joining the first two conditions. It is in these straight sections that a linear expansion of the mold system itself must also be introduced, operating concurrently with the hull material extrusion, in order to maintain the required flow of new hull material to maintain closure during expansion. This appears possible in principle, but would require highly specific compatibility between the material properties of the hull and of the mold, which must be capable of compatible co-extrusion at this location, without compromising quality of output. Preliminary examination suggests that the geometry issues could be resolved.

3. The third qualification to be noted is that for this concept to be viable, a very precise degree of control must exist over the flow rate of the material through the mold, and of the tensile properties of the material at different points within the mold, and of friction / slip between the extruded material and the mold wall, so that extrusion can only occur under conditions where the material remains firmly rooted in the mold, and has no opportunity to pull out of the mold, rupturing the hull containment in the process. Control of the dynamics may be aided by introduction of lubricant, heat, ultrasound energy, and alteration in atmospheric pressure differential across the hull membrane, to name a few possibilities.

4. The fourth qualification to be noted is that the physical and chemical processes involved in synthesizing and extruding the material of the hull must be capable of being embodied in a mullion system of feasible size. Theoretically this approach has attractive attributes in the possibility for continual slow growth, rather than discrete steps of relatively large scale, and may at some point be proven feasible.

5.3.8 Option C. Welding on of Folded Material and Cutting the Hull to Release

This is as conceptually simple and attracttive as it is unsettling to contemplate in detail. Either the welding on of the new folded material, or the cutting of the hull to release the new material, must be accomplished from the outside of the pressure hull while it is rotating, requiring a compete dependance on robotic capability without a clear means of testing before the decision is made to commit. Given the security and life-safety issues inherent in this circumstance, we are not yet persuaded of the feasibility of this approach.

5.3.9 Conclusion: Option A is Method of Choice, for now

Our investigation of the feasibility of these concepts therefore convinces us that Option A is the better choice at present. Option B is problematic with regard to the availability of a viable candidate material for synthesis and extrusion, while Option C may eventually be viable but requires a level of dependance on robotic capability that should be avoided if possible.

5.3.10 Pressure Hull Membrane and Cable Material – UHMWPE

The hull membrane and cables act together asa single structural system. Since the pressure hull material is fully shielded, the primary requirements are for the strength and toughness to resist atmospheric pressure, and a sufficient degree of transparency to sunlight. To demonstrate feasibility of our concept, in light of these requirements, and the conclusions of the previous paragraph,

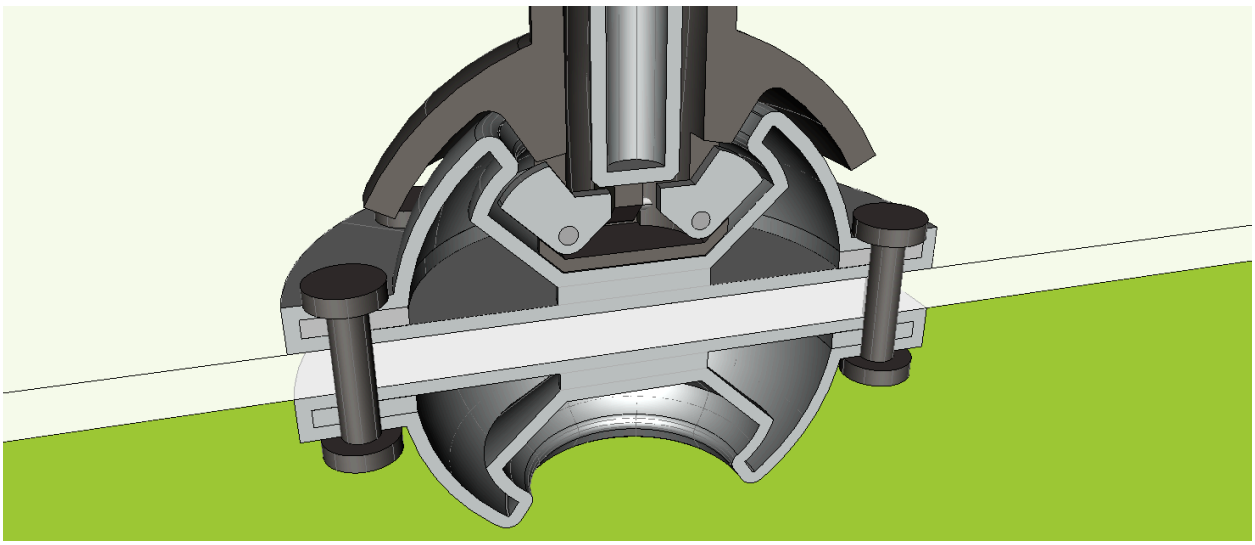

Figure 5.11: Hull Surface Robotic Foothold

This illustration shows the foot of a tensegrity robot locked into a hull surface foothold. depressing the central pushrod will retract the spring loaded locking dogs and release the foot, allowing it to move to the next foothold. The design provides hold capability from both inside and outside.

we have selected ultra high molecular weight polyethylene (UHMWPE) as the leading candidate material because of its low cost, well understood chemistry, and unmatched strength to weight ratio among materials that are currently available in bulk quantities, along with a serviceable level of translucency at 80-85% for a 1mm thickness. The material is flexible enough at this thickness to pursue expansion strategies based on folding. This is of great value in simplifying the challenge of devising an expandable hull. Although UHMWPE is subject to some creep under tensile load, the strategy of repeated renewal in the growth process should eliminate any long term problems, and the accessibility of all cables from the inside will aid in replacement of any cable that exceeds acceptable parameters.

The inside out strategy we have adopted is the strategy of molting found in nature, of growing a new skin within the protective confines of the old, which has used up its expansive capacity. Whereas in nature the old skin is discarded, in our case we will carefully disassemble and store the components of the obsolete hull for subsequent reprocessing and recycling, to be reused in the next subsequent growth iteration.

Given that the obsolete hull material must be carefully disassembled in a controlled manner, this must be accomplished by robots operating on the outside of the hull. In order for this to be done safely, both the inner and outer surface of the hull will be covered with a regularly spaced array of footholds to allow the robots to move about securely, on both the inner and outer surfaces of the hull.

5.4 Shield Concept – Development and Materials

The detailed configuration of the shielding as a separate structure will be a principal focus of Phase 2 research.

5.4.1 Transparency not Required

Given that the shield mass is water, transparency in the shield structure appears at first glance a very desirable trait. However the level of shielding for longterm protection from GCR is sufficiently great that very little light will pass through to the inside, and therefore transparency of the water bag material becomes a rather low priority compared to longevity under exposure to radiation.

Selection of materials for the shield structure will be a topic for Phase 2 research.

5.4.2 Growth and Maintainability

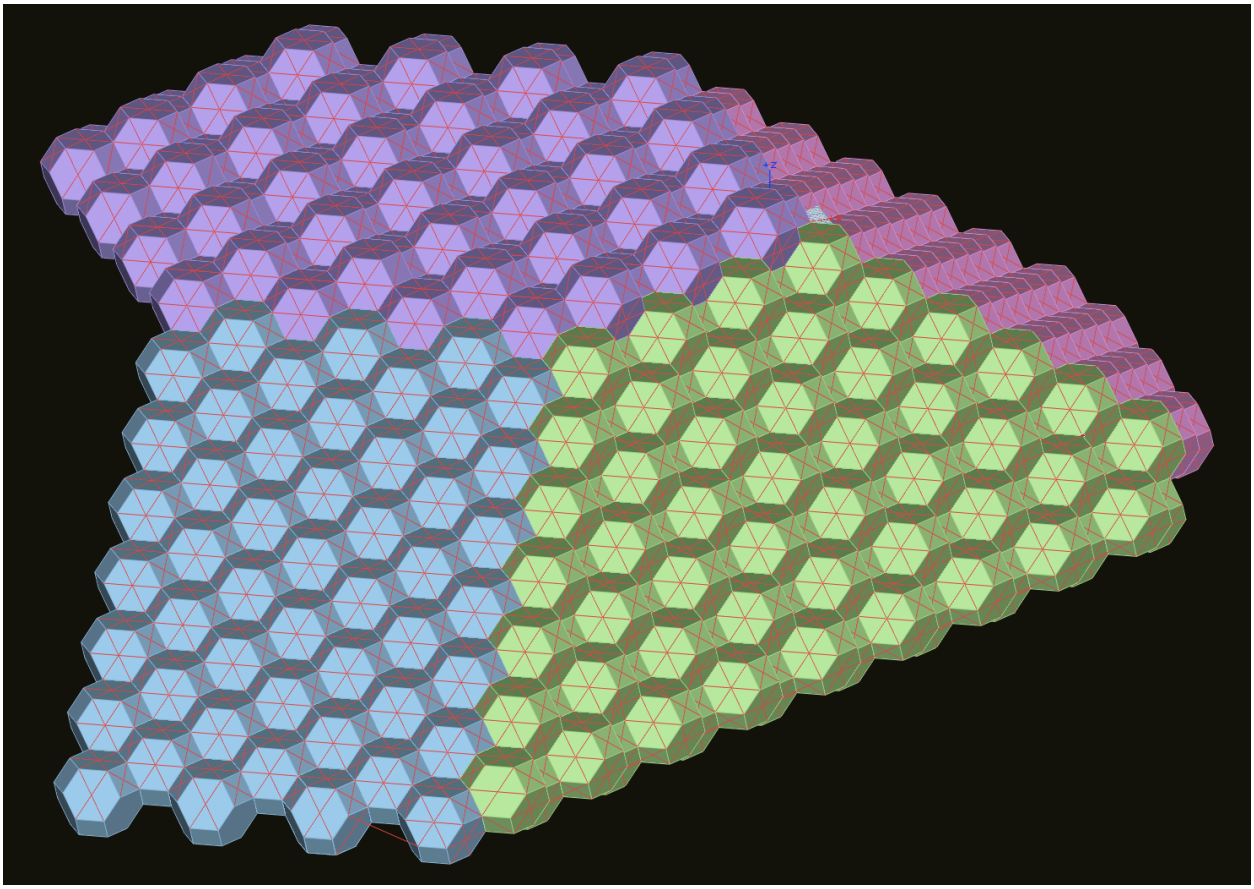

Figure 5.12: Schematic Truncated Octahedral Water Bag Array
As a space filling solid with no continuous through planes the truncated octahedron may be a suitable candidate for a modular approach to the design of a water bag shield structure. In this image the array of truncated octahedra shows the inherent packing flexibility of this space-filling form and thus its ability to closely approximate the shape required by the shield structure. All face diagonals of this solid are continuous throughout the array, allowing multiple suspension cable alignments. There are no other direct line penetrations possible through the array.

The configuration of the slowly rotating shield structure should be such as to ensure that the integrity of its components can be maintained and needed repairs carried out. Our strategy will employ a dynamically maintained layered approach configured for ease of repair or replacement.

One version of this would employ custom built layers of water bag containers, each layer comprising a tensegrity structure of minimum mass.

Another version would employ a standard modular water bag, of a space filing geometry, probably truncated octahedra, with continuous through cable suspension cables.

The structure will grow by the addition of new water containing layers across its outer surface, combined with a corresponding removal of layers from the inside surface. Provided that growth events are occurring with sufficient frequency that any given layer and associated cabling works its way through the system and is decommissioned from the inner surface before it has been degraded beyond its safety margins, this will naturally maintain the system in a functional state. At some point this requirement may not be met, and in this case a program of in depth refurbishment by turns from the outside and from the inside, will be required for continued safe operation.

If the modular design is feasible, the size selected for the water module will be a compromise between larger volume modules that are more efficient containers of water, and smaller units that are easier to maneuver and deploy / replace and involve less volume of water lost when punctured by micrometeorites, and where a given layer of modules will have less time fully exposed before being covered by another layer. If metal cables prove to have a markedly longer working life in the space environment, and if such cables are fabricated from asteroidal material, whatever mass penalties may be entailed may prove to be less significant for a very slowly rotating structure than the advantages of a long working life.

Long-term durability of the structure will hinge on simplicity and ease of maintenance, also the ability to incorporate improved technology as it becomes available.

5.4.3 Shield Structure Design Details - Modular Version

In the modular case, the shield structure will comprise multiple repeated layers of standard modular containers and their associated suspension cables, each capable of being selectively un-cinched and re-cinched for repair and or replacement. The cables collectively will comprise a tensegrity structural frame, with footholds for the service bots dedicated to the maintenance of the system. During a growth event, the inner layer of the system will be inspected and evaluated to determine which items are viable for continued service and which require recycling, then the water modules will be removed from the interior surface, as also the strut modules and cable harness that support them, and new or refurbished items will be added to the exterior surface of the shield structure. The modular containers will have a geometry that naturally precludes alignments offering unshielded pathways through the shield assembly. Individual containers will feature attachment fittings and a valve for filling and draining the water. The system as a whole will feature a network of fill pipes with local spigots for refilling of damaged and repaired containers by the attending service bot. A centrally located cluster of fill tanks of a self-sealing material will be located inboard of the shield wall with gravity feed outwards via the fill pipe network.

5.5 Means of Access, Interactions with the Environment

This section covers the design interactions between orientation of the habitat, light delivery systems, shielding deployment, means of boarding the habitat and receiving delivery of raw materials, and waste heat management.

5.5.1 Space Environment Interactions – Orientation, Light and Power, Means of Access

Calculations by Skelton (see § 6.1) show that expenditure of control energy to establish any secondary axis of rotation is prohibitively high for large rotating habitat structures. For this reason

the axis of rotation of the habitat must be perpendicular to the ecliptic plane.

5.5.2 Waste Heat Management, Diurnal Cycle

Because the habitat is oriented edge on towards the sun there are sideways facing surfaces that never receive the sun's rays directly and always have a clear view of the dark sky, which will be advantageous for dumping waste heat.

As part of the diurnal light management, Mirror 3 will have the electro-optical capacity for transparency, allowing the light to pass through to a bank of solar panels that will use the night period for power generation and storage in the CMG units. Additionally an electro-optical membrane will be installed inside the shield structure immediately after mirror 4 with the capacity to turn from transparent progressively to full mirror reflectance and back. This will be necessary for full control of the day/night cycle, and will aid in cooling the habitat during the night-time periods. The large mass of water in the shielding will act as a thermal flywheel to smooth out the temperature swings between day and night. Further analysis of this subject will be required in due course once other issues are satisfactorily resolved.

Preliminary thermal analysis of the primary mirror structure will be a goal for Phase 2.

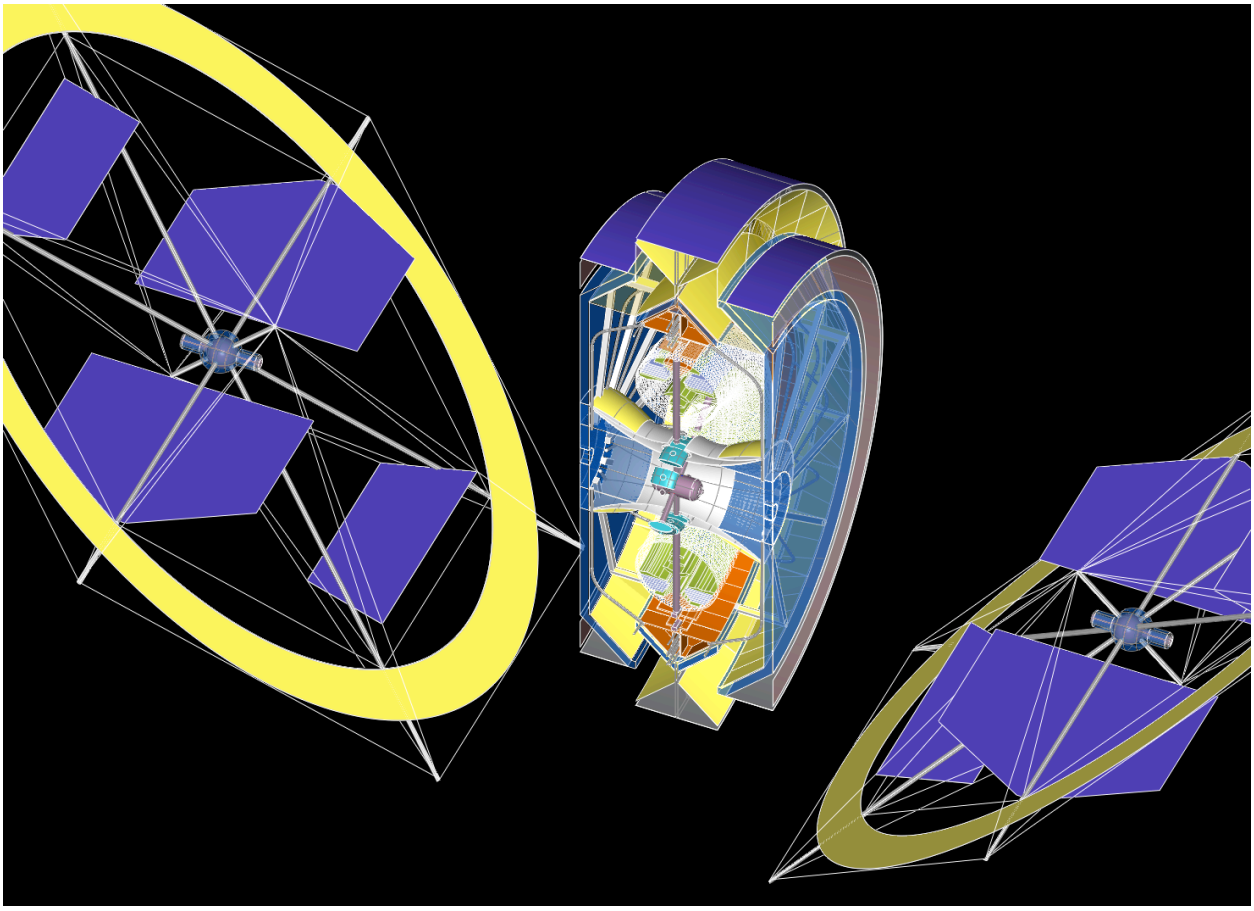

Figure 5.13: Mature Habitat Photovoltaic Arrays

Dual mirror configuration maximizes support for photovoltaic arrays. Power would be beamed to the habitat using microwave transmission.

5.5.3 Power systems

The demands of primary mirror geometry are a dominant influence and a structural support opportunity for solar collector arrays. The geometry of the solar panels must be arranged so as to avoid the axial alignment between the primary mirror hub and the main habitat docking port. An additional opportunity for solar panel deployment exists on the edge faces of the shield structure which have a periodic exposure to the sun as the shield structure rotates.

5.5.4 Materials – Mirror surfaces

At present the clear choice, where electro-optic function is not specified, is aluminum coated BoPET (Bi axially oriented polyethylene terephthalate) commonly referred to as Mylar.

5.5.5 Mirror System Growth

The mirrors are discussed in order starting with the Primary Mirror(s).

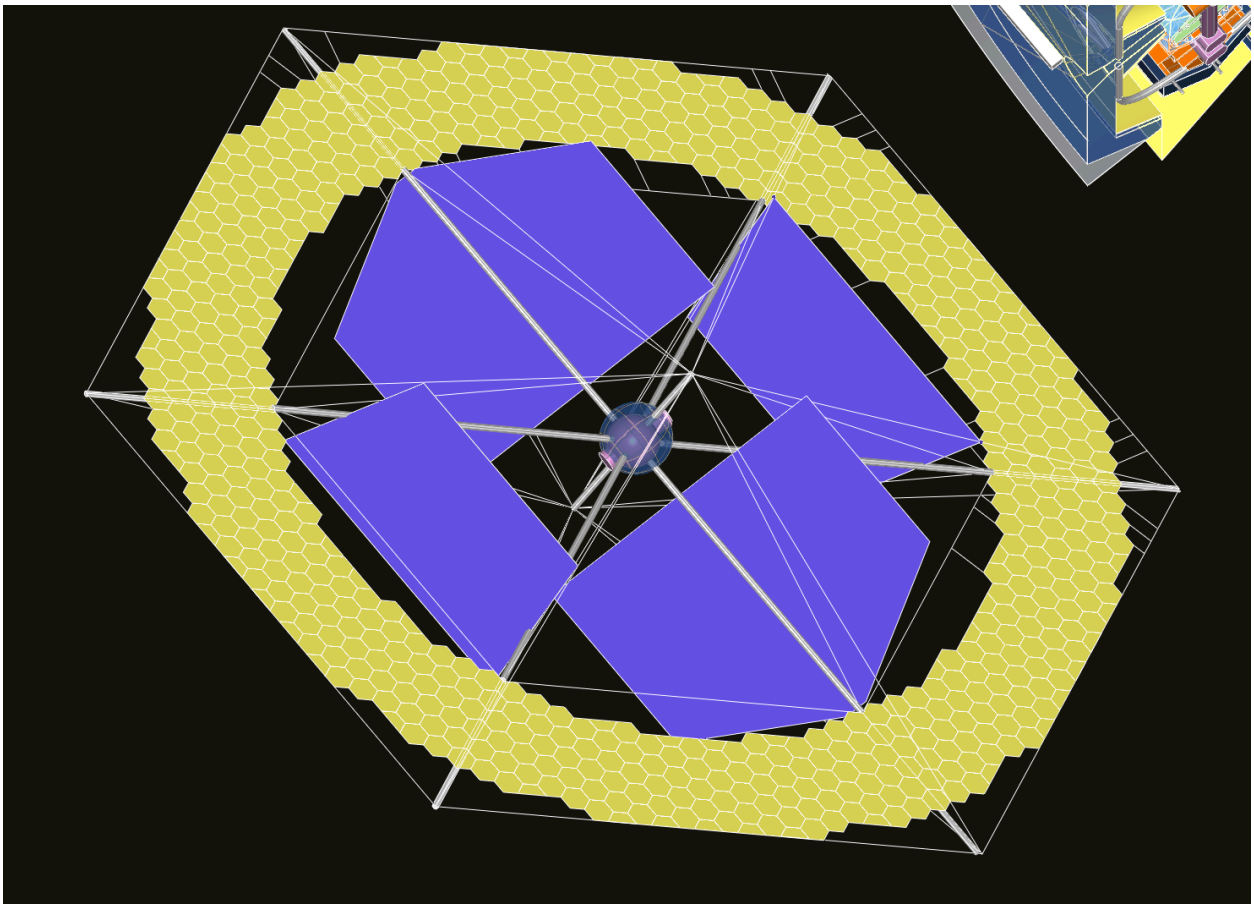

Figure 5.14: Primary Mirror and Photovoltaic Array at Deployment
The primary mirror of modular elongated hexagonal reflector units is shown with its tensegrity deployment structure and the array of photovoltaics this supports.

A. Primary Mirror

This will be inclined at 45 to the ecliptic plane with a projection along the solar axis and also along the habitat's central axis approximating that of a circular ring of constant thickness. The mirror surface will be comprised of many repeating modular units whose projections along both axes are hexagonal, allowing the expansion of the overall mirror dimensions over time. The support system for the mirror modules will be a tensegrity structure capable of expansion (the detail of this will be addressed in Phase 2) and featuring secure footholds for the attending service bots. Correct alignment of the mirror surfaces will be accomplished by means of adjustments to the tension elements of the tensegrity support structure, using a tunable optical feedback system. A centrally suspended service bus will contain station-keeping thrusters, fuel tanks and a docking port, while attitude control will be achieved by means of embedded CMG units, as elsewhere in the habitat.

B. Mirror 2

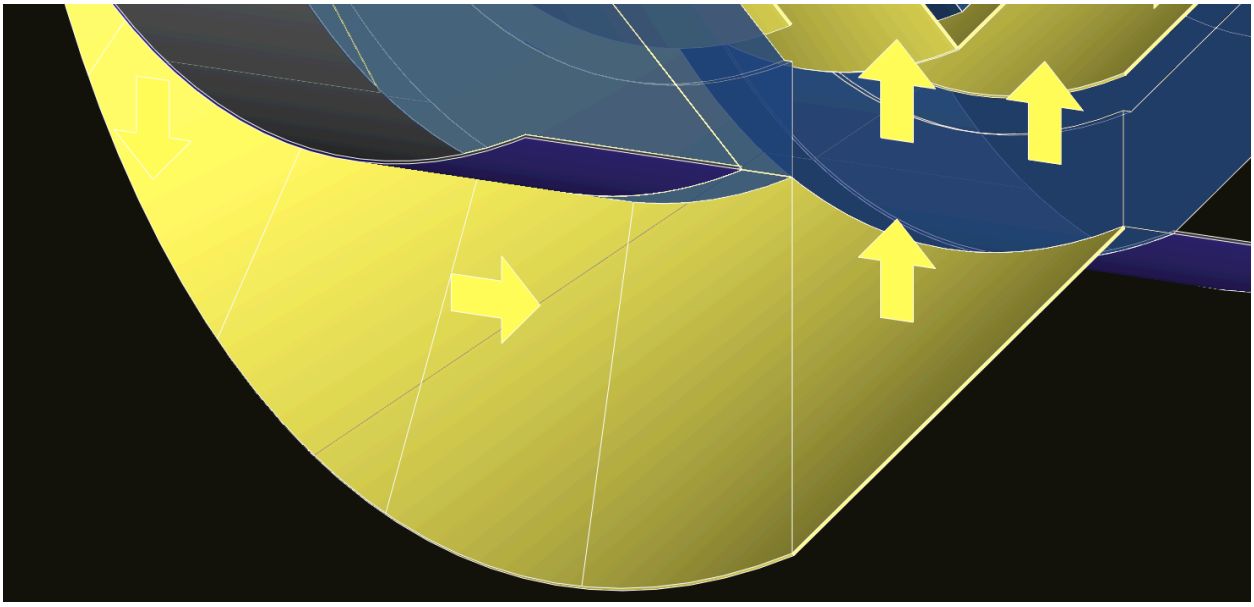

Figure 5.15: Mirror #2

Mirror #2 is a conical or frustum surface comprised of flat segments of mylar, and reflects light radially inwards to Mirror #3.

This mirror straddles the aperture leading to the interior of the shield structure. While theoretically this is a conical surface, in practice it will comprise a series of flat panels each of which overlaps its neighbor slightly, the aggregate of the whole approximating to a conical surface. The dimensions of these mirror panels and their immediate support structure will be the unit length, or a multiple, of the structural interval of the shield structure on which they are mounted, and the supporting struts will be anchored to the ends of the cross struts of the tensegrity harness supporting the shield structure. In the rest state between growth events, all of the immediate supporting structural elements appear as pairs of duplicate elements. This duplication allows them during a growth event to separate at the structural supports into spaced elements, providing room for the introduction of new elements with their own immediate supporting structural elements. For each mirror panel, a pair of radial tensegrity compression struts, oriented radially to the habitat axis, and

stiffened by tensegrity cross bracing struts, will hold circumferential cables defining the extremity of the mirror panels. Wire stays will tie down these struts perpendicular to the habitat axis across the aperture of the light guide-way. The mirror surface forms a tension membrane subject only to sufficient tensile load to keep it flat. Each panel of the mirror is thus self-supporting. During a growth event these panels will move apart from each other making space for the insertion of new mirror panels with their own support structure. Both the support posts and their wire stays will be extended, by means of already positioned material or by replacement with new material Additional mirror panel material will be added at the outer edge, or the existing panel may be replaced if in deteriorated condition.

C. Mirror 3 (Symmetrical Pair)

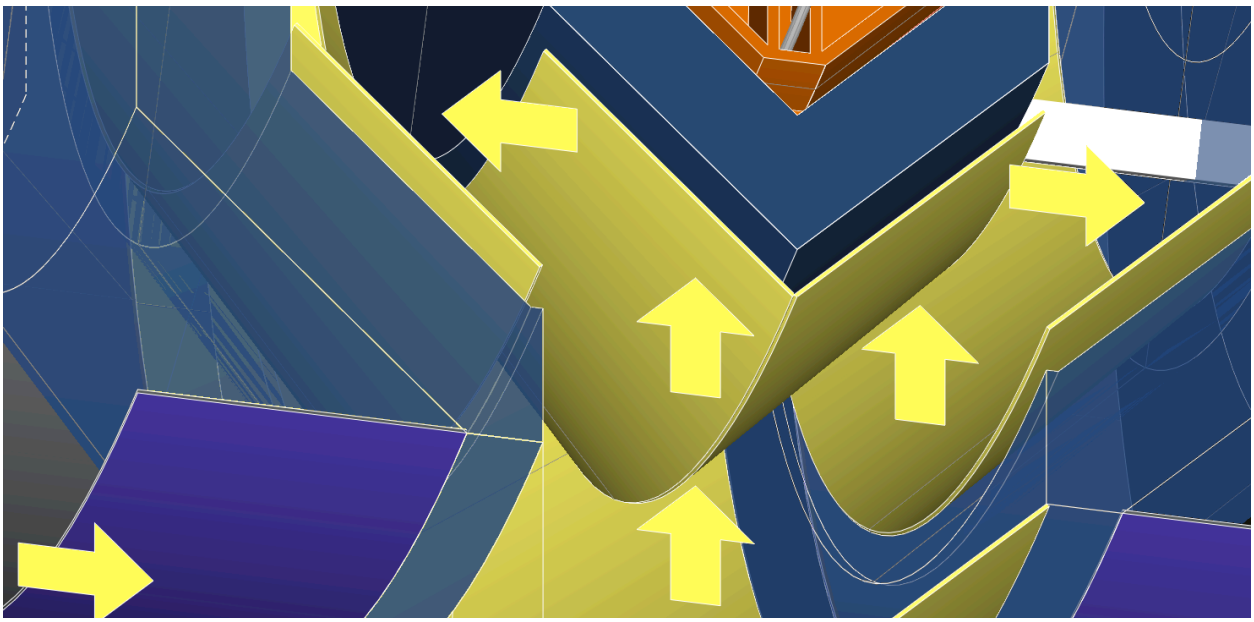

Figure 5.16: Mirrors #3 and #4
Mirror #3 is a conical or frustum surface comprised of flat segments of mylar, and reflects light from Mirror #2 axially outwards to Mirror #4.

This symmetrical mirror pair lies against the outside of the central V-shaped shield structure. It will be supported on standoff posts that are 2 unit modular extensions of the modular cross strut system bracing the tensegrity harness for the water modules comprising this section of the shield structure. This clearance space is to provide sufficient maneuvering room for service bots to add a new layer of water modules, in preparation for which each mirror section and its supporting post in turn will be extended outwards to preserve this required maneuvering room as new modules are placed into position. The comments from Mirror 2 regarding mirror growth are generally applicable here also.

D. Mirror 4 (Symmetrical Pair)

This symmetrical mirror pair lies against the inside of the shield structure parallel to and outboard from the central V-shaped shield structure. The comments from Mirror 2 regarding mirror growth are generally applicable here also.

E. Mirror 5 (Symmetrical Pair)

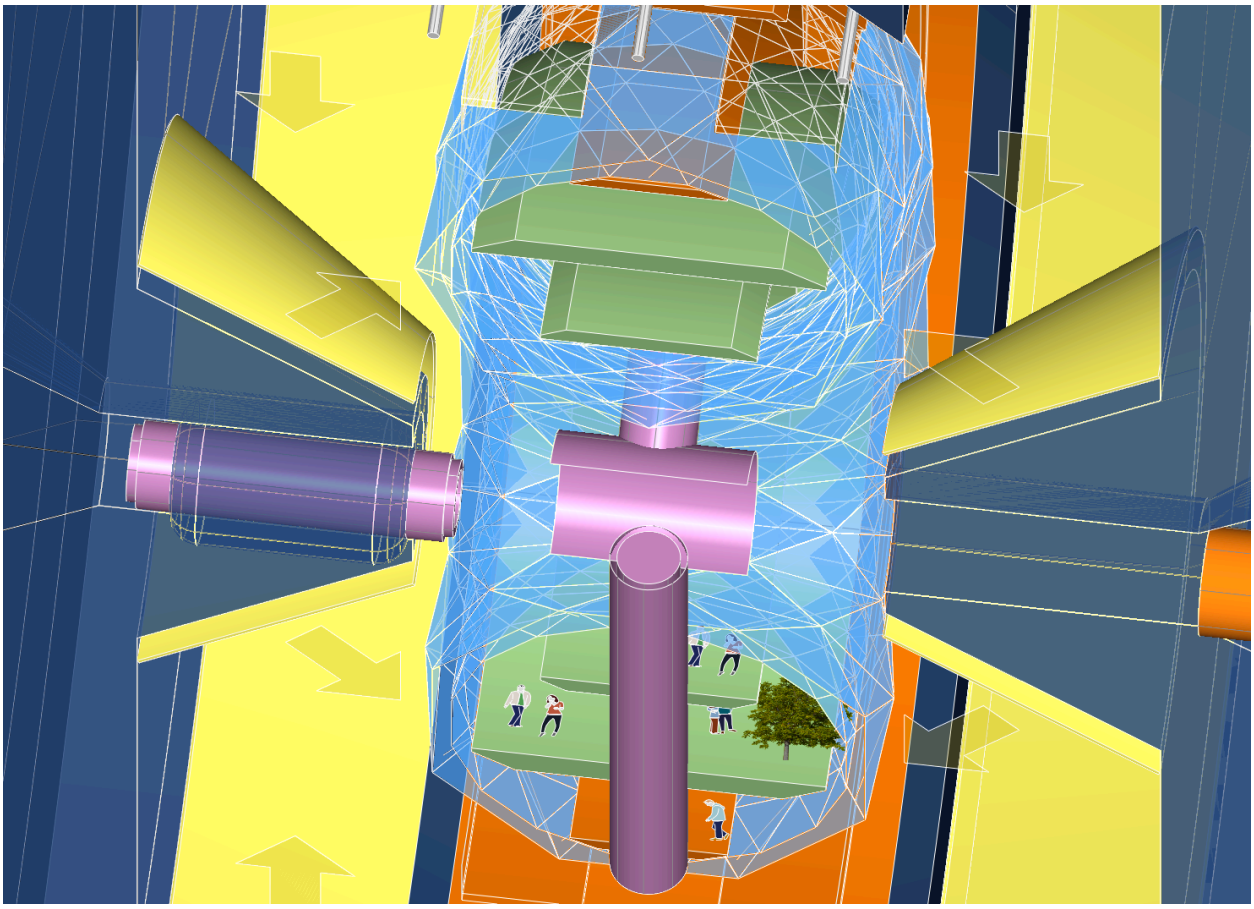

Figure 5.17: Mirrors #4 and #5

This image shows Mirror #5 wrapped around the central axis and Docking Ports. Mirror #5 is a conical or frustum surface comprised of flat segments of mylar, and reflects light from Mirror #4 diagonally into the habitat interior.

This symmetrical mirror pair lies against the inside of the shield structure lining the axial crew and passenger docking port on the one side and the corresponding location symmetrically opposite adjoining the construction staging area. For the former location, the earlier comments about growth methodology, standoff posts and clearance for removal of water modules apply. In the latter case, these will be modified in response to the growth requirements of the construction staging area, but these should be less demanding in structural terms.

Chapter 6

Designs of a Toroidal Habitat

6.1 Choosing a Spin Direction

The biological evidence suggests that man cannot thrive long term in space, raising a family, etc. in the absence of gravitational forces similar to earth. Since there are no earth sized celestial bodies nearby, it is incumbent upon the scientific community to create methods that can provide close to 1g loads by use of centrifugal force. Spinning bodies have been studied in [Stanford Torus] to provide centrifugal forces similar to the earth gravitational forces. Given that such a habitat must spin, the axis of spin must be chosen to satisfy light gathering considerations, precession control to follow the sun, and energy consumption. Appendices C and D derive the control torques that would be required to control precession of a sun-pointing spin axis if the habitat was a rigid spinning torus. These torques can be large and Appendix C determines what control forces are necessary to cause a small habitat ($R = 10m$, $r = 5m$) to rotate to follow the sun (spin axis pointing to the sun) and give 1/3 g centrifugal force to the small habitat having radii $R, r = 10m, 5m$. Appendix C shows that the required control torques are approximately 20 Newtons sinusoidally cycling at the frequency of the spin rotation 11 seconds per rotation. Appendix D determines what control forces are necessary to cause a large habitat having radii $R, r = 1000m, 500m$ to rotate to follow the sun and give 1g centrifugal force to the large habitat. This Appendix shows that the required control torques are approximately 2 million Newtons sinusoidally cycling at the frequency of the spin rotation 75 seconds per rotation.

Since large control torques and control energy are required to place the habitat spin axis in the ecliptic plane, (sun-pointing direction), on the basis of these studies we chose the spin axis to be perpendicular to the ecliptic plane, where no precession control torques are required (except for stability perturbations and transients), saving much energy.

6.2 A Continuum Design: A Pressurized Torus

The early study called the Stanford Torus shows the following data for their design, which was composed of an aluminum shell in torus shape with large radius R and small radius r, where P is the atmospheric pressure, M_S is the structural mass, M_A is the mass of the atmosphere, A_L is the

surface land area, and V is the longest line of sight.

$$\begin{aligned} P &= 0.5 \times 10^5 N/m^2 \quad (6.1)\\ R &= 830m \\ r &= 65m \\ M_S &= 150,000,000kg \\ M_A &= 44,000,000kg \\ A_L &= 0.68km^2 \\ V &= 0.64km. \end{aligned}$$

Because we seek lightweight semitransparent material for the hull for light-gathering purposes, we initially choose ultra high molecular weight polyethylene (UHMWPE) material for the hull, supported by a cable network made of the same material. However, as a point of reference, before adding any cables, one can compare the same size continuous torus using the UHMWPE material, where ρ and σ respectively, are the mass density and yield stress of the UHMWPE. Only two differences from the standard Stanford Torus will be made in these approximate calculations: The atmospheric pressure is doubled and the material is UHMWPE rather than aluminum.

$$\begin{aligned} P &= 10^5 N/m^2 \quad (6.2)\\ R &= 830m \quad (6.3)\\ r &= 65m \quad (6.4)\\ t &= Pr/\sigma = 1.2mm \quad (6.5)\\ M_S &= 3PV\frac{\rho}{\sigma} \quad (6.6)\\ &= 3P\pi r^2 2\pi R\frac{\rho}{\sigma} \quad (6.7)\\ &= 7,455,000kg \\ M_A &= 88,000,000kg \\ A_L &= 0.68km^2 \quad (6.8)\\ V &= 0.64km, \quad (6.9) \end{aligned}$$

where t is the hull thickness.

We imagine a startup habitat of small size, say $R, r = 10m, 5m$. The mass requirements and other properties of this startup are:

$$\begin{aligned} P &= 10^5 N/m^2 \quad (6.10)\\ R &= 10m \quad (6.11)\\ r &= 5m \quad (6.12)\\ t &= Pr/\sigma = 0.2mm \quad (6.13)\\ M_S &= 3PV\frac{\rho}{\sigma} \quad (6.14)\\ &= 3P\pi r^2 2\pi R\frac{\rho}{\sigma} \quad (6.15)\\ &= 531kg \\ M_A &= 6,000kg \\ A_L &= 0.68km^2 \quad (6.16)\\ V &= 0.0173km, \quad (6.17) \end{aligned}$$

As another reference point we compute the mass and wall thickness required to contain full atmospheric pressure of a Habitat of dimension $R = 405$, $r = 130$, using UHMWPE. The mass of pressure vessels in the shape of a torus is approximately

$$P = 10^5 N/m^2 \tag{6.18}$$
$$R = 405m \tag{6.19}$$
$$r = 130m \tag{6.20}$$
$$t = 4.8mm \tag{6.21}$$
$$M_S = 3PV\frac{\rho}{\sigma} \tag{6.22}$$
$$= 3P\pi r^2 2\pi R\frac{\rho}{\sigma} \tag{6.23}$$
$$= 14,550,810kg \tag{6.24}$$
$$M_A = 165,504,000kg \tag{6.25}$$
$$A_L = 0.66km^2 \tag{6.26}$$
$$V = 0.6km \tag{6.27}$$

where t is the wall thickness of the UHMWPE material.

We desire to grow the structure to ever-increasing sizes. It is difficult to "grow" the continuous material to make a larger torus from the smaller one, unless one can devise an extrusion process that is seamless. However, a larger issue is the light availability. A 1 mm sheet of UHMWPE allows 80% transmissibility of light, which will be needed for sufficient light in the habitat, aided by a set of mirrors to be described later. However, the above calculations show that the thickness required of UHMWPE is greater than $1mm$, so that a cable network will be added to support the hull membrane sufficiently to allow the membrane to be only 1mm thick. We also wish to grow the structure, so a discrete cabled structure is proposed which can grow in finite discrete amounts. This will be a cable network, where the space between the cables will be covered with a 1 mm thick hull material to contain the pressure.

We insert this calculation now.

Let a torus surface of radii R, r contain a discrete network of p circular cables around the large dimension and let q circular cables of radius r intersect the p cables orthogonally and be equally spaced radially around the large radius. All cables lie on the surface of the torus of radii R, r, creating curvilinear rectangular spaces between the cables. The largest such rectangular shapes occur near the outside of the torus dimension (radius $R + r$), but this section will be below ground level and light transmission is not an issue. The top half of the torus must transmit light, so the largest rectangular section of interest lies along the circular cables of radius R. The dimension of the sides of these curvilinear rectangular spaces are $2\pi R/q$ by $2\pi r/p$. Since we must fill this space with hull membrane material we desire the spaces to be square and subscribed by a circle of radius x, where $R/r = q/p$ makes the hull space square and $x/2 = \pi R/q$ fixes the size of the circular hull section, which will be a dome of radius $x/2$. The actual choice of the hull sections might be ellipsoidal rather than spherical, but our present purpose is only to get an approximation of the mass required. For these purposes these empty spaces can be capped by hemispherical domes of UHMWPE material 1mm thick and radius $x/2$. The mass of a spherical dome near the cables of

radius R, under pressure P is

$$m_h = \frac{3\rho}{4\sigma} PV \tag{6.28}$$
$$= \frac{3\rho}{4\sigma} P \frac{4}{3}\pi(\frac{x}{2})^3 \tag{6.29}$$
$$= \frac{\rho}{\sigma} P\pi \frac{x^3}{2} \tag{6.30}$$
$$= \frac{\rho}{\sigma} P\pi(\pi R/q)^3 \tag{6.31}$$
$$= \frac{\rho}{\sigma} P\pi^4(R/q)^3, \tag{6.32}$$

where, $p = rq/R$. This is the largest dome, capping the largest space between the cables. The remaining cables are closer together and hence the complexity p, q that allows 1mm domes on the largest space, will yield smaller domes throughout the rest of the structure that could allow less thickness than 1mm. As a very conservative mass estimate we assume for the moment that all domes are of the largest size, so that the total mass of the dome is over-estimated as just the number of domes times the mass of one dome. With this simplification, the total dome mass is the total hull mass, composed of pq half domes of UHMWPE material 1 mm thick is

$$M_H = pqm_h \tag{6.33}$$
$$= pq\frac{\rho}{\sigma} P\pi^4(R/q)^3 \tag{6.34}$$
$$= \frac{rq}{R} q\frac{\rho}{\sigma} P\pi^4(R/q)^3$$
$$= rR^2\pi^4 P\frac{\rho}{q\sigma}.$$

where the wall thickness of the domes is

$$t = \frac{P}{2\sigma}\frac{x}{2} \tag{6.35}$$
$$= \frac{P}{2\sigma}\frac{\pi R}{q} \tag{6.36}$$

Therefore, to fix the thickness to $t = 1$mm, we must choose the complexity $q = \frac{P}{2\sigma}\frac{\pi R}{t}$.

In conclusion, the lower bounds on complexity (p, q) of a tensegrity torus is fixed by the requirement of a specified thickness t of the hull material and is given by

$$q \geqslant \overline{q} = \frac{\pi RP}{2\sigma t} \tag{6.37}$$
$$p \geqslant \overline{p} = \frac{rq}{R} = \frac{\pi rP}{2\sigma t}. \tag{6.38}$$

Later we will examine tensegrity designs of different radii R, r. Then these lower bounds of complexity $\overline{p}, \overline{q}$ will be required of these subsequent tensegrity designs, where M_H is the hull mass from (6.33):

$$[R, r, \overline{p}, \overline{q}, M_H] = [10, 5, 4, 4, 438] \tag{6.39}$$
$$[R, r, \overline{p}, \overline{q}, M_H] = [830, 65, 4, 49, 3198464] \tag{6.40}$$
$$[R, r, \overline{p}, \overline{q}, M_H] = [405, 130, 8, 24, 3106963] \tag{6.41}$$

It is convenient to establish a conservative complexity well above these minimums $\overline{p}, \overline{q}$, so we will choose $q = 60$ and $p = \lfloor rq/R \rfloor$ (meaning the closest integer to the value rq/R) as safe margins for any habitat size, within the range $R \leqslant 830, r \leqslant 130$, unless the subsequent minimal mass analysis of the cable network determines that cable mass can be reduced by even larger complexity (This will not be the case, so complexity ($p = \lfloor rq/R \rfloor, q = 60$) is acceptable throughout, although minimal mass for smaller habitats will dictate lower complexity).

6.3 The Available Mathematical Tools for Tensegrity Engineering

Tensegrity concepts allow compressive and tensile elements to be configured in stable equilibria to form a desired shape, which is a torus in our case. The mathematical tools needed to do habitat design are given in Appendices E,F,G. The interested reader can follow these mathematical details, but here in the main text we will only discuss the data from those calculations.

Appendix E derives a mathematical model for a DHT (Double Helix Tensegrity) structure. A infinite number of stable shapes can be built from this double helix topology of compressive and tension members. We will use this architecture for our first torus design, to prove habitat feasibility. The mathematical analysis methods to treat tensegrity structures in an efficient systematic way is recent and the contents of Appendix A appears in a new AIAA paper [.].

Appendix F provides the mathematical techniques required to design tensegrity structures for minimal mass, while supporting the designed static loads.

Appendix G derives an efficient formulation of the dynamics of tensegrity structures, where the bars are rigid with mass and inertia, and the cables are elastic (nonlinear elasticity allowed).

6.4 Analytical Data for the Tensegrity Habitat

Appendices A and B provide the derivation and the computer calculations for a habitat composed of a DHT torus. The nonlinear equations that describe the equilibria are programmed specifically for the the DHT topology. We examine the freedom in this design to form the habitat. First there is freedom of complexity p and q, where p is the number of units around the small circumference of radius r, and q describes the number of units around the circumference of radius R.

Appendix A shows that the structural mass mass required of the small torus ($R = 10m, r = 5m$) to spin at a slow rate to give $1/3g$, with complexity $p, q = 6, 30$, is $16,000$kg, including the approximation for hull mass from (6.33), $M_H = 438$kg. Appendix B shows that the structural mass required of very large torus ($R = 1000m, r = 500m$) to spin at $1g$ with very low complexity, $p, q = 6, 30$, is 1.4334×10^{10}kg, including hull mass $M_H = 5.83 \times 10^7$kg.

These designs show that any compressive members employed in the tensegrity design have insignificant mass, and in fact are not needed for stability, since atmospheric pressure is large. Compressive members will be needed for control actuators using momentum exchange, but a later section will discuss control issues.

6.5 Analytical Formulas for a Tensegrity Torus

If the hull membrane mass is ignored, the computer calculations of Appendices A and B show that the complexity should be small to minimize mass. But the $1mm$ requirement of hull thickness may require a greater complexity to support the thin membrane. Note that *without* any cables the continuos UHMWPE torus is only $1.2mm$ thick for the size $R = 830, r = 65$, and $4.8mm$ thick for the size $R = 405, r = 130$. From light considerations, the desired thickness is $1mm$, so a cable

support system is needed and the tensegrity concepts will lead us to an acceptable cable network. Now we examine structural mass from a simplified analytical model of the tensegrity torus.

Appendices A and B perform a detail computer study, but devoid of insight in the role of each parameter. Therefore, it is aways instructive to sketch an approximation simple enough to allow analytical formulas relating all design variables to mass. This provides insight into the role of each parameter in the design. The following section provides such explanations with explicit analytical formulas of a simplified structure.

6.6 A Curvilinear Cable Network of Complexity p, q

For these purposes we imagine a polygon of degree p with equal length cables of length s_r forming the sides of the polygon. The radius of the p-polygon is r (the distance from the polygon center to each vertex), where r is the small radius of the habitat torus. Now we provide q of these p-polygons whose centers are arranged around a larger radius R which will be the large radius of the torus. Now we have an array of pq vertices that lie on the surface of a torus defined by the two radii (R, r). Now connect the vertices of adjacent p-polygons with cables of length s_{Ri} to form a discretized torus whose cross section across the small diameter is a p-polygon, and whose cross sections across the large dimension is a q-polygon passing through each vertex of the smaller p-polygon. There are p large polygons of degree q, and the radius of each of these q-polygons is labeled $R_i, i = 0, 1, 2, p-1$ (we define for $i = 0$, $R_0 = R$). One can visualize the construction of a uniform grid connecting the pq vertices described above, with p vertices around the smaller diameter and q vertices around the larger diameters.

We choose to design the p-polygon of cables to support atmospheric pressure P_a inside the torus,

$$P_a = 10^5 kg/m^2 \tag{6.42}$$

The pressurized surface area A_a of the torus is

$$A_a = 4\pi^2 Rr \tag{6.43}$$

so the total atmospheric force is F_a is

$$F_a = P_a A_a = 4\pi^2 P_a Rr. \tag{6.44}$$

Distributing this force evenly over the pq nodes of the structure yields the force acting at each node

$$f_a = F_a/pq. \tag{6.45}$$

This force will be balanced by the cables of length s_r, yielding tension in the typical cable s_r given by

$$t_r = f_a/(2\sin\theta_r), \tag{6.46}$$

where $\theta_r = \pi/p$. Each of the s_r cables have length

$$s_r = 2r\sin\theta_r. \tag{6.47}$$

The mass m_{s_r} of each cable at yield conditions is

$$m_{s_r} = \frac{\rho}{\sigma} t_r s_r \tag{6.48}$$
$$= \frac{\rho}{\sigma} f_a r \tag{6.49}$$
$$= \frac{\rho}{\sigma} F_a r/pq \tag{6.50}$$
$$= \frac{\rho}{\sigma} P_a A_a r/pq \tag{6.51}$$
$$= \frac{\rho}{\sigma} 4\pi^2 r^2 R P_a/pq, \tag{6.52}$$

where the cable material has mass density ρ and yield stress σ. There are p cables in each of the p polygons of radius r, and there are q of these p-polygons. Hence there is a total of pq cables of length s_r, and the total mass m_r of all cable polygons of radius r is

$$M_r = pqm_{s_r} = \frac{\rho}{\sigma} 4\pi^2 R r^2 P_a, \tag{6.53}$$

indicating that the total cable mass required to support the atmospheric pressure is independent of the number of cables used pq.

6.7 Centrifugal Forces From Deadloads

Now let us compute the mass of the p-polygons of degree q and radius $R_i, (i = 0, 1, 2, , p-1)$. These will support centrifugal forces. f_i is the centrifugal force acting radially outward at each node (vertex) of the q-polygon of radius R_i. To compute this force f_i, we assign mass to both the deadload mass M_D, and to the mass of the cables M_S. The deadload mass M_D is the sum of: the mass of the atmosphere M_{atm}, the mass of the hull surface M_H, and the mass of soil/water/infrastructure, labeled M_W.

From (6.33), $M_H = rR^2\pi^4 P\frac{\rho}{q\sigma}$. Also $M_{atm} = \rho_a V_a$, where volume is $V_a = 2\pi^2 r^2 R$, $\rho_a = 1.225 kg/m^3$, and $M_w = \rho_w V_w$, $\rho_w = 10^3 kg/m^3$, $V_w = 2r(2\pi R)\delta$, where the soil depth is $\delta = 1m$. Hence,

$$M_D = M_{atm} + M_H + M_W \tag{6.54}$$
$$= \rho_a(2\pi^2 r^2 R) + rR^2\pi^4 P\frac{\rho}{q\sigma} + \rho_w 4\pi r R\delta. \tag{6.55}$$

The centrifugal forces from the deadload mass will be supported by the outer half of the nodes (vertices) of the torus at radii $R_i, (i = 0, 1, 2...., p/2)$, where each of these nodes supports mass $2M_D/pq$. Hence the centrifugal force from deadloads acting at node with radius R_i is $(2M_D/pq)g_i$, where $g_i = R_i\omega^2$, and the angular velocity ω is determined by $g = 9.8m/s^2 = R\omega^2$. That is, $\omega^2 = g/R$, where g is the selected gravitation level of the habitat. Hence $g_i = gR_i/R$, where $R_i = R + r\sin 2\pi i/p$ for $(i = 0, 1, 2, ..., p/2)$, and $R_i = R - r\sin 2\pi i/p$ for $(i = p/2 + 1, ..., p - 1)$. For our calculations, we choose $g = 9.8m/s^2$. Therefore, the centrifugal force due to deadloads, f_i , acting at nodes of a q-polygon of radius R_i is,

$$f_i(R_i) = \frac{2gM_D}{pqR} R_i. \tag{6.56}$$

6.8 Centrifugal Forces From Cable Mass

The radius of the *ith* q-polygon is R_i, and the length of each cable is s_i,

$$s_i = 2R_i \sin\theta_R \tag{6.57}$$

$$R_i = (R + r\sin 2\pi i/p), \qquad i = 0, 1, 2..., p/2. \tag{6.58}$$

and the tension in this cable is

$$t_i = f_i(R_i)/(2\sin\theta_R) \tag{6.59}$$

$$f_i(R_i) = \frac{2gM_D}{pqR} R_i. \tag{6.60}$$

where $\theta_R = \pi/q$. Due to symmetry, there are two q-polygons of radius R_i. Hence the mass of these two q-polygons of cables is,

$$m_s(R_i) = 2q\frac{\rho}{\sigma} t_i s_i \tag{6.61}$$

$$= 2q\frac{\rho}{\sigma} f_i R_i \tag{6.62}$$

$$= 2q\frac{\rho}{\sigma}\frac{2gM_D}{pqR} R_i^2. \tag{6.63}$$

For $i < p/2$, the total mass of the q-polygon cable networks of radii R_i is

$$M_R = \frac{p}{2} 2q\frac{\rho}{\sigma}\frac{2gM_D}{pqR}\sum R_i^2 \tag{6.64}$$

$$= \frac{\rho}{\sigma}\frac{2gM_D}{R}\sum (R + r\sin 2\pi i/p)^2. \tag{6.65}$$

For the remaining cables in the q-polygons, where $R_i = R - r\sin 2\pi i/p$, the deadload does not contribute to the force or mass in these cables. In the plane of a p-polygon, the forces are radially outward from the center of the p-polygons, and the centrifugal forces are directed always in the same "vertical" direction. Hence, at the inner nodes of the torus, the outward forces from pressure exceed the inward forces from centrifugal forces if $f_a \sin 2\pi i/p > f_i$, where,

$$f_a = \frac{F_a}{pq} \tag{6.66}$$

$$= \frac{4\pi^2 P_a R r}{pq} \tag{6.67}$$

$$f_i = \frac{2gM_D}{pqR} R_i. \tag{6.68}$$

This implies that the centrifugal forces do not overcome the pressure forces and therefore, even without compressive members to resist, the centrifugal forces do not collapse the torus if,

$$P_a > \frac{gM_D}{2\pi^2 R^2}\left(\frac{R}{r\sin 2\pi/p} - 1\right). \tag{6.69}$$

This condition is well satisfied (by a factor of 10) in all of our designs.

Even though all of the q-polygon cables will be installed on the inner surface of the torus (with $R_i < R$), to facilitate hull installation, the mass of these cables will be insignificant compared to all other cables and will be omitted in our overall habitat mass calculations that follow.

The mass of the q-polygon cables, M_R, and the mass of the p-polygon cables M_r, add to give total cable network mass $M_S = M_R + M_r$.

$$M_S = M_r + M_R \tag{6.70}$$

$$= \frac{\rho}{\sigma} 4\pi^2 R r^2 P_a + \frac{\rho}{\sigma} \frac{2gM_D}{R} \sum (R + r \sin 2\pi i/p)^2, \tag{6.71}$$

where,

$$M_D = M_{atm} + M_H + M_W \tag{6.72}$$

$$= \rho_a (2\pi^2 r^2 R) + r R^2 \pi^4 P \frac{\rho}{q\sigma} + \rho_w 4\pi r R \delta. \tag{6.73}$$

The line of sight (unobstructed vision) is labeled V, and is computed by

$$V = 2r\sqrt{2\frac{R}{r} - 1}. \tag{6.74}$$

The land surface area is $A_l = 4\pi R r$.
These vision, land area, and mass calculations are given below

$$[R, r, V, A_l, p, q, M_S] = [10m, 5m, 17m, 628m^2, 30, 60, 1576kg] \tag{6.75}$$
$$[R, r, V, A_l, p, q, M_S] = [405m, 130m, 595m, 661619m^2, 20, 60, 83516117kg]$$
$$[R, r, V, A_l, p, q, M_S] = [830m, 65m, 1288m, 677955m^2, 5, 60, 19567582kg].$$

Note from (6.1) that the Stanford Torus has structural mass 1.5×10^8, which is approximately a factor of 8 more massive for the same dimensions $(R, r) = (830m, 65m)$.

6.9 Summary of mass properties

From the calculations above, we have the following conclusions. Using the UHMWPE material for cables and a 1mm hull, the structural mass required to build the habitat of size $(R, r) = (10m, 5m)$ is $1,576kg$. The structural mass required to build the habitat of size $(R, r) = (405m, 130m)$ is $83,516,117kg$. The structural mass required to build the habitat of size $(R, r) = (830m, 65m)$ is $19,567,582kg$.

Appendix A provides a design using the DHT topology, yielding masses: $1.6 \times 10^3 kg$ for $(R, r) = (10, 5)$, and $1.4 \times 10^1 0kg$ for $(R, r) = (1000m, 500m)$.

Notice that this DHT topology proved to be more massive than the curvilinear topology of the previous section. However the DHT topology provides much greater structural stiffness. The structural stiffness and the control laws will determine stability properties, and the amount of control energy required to meet the control performance objectives (minimal control energy, reasonably fast response to correct displacement errors or spin rate errors). So it is premature to discount the DHT topology, until the control studies are completed. However we have presented a design that is feasible.

6.10 Control Issues

There are three bodies to be controlled to keep their proper separation and angular velocities.

6.10.1 Control of the mirror and Solar Array

The solar array is fixed at the center of the large mirror reflecting light for the habitat. The mirror has an elliptical shape with an elliptical open space in the center, in which space the solar panels will be installed. The solar panels will always be parallel to the sun direction, while the mirror is 45 degrees from the sun direction. The solar panels will be fixed to the mirror in a way to avoid excessive stresses in either the mirror or the solar array, in the presence of the control forces and torques. The solar pressure will translate the center of mass away from the sun, and this must be countered by a control thrust from an ion engine, or some other pollution-free thruster. The attitude of the mirror/solar system will be control by momentum exchange. Solar power will speed up or slow down rotors located near the center of the structural mass. Three rotors is the minimal number for controllability, but no less that six rotors will be used and coordinated to achieve the desired control torques, while avoiding saturation of any individual rotor. That is, the freedom available by having six rotors to control only three things (the three attitudes of the mirro/solar system) allow choice of rotors to serve that function. That choice is made to keep any rotor below its critical speed (or, in the case of CMGs, to keep the gimbal angles away from their physical limits).

6.10.2 Control of the Shield

The shield is the most massive structure of the habitat system, being essentially two large disks (30m thick with water) shielding the habitat, but not touching it. The shield may rotate at a slow rpm, just for stability purpose, but the safety margins required to safely avoid collisions with the habitat inside must be studied to determine a desired spin rate for the shield. Angular momentum control will again be used to fine tune the displacements between the habitat and the shield, and small thrusters will be required to adjust translational positions.

6.10.3 Control of the Habitat

The excess energy from the solar arrays will be stored in "Fly-Wheels" (momentum storage wheels), where dc motors increase the spin rate of several rotors located throughout the habitat (the rotors will be located underneath the land area, since this area is for equipment, material storage, and momentum storage wheels and control actuators). This stored angular momentum serves two different functions. first the momentum can be changed as solar energy is converted to mechanical energy by using DC motors to increase or decrease the spin rate of selected rotors. Secondly the precession and attitude control torques will be generated by changing either the direction of the rotor spin axes, or by changing the rates of spin about those axes. The overall control objective will be *energy-management* to continually choose which rotor will be used to store more excess energy, and which will spend energy applying control torques to the habitat. The mathematical details of these control laws will follow in phase 2, but the mathematical analytical tools required to reach these objectives are available. These studies will locate the rotors and choose the number required for minimal energy control performance and adequate stability and safety margins.

References

[1] R. Skelton and M. de Oliveira, *Tensegrity Systems*. Springer, 2009.

[2] S. H. Juan, R. E. Skelton, and J. M. M. Tur, "Dynamically stable collision avoidance for tensegrity based robots," in *International Conference on Reconfigurable Mechanisms and Robots*, pp. 315–322, 2009.

[3] A. S. Wroldsen, M. C. de Oliveira, and R. E. Skelton, "Modelling and control of non-minimal non-linear realisations of tensegrity systems," *International Journal of Control*, vol. 82, no. 3, pp. 389–407, 2009.

[4] R. E. Skelton and M. C. de Oliveira, "Optimal complexity of deployable compressive structures," *Journal of the Franklin Institute - Engineering and Applied Mathematics*, vol. 347, no. 1, pp. 228–256, 2010.

[5] H. Johnson, "Space settlements: a design study," tech. rep., National Aeronautics and Space Admnistration, 1977.

[6] K. Nagase and R. Skelton, "Double helical tensegrity structures," *AIAA Journal*, (submitted).

[7] K. Nagase and R. Skelton, "Minimal mass tensegrity structures," *Journal of the International Association for Shell and Spatial Structures*, (to appear).

[8] R. B. Fuller, "Tensile-integrity structures." United States Patent 3,063,521, 1962.

[9] S. Sadao, "Fuller on tensegrity," *International Journal of Space Structures*, vol. 11, pp. 37–42, 1996.

[10] K. Miura and Y. Miyazaki, "Concept of the tension truss antenna," *AIAA Journal*, vol. 28, no. 6, pp. 1098–1104, 1990.

[11] L. A. Schmit, "Structural synthesis - its genesis and development," *AIAA Journal*, vol. 19, no. 10, pp. 1249–1263, 1981.

[12] Z. You and S. Pellegrino, "Cable-stiffened pantographic deployable structures part 1: Triangular mast," *AIAA Journal*, vol. 34, no. 4, pp. 813–820, 1996.

[13] C. Sultan and R. E. Skelton, "Deployment of tensegrity structures," *International Journal of Solids and Structures*, vol. 40, no. 18, pp. 4637–4657, 2003.

[14] S. Pellegrino, ed., *Deployable Structures*. Springer, 2001.

[15] L. Puig, A. Barton, and N. Rando, "A review on large deployable structures for astrophysics missions," *Acta Astronautica*, vol. 67, no. 1-2, pp. 12–26, 2010.

[16] J. B. Aldrich, *Control Synthesis for a Class of Light and Agile Robotic Tensegrity Structures*. PhD thesis, Department of Mechanical and Aerospace Engineering, University of California, San Diego,, 2004.

[17] C. Paul, F. J. Valero-Cuevas, and H. Lipson, "Design and control of tensegrity robots for locomotion," *IEEE Transactions on Robotics*, vol. 22, pp. 944–957, October 2006.

[18] M. Masic and R. E. Skelton, "Open-loop control of class-2 tensegrity towers," in *Proceedings of the SPIE Smart Structures and Materials: Modeling, Signal Processing, and Control* (R. C. Smith, ed.), vol. 5383, (San Diego, CA, USA), pp. 298–308, March 2004.

[19] F. Fraternali, L. Senatore, and C. Daraio, "Solitary waves on tensegrity lattices," *Journal of the Mechanics and Physics of Solids*, vol. 60, no. 6, pp. 1137–1144, 2012.

[20] D. E. Ingber, "The architecture of life," *Scientific American*, vol. 278, pp. 48–57, January 1998.

[21] C. Vera, R. E. Skelton, F. Bossens, and L. A. Sung, "3-D nanomechanics of an erythrocyte junctional complex in equibiaxial and anisotropic deformations," *Annals of Biomedical Engineering*, vol. 33, no. 10, pp. 1387–1404, 2005.

[22] A. Hanaor, "Prestressed pin-jointed structures - flexibility analysis and prestress design," *Computers and Structures*, vol. 28, no. 6, pp. 757–769, 1988.

[23] S. Pellegrino, "Analysis of prestressed mechanisms," *International Journal of Solids and Structures*, vol. 26, no. 12, pp. 1329–1350, 1990.

[24] D. Williamson, R. E. Skelton, and J. Han, "Equilibrium conditions of a tensegrity structure," *International Journal of Solids and Structures*, vol. 40, no. 23, pp. 6347–6367, 2003.

[25] B. de Jager and R. E. Skelton, "Stiffness of planar tensegrity truss topologies," *International Journal of Solids and Structures*, vol. 43, no. 5, pp. 1308–1330, 2006.

[26] S. Guest, "The stiffness of prestressed frameworks: A unifying approach," *International Journal of Solids and Structures*, vol. 43, no. 3-4, pp. 842–854, 2006.

[27] J. Y. Zhang and M. Ohsaki, "Stability conditions for tensegrity structures," *International Journal of Solids and Structures*, vol. 44, no. 11-12, pp. 3875–3886, 2007.

[28] R. Motro, "Forms and forces in tensegrity systems," in *Proceedings of Third International Conference on Space Structures*, pp. 180–185, 1984.

[29] S. Pellegrino, *Mechanics of Kinematically Indeterminate Structures*. PhD thesis, University of Cambridge, 1986.

[30] N. Vassart and R. Motro, "Multiparametered formfinding method: Application to tensegrity systems," *International Journal of Space Structures*, vol. 14, no. 2, pp. 147–154, 1999.

[31] M. Masic, R. E. Skelton, and P. E. Gill, "Algebraic tensegrity form-finding," *International Journal of Solids and Structures*, vol. 42, pp. 4833–4858, Aug. 2005.

[32] H. C. Tran and J. Lee, "Advanced form-finding of tensegrity structures," *Computers and Structures*, vol. 88, no. 3-4, pp. 237–246, 2010.

[33] R. Motro, S. Najari, and P. Jouanna, "Static and dynamic analysis of tensegrity systems," *Shell and Spatial Structures: Computational Aspects*, vol. 26, pp. 270–279, 1987.

[34] H. Murakami, "Static and dynamic analyses of tensegrity structures, part 1. nonlinear equations of motion," *International Journal of Solids and Structures*, vol. 38, no. 20, pp. 3599–3613, 2001.

[35] N. Kanchanasaratool and D. Williamson, "Modelling and control of class nsp tensegrity structures," *International Journal of Control*, vol. 75, no. 2, pp. 123–139, 2002.

[36] C. Sultan, M. Corless, and R. E. Skelton, "Linear dynamics of tensegrity structures," *Engineering Structures*, vol. 24, no. 6, pp. 671–685, 2002.

[37] R. Skelton, "Dynamics and control of tensegrity systems," *IUTAM Symposium on Vibration Control of Nonlinear Mechanisms and Structures: Solid Mechanics and its Applications*, vol. 130, pp. 309–318, 2005.

[38] R. Motro, *Tensegrity: Structural Systems for the Future*. London: Kogan Page Science, 2003.

[39] A. G. Tibert and S. Pellegrino, "Review of form-finding methods for tensegrity structures," *International Journal of Space Structures*, vol. 18, no. 4, pp. 209–223, 2003.

[40] S. H. Juan and J. M. Mirats-Tur, "Tensegrity frameworks: Static analysis review," *Mechanism and Machine Theory*, vol. 43, no. 7, pp. 859–881, 2008.

[41] J. M. Mirats-Tur and S. H. Juan, "Tensegrity frameworks: Dynamic analysis review and open problems," *Mechanism and Machine Theory*, vol. 44, no. 1, pp. 1–18, 2009.

[42] Y. Yoshimura, "On the mechanism of buckling of a circular cylindrical shell under axial compression," *Reports of the Institute of Science and Technology , University of Tokyo, Japan*, vol. 5, pp. 179–198; in Japanese, 1951.

[43] Y. Yoshimura, "On the mechanism of buckling of a circular cylindrical shell under axial compression," *National Advisory Committee for Aeronautics, Technical Memorandum 1390,* 1995, 1955.

[44] N. J. Hoff, W. A. Madsen, and J. Mayers, "Postbuckling equilibrium of axially compressed circular cylindrical shells," *AIAA Journal*, vol. 4, no. 1, pp. 126–133, 1966.

[45] K. Miura and H. Furuya, "Adaptive structure concept for future space applications," *AIAA Journal*, vol. 26, no. 8, pp. 995–1002, 1988.

[46] H. J. Schek, "The force density method for form finding and computation of general networks," *Computer Methods in Applied Mechanics and Engineering*, vol. 3, no. 1, pp. 115–134, 1974.

[47] M. Masic, R. E. Skelton, and P. E. Gill, "Optimization of tensegrity structures," *International Journal of Solids and Structures*, vol. 43, pp. 4687–4703, Aug. 2006.

[48] C. D. Meyer, *Matrix Analysis and Applied Linear Algebra*. SIAM, 2000.

[49] R. E. Skelton, T. Iwasaki, and K. Grigoriadis, *A Unified Algebraic Approach to Linear Control Design*. Taylor & Francis, 1998.

[50] S. Boyd and L. Vandenberghe, *Convex Optimization*. Cambridge University Press, 2004.

[51] M. Masic, R. Skelton, and P. Gill, "Optimization of tensegrity structures," *International Journal of Solids and Structures*, vol. 43, pp. 4687–4703, 2006.

[52] R. Motro, S. Najari, and P. Jouanna, "Static and dynamic analysis of tensegrity systems," in *Proceedings of ASCE International Symposium on Shells and Spatial Structures, Computational Aspects*, (New York, NY, USA), pp. 270–279, Springer, 1986.

[53] N. Kanchanasaratool and D. Williamson, "Modelling and control of class nsp tensegrity structures," *International Journal of Control*, vol. 75, pp. 123–139, 2002.

[54] C. Sultan, *Modeling, design, and control of tensegrity structures with applications*. PhD thesis, Purdue University, School of Aeronautics and Astronautics, West Lafayette, IN, 1999.

[55] R. E. Skelton, J. P. Pinaud, and D. L. Mingori, "Dynamics of the shell class of tensegrity structures," *Journal of the Franklin Institute*, vol. 338, no. 2-3, pp. 255–320, 2001.

[56] R. E. Skelton, "Dynamics and control of tensegrity systems," in *Proceedings of the IUTAM Symposium on Vibration Control of Nonlinear Mechanisms and Structures*, vol. 130, (Munich, Germany), pp. 309–318, July 2005.

[57] J. Mirats-Tur and S. Hernández, "Tensegrity frameworks: Dynamic analysis review and open problems," *International Journal of Mechanism and Machine Theory*, vol. 44, pp. 1–18, 2009.

[58] C. D. Meyer, *Matrix Analysis and Applied Linear Algebra*. SIAM, 2000.

[59] R. M. Murray, Z. Li, and S. S. Sastry, *A Mathematical Introduction to Robotic Manipulation*. CRC Press, 1994.

[60] J. Baumgrate, "Stabilization of constraints and integrals of motion in dynamical systems," *Computer Methods in Applied Mechanics and Engineering*, vol. 1, pp. 1–16, 1972.

[61] X. Yun and N. Sarkar, "Unified formulation of robotic system with holonomic and nonholonomic constraints," *IEEE Trans. Robotics and Automation*, vol. 14, pp. 640–650, 1998.

[62] J. J. Craig, *Introduction to Robotics: Mechanics and Control*. Peason Prentice Hall, 2005.

Appendix A

Minimal Mass Tensegrity Torus Design (small size)

A.1 Tensegrity Torus

We design a tensegrity torus shown in Fig. A.1. This torus is constructed from the Double Helical Tensegrity units as shown in Fig. A.2 [6]. Each unit has 2 bars (blue line) and 8 strings (red line). We have q units along the circumference of the torus (big radius), and p units along the circumference of the tube (small radius). Total number of the nodes is $2pq$. The torus spins about z axis to make the centrifugal force $g/3$ on the ground located inside the tube. Soil 1/3 meter deep and water 1 meter deep are arranged on the ground. Atmospheric pressure inside the tube is 1 atm.

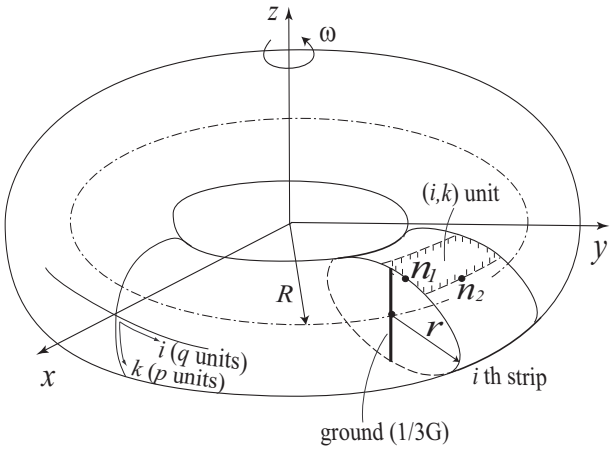

Figure A.1: Tensegrity torus

Physical parameters are given below:

(Size & Spin)
Radius of Torus : $R = 10$ [m]
Radius of Tube : $r = 5$ [m]
Angular Velocity : $\omega = \sqrt{g/3R} = 0.57[rad/sec] = 5.4[rpm]$

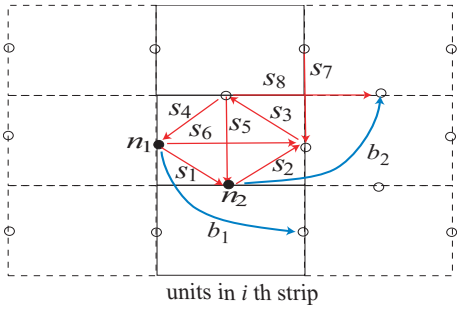

Figure A.2: Elements in unit (i, k)

*1/3g at center of tube

(Member Materials (Steel))
Mass density : $\rho = 7862[kg/m^3]$
Yield stress : $\sigma = 6.9 \times 10^8[N/m]$
Young's modulus : $E = 2.06 \times 10^{11}[N/m]$

(Ground Soil & Water)
Mass density of soil/water : $\rho_s = 2.0 \times 10^3[Kg/m^3]$, $\rho_w = 1.0 \times 10^3[Kg/m^3]$
Thickness of soil/water : $h_s = 1/3[m]$, $h_w = 1[m]$
Area of ground : $S_g = 2\pi R \times 2r = 6.28 \times 10^2[m^2]$
Mass of soil/water : $M_s = \rho_s h_s S_g = 4.19 \times 10^5[Kg]$,
$M_w = \rho_w h_w S_g = 6.28 \times 10^5[Kg]$

(Atmospheric Pressure)
Atmospheric Pressure : $P_s = 1[atm] = 10^5[N/m^2]$
Area of Tube : $S_a = 2\pi r \times 2\pi R = 1.97 \times 10^3[m^2]$

A.2 Minimal Mass Design

A.2.1 Problem settings

We minimize the mass subject to a force balance condition and a maximum stress constraint. The optimization problem is described by a linear program [1, 7]. For the first calculations, we only consider the yield stress constraint (no buckling).

For external force, we consider both the atmospheric pressure and the centrifugal force.

The atmospheric pressure is modeled as a nodal force outward along the radial direction of the small circle (tube) as shown in Fig. A.3. Nodal force from atmospheric pressure is given as:

$$w_{a_i} = P_a S_a / 2pq = 1.97 \times 10^8 / 2pq = 5.48 \times 10^5[N]$$

The centrifugal force comes from two sources, the ground mass (water and soil) and member mass (bar and string). Centrifugal force of the ground mass is modeled as nodal forces equally

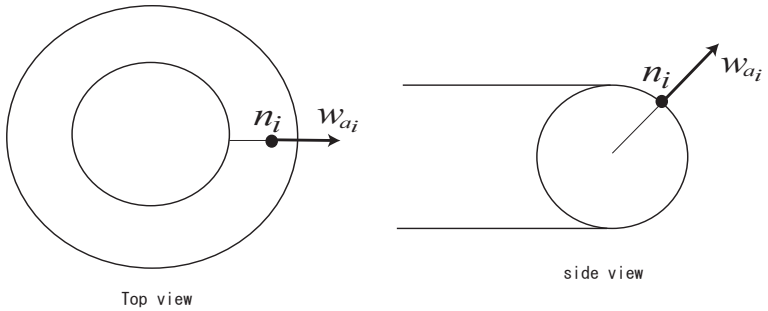

Figure A.3: Atmospheric Force

distributed to all the nodes as shown (Fig. A.4 (a)). Centrifugal force of the members is modeled as nodal forces equally distributed to two member nodes (Fig. A.4 (b)). These forces are given by:

$$w_{g_i} = (M_s + M_w)R\omega^2/2pq = 9.50 \times 10^3[N]$$
$$w_{m_i} = 1/2 \times m_i \times r_{G_i}\omega_2,$$

where m_i is the member mass.

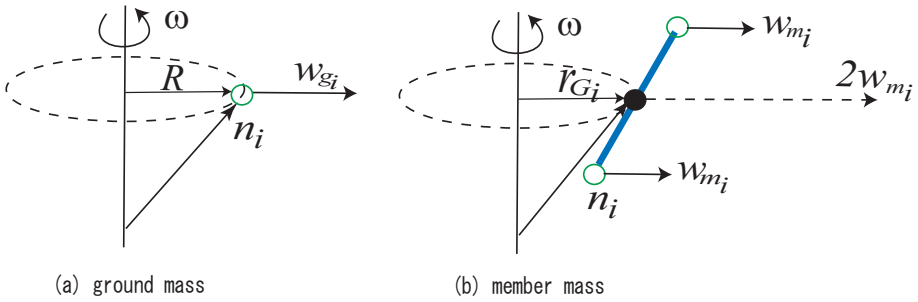

Figure A.4: Atmospheric Force

A.2.2 Optimal Structure for $(p, q) = (6, 30)$

To see which member carries forces dominantly, we pick the complexity $(p, q) = (6, 30)$ and check the member force and the mass. Overview of the torus is shown in Fig. A.5. The blue lines represent the bars (compressive members), and the red lines represent the strings (tensile members).

The member values are summarized in Fig. A.10, in the last page of this chapter. Owing to the symmetry, we only show the values in i^{th} strip. In the columns of the table, k represents the number of unit in the strip. Order of the units is shown in Fig. A.6. Variables in the rows on the left represent:

$\|\boldsymbol{b}_i\|$ $(\boldsymbol{s}_i\|)$	:	length of bar (string)
t_{b_i} (t_{s_i})	:	member force of bar (string)
m_{b_i} (m_{s_i})	:	mass of bar (string)
r_{b_i} (r_{s_i})	:	radius of bar (string)

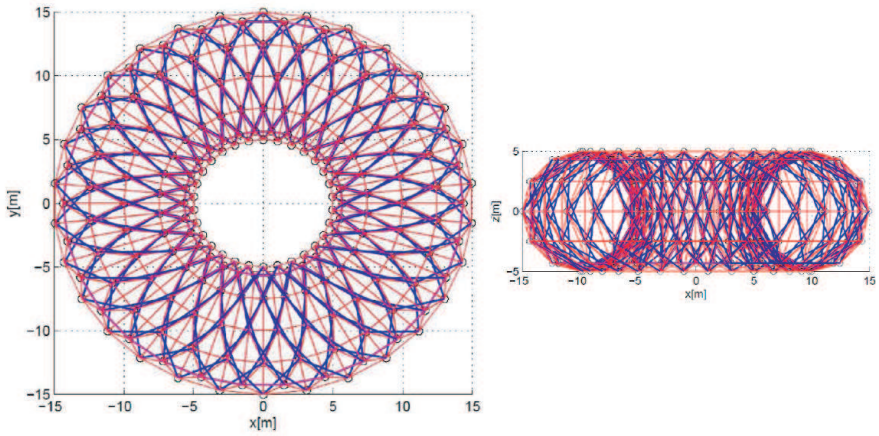

Figure A.5: Overview of torus with $(p, q) = (6, 30)$

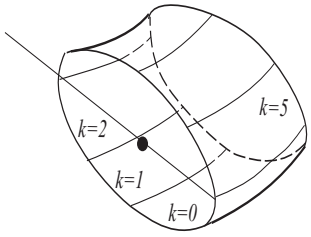

Figure A.6: Order of units in a strip

From the table, all the bars seem unnecessary. A torus with only strings is shown in Fig. A.7. The structure is stable from the stiffness analysis [7].

A.2.3 Stiffness

For later design, we will control the rotation of the torus. It will be useful to examine the bending stiffness about an axis in the plane of the large radius (see Fig. A.8). The bending stiffness can be calculated as follows.

From the stiffness analysis in [7], relationship between the force variation $d\boldsymbol{w}$ and the resultant node deflection $d\boldsymbol{n}$ is given by

$$d\boldsymbol{w} = \boldsymbol{K}_n d\boldsymbol{n}$$

where $\boldsymbol{K}_n$ is the stiffness matrix. To calculate the bending stiffness, we choose a set of forces shown in Fig. A.8. The forces are acting on the nodes in the cross-sections represented by the dotted lines. The force variation can be represented as $d\boldsymbol{w} = \boldsymbol{c}_d \delta w$, where $\boldsymbol{c}_d$ is a constant vector and δw is magnitude of the force. Suppose the node deflection is represented by $d\boldsymbol{n} = \boldsymbol{c}_d \delta n$. Substituting these variations to the stiffness equation, we have

$$\delta w = \underbrace{1/c_d^T K_n^{-1} c_d}_{\boldsymbol{K}_d} \delta n,$$

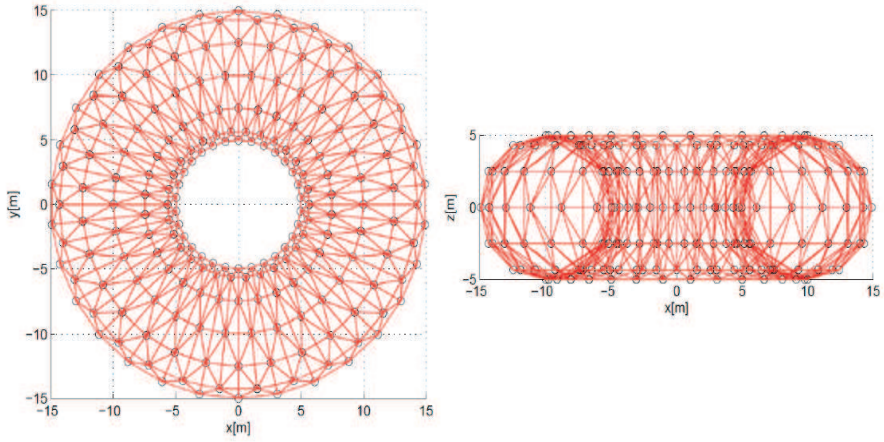

Figure A.7: Torus with dominant members

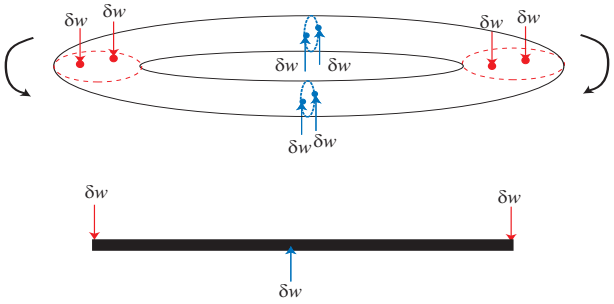

Figure A.8: Bending stiffness

where $\boldsymbol{K}_d$ is the bending stiffness.

For the minimal mass torus with the complexity $(p, q) = (6, 28)$, the bending stiffness $K_d = 4.02 \times 10^6 [Nm]$.

A.2.4 Optimal Complexity

For a given complexity (p, q), we get the minimum mass from the optimization problem. Repeating the calculation, we see the mass of the structure over the different complexities. The result is shown in Fig. A.9. The mass is slightly increases as the complexity increases, but it is almost unchanged.

A.2.5 Impact of ground mass

To see how the total member mass (bars and strings) changes when the ground mass increases, we increase the water depth from 1 [m] to 4 [m]. The results for $(p, q) = (6, 30)$ are summarized as:

(i) $h_w = 1 : M_w = 6.28 \times 10^5$ [Kg] $\rightarrow M = 1.56 \times 10^4$ [Kg]

(ii) $h_w = 4 : M_w = 2.51 \times 10^6$ [Kg] $\rightarrow M = 2.35 \times 10^4$ [Kg],

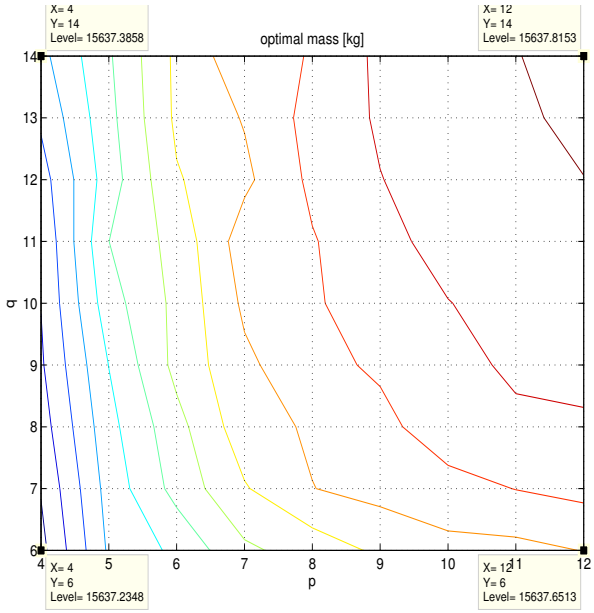

Figure A.9: Minimal mass over different complexity (p, q)

where h_w and M_w are the water depth and the water mass respectively, and M is the total member mass.

Although we increase the water mass by 4 times, the total member mass only increases by 1.5 times. This comes from the fact that the atmospheric pressure in the current design is dominant in the nodal forces, compared to the centrifugal forces of the ground mass.

R=10[m], r=5[m]
Atmospheric Presssure =1 [atm] -> Nodal force outward wp=5.48e+5 [N]
Ground Mass: Water=6.2832e+005[Kg], Soil=4.1888e+005[Kg]
Optimal Mass =1.5638e+004 (Bar=4.1824e-021[Kg], String=1.5638e+004[Kg])

Bar		k=0	k=1	k=2	k=3	k=4	k=5
‖bi‖ [m]	b1	5.5900E+00	5.2400E+00	5.1400E+00	5.2400E+00	5.5900E+00	5.8300E+00
	b2	5.7600E+00	5.3900E+00	5.1600E+00	5.1600E+00	5.3900E+00	5.7600E+00
tbi [N]	b1	5.1348E-20	3.8958E-20	2.2033E-18	2.4311E-20	6.7650E-21	2.3749E-21
	b2	5.6767E-22	1.3365E-30	4.0075E-21	2.2522E-20	1.0686E-20	7.8874E-21
mbi[Kg]	b1	3.2713E-24	2.3269E-24	1.2900E-22	1.4521E-24	4.3099E-25	1.5773E-25
	b1	3.7266E-26	8.2148E-35	2.3568E-25	1.3245E-24	6.5680E-25	5.1779E-25
rbi[m]	b1	4.8670E-15	4.2394E-15	3.1881E-14	3.3489E-15	1.7666E-15	1.0467E-15
	b2	5.1174E-16	2.4831E-20	1.3597E-15	3.2233E-15	2.2203E-15	1.9075E-15

String		k=0	k=1	k=2	k=3	k=4	k=5
‖si‖ [m]	s1	2.9400E+00	2.7400E+00	2.6500E+00	2.6800E+00	2.8400E+00	3.0100E+00
	s2	2.9400E+00	2.7400E+00	2.6500E+00	2.6800E+00	2.8400E+00	3.0100E+00
	s3	3.0100E+00	2.8400E+00	2.6800E+00	2.6500E+00	2.7400E+00	2.9400E+00
	s4	3.0100E+00	2.8400E+00	2.6800E+00	2.6500E+00	2.7400E+00	2.9400E+00
	s5	5.0000E+00	5.0000E+00	5.0000E+00	5.0000E+00	5.0000E+00	5.0000E+00
	s6	3.0000E+00	2.0900E+00	1.1900E+00	1.1900E+00	2.0900E+00	3.0000E+00
	s7	5.0000E+00	5.0000E+00	5.0000E+00	5.0000E+00	5.0000E+00	5.0000E+00
	s8	3.1400E+00	2.6100E+00	1.5700E+00	1.0500E+00	1.5700E+00	2.6100E+00
tsi [N]	s1	2.8045E+05	2.2936E+05	2.7931E+05	2.5284E+05	2.4661E+05	2.9599E+05
	s2	2.7882E+05	2.2572E+05	2.7002E+05	2.4658E+05	2.4435E+05	2.9460E+05
	s3	2.9526E+05	2.4595E+05	2.5040E+05	2.8061E+05	2.3117E+05	2.8167E+05
	s4	2.9387E+05	2.4369E+05	2.4414E+05	2.7132E+05	2.2754E+05	2.8004E+05
	s5	2.8006E+05	3.5412E+05	2.8623E+05	2.8339E+05	3.5308E+05	2.7866E+05
	s6	4.6644E+05	3.4202E+05	2.5881E+05	2.6383E+05	3.3607E+05	4.6281E+05
	s7	2.8720E+05	3.0948E+05	3.3387E+05	2.6050E+05	3.3210E+05	3.0886E+05
	s8	5.6605E+05	3.4198E+05	3.3542E+05	2.3823E+05	3.3641E+05	3.4497E+05
msi[Kg]	s1	9.4044E+00	7.1667E+00	8.4257E+00	7.7114E+00	7.9814E+00	1.0148E+01
	s2	9.3496E+00	7.0530E+00	8.1456E+00	7.5205E+00	7.9082E+00	1.0100E+01
	s3	1.0123E+01	7.9602E+00	7.6368E+00	8.4650E+00	7.2234E+00	9.4454E+00
	s4	1.0075E+01	7.8871E+00	7.4459E+00	8.1848E+00	7.1098E+00	9.3906E+00
	s5	1.5955E+01	2.0175E+01	1.6307E+01	1.6145E+01	2.0115E+01	1.5876E+01
	s6	1.5922E+01	8.1471E+00	3.4954E+00	3.5632E+00	8.0054E+00	1.5798E+01
	s7	1.6362E+01	1.7631E+01	1.9021E+01	1.4841E+01	1.8920E+01	1.7596E+01
	s8	2.0225E+01	1.0183E+01	5.9923E+00	2.8373E+00	6.0101E+00	1.0272E+01
rsi[m]	s1	1.1374E-02	1.0286E-02	1.1351E-02	1.0800E-02	1.0666E-02	1.1685E-02
	s2	1.1341E-02	1.0204E-02	1.1161E-02	1.0666E-02	1.0617E-02	1.1658E-02
	s3	1.1671E-02	1.0652E-02	1.0748E-02	1.1378E-02	1.0327E-02	1.1399E-02
	s4	1.1643E-02	1.0603E-02	1.0612E-02	1.1188E-02	1.0245E-02	1.1366E-02
	s5	1.1367E-02	1.2781E-02	1.1491E-02	1.1434E-02	1.2762E-02	1.1338E-02
	s6	1.4669E-02	1.2561E-02	1.0927E-02	1.1032E-02	1.2451E-02	1.4612E-02
	s7	1.1510E-02	1.1949E-02	1.2411E-02	1.0962E-02	1.2378E-02	1.1937E-02
	s8	1.6160E-02	1.2560E-02	1.2439E-02	1.0483E-02	1.2458E-02	1.2615E-02

Figure A.10: Member Values for $(p, q) = (6, 30)$

Appendix B

Minimal Mass Tensegrity Torus (full size)

B.1 Tensegrity Torus

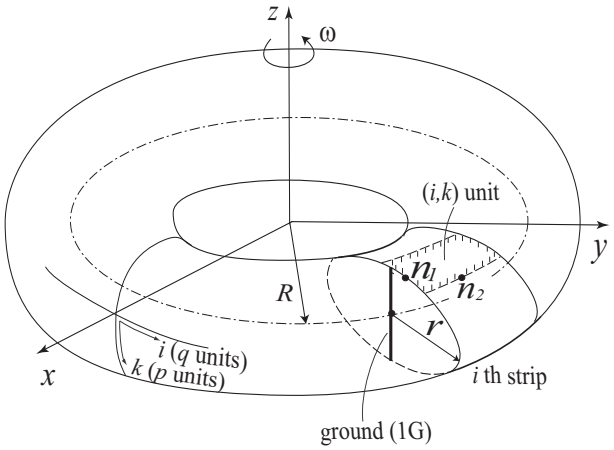

Figure B.1: Tensegrity torus

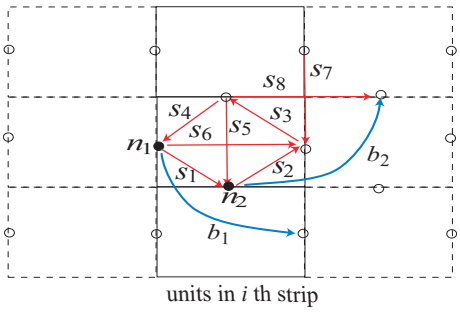

Figure B.2: Elements in unit (i, k)

We design a tensegrity torus shown in Fig. B.1. This torus is constructed from the Double

Helical Tensegrity units as shown in Fig. B.2 [6]. Each unit has 2 bars (blue line) and 8 strings (red line). We have q units along the circumference of the torus (big radius), and p units along the circumference of the tube (small radius). Total number of the nodes is $2pq$. The torus spins about z axis to make the centrifugal force $1g$ on the ground located inside the tube. Soil 1/3 meter deep and water 1 meter deep are arranged on the ground. Atmospheric pressure inside the tube is 1 atm.@

Physical parameters are given below:

(Size & Spin)

Radius of Torus	:	$R = 1000$ [m]
Radius of Tube	:	$r = 500$ [m]
Angular Velocity	:	$\omega = \sqrt{g/R} = 0.099[rad/sec] = 0.95[rpm]$
		*1g at center of tube

(Member Materials (Steel))

Mass density	:	$\rho = 7862[kg/m^3]$
Yield stress	:	$\sigma = 6.9 \times 10^8[N/m]$
Young's modulus	:	$E = 2.06 \times 10^{11}[N/m]$

(Ground Soil & Water)

Mass density of soil/water	:	$\rho_s = 2.0 \times 10^3[Kg/m^3]$, $\rho_w = 1.0 \times 10^3[Kg/m^3]$
Thickness of soil/water	:	$h_s = 1/3[m]$, $h_w = 1[m]$
Area of ground	:	$S_g = 2\pi R \times 2r = 6.28 \times 10^6[m^2]$
Mass of soil/water	:	$M_s = \rho_s h_s S_g = 4.19 \times 10^9[Kg]$,
		$M_w = \rho_w h_w S_g = 6.28 \times 10^9[Kg]$

(Atmospheric Pressure)

Atmospheric Pressure	:	$P_s = 1[atm] = 10^5[N/m^2]$
Area of Tube	:	$S_a = 2\pi r \times 2\pi R = 1.97 \times 10^7[m^2]$

B.2 Minimal Mass Design

B.2.1 Problem settings

We minimize the mass subject to a force balance condition and a maximum stress constraint. The optimization problem is described by a linear program [1, 7]. For the first calculations, we only consider the yield stress constraint (no buckling).

For external force, we consider both the atmospheric pressure and the centrifugal force.

The atmospheric pressure is modeled as a nodal force outward along the radial direction of the small circle (tube) as shown in Fig. B.3. Nodal force from atmospheric pressure is given as:

$$w_{a_i} = P_a S_a / 2pq = 1.97 \times 10^8 / 2pq = 5.48 \times 10^9[N]$$

The centrifugal force comes from two sources, the ground mass (water and soil) and member mass (bar and string). Centrifugal force of the ground mass is modeled as nodal forces equally distributed to all the nodes as shown (Fig. B.4 (a)). Centrifugal force of the members is modeled

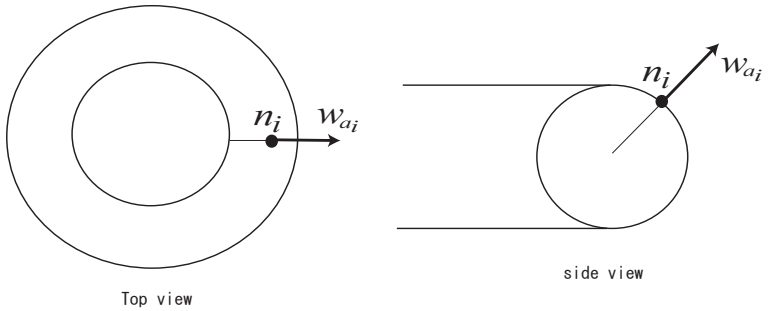

Figure B.3: Atmospheric Force

as nodal forces equally distributed to two member nodes (Fig. B.4 (b)). These forces are given by:

$$w_{g_i} = (M_s + M_w)R\omega^2/2pq = 2.85 \times 10^8[N]$$
$$w_{m_i} = 1/2 \times m_i \times r_{G_i}\omega_2,$$

where m_i is the member mass.

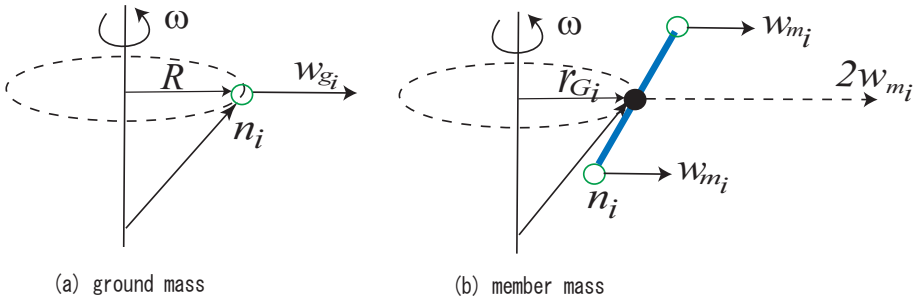

Figure B.4: Atmospheric Force

B.2.2 Optimal Structure for $(p, q) = (6, 30)$

To see which member carries forces dominantly, we pick the complexity $(p, q) = (6, 30)$ and check the member force and the mass. Overview of the torus is shown in Fig. B.5. The blue lines represent the bars (compressive members), and the red lines represent the strings (tensile members).

The member values are summarized in Fig. B.9, in the last page of this chapter. Owing to the symmetry, we only show the values in i^{th} strip. In the columns of the table, k represents the number of unit in the strip. Order of the units is shown in Fig. B.6. Variables in the rows on the left represent:

$\|\boldsymbol{b}_i\|$ $(\boldsymbol{s}_i\|)$	:	length of bar (string)
t_{b_i} (t_{s_i})	:	member force of bar (string)
m_{b_i} (m_{s_i})	:	mass of bar (string)
r_{b_i} (r_{s_i})	:	radius of bar (string)

From the table, all the bars and some strings seem unnecessary. A torus with dominant strings is shown in Fig. B.7. The structure is stable from the stiffness analysis [7].

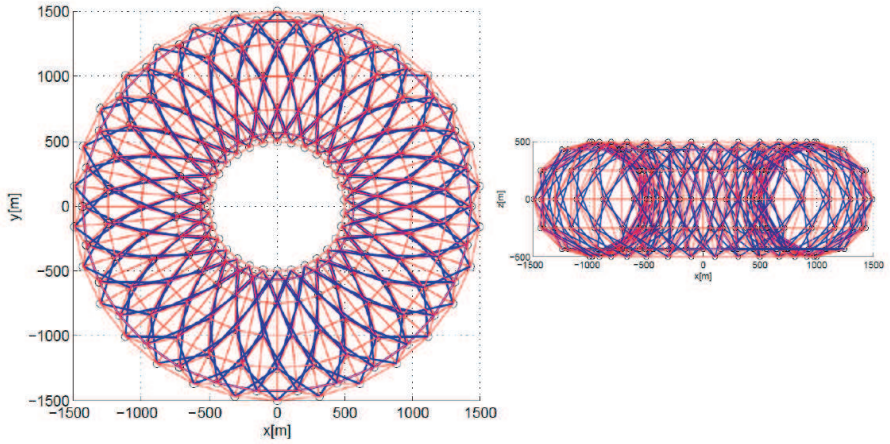

Figure B.5: Overview of torus with $(p, q) = (6, 30)$

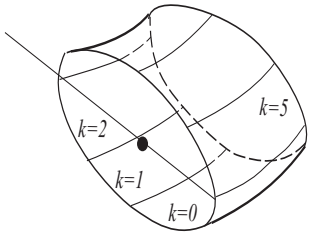

Figure B.6: Oder of units in a strip

B.2.3 Stiffness

For later design, we will control the rotation of the torus. It will be useful to examine the bending stiffness about an axis in the plane of the large radius (see Fig. B.8). The bending stiffness can be calculated as follows.

From the stiffness analysis in [7], relationship between the force variation $d\boldsymbol{w}$ and the resultant node deflection $d\boldsymbol{n}$ is given by

$$d\boldsymbol{w} = \boldsymbol{K}_n d\boldsymbol{n}$$

where $\boldsymbol{K}_n$ is the stiffness matrix. To calculate the bending stiffness, we choose a set of forces shown in Fig. B.8. The forces are acting on the nodes in the cross-sections represented by the dotted lines. The force variation can be represented as $d\boldsymbol{w} = \boldsymbol{c}_d \delta w$, where $\boldsymbol{c}_d$ is a constant vector and δw is magnitude of the force. Suppose the node deflection is represented by $d\boldsymbol{n} = \boldsymbol{c}_d \delta n$. Substituting these variations to the stiffness equation, we have

$$\delta w = \underbrace{1/c_d^T K_n^{-1} c_d}_{\boldsymbol{K}_d} \delta n,$$

where $\boldsymbol{K}_d$ is the bending stiffness.

For the minimal mass torus with the complexity $(p, q) = (6, 28)$, the bending stiffness $K_d = 2.29 \times 10^8 [Nm]$.

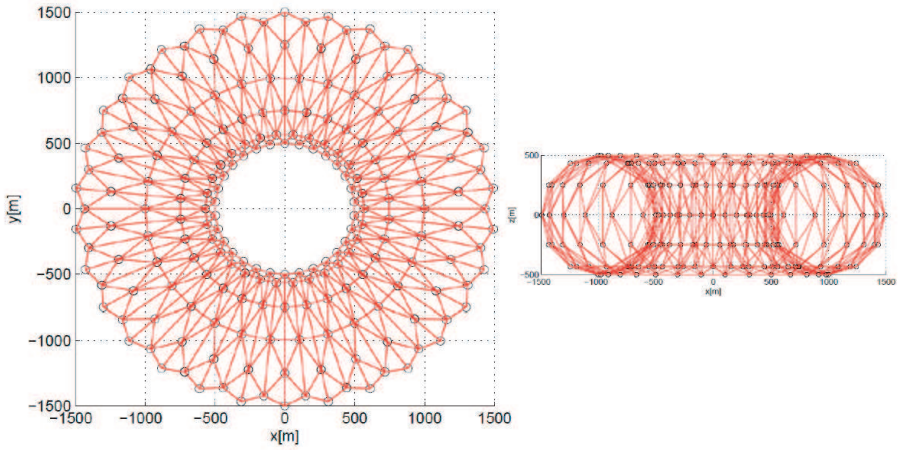

Figure B.7: Torus with dominant members

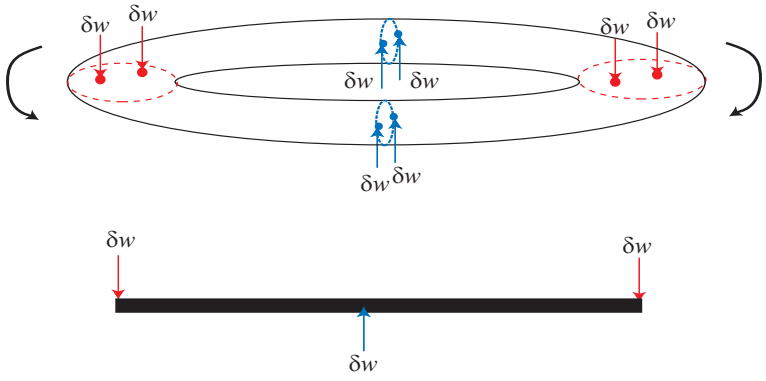

Figure B.8: Bending stiffness

R=1000[m], r=500[m]
Atmospheric Presssure =1 [atm] -> Nodal force outward wp=5.4831e+009 [N]
Ground Mass: Water=6.2832e+009[Kg], Soil=4.1888e+009[Kg]
Optimal Mass =1.4276e+010 (Bar=5.4188e-010[Kg], String=1.4276e+010[Kg])

Bar		k=0	k=1	k=2	k=3	k=4	k=5
‖bi‖ [m]	b1	5.5900E+02	5.2400E+02	5.1400E+02	5.2400E+02	5.5900E+02	5.8300E+02
	b2	5.7600E+02	5.3900E+02	5.1600E+02	5.1600E+02	5.3900E+02	5.7600E+02
tbi [N]	b1	2.2600E-10	2.6400E-10	2.8000E-10	2.6400E-10	2.2600E-10	2.0400E-10
	b2	2.1000E-10	2.4600E-10	2.7600E-10	2.7600E-10	2.4600E-10	2.1000E-10
mbi[Kg]	b1	1.4400E-12	1.5800E-12	1.6400E-12	1.5800E-12	1.4400E-12	1.3600E-12
	b1	1.3800E-12	1.5100E-12	1.6300E-12	1.6300E-12	1.5100E-12	1.3800E-12
rbi[m]	b1	3.2300E-10	3.4900E-10	3.6000E-10	3.4900E-10	3.2300E-10	3.0700E-10
	b2	3.1100E-10	3.3700E-10	3.5700E-10	3.5700E-10	3.3700E-10	3.1100E-10

String		k=0	k=1	k=2	k=3	k=4	k=5
‖si‖ [m]	s1	2.9400E+02	2.7400E+02	2.6500E+02	2.6800E+02	2.8400E+02	3.0100E+02
	s2	2.9400E+02	2.7400E+02	2.6500E+02	2.6800E+02	2.8400E+02	3.0100E+02
	s3	3.0100E+02	2.8400E+02	2.6800E+02	2.6500E+02	2.7400E+02	2.9400E+02
	s4	3.0100E+02	2.8400E+02	2.6800E+02	2.6500E+02	2.7400E+02	2.9400E+02
	s5	5.0000E+02	5.0000E+02	5.0000E+02	5.0000E+02	5.0000E+02	5.0000E+02
	s6	3.0000E+02	2.0900E+02	1.1900E+02	1.1900E+02	2.0900E+02	3.0000E+02
	s7	5.0000E+02	5.0000E+02	5.0000E+02	5.0000E+02	5.0000E+02	5.0000E+02
	s8	3.1400E+02	2.6100E+02	1.5700E+02	1.0500E+02	1.5700E+02	2.6100E+02
tsi [N]	s1	1.9500E+09	9.8500E+08	3.4100E+09	2.4000E+09	4.4000E+08	3.5800E+09
	s2	1.9500E+09	9.9400E+08	3.4300E+09	2.4100E+09	4.4600E+08	3.5800E+09
	s3	3.5800E+09	4.4600E+08	2.4100E+09	3.4000E+09	9.7500E+08	1.9500E+09
	s4	3.5800E+09	4.5200E+08	2.4200E+09	3.4300E+09	9.8400E+08	1.9500E+09
	s5	2.9200E+09	6.4700E+09	2.2300E+09	2.2400E+09	6.4800E+09	2.9300E+09
	s6	1.0200E-08	1.8500E+09	3.9900E+09	3.9700E+09	1.8800E+09	1.0200E-08
	s7	1.8500E+09	5.2600E+09	4.3200E+09	1.7500E+09	4.3300E+09	5.2600E+09
	s8	9.2300E-09	1.4700E-08	7.8000E+09	1.8500E+09	7.7900E+09	1.4700E-08
msi[Kg]	s1	6.5400E+06	3.0800E+06	1.0300E+07	7.3100E+06	1.4200E+06	1.2300E+07
	s2	6.5500E+06	3.1100E+06	1.0300E+07	7.3500E+06	1.4400E+06	1.2300E+07
	s3	1.2300E+07	1.4400E+06	7.3400E+06	1.0300E+07	3.0500E+06	6.5200E+06
	s4	1.2300E+07	1.4600E+06	7.3900E+06	1.0300E+07	3.0800E+06	6.5400E+06
	s5	1.6700E+07	3.6900E+07	1.2700E+07	1.2800E+07	3.6900E+07	1.6700E+07
	s6	3.4800E-11	4.4200E+06	5.3900E+06	5.3700E+06	4.4800E+06	3.4800E-11
	s7	1.0500E+07	2.9900E+07	2.4600E+07	9.9500E+06	2.4700E+07	3.0000E+07
	s8	3.3000E-11	4.3700E-11	1.3900E+07	2.2100E+06	1.3900E+07	4.3700E-11
rsi[m]	s1	9.4800E-01	6.7400E-01	1.2500E+00	1.0500E+00	4.5100E-01	1.2800E+00
	s2	9.4900E-01	6.7700E-01	1.2600E+00	1.0500E+00	4.5300E-01	1.2900E+00
	s3	1.2800E+00	4.5400E-01	1.0500E+00	1.2500E+00	6.7100E-01	9.4700E-01
	s4	1.2900E+00	4.5700E-01	1.0600E+00	1.2600E+00	6.7400E-01	9.4800E-01
	s5	1.1600E+00	1.7300E+00	1.0100E+00	1.0200E+00	1.7300E+00	1.1600E+00
	s6	2.1700E-09	9.2500E-01	1.3600E+00	1.3500E+00	9.3100E-01	2.1700E-09
	s7	9.2300E-01	1.5600E+00	1.4100E+00	8.9800E-01	1.4100E+00	1.5600E+00
	s8	2.0600E-09	2.6000E-09	1.9000E+00	9.2500E-01	1.9000E+00	2.6000E-09

Figure B.9: Member Values for $(p, q) = (6, 30)$

Appendix C

Dynamics and Control of Rigid Torus (small size)

C.1 Abstract

To approximate the control forces required for both a 1/3-g rotation and a sun-following precession, we start with a rigid habitat of the appropriate dimensions and simulate the dynamic response to an initial error, to determine how large the control torques must be in the later structure design studies.

C.2 Introduction

One must determine whether the static or dynamic forces dominate the design and stiffness requirements of the structure. Toward this end we first assume a rigid structure to determine the control forces that would be required if the habitat was a rigid body. These control forces can then (later in our study) be applied to the actual tensegrity flexible habitat to get a first approximation to the impact of dynamics forces, as compared to the static forces that were used in the original habitat concept. This is important since one cannot a priori say which has the greater impact on the design and stiffness requirements of the structure. In other words the design of the structure and the design of the control system are not independent problems.

C.3 Control Requirements

We must satisfy two goals: i) spin the habitat to achieve 1/3g centrifugal force, ii) spin the habitat about another axis so that the habitat is always pointing toward the sun (that is, the axis perpendicular to the plane of the torus is always pointing toward the sun).

One may ask whether these goals can be met without the use of any control forces. To meet the 1/3-g goal, a steady state stable spin about a specific fixed vector in space can be maintained as a stable equilibrium if the spin axis corresponds to the body axis with the largest inertia (this corresponds to an axis perpendicular to the plane of the torus).

But control forces are generally required if one seeks to maintain this spin condition in the presence of energy dissipation within the habitat, and/or if one adds the requirement for the spin axis to also follow the sun. The spin about the solar-pointing axis gives the 1/3-g and the movement around the sun requires the 360 degrees/year precession.

Let's imagine three coordinate systems. The coordinate frame $\underline{\boldsymbol{B}}$ represents the frame fixed in the spinning torus (called the Body Frame). The frame $\underline{\boldsymbol{X}}$ represents a frame whose axis $\underline{\boldsymbol{x}}_3$, aligns with the inertial axis $\underline{\boldsymbol{e}}_3$, but the $\underline{\boldsymbol{X}}$ rotates about its $\underline{\boldsymbol{x}}_3$ with the fixed rate $\Omega_3 = 360$ degrees/year. The frame $\underline{\boldsymbol{E}}$ represents an inertially-fixed frame. The control objective is to cause the body axis $\underline{\boldsymbol{b}}_2$ to align with $\underline{\boldsymbol{x}}_2$, and rotate the body about the axis $\underline{\boldsymbol{x}}_2$ with rate Ω_2 to cause the 1/3-g accelerations in the habitat.

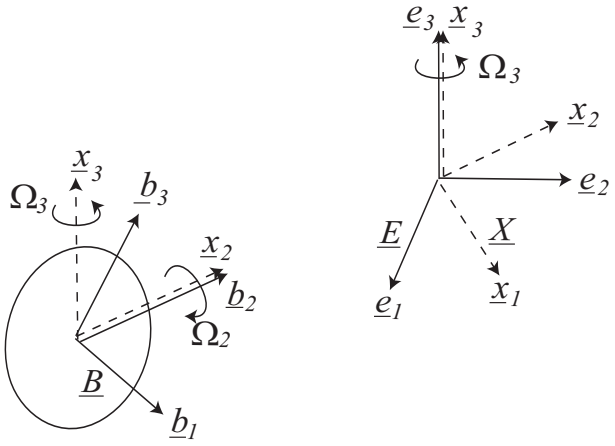

Figure C.1: Rigid body motion and coordinate Frames

Notation

$\underline{\boldsymbol{E}} = [\underline{\boldsymbol{e}}_1, \underline{\boldsymbol{e}}_2, \underline{\boldsymbol{e}}_3]$	=	Inertial Frame
$\underline{\boldsymbol{B}} = [\underline{\boldsymbol{b}}_1, \underline{\boldsymbol{b}}_2, \underline{\boldsymbol{b}}_3]$	=	Body Frame
$\underline{\boldsymbol{X}} = [\underline{\boldsymbol{x}}_1, \underline{\boldsymbol{x}}_2, \underline{\boldsymbol{x}}_3]$	=	Spinning Reference Frame
$\boldsymbol{\Theta}^B$	=	Rotation Matrix from $\underline{\boldsymbol{E}}$ to $\underline{\boldsymbol{B}}$
$\boldsymbol{\Theta}^X$	=	Rotation Matrix from $\underline{\boldsymbol{E}}$ to $\underline{\boldsymbol{X}}$
$\underline{\boldsymbol{\omega}}$	=	Angular Velocity of Rigid Body
$\underline{\bar{\boldsymbol{\omega}}}$	=	Target Value for $\underline{\boldsymbol{\omega}}$
$\underline{\boldsymbol{T}}$	=	Applied Torque to Rigid Body

For a vector $\underline{\boldsymbol{v}}$, we describe coordinates in a frame $\underline{\boldsymbol{A}}$ as $\boldsymbol{v}^A$, i.e., $\underline{\boldsymbol{v}} = \underline{\boldsymbol{A}}\boldsymbol{v}^A$, where $\underline{\boldsymbol{A}}$ is a matrix whose columns are composed of the coordinates of the base vectors. The body frame $\underline{\boldsymbol{B}}$ and the spinning frame $\underline{\boldsymbol{X}}$ are related to the inertial frame $\underline{\boldsymbol{E}}$ by

$$\underline{\boldsymbol{X}} = \underline{\boldsymbol{E}}\boldsymbol{\Theta}^X, \ \underline{\boldsymbol{B}} = \underline{\boldsymbol{E}}\boldsymbol{\Theta}^B. \tag{C.1}$$

Let the vectors $\boldsymbol{\omega}^X, \boldsymbol{\omega}^B$ denote the angular velocity vectors of these frames, expressed in frame coordinates $\underline{\boldsymbol{X}}$ and $\underline{\boldsymbol{B}}$, respectively. Then the relationship between the direction cosine matrices and the angular velocity vectors is given by,

$$\dot{\boldsymbol{\Theta}}^B = \boldsymbol{\Theta}^B\tilde{\boldsymbol{\omega}}^B, \quad \dot{\boldsymbol{\Theta}}^X = \boldsymbol{\Theta}^X\tilde{\boldsymbol{\omega}}^X, \tag{C.2}$$

where $\widetilde{\boldsymbol{\omega}}^B$ and $\widetilde{\boldsymbol{\omega}}^X$ represent skew-symmetric matrices.

C.4 Control of Rigid Body Rotation

C.4.1 Target Value

Suppose the target value of angular velocity of the rigid body $\underline{\boldsymbol{\omega}}$ is given in $\underline{\boldsymbol{X}}$ as

$$\begin{aligned}
\underline{\overline{\boldsymbol{\omega}}} &= \Omega_2 \underline{\boldsymbol{x}}_2 + \Omega_3 \underline{\boldsymbol{e}}_3 && \text{(C.3)}\\
&= \Omega_2 \underline{\boldsymbol{x}}_2 + \Omega_3 \underline{\boldsymbol{x}}_3 && \text{(C.4)}\\
&= \underline{\boldsymbol{X}} \boldsymbol{\Omega}^X && \text{(C.5)}\\
&= \underline{\boldsymbol{E}} \boldsymbol{\Theta}^X \boldsymbol{\Omega}^X && \text{(C.6)}\\
&= \underline{\boldsymbol{B}} (\boldsymbol{\Theta}^B)^T \boldsymbol{\Theta}^X \boldsymbol{\Omega}^X, && \text{(C.7)}
\end{aligned}$$

where $\boldsymbol{\Omega}^X$ is a pre-specified constant vector (target value described in $\underline{\boldsymbol{X}}$). In our case we have chosen $(\boldsymbol{\Omega}^X)^T = [0, \Omega_2, \Omega_3]$.

Define the error vector

$$\underline{\boldsymbol{\omega}}_e = \underline{\boldsymbol{\omega}} - \underline{\overline{\boldsymbol{\omega}}}, \tag{C.8}$$

which is the difference between the actual instantaneous value of the body angular velocity and the desired value. From (C.1) and (C.7), we have

$$\underline{\boldsymbol{\omega}}_e = \underline{\boldsymbol{B}} \boldsymbol{\omega}^B - \underline{\boldsymbol{B}} (\boldsymbol{\Theta}^{\boldsymbol{B}})^T \boldsymbol{\Theta}^X \boldsymbol{\Omega}^X = \underline{\boldsymbol{B}} \underbrace{\left(\boldsymbol{\omega}^B - (\boldsymbol{\Theta}^B)^T \boldsymbol{\Theta}^X \boldsymbol{\Omega}^X \right)}_{\boldsymbol{\omega}_e^B}. \tag{C.9}$$

Our goal now is to find a control torque vector $\underline{\boldsymbol{T}}$ that can be applied to the rigid body habitat to cause the error $\underline{\boldsymbol{\omega}}_e$ to go to zero, regardless of the initial error. First we must write the dynamic equations of motion of the rigid spinning habitat.

C.4.2 Rigid Body Motion

Rotational motion of a rigid body represented in the body frame $\underline{\boldsymbol{B}}$ is given by

$$\boldsymbol{J}^B \dot{\boldsymbol{\omega}}^B + \widetilde{\boldsymbol{\omega}}^B \boldsymbol{J}^B \boldsymbol{\omega}^B = \boldsymbol{T}^B, \tag{C.10}$$

where $\boldsymbol{J}^B$ is the inertia matrix about the body axes $\underline{\boldsymbol{b}}_1, \underline{\boldsymbol{b}}_2, \underline{\boldsymbol{b}}_3$, and $\boldsymbol{T}^B$ is the control torque vector expressed in $\underline{\boldsymbol{B}}$.

Note from (C.9) that $\boldsymbol{\omega}_e^B$ is given by

$$\boldsymbol{\omega}_e^B = \boldsymbol{\omega}^B - (\boldsymbol{\Theta}^B)^T \boldsymbol{\Theta}^X \boldsymbol{\Omega}^X, \tag{C.11}$$

and its derivative is

$$\begin{aligned}
\dot{\boldsymbol{\omega}}_e^B &= \dot{\boldsymbol{\omega}}^B - (\dot{\boldsymbol{\Theta}}^B)^T \boldsymbol{\Theta}^X \boldsymbol{\Omega}^X - (\boldsymbol{\Theta}^B)^T \dot{\boldsymbol{\Theta}}^X \boldsymbol{\Omega}^X && \text{(C.12)}\\
&= \dot{\boldsymbol{\omega}}^B - \widetilde{\boldsymbol{\mu}} \boldsymbol{\omega}^B - (\boldsymbol{\Theta}^B)^T \boldsymbol{\Theta}^X \widetilde{\boldsymbol{\omega}}^X \boldsymbol{\Omega}^X, && \text{(C.13)}
\end{aligned}$$

where $\boldsymbol{\mu} = (\boldsymbol{\Theta}^B)^T \boldsymbol{\Theta}^X \Omega^X$ ($\widetilde{\boldsymbol{\mu}}$ is a skew symmetric matrix), and where the second expression follows from the use of (C.2). Equations (C.10) and (C.2) form a set of differential equations to give

the exact motion of the rigid body, producing both $\boldsymbol{\omega}^B(t)$ and $\boldsymbol{\Theta}^B(t)$, starting from any initials conditions $\boldsymbol{\omega}(0)$, $\boldsymbol{\Theta}^B(0)$. In our case $(\boldsymbol{\omega}^X)^T = [0, 0, \Omega_3]$ is constant, and $\boldsymbol{\Theta}^X(t)$ is a known matrix given by

$$\boldsymbol{\Theta}^X(t) = \begin{bmatrix} \cos\Omega_3 t & -\sin\Omega_3 t & 0 \\ \sin\Omega_3 t & \cos\Omega_3 t & 0 \\ 0 & 0 & 1 \end{bmatrix}. \tag{C.14}$$

C.4.3 Control

We must cause the error $\boldsymbol{\omega}_e^B$ to go to zero, by proper choice of the control torque $\boldsymbol{T}^B$. Our approach is to find the control that will cause the error to be a stable solution to a linear system of equations. We choose to make $\boldsymbol{\omega}_e^B$ follow the dynamics given by

$$\dot{\boldsymbol{\omega}}_e^B = \boldsymbol{A}\boldsymbol{\omega}_e^B, \tag{C.15}$$

where $\boldsymbol{A}$ is a chosen constant matrix whose eigenvalues are all in the left-hand plane. Substitution of (C.11) and (C.13) into (C.15) gives

$$\dot{\boldsymbol{\omega}}^B - \widetilde{\boldsymbol{\mu}}\boldsymbol{\omega}^B - (\boldsymbol{\Theta}^B)^T\boldsymbol{\Theta}^X\widetilde{\boldsymbol{\omega}}^X\boldsymbol{\Omega}^X = \boldsymbol{A}\Big(\boldsymbol{\omega}^B - (\boldsymbol{\Theta}^B)^T\boldsymbol{\Theta}^X\boldsymbol{\Omega}^X\Big). \tag{C.16}$$

Multiplying $\boldsymbol{J}^B$ from the left, and using (C.10), we have the required control torque,

$$\boldsymbol{T}^B = \Big(\widetilde{\boldsymbol{\omega}}^B\boldsymbol{J}^B + \boldsymbol{J}^B\boldsymbol{A} + \boldsymbol{J}^B\widetilde{\boldsymbol{\mu}}\Big)\boldsymbol{\omega}^B + \boldsymbol{J}^B\Big((\boldsymbol{\Theta}^B)^T\boldsymbol{\Theta}^X\widetilde{\boldsymbol{\omega}}^X - \boldsymbol{A}(\boldsymbol{\Theta}^B)^T\boldsymbol{\Theta}^X\Big)\boldsymbol{\Omega}^X \tag{C.17}$$

From (C.10) and (C.17), the closed loop system is given by

$$\dot{\boldsymbol{\omega}}^B = (\boldsymbol{A} + \widetilde{\boldsymbol{\mu}})\boldsymbol{\omega}^B + \Big((\boldsymbol{\Theta}^B)^T\boldsymbol{\Theta}^X\widetilde{\boldsymbol{\omega}}^X - \boldsymbol{A}(\boldsymbol{\Theta}^B)^T\boldsymbol{\Theta}^X\Big)\boldsymbol{\Omega}^X. \tag{C.18}$$

C.5 Simulation

C.5.1 Simulation settings

For a rigid body, we consider a thin disk shown in Fig. C.2. The outer and inner radii of the disk are r_1 and r_2 respectively, and the mass is M. We choose $\underline{\boldsymbol{b}}_2$ axis of the body frame to align with the center axis of the disk. At the initial state, the spinning frame $\underline{\boldsymbol{X}}$ and the body frame $\underline{\boldsymbol{B}}$ coincide with the inertial frame $\underline{\boldsymbol{E}}$. The frame $\underline{\boldsymbol{X}}$ spins about $\underline{\boldsymbol{x}}_3$ axis with the angular velocity ω_3^X (360 deg per year). The disk is controlled to follow $\underline{\boldsymbol{X}}$ while spinning about $\underline{\boldsymbol{x}}_2$ axis with the angular velocity ω_2^X (1/3 g at the middle of the disk radius). Parameters are given as follows.

Physical Parameter:
$r_1 = 15$ [m]
$r_2 = 5$ [m]
$M = 10^6$ [Kg]
$J_2^B = M/2(r_2^2 + r_1^2)$ [Kgm^2]
$J_{1,3}^B = J_2^B/2$ [Kgm^2]

Initial Condition:
$\boldsymbol{\omega}_X = [0\ 0\ \omega_3^X]^T$
$\boldsymbol{\omega}_B(0) = [0\ \omega_2^X\ \omega_3^X]^T$

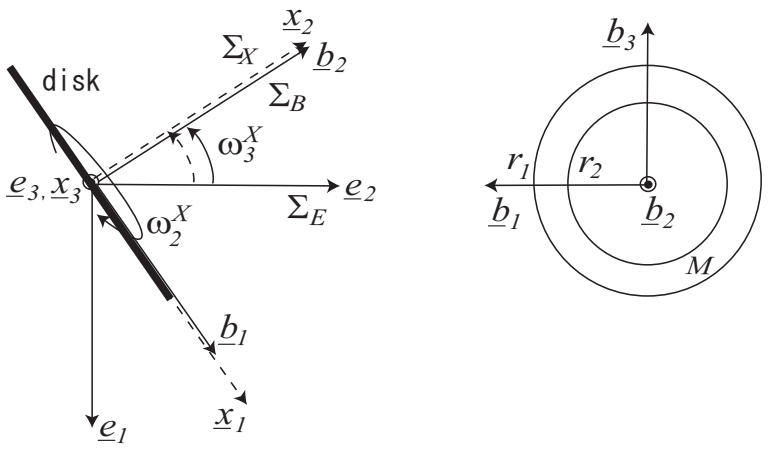

Figure C.2: Spinning disk and coordinates

$\boldsymbol{\Theta}^B(0) = \boldsymbol{I}_3$
where
$\omega_3^X = (360/365)(\pi/180)/(24 \cdot 3600) = 1.99 \times 10^{-7}$ [rad/sec]
$\omega_2^X = \sqrt{g/3/\{(r_1+r_2)/2\}} = 0.57$ [rad/sec]

Control:
$\boldsymbol{A} = -\varepsilon \boldsymbol{I}_3 \quad (\varepsilon = 1 \times 10^{-3})$
$\boldsymbol{\Omega}^X = [0\ \omega_2^X\ \omega_3^X]^T$

C.5.2 Simulation results

Figure C.3 shows time histories of the rigid body angular velocity $\boldsymbol{\omega}^B$, the control error $\boldsymbol{\omega}_e^B$, and the control torque $\boldsymbol{T}^B$. The magnitude of the control torque (bottom) is about 15 [Nm]. Because the error $\boldsymbol{\omega}_e^B$ is zero in this case from the initial condition, this torque corresponds to the torque used for the disk to follow the spinning frame $\underline{\boldsymbol{X}}$ in steady state.

Next we examine the control torque to attenuate the error $\boldsymbol{\omega}_e^B$. Figure C.4 (a) shows the response with an initial error $\omega_2^B(0) = 0.99\,\omega_2^X$. To attenuate ω_2^B, we need about 700 [Nm] at maximum. To see the effect of the control gain ε, Fig. C.4 (b) shows the response with a gain $\varepsilon = 10^{-2}$ (10 times bigger). As expected, we see rapid convergence in the control error (middle) by using larger control torque (bottom).

C.6 Conclusions

This report determines what control forces are necessary to cause the habitat to rotate to follow the sun and give 1/3 g centrifugal force the habitat. This conclusion is that the required control torques are approximately 20 Newtons sinusoidally cycling at the frequency of the spin rotation 11 seconds per rotation. Later work will compute the torque necessary to control the flexible structure.

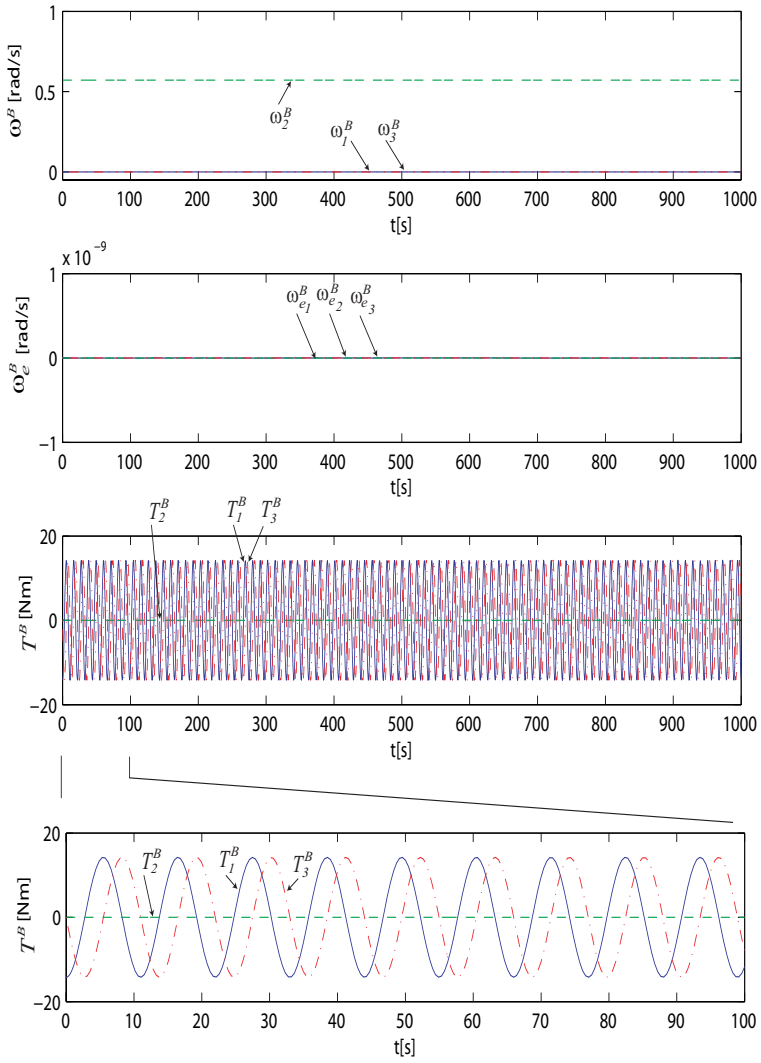

Figure C.3: Time history (no initial error)

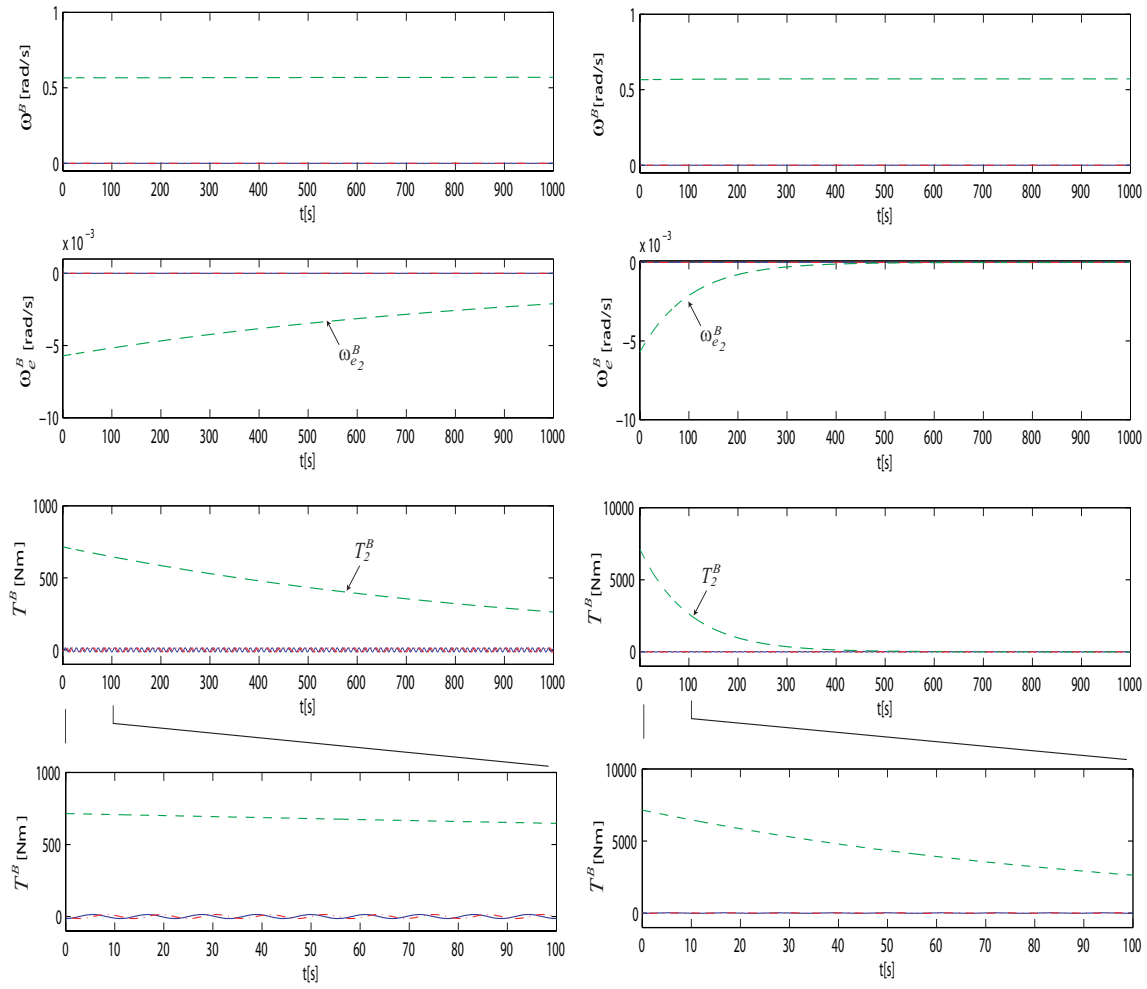

Figure C.4: Time history with initial error ($\omega_2^B(0) = 0.99\omega_2^X$)

Appendix D

Dynamics and Control of Rigid Torus (full size)

D.1 Abstract

To approximate the control forces required for both a 1-g rotation and a sun-following precession, we start with a rigid habitat of the appropriate dimensions and simulate the dynamic response to an initial error, to determine how large the control torques must be in the later structure design studies.

D.2 Introduction

One must determine whether the static or dynamic forces dominate the design and stiffness requirements of the structure. Toward this end we first assume a rigid structure to determine the control forces that would be required if the habitat was a rigid body. These control forces can then (later in our study) be applied to the actual tensegrity flexible habitat to get a first approximation to the impact of dynamics forces, as compared to the static forces that were used in the original habitat concept. This is important since one cannot a priori say which has the greater impact on the design and stiffness requirements of the structure. In other words the design of the structure and the design of the control system are not independent problems.

D.3 Control Requirements

We must satisfy two goals: i) spin the habitat to achieve 1g centrifugal force, ii) spin the habitat about another axis so that the habitat is always pointing toward the sun (that is, the axis perpendicular to the plane of the torus is always pointing toward the sun).

One may ask whether these goals can be met without the use of any control forces. To meet the 1-g goal, a steady state stable spin about a specific fixed vector in space can be maintained as a stable equilibrium if the spin axis corresponds to the body axis with the largest inertia (this corresponds to an axis perpendicular to the plane of the torus).

But control forces are generally required if one seeks to maintain this spin condition in the presence of energy dissipation within the habitat, and/or if one adds the requirement for the spin axis to also follow the sun. The spin about the solar-pointing axis gives the 1-g and the movement around the sun requires the 360 degrees/year precession.

Let's imagine three coordinate systems. The coordinate frame $\underline{\boldsymbol{B}}$ represents the frame fixed in the spinning torus (called the Body Frame). The frame $\underline{\boldsymbol{X}}$ represents a frame whose axis $\underline{\boldsymbol{x}}_3$, aligns with the inertial axis $\underline{\boldsymbol{e}}_3$, but the $\underline{\boldsymbol{X}}$ rotates about its $\underline{\boldsymbol{x}}_3$ with the fixed rate $\Omega_3 = 360$ degrees/year. The frame $\underline{\boldsymbol{E}}$ represents an inertially-fixed frame. The control objective is to cause the body axis $\underline{\boldsymbol{b}}_2$ to align with $\underline{\boldsymbol{x}}_2$, and rotate the body about the axis $\underline{\boldsymbol{x}}_2$ with rate Ω_2 to cause the 1-g accelerations in the habitat.

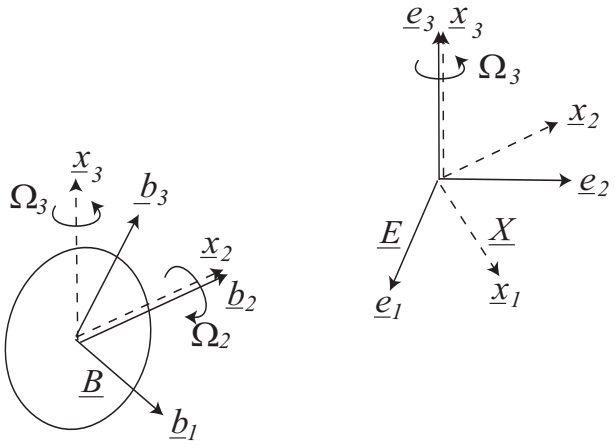

Figure D.1: Rigid body motion and coordinate Frames

Notation

$\underline{\boldsymbol{E}} = [\underline{\boldsymbol{e}}_1, \underline{\boldsymbol{e}}_2, \underline{\boldsymbol{e}}_3]$	=	Inertial Frame
$\underline{\boldsymbol{B}} = [\underline{\boldsymbol{b}}_1, \underline{\boldsymbol{b}}_2, \underline{\boldsymbol{b}}_3]$	=	Body Frame
$\underline{\boldsymbol{X}} = [\underline{\boldsymbol{x}}_1, \underline{\boldsymbol{x}}_2, \underline{\boldsymbol{x}}_3]$	=	Spinning Reference Frame
$\boldsymbol{\Theta}^B$	=	Rotation Matrix from $\underline{\boldsymbol{E}}$ to $\underline{\boldsymbol{B}}$
$\boldsymbol{\Theta}^X$	=	Rotation Matrix from $\underline{\boldsymbol{E}}$ to $\underline{\boldsymbol{X}}$
$\underline{\boldsymbol{\omega}}$	=	Angular Velocity of Rigid Body
$\underline{\bar{\boldsymbol{\omega}}}$	=	Target Value for $\underline{\boldsymbol{\omega}}$
$\underline{\boldsymbol{T}}$	=	Applied Torque to Rigid Body

For a vector $\underline{\boldsymbol{v}}$, we describe coordinates in a frame $\underline{\boldsymbol{A}}$ as $\boldsymbol{v}^A$, i.e., $\underline{\boldsymbol{v}} = \underline{\boldsymbol{A}}\boldsymbol{v}^A$, where $\underline{\boldsymbol{A}}$ is a matrix whose columns are composed of the coordinates of the base vectors. The body frame $\underline{\boldsymbol{B}}$ and the spinning frame $\underline{\boldsymbol{X}}$ are related to the inertial frame $\underline{\boldsymbol{E}}$ by

$$\underline{\boldsymbol{X}} = \underline{\boldsymbol{E}}\boldsymbol{\Theta}^X, \ \underline{\boldsymbol{B}} = \underline{\boldsymbol{E}}\boldsymbol{\Theta}^B. \tag{D.1}$$

Let the vectors $\boldsymbol{\omega}^X, \boldsymbol{\omega}^B$ denote the angular velocity vectors of these frames, expressed in frame coordinates $\underline{\boldsymbol{X}}$ and $\underline{\boldsymbol{B}}$, respectively. Then the relationship between the direction cosine matrices and the angular velocity vectors is given by,

$$\dot{\boldsymbol{\Theta}}^B = \boldsymbol{\Theta}^B \widetilde{\boldsymbol{\omega}}^B, \quad \dot{\boldsymbol{\Theta}}^X = \boldsymbol{\Theta}^X \widetilde{\boldsymbol{\omega}}^X, \tag{D.2}$$

where $\widetilde{\boldsymbol{\omega}}^B$ and $\widetilde{\boldsymbol{\omega}}^X$ represent skew-symmetric matrices.

D.4 Control of Rigid Body Rotation

D.4.1 Target Value

Suppose the target value of angular velocity of the rigid body $\underline{\boldsymbol{\omega}}$ is given in $\underline{\boldsymbol{X}}$ as

$$\begin{aligned}\underline{\overline{\boldsymbol{\omega}}} &= \Omega_2 \underline{\boldsymbol{x}}_2 + \Omega_3 \underline{\boldsymbol{e}}_3 && \text{(D.3)}\\ &= \Omega_2 \underline{\boldsymbol{x}}_2 + \Omega_3 \underline{\boldsymbol{x}}_3 && \text{(D.4)}\\ &= \underline{\boldsymbol{X}} \boldsymbol{\Omega}^X && \text{(D.5)}\\ &= \underline{\boldsymbol{E}} \boldsymbol{\Theta}^X \boldsymbol{\Omega}^X && \text{(D.6)}\\ &= \underline{\boldsymbol{B}} (\boldsymbol{\Theta}^B)^T \boldsymbol{\Theta}^X \boldsymbol{\Omega}^X, && \text{(D.7)}\end{aligned}$$

where $\boldsymbol{\Omega}^X$ is a pre-specified constant vector (target value described in $\underline{\boldsymbol{X}}$). In our case we have chosen $(\boldsymbol{\Omega}^X)^T = [0, \Omega_2, \Omega_3]$.

Define the error vector

$$\underline{\boldsymbol{\omega}}_e = \underline{\boldsymbol{\omega}} - \underline{\overline{\boldsymbol{\omega}}}, \tag{D.8}$$

which is the difference between the actual instantaneous value of the body angular velocity and the desired value. From (D.1) and (D.7), we have

$$\underline{\boldsymbol{\omega}}_e = \underline{\boldsymbol{B}} \boldsymbol{\omega}^B - \underline{\boldsymbol{B}} (\boldsymbol{\Theta}^{\boldsymbol{B}})^T \boldsymbol{\Theta}^X \boldsymbol{\Omega}^X = \underline{\boldsymbol{B}} \underbrace{\left(\boldsymbol{\omega}^B - (\boldsymbol{\Theta}^B)^T \boldsymbol{\Theta}^X \boldsymbol{\Omega}^X \right)}_{\boldsymbol{\omega}_e^B}. \tag{D.9}$$

Our goal now is to find a control torque vector $\underline{\boldsymbol{T}}$ that can be applied to the rigid body habitat to cause the error $\underline{\boldsymbol{\omega}}_e$ to go to zero, regardless of the initial error. First we must write the dynamic equations of motion of the rigid spinning habitat.

D.4.2 Rigid Body Motion

Rotational motion of a rigid body represented in the body frame $\underline{\boldsymbol{B}}$ is given by

$$\boldsymbol{J}^B \dot{\boldsymbol{\omega}}^B + \widetilde{\boldsymbol{\omega}}^B \boldsymbol{J}^B \boldsymbol{\omega}^B = \boldsymbol{T}^B, \tag{D.10}$$

where $\boldsymbol{J}^B$ is the inertia matrix about the body axes $\underline{\boldsymbol{b}}_1, \underline{\boldsymbol{b}}_2, \underline{\boldsymbol{b}}_3$, and $\boldsymbol{T}^B$ is the control torque vector expressed in $\underline{\boldsymbol{B}}$.

Note from (D.9) that $\boldsymbol{\omega}_e^B$ is given by

$$\boldsymbol{\omega}_e^B = \boldsymbol{\omega}^B - (\boldsymbol{\Theta}^B)^T \boldsymbol{\Theta}^X \boldsymbol{\Omega}^X, \tag{D.11}$$

and its derivative is

$$\begin{aligned}\dot{\boldsymbol{\omega}}_e^B &= \dot{\boldsymbol{\omega}}^B - (\dot{\boldsymbol{\Theta}}^B)^T \boldsymbol{\Theta}^X \boldsymbol{\Omega}^X - (\boldsymbol{\Theta}^B)^T \dot{\boldsymbol{\Theta}}^X \boldsymbol{\Omega}^X && \text{(D.12)}\\ &= \dot{\boldsymbol{\omega}}^B - \widetilde{\boldsymbol{\mu}} \boldsymbol{\omega}^B - (\boldsymbol{\Theta}^B)^T \boldsymbol{\Theta}^X \widetilde{\boldsymbol{\omega}}^X \boldsymbol{\Omega}^X, && \text{(D.13)}\end{aligned}$$

where $\boldsymbol{\mu} = (\boldsymbol{\Theta}^B)^T \boldsymbol{\Theta}^X \Omega^X$ ($\widetilde{\boldsymbol{\mu}}$ is a skew symmetric matrix), and where the second expression follows from the use of (D.2). Equations (D.10) and (D.2) form a set of differential equations to give

the exact motion of the rigid body, producing both $\boldsymbol{\omega}^B(t)$ and $\boldsymbol{\Theta}^B(t)$, starting from any initials conditions $\boldsymbol{\omega}(0)$, $\boldsymbol{\Theta}^B(0)$. In our case $(\boldsymbol{\omega}^X)^T = [0, 0, \Omega_3]$ is constant, and $\boldsymbol{\Theta}^X(t)$ is a known matrix given by

$$\boldsymbol{\Theta}^X(t) = \begin{bmatrix} \cos\Omega_3 t & -\sin\Omega_3 t & 0 \\ \sin\Omega_3 t & \cos\Omega_3 t & 0 \\ 0 & 0 & 1 \end{bmatrix}. \tag{D.14}$$

D.4.3 Control

We must cause the error $\boldsymbol{\omega}_e^B$ to go to zero, by proper choice of the control torque $\boldsymbol{T}^B$. Our approach is to find the control that will cause the error to be a stable solution to a linear system of equations. We choose to make $\boldsymbol{\omega}_e^B$ follow the dynamics given by

$$\dot{\boldsymbol{\omega}}_e^B = \boldsymbol{A}\boldsymbol{\omega}_e^B, \tag{D.15}$$

where $\boldsymbol{A}$ is a chosen constant matrix whose eigenvalues are all in the left-hand plane. Substitution of (D.11) and (D.13) into (D.15) gives

$$\dot{\boldsymbol{\omega}}^B - \widetilde{\boldsymbol{\mu}}\boldsymbol{\omega}^B - (\boldsymbol{\Theta}^B)^T\boldsymbol{\Theta}^X\widetilde{\boldsymbol{\omega}}^X\boldsymbol{\Omega}^X = \boldsymbol{A}\Big(\boldsymbol{\omega}^B - (\boldsymbol{\Theta}^B)^T\boldsymbol{\Theta}^X\boldsymbol{\Omega}^X\Big). \tag{D.16}$$

Multiplying $\boldsymbol{J}^B$ from the left, and using (D.10), we have the required control torque,

$$\boldsymbol{T}^B = \Big(\widetilde{\boldsymbol{\omega}}^B\boldsymbol{J}^B + \boldsymbol{J}^B\boldsymbol{A} + \boldsymbol{J}^B\widetilde{\boldsymbol{\mu}}\Big)\boldsymbol{\omega}^B + \boldsymbol{J}^B\Big((\boldsymbol{\Theta}^B)^T\boldsymbol{\Theta}^X\widetilde{\boldsymbol{\omega}}^X - \boldsymbol{A}(\boldsymbol{\Theta}^B)^T\boldsymbol{\Theta}^X\Big)\boldsymbol{\Omega}^X \tag{D.17}$$

From (D.10) and (D.17), the closed loop system is given by

$$\dot{\boldsymbol{\omega}}^B = (\boldsymbol{A} + \widetilde{\boldsymbol{\mu}})\boldsymbol{\omega}^B + \Big((\boldsymbol{\Theta}^B)^T\boldsymbol{\Theta}^X\widetilde{\boldsymbol{\omega}}^X - \boldsymbol{A}(\boldsymbol{\Theta}^B)^T\boldsymbol{\Theta}^X\Big)\boldsymbol{\Omega}^X. \tag{D.18}$$

D.5 Simulation

D.5.1 Simulation settings

For a rigid body, we consider a thin disk shown in Fig. D.2. The outer and inner radii of the disk are r_1 and r_2 respectively, and the mass is M. We choose $\underline{\boldsymbol{b}}_2$ axis of the body frame to align with the center axis of the disk. At the initial state, the spinning frame $\underline{\boldsymbol{X}}$ and the body frame $\underline{\boldsymbol{B}}$ coincide with the inertial frame $\underline{\boldsymbol{E}}$. The frame $\underline{\boldsymbol{X}}$ spins about $\underline{\boldsymbol{x}}_3$ axis with the angular velocity ω_3^X (360 deg per year). The disk is controlled to follow $\underline{\boldsymbol{X}}$ while spinning about $\underline{\boldsymbol{x}}_2$ axis with the angular velocity ω_2^X (1 G at the middle of the disk radius). Parameters are given as follows.

Physical Parameter:
r_1 = 1500 [m]
r_2 = 500 [m]
M = 10^8 [Kg]
J_2^B = $M/2(r_2^2 + r_1^2)$ [Kgm^2]
$J_{1,3}^B$ = $J_2^B/2$ [Kgm^2]

Initial Condition:
$\boldsymbol{\omega}_X$ = $[0\ 0\ \omega_3^X]^T$
$\boldsymbol{\omega}_B(0)$ = $[0\ \omega_2^X\ \omega_3^X]^T$

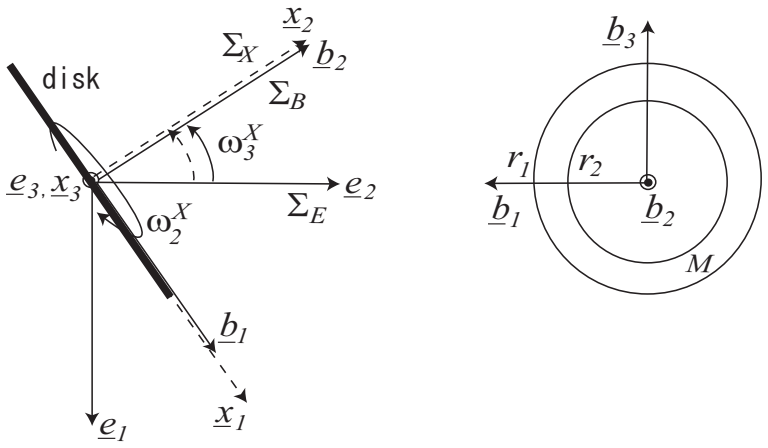

Figure D.2: Spinning disk and coordinates

$\boldsymbol{\Theta}^B(0) = \boldsymbol{I}_3$
where
$\omega_3^X = (360/365)(\pi/180)/(24 \cdot 3600) = 1.99 \times 10^{-7}$ [rad/sec]
$\omega_2^X = \sqrt{g/\{(r_1 + r_2)/2\}} = 9.90 \times 10^{-2}$ [rad/sec]

Control:
$\boldsymbol{A} = -\varepsilon \boldsymbol{I}_3 \quad (\varepsilon = 1 \times 10^{-3})$
$\boldsymbol{\Omega}^X = [0\ \omega_2^X\ \omega_3^X]^T$

D.5.2 Simulation results

Figure D.3 shows time histories of the rigid body angular velocity $\boldsymbol{\omega}^B$, the control error $\boldsymbol{\omega}_e^B$, and the control torque $\boldsymbol{T}^B$. The magnitude of the control torque (bottom) is about 2×10^6 [Nm]. Because the error $\boldsymbol{\omega}_e^B$ is zero in this case from the initial condition, this torque corresponds to the torque used for the disk to follow the spinning frame $\underline{\boldsymbol{X}}$ in steady state.

Next we examine the control torque to attenuate the error $\boldsymbol{\omega}_e^B$. Figure D.4 (a) shows the response with an initial error $\omega_2^B(0) = 0.99\,\omega_2^X$. To attenuate ω_2^B, we need 10^8 [Nm] at maximum. To see the effect of the control gain ε, Fig. D.4 (b) shows the response with a gain $\varepsilon = 10^{-2}$ (10 times bigger). As expected, we see rapid convergence in the control error (middle) by using larger control torque (bottom).

D.6 Conclusions

This report determines what control forces are necessary to cause the habitat to rotate to follow the sun and give 1g centrifugal force the habitat. This conclusion is that the required control torques are approximately 2 million Newtons sinusoidally cycling at the frequency of the spin rotation 75 seconds per rotation. Later work will compute the torque necessary to control the flexible structure.

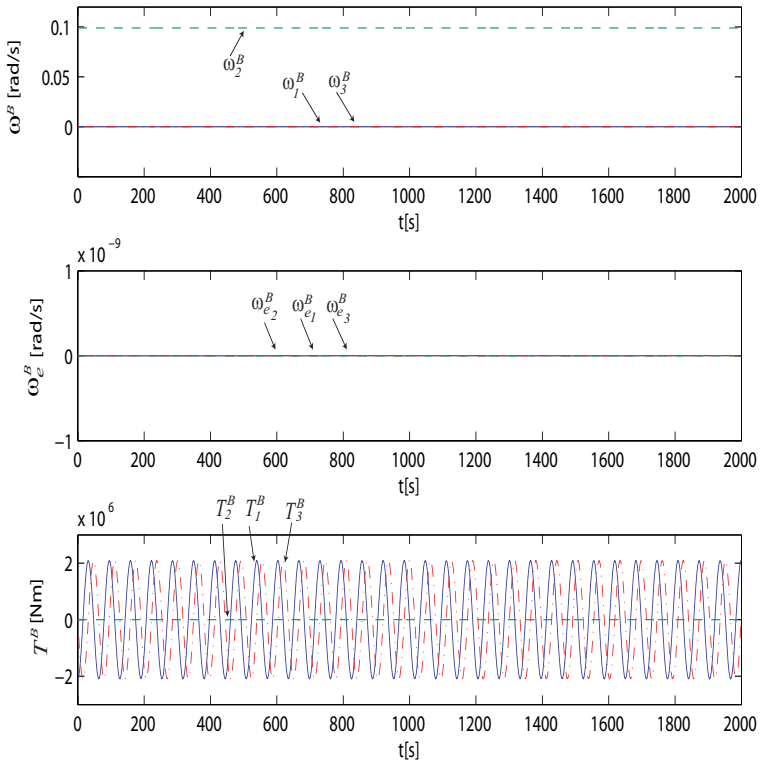

Figure D.3: Time history (no initial error)

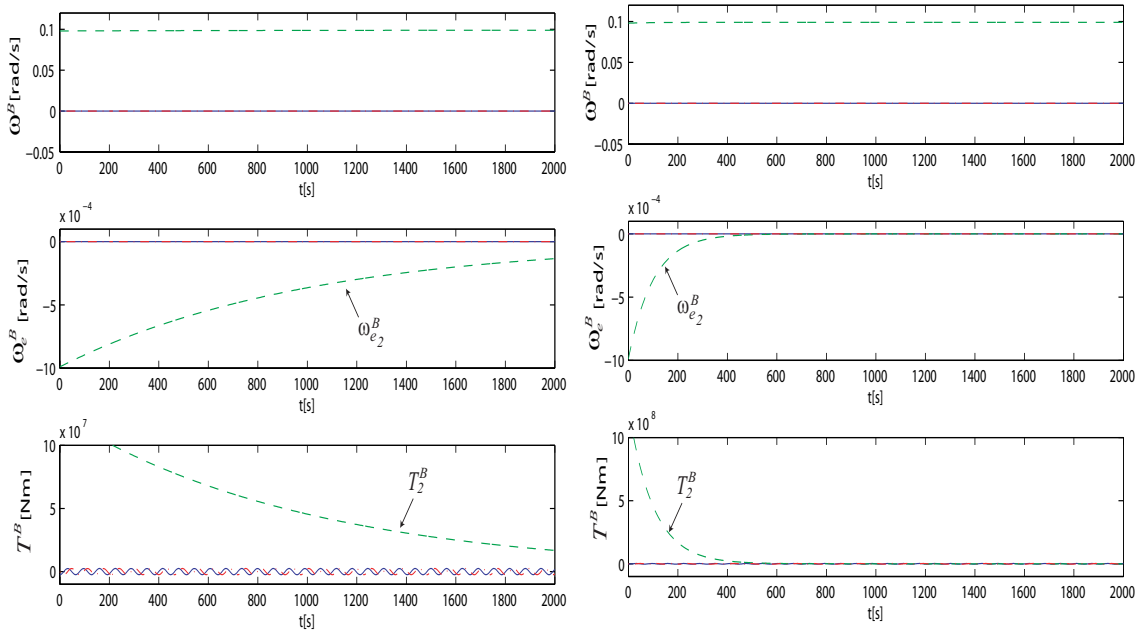

Figure D.4: Time history with initial error ($\omega_2^B(0) = 0.99\omega_2^X$)

Appendix E

Double Helix Tensegrity Structures

E.1 Abstract

This paper describes a class of tensegrity systems that are formed from a common type of connectivity, having a double helix configuration. We will call structures made from such internal patterns a *Double Helix Tensegrity* (DHT). This paper derives the connectivity matrix for the DHT class of structures. This generalized common mathematical formulation will allow efficient computations for a large class of tensegrity systems which can have many different configurations, albeit employing the same rules for connecting components. Special cases of these configurations include torus, cylinders, paraboloids, spheres, ellipsoids, and other configurations.

Nomenclature

$\boldsymbol{B}$ = bar matrix
$\boldsymbol{B}_i$ = bar matrix of the i^{th} row units
$\boldsymbol{B}(i,k)$ = bar matrix of the unit (i,k)
$\boldsymbol{b}_\ell(i,k)$ = bar vector of the unit (i,k)
$\boldsymbol{C}_B$ = bar connectivity matrix
$\boldsymbol{C}_S$ = string connectivity matrix
$\boldsymbol{I}_n$ = $n \times n$ unit matrix
i = row index of a unit
k = column index of a unit
$\boldsymbol{N}$ = node matrix
$\boldsymbol{N}_i$ = node matrix of the i^{th} row units
$\boldsymbol{N}(i,k)$ = node matrix of the unit (i,k)
$\boldsymbol{n}_\ell(i,k)$ = node vector of the unit (i,k)
p = number of units in row
q = number of units in column
$\mathbb{R}^{m\times n}$ = $m \times n$ real matrix
$\boldsymbol{S}$ = string matrix
$\boldsymbol{S}_i$ = string matrix of the i^{th} row units
$\boldsymbol{S}(i,k)$ = string matrix of the unit (i,k)
$\boldsymbol{s}_\ell(i,k)$ = string vector of the unit (i,k)
$\boldsymbol{W}$ = external force matrix
γ_i = force density of the string $\boldsymbol{s}_i$

λ_i = force density of the bar $\boldsymbol{b}_i$

E.2 Background

Tensegrity systems employ axially-loaded compressive and tensile elements to form stiff or deployable structures. One may select a special repetitive pattern of the element connections that form a tensegrity structure (in the same way one might choose a particular type of element in the Finite Element Method for analysis of structures). In this paper, we consider a fabrication *material* that is composed of one dimensional objects (bars and strings, sticks and cables, etc.), and we shall make final three-dimensional structures by *cutting out* the material, *sewing up* the material.

One may see similarity between this approach and the oldest forms of material design. The oldest forms of material design chose: i) one-dimensional objects (e.g. sticks, reeds, hair, plant fibers), ii) connections of the one-dimensional objects to form a two-dimensional object (e.g. weaving pattern as in a blanket or basket), and iii) rules of closure of the two-dimensional object to form a three-dimensional object (e.g. clothing, baskets). This was distinct from other methods of using continua (e.g. clay) to form three-dimensional objects.

As a first step of this design approach for tensegrity structures, we start with a particular choice of material topology inspired by the ancient artform of origami, which we will call DHT (Double Helix Tensegrity) topology. A variety of enclosure rules for the DHT material sheet will form a large variety of three-dimensional structures useful for many engineering purposes.

E.3 Introduction

The acronym *tensegrity* is a word coined by Buckminster Fuller [8, 9] to describe an artform created by Kenneth Snelson. Tensegrity structures are made up from axially-loaded members (bars and strings) by using frictionless ball joints or other mechanical choices. They can have very high stiffness/weight ratio, and can be easily deformable by stretching/shortening some of the members by pulleys or other kind of actuators. In addition, avoiding material bending will allow us to establish simple and accurate mathematical models for static and dynamic analysis.

Tensegrity structures have been widely studied from different viewpoints. Applications of tensegrity structures are found in deployable structures [10, 11, 12, 13, 14, 15], robots [16, 17, 18], acoustic devices [19], as well as biological modeling of cell cytoskeletons and red blood cells [20, 21]. Static analysis of tensegrity includes prestressed structures analysis [22, 23, 24], stability or stiffness analysis [25, 26, 27], and form-finding methods [28, 29, 30, 31, 32]. Dynamics of tensegrity were first studied by [33] and were developed by many researchers including [34, 35, 36, 37]. Deeper historical background on tensegrity structures are found in [38, 1]. Reviews of static and dynamic analysis are found in [39, 40] and [41] respectively.

Few of the myriad of tensegrity topologies studied in the literatures have common connectivity rule, and engineers will be required to start from choice of members (bars, strings) and their connections to build a tensegrity. Yet there will exist subsets of tensegrity structures that have a common connectivity rule. The purpose of this paper is to investigate a class of tensegrities produced from a choice of the same material topology, which we will call DHT (Double Helix Tensegrity) topology. A variety of enclosure rules will form a large variety of three-dimensional structures. Mathematically, connections of the members are described by a matrix called the connectivity matrix. We will derive the connectivity matrix for two typical enclosure rules to form torus and cylindrical types of structures. There are an infinite number of shapes generated

from the same connectivity matrix by choosing different node locations. We will also provide the node locations to form some typical shapes including circular torus, elliptic torus, cylinders, paraboloids, and spheres. Although we specifically consider the material topology described by the DHT topology, one can easily add, delete, or exchange the members by modifying the connectivity matrix. Once we have the connectivity matrix in hand, we can analyze both the statics and dynamics in a systematic way. As an application of the derived connectivity matrix, a minimal mass design of a DHT cylinder subject to the equilibrium and yield stress constraints is shown in the numerical example.

This paper is organized as follows. Section E.4 describes a motivation and precise description of the DHT topology. Section E.5 presents the connectivity matrix of the internal units of the DHT. As a typical enclosure rule for the DHT sheet, Section E.6 shows an enclosure rule and its connectivity matrix for torus-type structures. Node locations to produce some typical shapes including circular torus, elliptic torus, are also presented. Section E.7 discusses an enclosure rule and its connectivity matrix for cylindrical-type structures. Node location for cylinders, paraboloids, and spheres are also presented. A numerical example of a minimal mass design of a DHT cylinder is described in Sec. E.8. Section E.9 concludes the paper.

E.4 Double Helix Tensegrity Topology

E.4.1 Motivation

Our material topology is inspired by the ancient artform of origami, called the Yoshimura pattern. The Yoshimura pattern was originally investigated to analyze the mechanics of the buckling of circular cylindrical shells under axial compression [42, 43, 44]. Later it was adopted to deployable structures [45]. Figure E.1 (a) shows a model of the Yoshimura-pattern cylinder. The surface of the cylinder is composed of rhombuses folded along the diagonal line. The structure can be folded along this folding line if we cut off the side of the cylinder. To prevent this motion, we use spirals of bars to stretch out the nodes of the rhombuses, as shown in Fig E.1 (b). The bars in the figure are connected by ball joints, and they support an elastic stretchable membrane at the joints. In Fig. E.1 (a), these bars are located to stretch out the nodes of adjacent rhombuses as shown in the dotted lines (red). These bars make double helical chains inside the cylinder. The elastic membrane carries tension, and it can be replaced by strings connecting the nodes. Hence we place strings on the edges and add one diagonal (bridging) string, as shown in the solid lines (blue) in Fig E.1 (a). This process leads to a material topology which we call the DHT topology shown in Figs. E.2 and E.3, described in detail in the next section.

A variety of enclosure rules for the DHT sheet will form a large variety of three-dimensional structures as described in the following sections. In addition, although we specifically consider this type of the topology, we can easily add, delete, or exchange the members by modifying the connectivity matrix which we will derive. If we want to retrieve the original Yoshimura pattern, for example, we just delete the columns of the connectivity matrix corresponding to the bars and the added bridging strings. If we want to make a cylinder with bars located on the edges of the Yoshimura pattern, we replace the connectivity matrix for strings with that for bars.

E.4.2 DHT unit

The topology of the DHT (Double Helix Tensegrity) unit is defined and shown in Fig. E.2. Vectors $\boldsymbol{n}_1(i,k),\ \boldsymbol{n}_2(i,k) \in \mathbb{R}^3$ represent the position of the nodes in the unit (i,k), $(i = 0, \cdots, q-1,\ k = 0, \cdots, p-1)$, where q and p respectively are the number of units in the vertical and horizontal

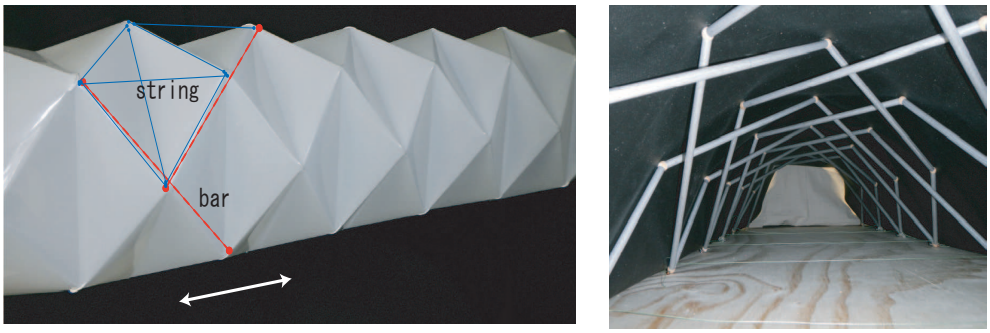

(a) Yoshimura-pattern cylinder (b) Double helix frame

Figure E.1: A cylinder made from Yoshimura pattern

direction. The unit (i, k) has 2 bars represented by directed vectors $\boldsymbol{b}_1(i, k)$, $\boldsymbol{b}_2(i, k) \in \mathbb{R}^3$, shown as the curved lines in Fig. E.2 (the real bars are straight however), and 8 strings represented by directed vectors $\boldsymbol{s}_1(i, k), \cdots, \boldsymbol{s}_8(i, k) \in \mathbb{R}^3$. Figure E.3 illustrates the complete set of pq units for $(p, q) = (4, 4)$, where the nodes are located on a cylindrical surface. Inside the area of the dashed lines, there are p units around the circumference and q units along the vertical direction. The nodes $\boldsymbol{n}_1(i, k)$ and $\boldsymbol{n}_2(i, k)$ are indicated by marks ○ and □ respectively. The bars and strings are represented by thick (blue) and thin (red) lines. Elements of the typical (i, k) unit are indicated by dotted lines. The boundary elements of the pq units will be handled by the boundary condition (enclosure rule).

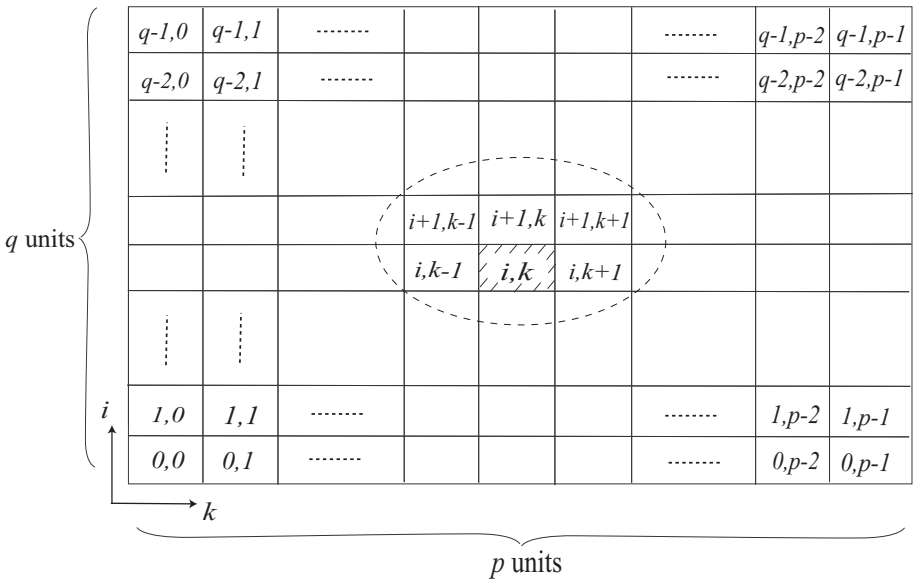

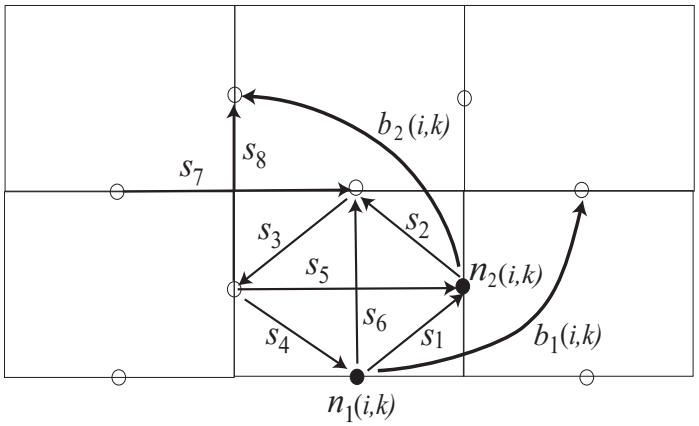

$$N(i,k)=[\,n_1(i,k)\;\; n_2(i,k)\,]$$

Figure E.2: The Double Helix Tensegrity (DHT) unit

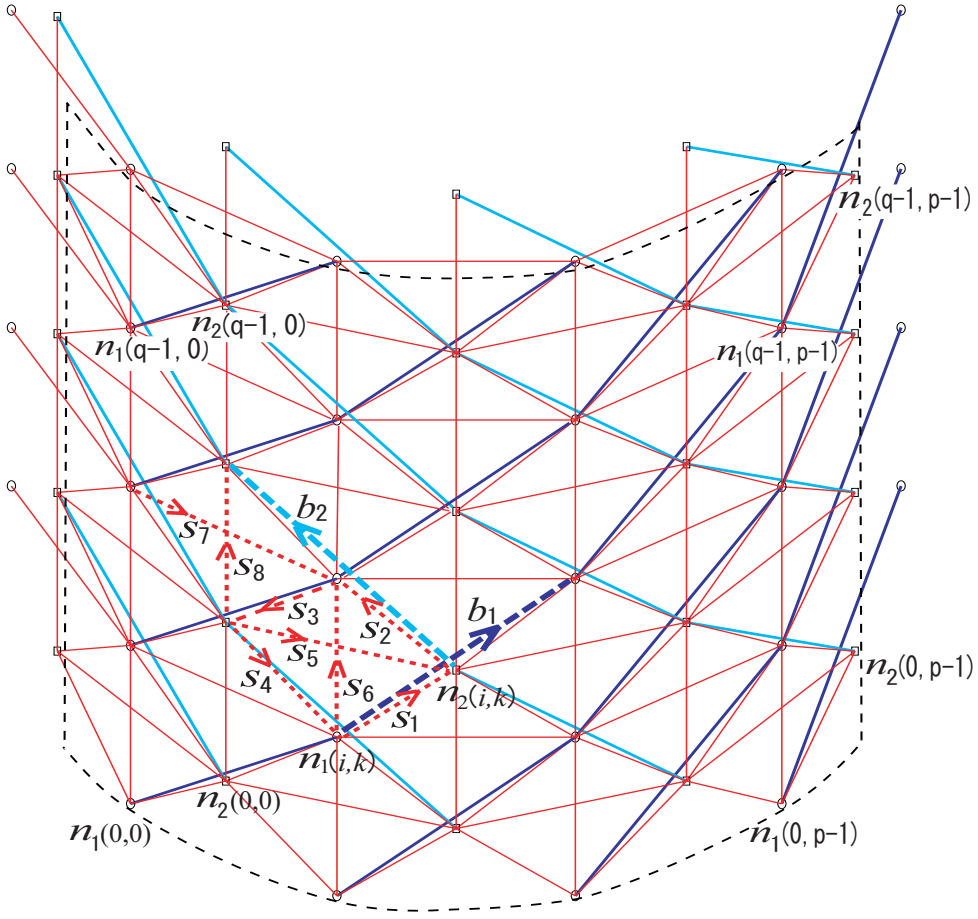

Figure E.3: Complete set of DHT units ($p = 4$, $q = 4$)

E.4.3 Connectivity matrix

Define a matrix $\boldsymbol{N}$ whose i^{th} column is the three-dimensional vector $\boldsymbol{n}_i \in \mathbb{R}^3$ locating the i^{th} node of the network ($\boldsymbol{N} = [\cdots, \boldsymbol{n}_i, \cdots]$). Define matrices $\boldsymbol{B}$ ($\boldsymbol{S}$) respectively such that the i^{th} columns are the three-dimensional vectors $\boldsymbol{b}_i$ ($\boldsymbol{s}_i$) $\in \mathbb{R}^3$ that lie along the i^{th} bar (i^{th} string) within the network ($\boldsymbol{B} = [\cdots, \boldsymbol{b}_i, \cdots]$, $\boldsymbol{S} = [\cdots, \boldsymbol{s}_i, \cdots]$). Define the (i, j) element of a matrix $\boldsymbol{C}_B$ to be:

$$[\boldsymbol{C}_B]_{ij} = \begin{cases} -1, & \text{if } \boldsymbol{b}_i \text{ is directed away from the node } \boldsymbol{n}_j \\ 1, & \text{if } \boldsymbol{b}_i \text{ is directed toward } \boldsymbol{n}_j \\ 0, & \text{if } \boldsymbol{b}_i \text{ does not touch } \boldsymbol{n}_j. \end{cases} \tag{E.1}$$

Matrix $\boldsymbol{C}_S$ is constructed the same way. The bar and string matrices $\boldsymbol{B}$ and $\boldsymbol{S}$ are related to the node matrix $\boldsymbol{N}$ by these *connectivity matrices* $\boldsymbol{C}_B$, $\boldsymbol{C}_S$ as

$$\boldsymbol{B} = \boldsymbol{N}\boldsymbol{C}_B^T, \quad \boldsymbol{S} = \boldsymbol{N}\boldsymbol{C}_S^T. \tag{E.2}$$

Note that each column of $\boldsymbol{C}_B^T$ and $\boldsymbol{C}_S^T$ defines a bar and a string respectively. We can easily add, delete, or exchange the members by adding, deleting, or exchanging the columns of the connectivity matrix. Note that the connectivity matrix is nothing to do with the member location, which is specified by $\boldsymbol{N}$.

We can utilize the connectivity matrix for a variety of analysis and design problems. It has been shown, for example, that all equilibria of tensegrity systems under an external load $\boldsymbol{W}$ (i^{th} column of $\boldsymbol{W}$ represents the external force acting on the i^{th} node) satisfy, [24], Chapter 2 of [1],

$$\boldsymbol{N}\boldsymbol{K} = \boldsymbol{W}, \ \boldsymbol{K} = \boldsymbol{C}_S^T \widehat{\boldsymbol{\gamma}} \boldsymbol{C}_S - \boldsymbol{C}_B^T \widehat{\boldsymbol{\lambda}} \boldsymbol{C}_B, \tag{E.3}$$

where $\widehat{\boldsymbol{\gamma}}$ ($\widehat{\boldsymbol{\lambda}}$) are diagonal matrices, where $[\widehat{\boldsymbol{\gamma}}]_{ii} = \gamma_i$ is the force density [46] (member force divided by length) in the string $\boldsymbol{s}_i$, and $[\widehat{\boldsymbol{\lambda}}]_{ii} = \lambda_i$ is the force density in the bar $\boldsymbol{b}_i$. Signs of the force densities λ_i (γ_i) are selected to be positive when they are compressed (stretched), respectively. We can use the connectivity matrix for a variety of analysis and design problems including form-finding [31, 32], stiffness or stability analysis, [27], chapter 2 of [1], optimal structure design [47], and dynamic analysis, [37], chapter 5 of [1].

To handle the DHT units in order, we shall consider the blocks by ordered rows, starting at the bottom. For this purpose, define the matrices whose columns are composed of the elements of the (i, k) unit as

$$\boldsymbol{N}(i,k) = \begin{bmatrix} \boldsymbol{n}_1(i,k) & \boldsymbol{n}_2(i,k) \end{bmatrix} \in \mathbb{R}^{3\times 2} \tag{E.4}$$

$$\boldsymbol{B}(i,k) = \begin{bmatrix} \boldsymbol{b}_1(i,k) & \boldsymbol{b}_2(i,k) \end{bmatrix} \in \mathbb{R}^{3\times 2} \tag{E.5}$$

$$\boldsymbol{S}(i,k) = \begin{bmatrix} \boldsymbol{s}_1(i,k) & \cdots & \boldsymbol{s}_8(i,k) \end{bmatrix} \in \mathbb{R}^{3\times 8}. \tag{E.6}$$

Collecting these matrices in a row from the left ($\boldsymbol{N}_i = [\boldsymbol{N}(i,0), \cdots, \boldsymbol{N}(i,p-1)]$), and stacking them from the bottom, we have

$$\begin{aligned} \boldsymbol{N} &= \begin{bmatrix} \boldsymbol{N}_0 & \boldsymbol{N}_1 & \cdots\cdots & \boldsymbol{N}_{q-1} \end{bmatrix} \\ &= \begin{bmatrix} \boldsymbol{N}(0,0) \cdots \boldsymbol{N}(0,p-1) \,|\, \cdots\cdots \,|\, \boldsymbol{N}(q-1,0) \cdots \boldsymbol{N}(q-1,p-1) \end{bmatrix} \end{aligned} \tag{E.7}$$

$$\begin{aligned} \boldsymbol{B} &= \begin{bmatrix} \boldsymbol{B}_0 & \boldsymbol{B}_1 & \cdots\cdots & \boldsymbol{B}_{q-1} \end{bmatrix} \\ &= \begin{bmatrix} \boldsymbol{B}(0,0) \cdots \boldsymbol{B}(0,p-1) \,|\, \cdots\cdots \,|\, \boldsymbol{B}(q-1,0) \cdots \boldsymbol{B}(q-1,p-1) \end{bmatrix} \end{aligned} \tag{E.8}$$

$$\begin{aligned} \boldsymbol{S} &= \begin{bmatrix} \boldsymbol{S}_0 & \boldsymbol{S}_1 & \cdots\cdots & \boldsymbol{S}_{q-1} \end{bmatrix} \\ &= \begin{bmatrix} \boldsymbol{S}(0,0) \cdots \boldsymbol{S}(0,p-1) \,|\, \cdots\cdots \,|\, \boldsymbol{S}(q-1,0) \cdots \boldsymbol{S}(q-1,p-1) \end{bmatrix}. \end{aligned} \tag{E.9}$$

In the next section, we will derive the connectivity matrix of the internal units of the DHT topology.

E.5 Connectivity Matrix for Internal Units

From the topology given in Fig. E.2, we can determine the relationship between $\boldsymbol{N}(i,k)$ and $\boldsymbol{B}(i,k)$, $\boldsymbol{S}(i,k)$ for the internal units.

The bars $\boldsymbol{b}_1(i,k)$ and $\boldsymbol{b}_2(i,k)$ in the unit (i,k) are connected to two other units $\boldsymbol{N}(i+1,k-1)$ and $\boldsymbol{N}(i+1,k+1)$. Hence for some connectivity matrices $\boldsymbol{C}^T_{B_{ik}}(\alpha,\beta) \in \mathbb{R}^{2\times 2}$,

$$\begin{aligned}\boldsymbol{B}(i,k) =& \boldsymbol{N}(i,k)\boldsymbol{C}^T_{B_{ik}}(i,k) + \boldsymbol{N}(i+k,k-1)\boldsymbol{C}^T_{B_{ik}}(i+1,k-1)\\ &+ \boldsymbol{N}(i+1,k+1)\boldsymbol{C}^T_{B_{ik}}(i+1,k+1),\end{aligned}$$

where

$$\boldsymbol{C}^T_{B_{ik}}(i,k) = -\boldsymbol{I}_2$$

$$\boldsymbol{C}^T_{B_{ik}}(i+1,k-1) = \begin{bmatrix}\boldsymbol{0} & \boldsymbol{e}_2\end{bmatrix} = \boldsymbol{E}_2 \in \mathbb{R}^{2\times 2}, \quad \boldsymbol{e}_2 = \begin{bmatrix}0\\1\end{bmatrix} \tag{E.10}$$

$$\boldsymbol{C}^T_{B_{ik}}(i+1,k+1) = \begin{bmatrix}\boldsymbol{e}_1 & \boldsymbol{0}\end{bmatrix} = \boldsymbol{E}_1 \in \mathbb{R}^{2\times 2}, \quad \boldsymbol{e}_1 = \begin{bmatrix}1\\0\end{bmatrix}. \tag{E.11}$$

So for the interior bars, $i = 1,\cdots,q-2$, $k = 1,\cdots,p-2$, we have

$$\boldsymbol{B}(i,k) = -\boldsymbol{N}(i,k) + \boldsymbol{N}(i+1,k-1)\boldsymbol{E}_2 + \boldsymbol{N}(i+1,k+1)\boldsymbol{E}_1. \tag{E.12}$$

Likewise for the interior strings and some connectivity matrices $\boldsymbol{C}^T_{S_{ik}}(\alpha,\beta) \in \mathbb{R}^{2\times 8}$,

$$\begin{aligned}\boldsymbol{S}(i,k) =& \boldsymbol{N}(i,k-1)\boldsymbol{C}^T_{S_{ik}}(i,k-1) + \boldsymbol{N}(i,k)\boldsymbol{C}^T_{S_{ik}}(i,k)\\ &+ \boldsymbol{N}(i+1,k-1)\boldsymbol{C}^T_{S_{ik}}(i+1,k-1) + \boldsymbol{N}(i+1,k)\boldsymbol{C}^T_{S_{ik}}(i+1,k),\end{aligned}$$

where

$$\boldsymbol{C}^T_{S_{ik}}(i,k-1) = \begin{bmatrix}\boldsymbol{0},\boldsymbol{0},\boldsymbol{e}_2,-\boldsymbol{e}_2,-\boldsymbol{e}_2,\boldsymbol{0},\boldsymbol{0},-\boldsymbol{e}_2\end{bmatrix} \equiv \boldsymbol{\Theta}_1 \in \mathbb{R}^{2\times 8} \tag{E.13}$$

$$\boldsymbol{C}^T_{S_{ik}}(i,k) = \begin{bmatrix}\boldsymbol{e}_2-\boldsymbol{e}_1,-\boldsymbol{e}_2,\boldsymbol{0},\boldsymbol{e}_1,\boldsymbol{e}_2,-\boldsymbol{e}_1,\boldsymbol{0},\boldsymbol{0}\end{bmatrix} \equiv \boldsymbol{\Theta}_2 \in \mathbb{R}^{2\times 8} \tag{E.14}$$

$$\boldsymbol{C}^T_{S_{ik}}(i+1,k-1) = \begin{bmatrix}\boldsymbol{0},\boldsymbol{0},\boldsymbol{0},\boldsymbol{0},\boldsymbol{0},\boldsymbol{0},-\boldsymbol{e}_1,\boldsymbol{e}_2\end{bmatrix} \equiv \boldsymbol{\Theta}_3 \in \mathbb{R}^{2\times 8} \tag{E.15}$$

$$\boldsymbol{C}^T_{S_{ik}}(i+1,k) = \begin{bmatrix}\boldsymbol{0},\boldsymbol{e}_1,-\boldsymbol{e}_1,\boldsymbol{0},\boldsymbol{0},\boldsymbol{e}_1,\boldsymbol{e}_1,\boldsymbol{0}\end{bmatrix} \equiv \boldsymbol{\Theta}_4 \in \mathbb{R}^{2\times 8}. \tag{E.16}$$

Hence for the interior strings, $i = 1,\cdots,q-2,\ k = 1,\cdots,p-2$, we have

$$\begin{aligned}\boldsymbol{S}(i,k) =& \boldsymbol{N}(i,k-1)\boldsymbol{\Theta}_1 + \boldsymbol{N}(i,k)\boldsymbol{\Theta}_2\\ &+ \boldsymbol{N}(i+1,k-1)\boldsymbol{\Theta}_3 + \boldsymbol{N}(i+1,k)\boldsymbol{\Theta}_4.\end{aligned} \tag{E.17}$$

Based on the above connectivity matrices, final three-dimensional structures are formed by specifying an enclosure rule (boundary condition) and a node location. Two typical enclosure rules are given in the following sections. Our first result will focus on torus-type structures.

E.6 Torus-type Structures

E.6.1 Torus Boundary Condition and Connectivity Matrix

By closing the DHT sheet about the vertical axis in Fig. E.2, the resulting 3-dimensional shape would be a cylinder. Connecting the top and the bottom of the cylinder together, the resulting structure forms a torus, as illustrated in Fig. E.4.

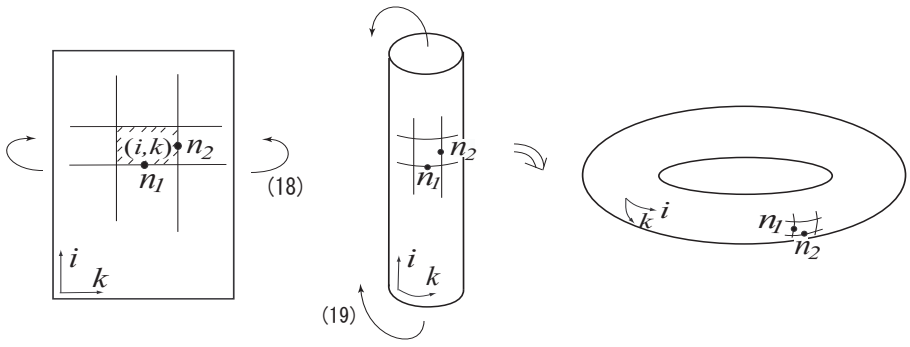

Figure E.4: Torus formed from the DHT sheet

The boundary condition to form a torus is represented by

$$\boldsymbol{N}(i,-1) = \boldsymbol{N}(i,p-1),\ \boldsymbol{N}(i,0) = \boldsymbol{N}(i,p) \tag{E.18}$$

$$\boldsymbol{N}(-1,k) = \boldsymbol{N}(q-1,k),\ \boldsymbol{N}(0,k) = \boldsymbol{N}(q,k). \tag{E.19}$$

By applying the above periodic conditions, the bar and string matrices can be written by (E.12) and (E.17), even for the boundaries $i = 0, q-1$ and $k = 0, p-1$, that is,

$$\boldsymbol{B}(i,k) = -\boldsymbol{N}(i,k) + \boldsymbol{N}(i+1,k-1)\boldsymbol{E}_2 + \boldsymbol{N}(i+1,k+1)\boldsymbol{E}_1 \tag{E.20}$$

$$\begin{aligned}\boldsymbol{S}(i,k) = {} & \boldsymbol{N}(i,k-1)\boldsymbol{\Theta}_1 + \boldsymbol{N}(i,k)\boldsymbol{\Theta}_2 \\ & + \boldsymbol{N}(i+1,k-1)\boldsymbol{\Theta}_3 + \boldsymbol{N}(i+1,k)\boldsymbol{\Theta}_4\end{aligned} \tag{E.21}$$

$(i = 0, \cdots, q-1;\ k = 0, \cdots, p-1).$

The connectivity matrices for the torus-type structures are given in the following theorems.

Theorem E.6.1. *To form a torus-type structure, where the nodes can lie anywhere in the 3-D space, the boundaries are closed in the fashion as (E.18) and (E.19). Then the bar matrix* $\boldsymbol{B}$ *defined by (E.8) and (E.20) is related to the node matrix* $\boldsymbol{N}$ *defined by (E.7) as follows:*

$$\boldsymbol{B} = \boldsymbol{N}\boldsymbol{C}_B^T, \tag{E.22}$$

where

$$\begin{aligned}\boldsymbol{C}_B^T &= \begin{bmatrix}\boldsymbol{C}_{B_0}^T & \boldsymbol{C}_{B_1}^T & \cdots & \boldsymbol{C}_{B_{q-1}}^T\end{bmatrix} \\ &= \begin{bmatrix} -\boldsymbol{I}_{2p} & \boldsymbol{0} & \boldsymbol{0} & \cdots & \boldsymbol{0} & \boldsymbol{\Phi} \\ \boldsymbol{\Phi} & -\boldsymbol{I}_{2p} & \boldsymbol{0} & \ddots & \boldsymbol{0} & \boldsymbol{0} \\ \boldsymbol{0} & \boldsymbol{\Phi} & -\boldsymbol{I}_{2p} & \ddots & \boldsymbol{0} & \boldsymbol{0} \\ \vdots & \ddots & \ddots & \ddots & \ddots & \vdots \\ \boldsymbol{0} & \boldsymbol{0} & \boldsymbol{0} & \ddots & -\boldsymbol{I}_{2p} & \boldsymbol{0} \\ \boldsymbol{0} & \boldsymbol{0} & \boldsymbol{0} & \cdots & \boldsymbol{\Phi} & -\boldsymbol{I}_{2p} \end{bmatrix} \in \mathbb{R}^{2pq\times 2pq},\end{aligned} \tag{E.23}$$

where

$$\boldsymbol{\Phi} = \begin{bmatrix} \mathbf{0} & \boldsymbol{E}_2 & \mathbf{0} & \cdots & \mathbf{0} & \boldsymbol{E}_1 \\ \boldsymbol{E}_1 & \mathbf{0} & \boldsymbol{E}_2 & \ddots & \mathbf{0} & \mathbf{0} \\ \mathbf{0} & \boldsymbol{E}_1 & \mathbf{0} & \ddots & \mathbf{0} & \mathbf{0} \\ \vdots & \ddots & \ddots & \ddots & \ddots & \vdots \\ \mathbf{0} & \mathbf{0} & \mathbf{0} & \ddots & \mathbf{0} & \boldsymbol{E}_2 \\ \boldsymbol{E}_2 & \mathbf{0} & \mathbf{0} & \cdots & \boldsymbol{E}_1 & \mathbf{0} \end{bmatrix} \in \mathbb{R}^{2p \times 2p}. \tag{E.24}$$

The matrices $\boldsymbol{E}_1$ and $\boldsymbol{E}_2$ are defined by (E.10) and (E.11).

Proof. Note that the i^{th} block of columns of $\boldsymbol{C}_B^T$ provides the connectivity information for the i^{th} block of columns of $\boldsymbol{B}$, namely, $\boldsymbol{B}_i$.

Hence (E.22) and (E.23) mean

$$\begin{aligned} \boldsymbol{B}_i &= \boldsymbol{N}\boldsymbol{C}_{B_i}^T \\ &= \begin{cases} -\boldsymbol{N}_i + \boldsymbol{N}_{i+1}\boldsymbol{\Phi} & (i = 0, \cdots q-2) \\ -\boldsymbol{N}_{q-1} + \boldsymbol{N}_0\boldsymbol{\Phi} & (i = q-1) \end{cases} \\ &= -\boldsymbol{N}_i + \boldsymbol{N}_{i+1}\boldsymbol{\Phi} \qquad (i = 0, \cdots q-1). \end{aligned}$$

Here we use the periodic rule in the vertical direction $\boldsymbol{N}_0 = \boldsymbol{N}_q$ from (E.19). Substituting (E.24) to the above equation, we get

$$\begin{aligned} \boldsymbol{B}_i \;=\; & \big[\boldsymbol{B}(i,0) \;\cdots\; \boldsymbol{B}(i,k) \;\cdots\; \boldsymbol{B}(i,p-1)\big] \\ =\; & \Big[-\boldsymbol{N}(i,0) + \boldsymbol{N}(i+1,p-1)\boldsymbol{E}_2 + \boldsymbol{N}(i+1,1)\boldsymbol{E}_1 \,|\, \cdots \\ & \qquad | \, -\boldsymbol{N}(i,k) + \boldsymbol{N}(i+1,k-1)\boldsymbol{E}_2 + \boldsymbol{N}(i+1,k+1)\boldsymbol{E}_1 \,|\, \cdots \\ & \qquad | \, -\boldsymbol{N}(i,p-1) + \boldsymbol{N}(i+1,p-2)\boldsymbol{E}_2 + \boldsymbol{N}(i+1,0)\boldsymbol{E}_1 \Big] \\ & (i = 0, \cdots, q-1). \end{aligned}$$

Using the periodic rule in the horizontal direction $\boldsymbol{N}(i+1,p-1) = \boldsymbol{N}(i+1,-1)$ and $\boldsymbol{N}(i+1,0) = \boldsymbol{N}(i+1,p)$ from (E.18), we get

$$\begin{aligned} &\boldsymbol{B}(i,k) = -\boldsymbol{N}(i,k) + \boldsymbol{N}(i+1,k-1)\boldsymbol{E}_2 + \boldsymbol{N}(i+1,k+1)\boldsymbol{E}_1 \\ &(i = 0, \cdots, q-1;\; k = 0, \cdots, p-1), \end{aligned}$$

which is equivalent to (E.20). □

Theorem E.6.2. *Under the same assumption in Theorem E.6.1, the string matrix $\boldsymbol{S}$ defined by (E.9) and (E.21) is related to the node matrix $\boldsymbol{N}$ defined by (E.7) as follows:*

$$\boldsymbol{S} = \boldsymbol{N}\boldsymbol{C}_S^T, \tag{E.25}$$

where

$$\begin{aligned}\boldsymbol{C}_S^T &= \left[\boldsymbol{C}_{S_0}^T\ \boldsymbol{C}_{S_1}^T\ \cdots\ \boldsymbol{C}_{S_{q-1}}^T\right] \\ &= \begin{bmatrix} \boldsymbol{\Psi}_1 & \mathbf{0} & \mathbf{0} & \cdots & \mathbf{0} & \boldsymbol{\Psi}_2 \\ \boldsymbol{\Psi}_2 & \boldsymbol{\Psi}_1 & \mathbf{0} & \ddots & \mathbf{0} & \mathbf{0} \\ \mathbf{0} & \boldsymbol{\Psi}_2 & \boldsymbol{\Psi}_1 & \ddots & \mathbf{0} & \mathbf{0} \\ \vdots & \ddots & \ddots & \ddots & \ddots & \vdots \\ \mathbf{0} & \mathbf{0} & \mathbf{0} & \ddots & \boldsymbol{\Psi}_1 & \mathbf{0} \\ \mathbf{0} & \mathbf{0} & \mathbf{0} & \cdots & \boldsymbol{\Psi}_2 & \boldsymbol{\Psi}_1 \end{bmatrix} \in \mathbb{R}^{2pq\times 8pq}, \end{aligned} \tag{E.26}$$

where

$$\boldsymbol{\Psi}_1 = \begin{bmatrix} \boldsymbol{\Theta}_2 & \boldsymbol{\Theta}_1 & \mathbf{0} & \cdots & \mathbf{0} & \mathbf{0} \\ \mathbf{0} & \boldsymbol{\Theta}_2 & \boldsymbol{\Theta}_1 & \cdots & \mathbf{0} & \mathbf{0} \\ \mathbf{0} & \mathbf{0} & \boldsymbol{\Theta}_2 & \ddots & \mathbf{0} & \mathbf{0} \\ \vdots & \ddots & \ddots & \ddots & \ddots & \vdots \\ \mathbf{0} & \mathbf{0} & \mathbf{0} & \ddots & \boldsymbol{\Theta}_2 & \boldsymbol{\Theta}_1 \\ \boldsymbol{\Theta}_1 & \mathbf{0} & \mathbf{0} & \cdots & \mathbf{0} & \boldsymbol{\Theta}_2 \end{bmatrix} \in \mathbb{R}^{2p\times 8p} \tag{E.27}$$

$$\boldsymbol{\Psi}_2 = \begin{bmatrix} \boldsymbol{\Theta}_4 & \boldsymbol{\Theta}_3 & \mathbf{0} & \cdots & \mathbf{0} & \mathbf{0} \\ \mathbf{0} & \boldsymbol{\Theta}_4 & \boldsymbol{\Theta}_3 & \ddots & \mathbf{0} & \mathbf{0} \\ \mathbf{0} & \mathbf{0} & \boldsymbol{\Theta}_4 & \ddots & \mathbf{0} & \mathbf{0} \\ \vdots & \ddots & \ddots & \ddots & \ddots & \vdots \\ \mathbf{0} & \mathbf{0} & \mathbf{0} & \ddots & \boldsymbol{\Theta}_4 & \boldsymbol{\Theta}_3 \\ \boldsymbol{\Theta}_3 & \mathbf{0} & \mathbf{0} & \cdots & \mathbf{0} & \boldsymbol{\Theta}_4 \end{bmatrix} \in \mathbb{R}^{2p\times 8p}. \tag{E.28}$$

The matrices $\boldsymbol{\Theta}_1$-$\boldsymbol{\Theta}_4$ *are defined by (E.13)-(E.16).*

Proof. Proof is similar to the proof of Theorem E.6.1. Note that the i^{th} column of $\boldsymbol{C}_S^T$ defines the strings in the i^{th} column $\boldsymbol{S}_i$. Using the vertical periodic condition $\boldsymbol{N}_q = \boldsymbol{N}_0$, we see that (E.25) and (E.26) mean

$$\begin{aligned}\boldsymbol{S}_i &= \boldsymbol{N}\boldsymbol{C}_{S_i}^T \\ &= \boldsymbol{N}_i\boldsymbol{\Psi}_1 + \boldsymbol{N}_{i+1}\boldsymbol{\Psi}_2 \qquad (i = 0, \cdots q-1).\end{aligned}$$

Substituting (E.27) and (E.28) to the above equation, and using the horizontal periodic condition $\boldsymbol{N}(i, p-1) = \boldsymbol{N}(i, -1)$, we get

$$\begin{aligned}\boldsymbol{S}(i,k) = &\boldsymbol{N}(i,k-1)\boldsymbol{\Theta}_1 + \boldsymbol{N}(i,k)\boldsymbol{\Theta}_2 \\ &+ \boldsymbol{N}(i+1,k-1)\boldsymbol{\Theta}_3 + \boldsymbol{N}(i+1,k)\boldsymbol{\Theta}_4 \\ &(i = 0, \cdots, q-1;\ k = 0, \cdots, p-1),\end{aligned}$$

which is equivalent to (E.21). □

Using the connectivity matrices derived in the above theorems, we can make a variety of structures by choosing different node locations. Some typical choices are given in the next section.

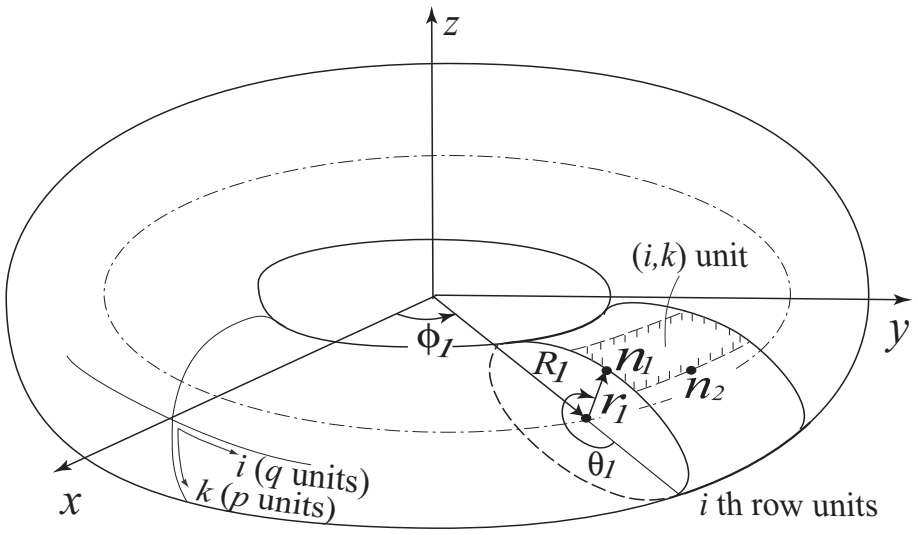

Figure E.5: Coordinate for torus

E.6.2 Torus Node Locations

Figure E.5 shows a typical coordinate used for the torus configuration. The strip of the tube represents the i^{th} row units, and the shaded area represents the (i,k) unit. To locate $\boldsymbol{n}_1(i,k)$, define the vectors $\boldsymbol{R}_1(i,k)$, $\boldsymbol{r}_1(i,k)$ and the angles $\phi_1(i,k)$, $\theta_1(i,k)$ as shown in Fig. E.5. For $\boldsymbol{n}_2(i,k)$, define $\boldsymbol{R}_2(i,k)$, $\boldsymbol{r}_2(i,k)$ and $\phi_2(i,k)$, $\theta_2(i,k)$ the same way. Then $\boldsymbol{n}_\ell(i,k)$ $(\ell = 1,2)$ is written by

$$\boldsymbol{n}_\ell(i,k) = \boldsymbol{R}_\ell(i,k) + \boldsymbol{r}_\ell(i,k). \tag{E.29}$$

The vectors $\boldsymbol{R}_\ell(i,k)$ and $\boldsymbol{r}_\ell(i,k)$ will be functions of the angles $\phi_\ell(i,k)$ and $\theta_\ell(i,k)$. If we assign these angles equally to each unit,

$$\phi_\ell(i,k) = \{2i + (\ell - 1)\}\,\frac{\pi}{q} \tag{E.30}$$

$$\theta_\ell(i,k) = \{2k + \ell\}\,\frac{\pi}{p}. \tag{E.31}$$

The smaller radius $\boldsymbol{r}_\ell(i,k)$ specifies the shape of the cross-section of the tube and the larger radius $\boldsymbol{R}_\ell(i,k)$ defines the trajectory of revolution about the z axis. We can make many shapes by specifying $\boldsymbol{R}_\ell(i,k)$, $\boldsymbol{r}_\ell(i,k)$. Some typical shapes are given in the following corollaries.

If we set both the cross-section of the tube and the trajectory of revolution to be circles, the resultant structure forms a shape shown in Fig. E.6 (a), which we call the circular torus.

Corollary E.6.1. (Circular Torus) *Given the number of units p, q, locate the node* $\boldsymbol{N}(i,k) =$

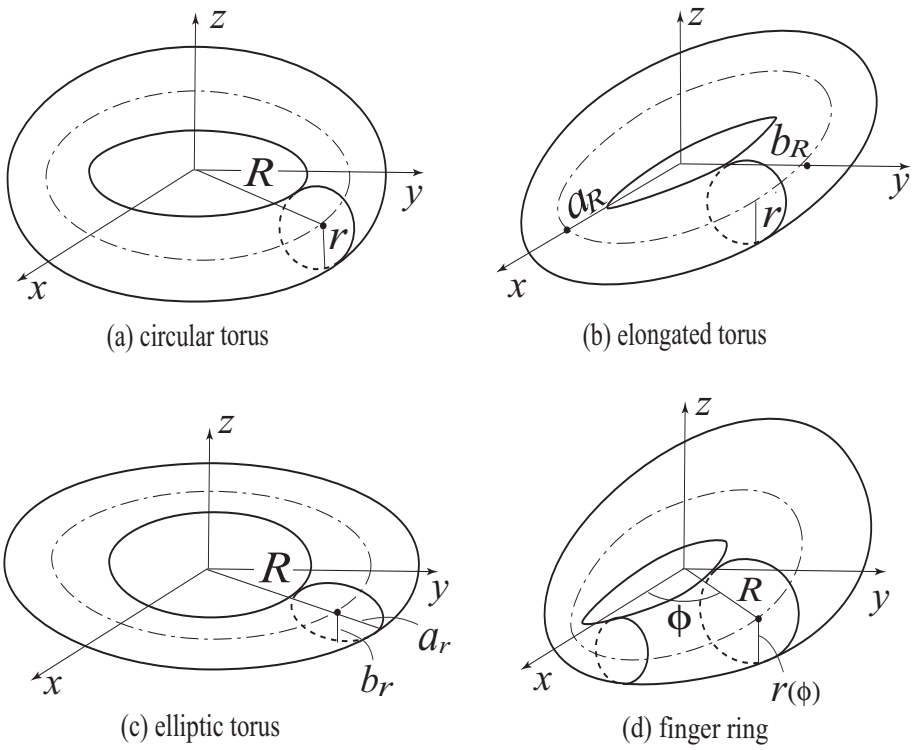

Figure E.6: Torus-type Structures

$[\boldsymbol{n}_1(i,k)\ \boldsymbol{n}_2(i,k)]$ *by (E.29)-(E.31) with*

$$\boldsymbol{R}_\ell(i,k) = \begin{bmatrix} R\cos\phi_\ell(i,k) \\ R\sin\phi_\ell(i,k) \\ 0 \end{bmatrix} \tag{E.32}$$

$$\boldsymbol{r}_\ell(i,k) = \begin{bmatrix} r\cos\theta_\ell(i,k)\cos\phi_\ell(i,k) \\ r\cos\theta_\ell(i,k)\sin\phi_\ell(i,k) \\ -r\sin\theta_\ell(k) \end{bmatrix} \tag{E.33}$$

$(\ell = 1, 2)$*, where* $R > 0$ *and* $r > 0$*. Define the bars and the strings by (E.22)-(E.24) and (E.25)-(E.28) respectively. Then the resulting surface forms the circular torus as shown in Fig. E.6 (a).*

Figure E.7 shows a numerical example for the circular torus with different complexity (p, q). We see that the shape gets closer to the smooth surface torus as the number of the units p, q approaches infinity.

If we choose an ellipse as the trajectory of revolution instead, the resultant structure becomes Fig. E.6 (b), which we call the elongated torus.

Corollary E.6.2. (Elongated Torus) *Under the same assumption in Corollary E.6.1, set* $\boldsymbol{R}_\ell(i,k)$

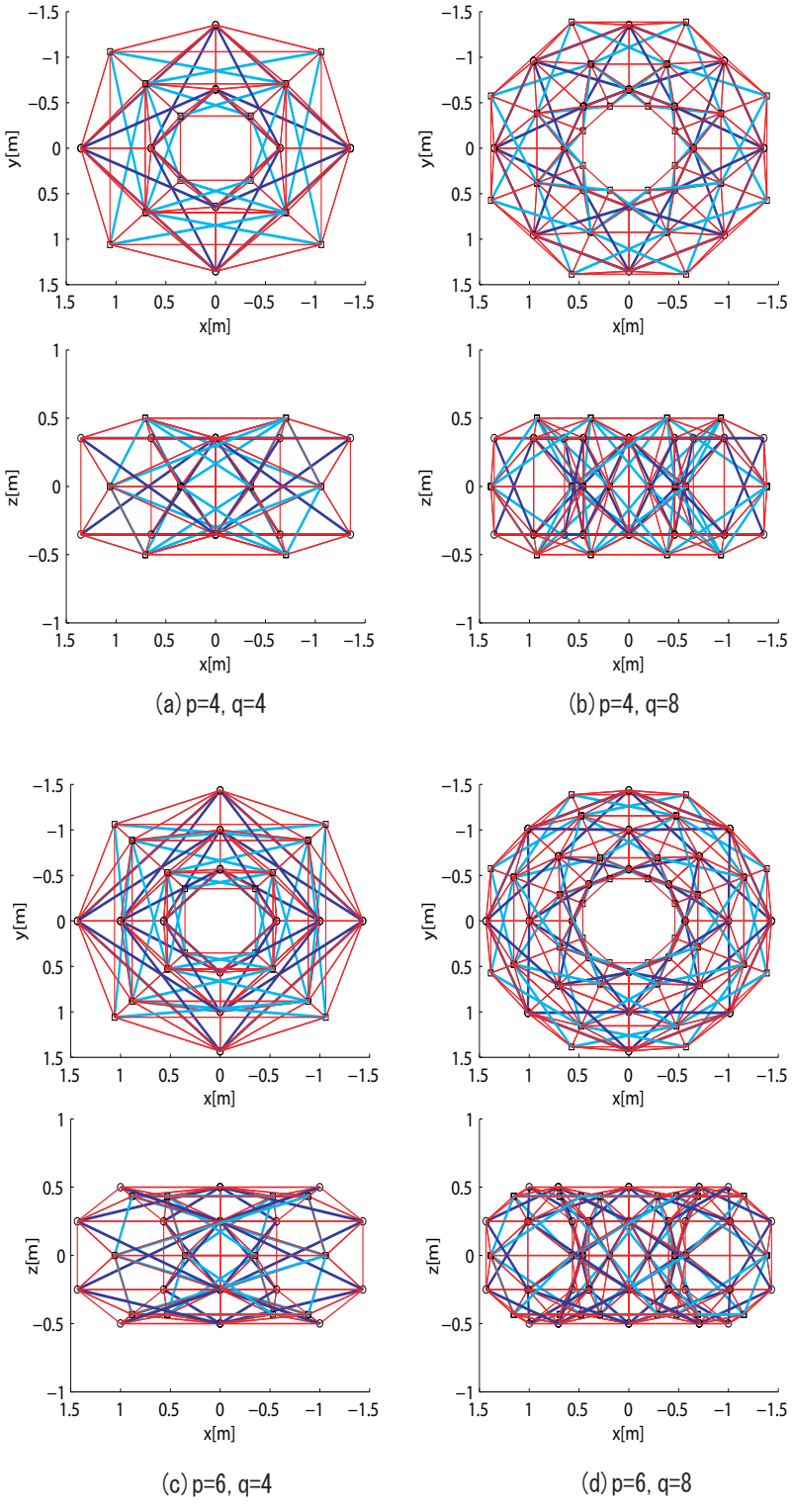

Figure E.7: Circular torus with different complexity (p, q), ($R = 1$ [m], $r = 0.5$ [m])

and $\boldsymbol{r}_\ell(i,k)$ $(\ell = 1,2)$ *by*

$$\boldsymbol{R}_\ell(i,k) = \begin{bmatrix} a_R \cos\phi_\ell(i,k) \\ b_R \sin\phi_\ell(i,k) \\ 0 \end{bmatrix} \tag{E.34}$$

$$\boldsymbol{r}_\ell(i,k) = \begin{bmatrix} r\cos\theta_\ell(i,k)\cos\phi_\ell(i,k) \\ r\cos\theta_\ell(i,k)\sin\phi_\ell(i,k) \\ -r\sin\theta_\ell(i,k) \end{bmatrix}, \tag{E.35}$$

where $a_R > 0$, $b_R > 0$ *and* $r > 0$. *Then the resulting surface forms the elongated torus as shown in Fig. E.6 (b).*

If we choose an ellipse as the cross-section of the tube, the resultant structure becomes Fig. E.6 (c), which we call the elliptic torus.

Corollary E.6.3. (Elliptic Torus) *Under the same assumption in Corollary E.6.1, set* $\boldsymbol{R}_\ell(i,k)$ *and* $\boldsymbol{r}_\ell(i,k)$ $(\ell = 1,2)$ *by*

$$\boldsymbol{R}_\ell(i,k) = \begin{bmatrix} R\cos\phi_\ell(i,k) \\ R\sin\phi_\ell(i,k) \\ 0 \end{bmatrix} \tag{E.36}$$

$$\boldsymbol{r}_\ell(i,k) = \begin{bmatrix} a_r\cos\theta_\ell(i,k)\cos\phi_\ell(i,k) \\ a_r\cos\theta_\ell(i,k)\sin\phi_\ell(i,k) \\ -b_r\sin\theta_\ell(i,k) \end{bmatrix}, \tag{E.37}$$

where $R > 0$, $a_r > 0$, $b_r > 0$. *Then the resulting surface forms the elliptic torus as shown in Fig. E.6 (c).*

We can also make the cross-section of the tube vary along the trajectory of revolution. One simple example is given in the next corollary, which we call the finger ring, as shown in Fig. E.6 (d).

Corollary E.6.4. (Finger ring) *Under the same assumption in Corollary E.6.1, set* $\boldsymbol{R}_\ell(i,k)$ *and* $\boldsymbol{r}_\ell(i,k)$ $(\ell = 1,2)$ *by*

$$\boldsymbol{R}_\ell(i,k) = \begin{bmatrix} R\cos\phi_\ell(i,k) \\ R\sin\phi_\ell(i,k) \\ 0 \end{bmatrix} \tag{E.38}$$

$$\boldsymbol{r}_\ell(i,k) = \begin{bmatrix} r(\phi_\ell(i,k))\cos\theta_\ell(i,k)\cos\phi_\ell(i,k) \\ r(\phi_\ell(i,k))\cos\theta_\ell(i,k)\sin\phi_\ell(i,k) \\ -r(\phi_\ell(i,k))\sin\theta_\ell(i,k) \end{bmatrix}, \tag{E.39}$$

where $R > 0$ *and*

$$r(\phi_\ell(i,k)) = \begin{cases} k_r\phi_\ell(i,k) + r_0 & \big(\phi_\ell(i,k) \le \pi\big) \\ -k_r\Big(\phi_\ell(i,k) - \pi\Big) + r_f & \big(\phi_\ell(i,k) > \pi\big) \end{cases}, \tag{E.40}$$

where $k_r = (r_f - r_0)/\pi$, *where* $r_0 > 0$, $r_f > 0$ *specify the minimum and maximum radius of the tube. Then the resulting surface forms the finger ring as shown in Fig. E.6 (d).*

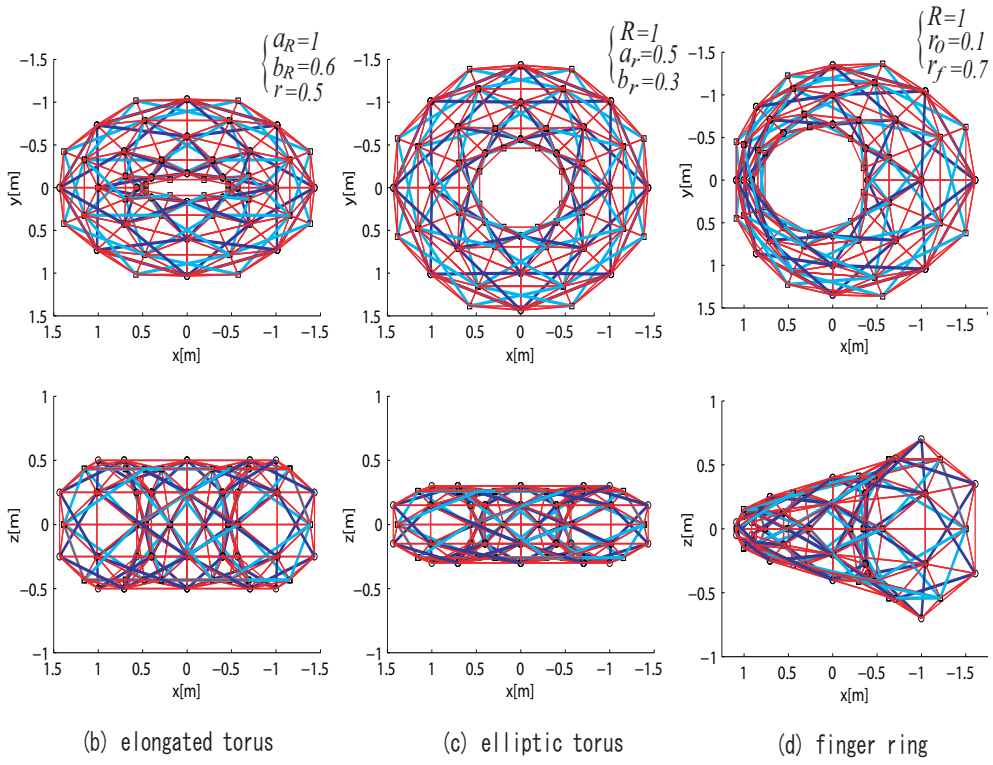

(b) elongated torus (c) elliptic torus (d) finger ring

Figure E.8: Torus-type structures ($p = 6,\ q = 8$)

The varying radius $r(\phi_\ell(i,k))$ in (E.40) is defined by two lines symmetric about $\phi_\ell(i,k) = \pi$.

Figure E.8 shows numerical examples of the torus-type structures obtained from Corollaries E.6.2-E.6.4. Although our choice of the shapes is simply made from geometrical view points, we confirm that all the torus-type structures in the above examples are stable from the stiffness analysis. More precisely, we calculate a prestress pattern (force densities) satisfying the equilibrium condition (E.3), then evaluate the stiffness matrix at the equilibrium, Chapter 2 of [1]. Eigen values of all the stiffness matrices for the above structures are positive except for the six rigid modes.

E.7 Cylindrical-type Structures

E.7.1 Cylinder Boundary Condition and Connectivity Matrix

Closing the structure about the vertical axis of Fig. E.2 yields a cylinder. Typical boundary condition for the top and the bottom units are shown in Fig E.9. As for the bottom units, the string $\underline{\boldsymbol{s}}_7$ is added, and the string $\boldsymbol{s}_4$ is replaced by the bar $\underline{\boldsymbol{b}}_2$, compared to the general (i,k) unit in Fig. E.2. As for the top units, the top node $\boldsymbol{n}_1(q,k)$ is added, the bar $\boldsymbol{b}_2$ and the string $\boldsymbol{s}_8$ are removed, and the string $\boldsymbol{s}_2$ is replaced by the bar $\overline{\boldsymbol{b}}_2$.

For the above modification, we redefine the bar and the string matrices of the top and the bottom units as

$$\boldsymbol{B}(0,k) = \left[\boldsymbol{b}_1(0,k)\ \boldsymbol{b}_2(0,k) \mid \underline{\boldsymbol{b}}_2(0,k)\right] \in \mathbb{R}^{3\times 3} \tag{E.41}$$

$$\boldsymbol{S}(0,k) = \left[\boldsymbol{s}_1(0,k)\ \cdots\ \boldsymbol{s}_3(0,k)\ \boldsymbol{s}_5(0,k)\cdots\boldsymbol{s}_8(0,k) \mid \underline{\boldsymbol{s}}_7(0,k)\right] \in \mathbb{R}^{3\times 8}, \tag{E.42}$$

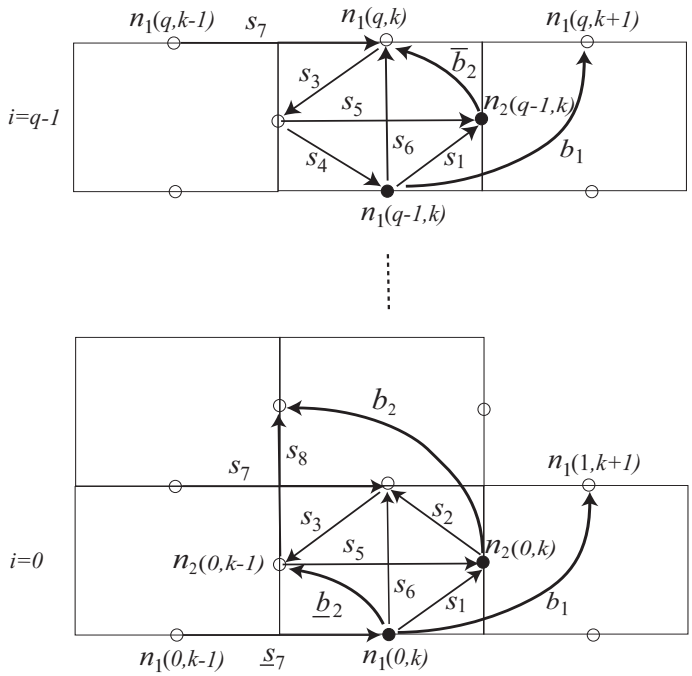

Figure E.9: Top and bottom units for cylinder

and

$$\boldsymbol{B}(q-1,k) = \left[\boldsymbol{b}_1(q-1,k)\ \overline{\boldsymbol{b}}_2(q-1,k)\right] \in \mathbb{R}^{3\times 2} \tag{E.43}$$

$$\boldsymbol{S}(q-1,k) = \left[\boldsymbol{s}_1(q-1,k)\ \boldsymbol{s}_3(q-1,k)\ \cdots\ \boldsymbol{s}_7(q-1,k)\right] \in \mathbb{R}^{3\times 6}, \tag{E.44}$$

where $k = 0, \cdots, q-1$. Define the top node matrix by

$$\boldsymbol{N}(q,k) = \left[\boldsymbol{n}_1(q,k)\right] \in \mathbb{R}^{3\times 1}. \tag{E.45}$$

By using the above definitions (E.41)-(E.45) and the horizontal periodic role (E.18), the bar matrix at the unit (i,k), for $k = 0, \cdots, p-1$, is written by

$$\boldsymbol{B}(i,k) = \begin{cases} \boldsymbol{N}(0,k-1)\underline{\boldsymbol{E}}_3 - \boldsymbol{N}(0,k)\underline{\boldsymbol{E}}_4 + \boldsymbol{N}(1,k-1)\underline{\boldsymbol{E}}_2 + \boldsymbol{N}(1,k+1)\underline{\boldsymbol{E}}_1 \\ \qquad\qquad\qquad\qquad\qquad\qquad\qquad\qquad (i=0) \\ -\boldsymbol{N}(i,k) + \boldsymbol{N}(i+1,k-1)\boldsymbol{E}_2 + \boldsymbol{N}(i+1,k+1)\boldsymbol{E}_1 \\ \qquad\qquad\qquad\qquad\qquad\qquad\qquad\qquad (i=1,\cdots,q-2) \\ -\boldsymbol{N}(q-1,k) + \boldsymbol{N}(q,k)\overline{\boldsymbol{E}}_2 + \boldsymbol{N}(q,k+1)\overline{\boldsymbol{E}}_1 \qquad (i=q-1) \end{cases}, \tag{E.46}$$

where $\boldsymbol{E}_1$ and $\boldsymbol{E}_2$ are defined by (E.10) and (E.11), and where

$$\underline{\boldsymbol{E}}_3 = \left[\boldsymbol{0}\ \boldsymbol{0} \mid \boldsymbol{e}_2\right] \in \mathbb{R}^{2\times 3} \tag{E.47}$$

$$\underline{\boldsymbol{E}}_4 = \left[\boldsymbol{I}_2 \mid \boldsymbol{e}_1\right] \in \mathbb{R}^{2\times 3} \tag{E.48}$$

$$\underline{\boldsymbol{E}}_2 = \left[\boldsymbol{E}_2 \mid \boldsymbol{0}\right] \in \mathbb{R}^{2\times 3} \tag{E.49}$$

$$\underline{\boldsymbol{E}}_1 = \left[\boldsymbol{E}_1 \mid \boldsymbol{0}\right] \in \mathbb{R}^{2\times 3}, \tag{E.50}$$

and

$$\overline{\boldsymbol{E}}_2 = \begin{bmatrix} 0 & 1 \end{bmatrix} \in \mathbb{R}^{1\times 2} \tag{E.51}$$

$$\overline{\boldsymbol{E}}_1 = \begin{bmatrix} 1 & 0 \end{bmatrix} \in \mathbb{R}^{1\times 2}. \tag{E.52}$$

The vectors $\boldsymbol{e}_1$ and $\boldsymbol{e}_2$ are defined in (E.10) and (E.11). The middle equation of (E.46) for the internal units ($i = 1, \cdots, q-2$) is equivalent to (E.12).

Similarly, for $k = 0, \cdots, p-1$, the string matrix at the unit (i,k) is written by

$$\boldsymbol{S}(i,k) = \begin{cases} \boldsymbol{N}(0,k-1)\underline{\boldsymbol{\Theta}}_1 + \boldsymbol{N}(0,k)\underline{\boldsymbol{\Theta}}_2 + \boldsymbol{N}(1,k-1)\underline{\boldsymbol{\Theta}}_3 + \boldsymbol{N}(1,k)\underline{\boldsymbol{\Theta}}_4 \\ \qquad\qquad (i=0) \\ \boldsymbol{N}(i,k-1)\boldsymbol{\Theta}_1 + \boldsymbol{N}(i,k)\boldsymbol{\Theta}_2 + \boldsymbol{N}(i+1,k-1)\boldsymbol{\Theta}_3 + \boldsymbol{N}(i+1,k)\boldsymbol{\Theta}_4 \\ \qquad\qquad (i=1,\cdots,q-2) \\ \boldsymbol{N}(q-1,k-1)\overline{\boldsymbol{\Theta}}_1 + \boldsymbol{N}(q-1,k)\overline{\boldsymbol{\Theta}}_2 + \boldsymbol{N}(q,k-1)\overline{\boldsymbol{\Theta}}_3 + \boldsymbol{N}(q,k)\overline{\boldsymbol{\Theta}}_4 \\ \qquad\qquad (i=q-1) \end{cases}, \tag{E.53}$$

where $\boldsymbol{\Theta}_1$-$\boldsymbol{\Theta}_4$ are defined by (E.13)-(E.16), and where

$$\underline{\boldsymbol{\Theta}}_1 = \begin{bmatrix} \boldsymbol{\Theta}_1(1\text{-}3, 5\text{-}8) \mid -\boldsymbol{e}_1 \end{bmatrix} \in \mathbb{R}^{2\times 8} \tag{E.54}$$

$$\underline{\boldsymbol{\Theta}}_2 = \begin{bmatrix} \boldsymbol{\Theta}_2(1\text{-}3, 5\text{-}8) \mid \boldsymbol{e}_1 \end{bmatrix} \in \mathbb{R}^{2\times 8} \tag{E.55}$$

$$\underline{\boldsymbol{\Theta}}_3 = \begin{bmatrix} \boldsymbol{\Theta}_3(1\text{-}3, 5\text{-}8) \mid \boldsymbol{0} \end{bmatrix} \in \mathbb{R}^{2\times 8} \tag{E.56}$$

$$\underline{\boldsymbol{\Theta}}_4 = \begin{bmatrix} \boldsymbol{\Theta}_4(1\text{-}3, 5\text{-}8) \mid \boldsymbol{0} \end{bmatrix} \in \mathbb{R}^{2\times 8}, \tag{E.57}$$

and

$$\overline{\boldsymbol{\Theta}}_1 = \boldsymbol{\Theta}_1(1, 3\text{-}7) \in \mathbb{R}^{2\times 6} \tag{E.58}$$

$$\overline{\boldsymbol{\Theta}}_2 = \boldsymbol{\Theta}_2(1, 3\text{-}7) \in \mathbb{R}^{2\times 6} \tag{E.59}$$

$$\overline{\boldsymbol{\Theta}}_3 = \begin{bmatrix} 1 & 0 \end{bmatrix} \boldsymbol{\Theta}_3(1, 3\text{-}7) \in \mathbb{R}^{1\times 6} \tag{E.60}$$

$$\overline{\boldsymbol{\Theta}}_4 = \begin{bmatrix} 1 & 0 \end{bmatrix} \boldsymbol{\Theta}_4(1, 3\text{-}7) \in \mathbb{R}^{1\times 6}. \tag{E.61}$$

The matrix $\boldsymbol{\Theta}_\ell(1\text{-}3, 5\text{-}8)$ ($\ell = 1, \cdots, 4$) is defined by $\boldsymbol{\Theta}_\ell$ deleting the 4th column. The matrix $\boldsymbol{\Theta}_\ell(1, 3\text{-}7)$ is defined similarly, by deleting columns 2 and 8. The middle equation of (E.53) for the internal units ($i = 1, \cdots, q-2$) is equivalent to (E.17).

The connectivity matrices for the cylindrical-type structures are given in the following theorems. Define the *augmented* nodal matrix

$$\overline{\boldsymbol{N}} = \big[\underbrace{\boldsymbol{N}_0\ \boldsymbol{N}_1\ \cdots\cdots\ \boldsymbol{N}_{q-1}}_{\boldsymbol{N}} \mid \boldsymbol{N}_q \big], \tag{E.62}$$

where

$$\boldsymbol{N}_q = \begin{bmatrix} \boldsymbol{N}(q,0) \cdots \boldsymbol{N}(q,p-1) \end{bmatrix},$$

where the matrix $\boldsymbol{N}(q,k)$ is defined by (E.45).

Theorem E.7.1. *To form a cylindrical-type structure, where the nodes can lie anywhere in the 3-D space, the top and the bottom boundaries are terminated as shown in Fig. E.9, and the horizontal boundaries are closed in the fashion as in (E.18).*

Then the bar matrix $\boldsymbol{B}$ *defined by (E.8) and (E.46) is related to the node matrix* $\overline{\boldsymbol{N}}$ *defined by (E.62) as follows:*

$$\boldsymbol{B} = \overline{\boldsymbol{N}}\boldsymbol{C}_B^T, \tag{E.63}$$

where

$$\begin{aligned}\boldsymbol{C}_B^T &= \begin{bmatrix}\boldsymbol{C}_{B_0}^T & \boldsymbol{C}_{B_1}^T & \cdots & \boldsymbol{C}_{B_{q-1}}^T\end{bmatrix} \\ &= \left[\begin{array}{cccccc} -\underline{\boldsymbol{I}} & \boldsymbol{0} & \boldsymbol{0} & \cdots & \boldsymbol{0} & \boldsymbol{0} \\ \underline{\boldsymbol{\Phi}} & -\boldsymbol{I}_{2p} & \boldsymbol{0} & \ddots & \boldsymbol{0} & \boldsymbol{0} \\ \boldsymbol{0} & \boldsymbol{\Phi} & -\boldsymbol{I}_{2p} & \ddots & \boldsymbol{0} & \boldsymbol{0} \\ \vdots & \ddots & \ddots & \ddots & \ddots & \vdots \\ \boldsymbol{0} & \boldsymbol{0} & \boldsymbol{0} & \ddots & -\boldsymbol{I}_{2p} & \boldsymbol{0} \\ \boldsymbol{0} & \boldsymbol{0} & \boldsymbol{0} & \cdots & \boldsymbol{\Phi} & -\boldsymbol{I}_{2p} \\ \hline \boldsymbol{0} & \boldsymbol{0} & \boldsymbol{0} & \cdots & \boldsymbol{0} & \overline{\boldsymbol{\Phi}} \end{array}\right] \in \mathbb{R}^{(2q+1)p\times(2q+1)p},\end{aligned} \tag{E.64}$$

where $\boldsymbol{\Phi}$ *is defined by (E.24), and where*

$$\underline{\boldsymbol{I}} = \begin{bmatrix} \underline{\boldsymbol{E}}_4 & -\underline{\boldsymbol{E}}_3 & \boldsymbol{0} & \cdots & \boldsymbol{0} & \boldsymbol{0} \\ \boldsymbol{0} & \underline{\boldsymbol{E}}_4 & -\underline{\boldsymbol{E}}_3 & \cdots & \boldsymbol{0} & \boldsymbol{0} \\ \boldsymbol{0} & \boldsymbol{0} & \underline{\boldsymbol{E}}_4 & \ddots & \boldsymbol{0} & \boldsymbol{0} \\ \vdots & \ddots & \ddots & \ddots & \ddots & \vdots \\ \boldsymbol{0} & \boldsymbol{0} & \boldsymbol{0} & \ddots & \underline{\boldsymbol{E}}_4 & -\underline{\boldsymbol{E}}_3 \\ -\underline{\boldsymbol{E}}_3 & \boldsymbol{0} & \boldsymbol{0} & \cdots & \boldsymbol{0} & \underline{\boldsymbol{E}}_4 \end{bmatrix} \in \mathbb{R}^{2p\times 3p} \tag{E.65}$$

$$\underline{\boldsymbol{\Phi}} = \begin{bmatrix} \boldsymbol{0} & \underline{\boldsymbol{E}}_2 & \boldsymbol{0} & \cdots & \boldsymbol{0} & \underline{\boldsymbol{E}}_1 \\ \underline{\boldsymbol{E}}_1 & \boldsymbol{0} & \underline{\boldsymbol{E}}_2 & \ddots & \boldsymbol{0} & \boldsymbol{0} \\ \boldsymbol{0} & \underline{\boldsymbol{E}}_1 & \boldsymbol{0} & \ddots & \boldsymbol{0} & \boldsymbol{0} \\ \vdots & \ddots & \ddots & \ddots & \ddots & \vdots \\ \boldsymbol{0} & \boldsymbol{0} & \boldsymbol{0} & \ddots & \boldsymbol{0} & \underline{\boldsymbol{E}}_2 \\ \underline{\boldsymbol{E}}_2 & \boldsymbol{0} & \boldsymbol{0} & \cdots & \underline{\boldsymbol{E}}_1 & \boldsymbol{0} \end{bmatrix} \in \mathbb{R}^{2p\times 3p}, \tag{E.66}$$

and

$$\overline{\boldsymbol{\Phi}} = \begin{bmatrix} \overline{\boldsymbol{E}}_2 & \boldsymbol{0} & \boldsymbol{0} & \cdots & \boldsymbol{0} & \overline{\boldsymbol{E}}_1 \\ \overline{\boldsymbol{E}}_1 & \overline{\boldsymbol{E}}_2 & \boldsymbol{0} & \cdots & \boldsymbol{0} & \boldsymbol{0} \\ \boldsymbol{0} & \overline{\boldsymbol{E}}_1 & \overline{\boldsymbol{E}}_2 & \ddots & \boldsymbol{0} & \boldsymbol{0} \\ \vdots & \ddots & \ddots & \ddots & \ddots & \vdots \\ \boldsymbol{0} & \boldsymbol{0} & \boldsymbol{0} & \ddots & \overline{\boldsymbol{E}}_2 & \boldsymbol{0} \\ \boldsymbol{0} & \boldsymbol{0} & \boldsymbol{0} & \cdots & \overline{\boldsymbol{E}}_1 & \overline{\boldsymbol{E}}_2 \end{bmatrix} \in \mathbb{R}^{p\times 2p}. \tag{E.67}$$

Matrices $\underline{\boldsymbol{E}}_1$-$\underline{\boldsymbol{E}}_4$ *and* $\overline{\boldsymbol{E}}_1$, $\overline{\boldsymbol{E}}_2$ *are defined by (E.47)-(E.52).*

Proof. From (E.63) and (E.64),

$$\boldsymbol{B}_i = \begin{cases} -\boldsymbol{N}_0\underline{\boldsymbol{I}} + \boldsymbol{N}_1\underline{\boldsymbol{\Phi}} & (i=0) \\ -\boldsymbol{N}_i + \boldsymbol{N}_{i+1}\boldsymbol{\Phi} & (i=1,\cdots q-2) \\ -\boldsymbol{N}_{q-1} + \boldsymbol{N}_q\overline{\boldsymbol{\Phi}} & (i=q-1). \end{cases}$$

Substituting (E.24) and (E.65)-(E.67) to the above equation, and noting the horizontal periodic rule (E.18), we see that the above equation is equivalent to (E.46). □

Theorem E.7.2. *Under the same assumption in Theorem E.7.1, the string matrix $\boldsymbol{S}$ defined by (E.9) and (E.53) is related to the node matrix $\overline{\boldsymbol{N}}$ defined by (E.62) as follows:*

$$\boldsymbol{S} = \overline{\boldsymbol{N}}\boldsymbol{C}_S^T, \tag{E.68}$$

where

$$\begin{aligned} \boldsymbol{C}_S^T &= \begin{bmatrix} \boldsymbol{C}_{S_0}^T & \boldsymbol{C}_{S_1}^T & \cdots & \boldsymbol{C}_{S_{q-1}}^T \end{bmatrix} \\ &= \left[\begin{array}{cccccc} \underline{\boldsymbol{\Psi}}_1 & \boldsymbol{0} & \boldsymbol{0} & \cdots & \boldsymbol{0} & \boldsymbol{0} \\ \underline{\boldsymbol{\Psi}}_2 & \boldsymbol{\Psi}_1 & \boldsymbol{0} & \ddots & \boldsymbol{0} & \boldsymbol{0} \\ \boldsymbol{0} & \boldsymbol{\Psi}_2 & \boldsymbol{\Psi}_1 & \ddots & \boldsymbol{0} & \boldsymbol{0} \\ \vdots & \ddots & \ddots & \ddots & \ddots & \vdots \\ \boldsymbol{0} & \boldsymbol{0} & \boldsymbol{0} & \ddots & \boldsymbol{\Psi}_1 & \boldsymbol{0} \\ \boldsymbol{0} & \boldsymbol{0} & \boldsymbol{0} & \cdots & \boldsymbol{\Psi}_2 & \overline{\boldsymbol{\Psi}}_1 \\ \hline \boldsymbol{0} & \boldsymbol{0} & \boldsymbol{0} & \cdots & \boldsymbol{0} & \overline{\boldsymbol{\Psi}}_2 \end{array}\right] \in \mathbb{R}^{(2q+1)p\times(8q-2)p}, \end{aligned} \tag{E.69}$$

where $\boldsymbol{\Psi}_1$ and $\boldsymbol{\Psi}_2$ are defined by (E.27) and (E.28), and where

$$\underline{\boldsymbol{\Psi}}_1 = \begin{bmatrix} \underline{\boldsymbol{\Theta}}_2 & \underline{\boldsymbol{\Theta}}_1 & \boldsymbol{0} & \cdots & \boldsymbol{0} & \boldsymbol{0} \\ \boldsymbol{0} & \underline{\boldsymbol{\Theta}}_2 & \underline{\boldsymbol{\Theta}}_1 & \cdots & \boldsymbol{0} & \boldsymbol{0} \\ \boldsymbol{0} & \boldsymbol{0} & \underline{\boldsymbol{\Theta}}_2 & \ddots & \boldsymbol{0} & \boldsymbol{0} \\ \vdots & \ddots & \ddots & \ddots & \ddots & \vdots \\ \boldsymbol{0} & \boldsymbol{0} & \boldsymbol{0} & \ddots & \underline{\boldsymbol{\Theta}}_2 & \underline{\boldsymbol{\Theta}}_1 \\ \underline{\boldsymbol{\Theta}}_1 & \boldsymbol{0} & \boldsymbol{0} & \cdots & \boldsymbol{0} & \underline{\boldsymbol{\Theta}}_2 \end{bmatrix} \in \mathbb{R}^{2p\times 8p} \tag{E.70}$$

$$\underline{\boldsymbol{\Psi}}_2 = \begin{bmatrix} \underline{\boldsymbol{\Theta}}_4 & \underline{\boldsymbol{\Theta}}_3 & \boldsymbol{0} & \cdots & \boldsymbol{0} & \boldsymbol{0} \\ \boldsymbol{0} & \underline{\boldsymbol{\Theta}}_4 & \underline{\boldsymbol{\Theta}}_3 & \ddots & \boldsymbol{0} & \boldsymbol{0} \\ \boldsymbol{0} & \boldsymbol{0} & \underline{\boldsymbol{\Theta}}_4 & \ddots & \boldsymbol{0} & \boldsymbol{0} \\ \vdots & \ddots & \ddots & \ddots & \ddots & \vdots \\ \boldsymbol{0} & \boldsymbol{0} & \boldsymbol{0} & \ddots & \underline{\boldsymbol{\Theta}}_4 & \underline{\boldsymbol{\Theta}}_3 \\ \underline{\boldsymbol{\Theta}}_3 & \boldsymbol{0} & \boldsymbol{0} & \cdots & \boldsymbol{0} & \underline{\boldsymbol{\Theta}}_4 \end{bmatrix} \in \mathbb{R}^{2p\times 8p}, \tag{E.71}$$

and

$$\overline{\boldsymbol{\Psi}}_1 = \begin{bmatrix} \overline{\boldsymbol{\Theta}}_2 & \overline{\boldsymbol{\Theta}}_1 & \mathbf{0} & \cdots & \mathbf{0} & \mathbf{0} \\ \mathbf{0} & \overline{\boldsymbol{\Theta}}_2 & \overline{\boldsymbol{\Theta}}_1 & \cdots & \mathbf{0} & \mathbf{0} \\ \mathbf{0} & \mathbf{0} & \overline{\boldsymbol{\Theta}}_2 & \ddots & \mathbf{0} & \mathbf{0} \\ \vdots & \ddots & \ddots & \ddots & \ddots & \vdots \\ \mathbf{0} & \mathbf{0} & \mathbf{0} & \ddots & \overline{\boldsymbol{\Theta}}_2 & \overline{\boldsymbol{\Theta}}_1 \\ \overline{\boldsymbol{\Theta}}_1 & \mathbf{0} & \mathbf{0} & \cdots & \mathbf{0} & \overline{\boldsymbol{\Theta}}_2 \end{bmatrix} \in \mathbb{R}^{2p \times 6p} \tag{E.72}$$

$$\overline{\boldsymbol{\Psi}}_2 = \begin{bmatrix} \overline{\boldsymbol{\Theta}}_4 & \overline{\boldsymbol{\Theta}}_3 & \mathbf{0} & \cdots & \mathbf{0} & \mathbf{0} \\ \mathbf{0} & \overline{\boldsymbol{\Theta}}_4 & \overline{\boldsymbol{\Theta}}_3 & \ddots & \mathbf{0} & \mathbf{0} \\ \mathbf{0} & \mathbf{0} & \overline{\boldsymbol{\Theta}}_4 & \ddots & \mathbf{0} & \mathbf{0} \\ \vdots & \ddots & \ddots & \ddots & \ddots & \vdots \\ \mathbf{0} & \mathbf{0} & \mathbf{0} & \ddots & \overline{\boldsymbol{\Theta}}_4 & \overline{\boldsymbol{\Theta}}_3 \\ \overline{\boldsymbol{\Theta}}_3 & \mathbf{0} & \mathbf{0} & \cdots & \mathbf{0} & \overline{\boldsymbol{\Theta}}_4 \end{bmatrix} \in \mathbb{R}^{p \times 6p}. \tag{E.73}$$

The matrices $\underline{\boldsymbol{\Theta}}_1$-$\underline{\boldsymbol{\Theta}}_4$ *and* $\overline{\boldsymbol{\Theta}}_1$-$\overline{\boldsymbol{\Theta}}_4$ *are defined by (E.54)-(E.61).*

Proof. From (E.68) and (E.69),

$$\boldsymbol{S}_i = \begin{cases} \boldsymbol{N}_0 \underline{\boldsymbol{\Psi}}_1 + \boldsymbol{N}_1 \underline{\boldsymbol{\Psi}}_2 & (i = 0) \\ \boldsymbol{N}_i \boldsymbol{\Psi}_1 + \boldsymbol{N}_{i+1} \boldsymbol{\Psi}_2 & (i = 1, \cdots q-2) \\ \boldsymbol{N}_{q-1} \overline{\boldsymbol{\Psi}}_1 + \boldsymbol{N}_q \overline{\boldsymbol{\Psi}}_2 & (i = q-1). \end{cases}$$

Substituting (E.27), (E.28) and (E.70)-(E.73) to the above equation, and noting the horizontal periodic rule (E.18), we see that the above equation is equivalent to (E.53). □

E.7.2 Cylinder Node Locations

Figure E.10 shows a typical coordinate used for the cylindrical configuration. The horizontal strip of the cylinder represents the i^{th} row units, and the shaded area represents the (i,k) unit. To locate $\boldsymbol{n}_1(i,k)$, define the vectors $\boldsymbol{z}_1(i,k)$, $\boldsymbol{r}_1(i,k)$ and the angle $\theta_1(i,k)$ as shown in Fig. E.10. For $\boldsymbol{n}_2(i,k)$, define $\boldsymbol{z}_2(i,k)$, $\boldsymbol{r}_2(i,k)$ and $\theta_2(i,k)$ the same way. Then $\boldsymbol{n}_\ell(i,k)$ $(\ell = 1,2)$ is written by

$$\boldsymbol{n}_\ell(i,k) = \boldsymbol{z}_\ell(i,k) + \boldsymbol{r}_\ell(i,k), \tag{E.74}$$

where

$$\boldsymbol{z}_\ell(i,k) = \begin{bmatrix} 0 \\ 0 \\ z_\ell(i,k) \end{bmatrix}, \tag{E.75}$$

where $z_\ell(i,k) = |\boldsymbol{z}_\ell(i,k)|$. The vector $\boldsymbol{r}_\ell(i,k)$ will be a function of $z_\ell(i,k)$ and $\theta_\ell(i,k)$. If we assign the height and the angle equally to each unit, $z_\ell(i,k)$ and $\theta_\ell(i,k)$ are given by

$$z_\ell(i,k) = \{2i + (\ell - 1)\} \frac{L}{2q} \tag{E.76}$$

$$\theta_\ell(i,k) = \{2k + \ell\} \frac{\pi}{p}, \tag{E.77}$$

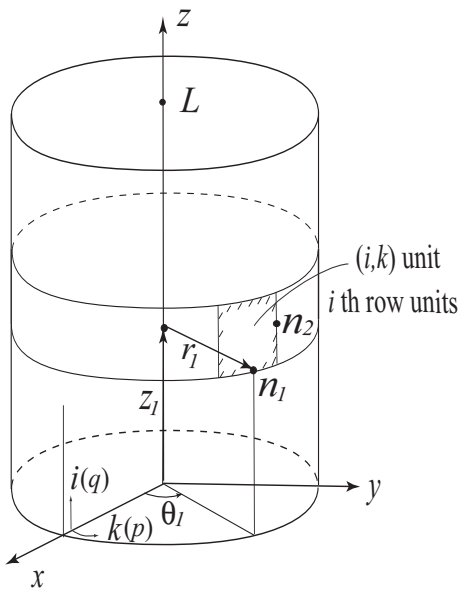

Figure E.10: Coordinate for cylinder

where L represents the length of the cylinder.

The radius $\boldsymbol{r}_\ell(i,k)$ specifies the shape of the cross-section varying along the axis of the cylinder. We can make many shapes by specifying $\boldsymbol{r}_\ell(i,k)$. Some typical shapes are given in the following corollaries.

If we choose the cross-section to be a circle with constant radius, the resulting structure forms a right circular cylinder shown in Fig. E.11 (a).

Corollary E.7.1. (Right Circular Cylinder) *Given the number of units p, q and the height L, locate the node $\boldsymbol{N}(i,k) = [\boldsymbol{n}_1(i,k)\ \boldsymbol{n}_2(i,k)]$ by (E.74)-(E.77) with*

$$\boldsymbol{r}_\ell(i,k) = \begin{bmatrix} r\cos\theta_\ell(i,k) \\ r\sin\theta_\ell(i,k) \\ 0 \end{bmatrix} \tag{E.78}$$

($\ell = 1,2$), where $r > 0$. Define the bars and the strings by (E.63)-(E.67) and (E.68)-(E.73) respectively. Then the resulting surface forms the right circular cylinder as shown in Fig. E.11 (a).

Figure E.12 shows a numerical example for the right circular cylinder with different complexity (p,q).

If we choose the cross-section to be an ellipse, the resulting structure forms a right elliptic cylinder shown in Fig. E.11 (b).

Corollary E.7.2. (Right Elliptic Cylinder) *Under the same assumption in Corollary E.7.1, set $\boldsymbol{r}_\ell(i,k)$ ($\ell = 1,2$) by*

$$\boldsymbol{r}_\ell(i,k) = \begin{bmatrix} a_r\cos\theta_\ell(i,k) \\ b_r\sin\theta_\ell(i,k) \\ 0 \end{bmatrix}, \tag{E.79}$$

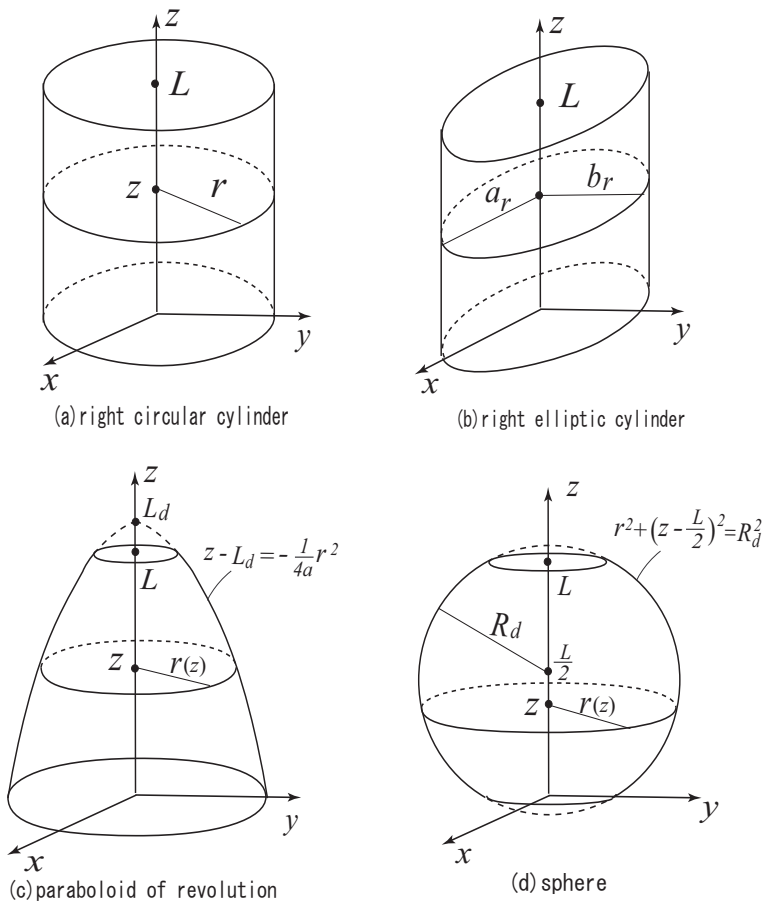

Figure E.11: Cylindrical-type structures

where $a_r > 0$, $b_r > 0$. Then the resulting surface forms the right elliptic cylinder as shown in Fig. E.11 (b).

We can make the cross-section vary along the axis of the cylinder. Typical examples are a paraboloid of revolution and a sphere shown Fig. E.11 (c) and (d).

Corollary E.7.3. (Paraboloid of Revolution) *Under the same assumption in Corollary E.7.1, set $\boldsymbol{r}_\ell(i,k)$ $(\ell = 1, 2)$ by*

$$\boldsymbol{r}_\ell(i,k) = \begin{bmatrix} r(z_\ell(i,k))\cos\theta_\ell(i,k) \\ r(z_\ell(i,k))\sin\theta_\ell(i,k) \\ 0 \end{bmatrix}, \tag{E.80}$$

where

$$r(z_\ell(i,k)) = \sqrt{4a\,(L_d - z_\ell(i,k))}, \tag{E.81}$$

where $a > 0$ and $L_d > L$ specify the focus and the height of the paraboloid of revolution. Then the resulting surface forms the paraboloid of revolution as shown in Fig. E.11 (c).

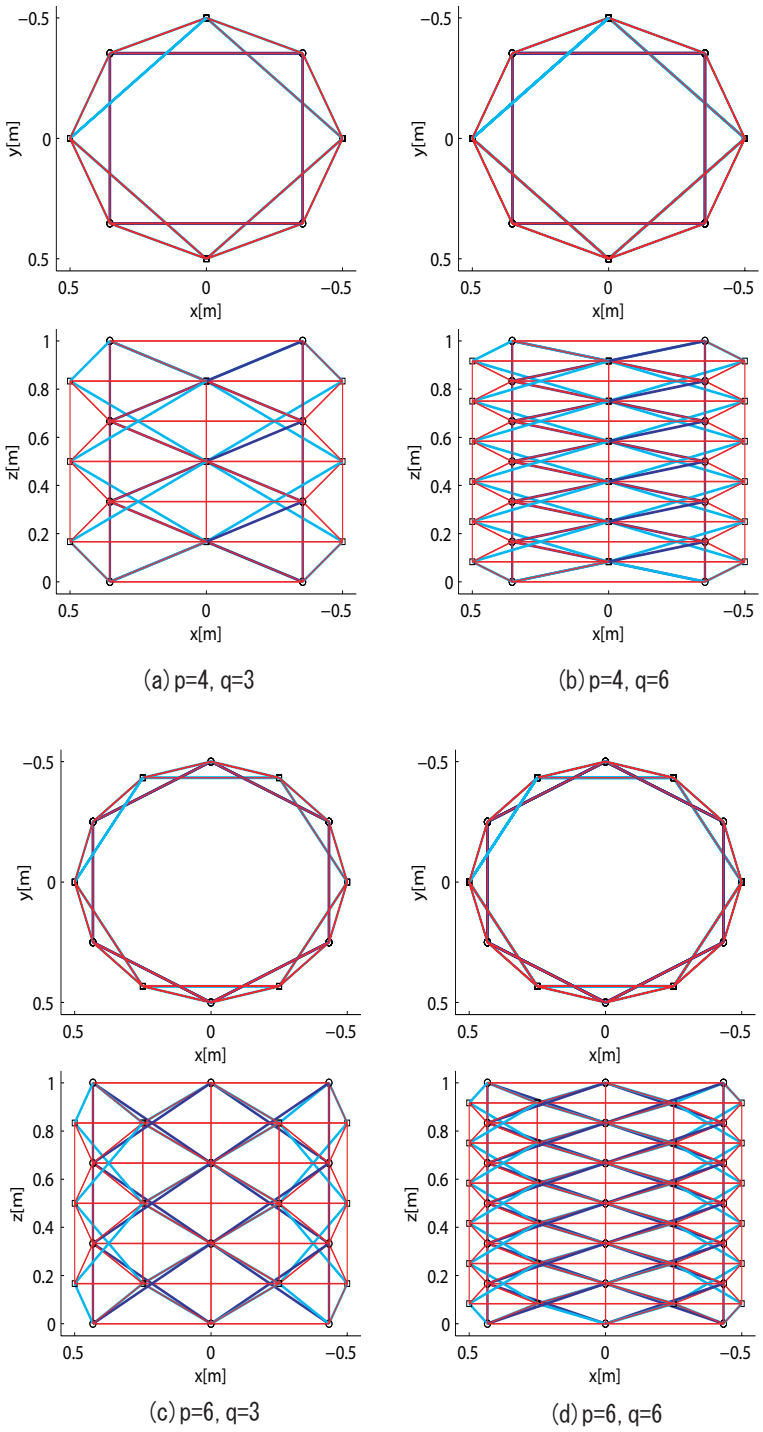

Figure E.12: Right circular cylinder with different complexity (p, q), $(L = 1,\ R = 0.5)$

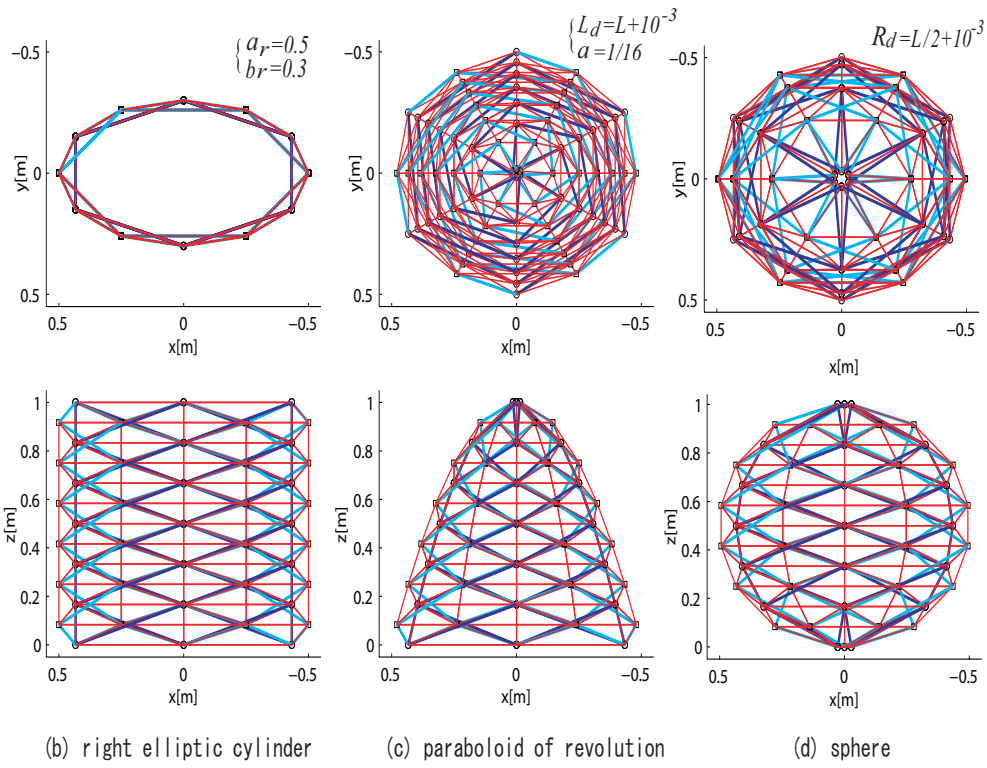

(b) right elliptic cylinder (c) paraboloid of revolution (d) sphere

Figure E.13: Cylindrical-type structures ($p = 6,\ q = 6$; $L = 1$[m])

Corollary E.7.4. (Sphere) *Under the same assumption in Corollary E.7.1, set* $\boldsymbol{r}_\ell(i,k)$ $(\ell = 1, 2)$ *by*

$$\boldsymbol{r}_\ell(i,k) = \begin{bmatrix} r(z_\ell(i,k))\cos\theta_\ell(i,k) \\ r(z_\ell(i,k))\sin\theta_\ell(i,k) \\ 0 \end{bmatrix}, \tag{E.82}$$

where

$$r(z_\ell(i,k)) = \sqrt{R_d^2 - \left(z_\ell(i,k) - \frac{L}{2}\right)^2}, \tag{E.83}$$

where $R_d > L/2$ *specifies the radius of the sphere. Then the resulting surface forms the sphere as shown in Fig. E.11 (d).*

Figure E.13 shows numerical examples of the cylindrical-type structures obtained from Corollaries E.7.2-E.7.4. We confirm that all the cylindrical-type structures in the above examples are stable from the stiffness analysis.

Remark 1. *In Corollaries E.7.3 and E.7.4, we exclude the limiting case* $L_d = L$ *or* $R_d = L/2$ *to avoid the top and the bottom nodes overlapping each other. We can also handle such cases by diminishing the overlapping nodes by introducing some variable transformation*

$$\overline{\boldsymbol{N}} = \widetilde{\boldsymbol{N}}\boldsymbol{T}.$$

If two of three nodes are overlapping, for example, the transformation will be $[\boldsymbol{n}_1\ \boldsymbol{n}_2\ \boldsymbol{n}_3] = [\boldsymbol{n}_1\ \boldsymbol{n}_2]\underbrace{\begin{bmatrix}1 & 0 & 0\\ 0 & 1 & 1\end{bmatrix}}_{\boldsymbol{T}}$. *The new connectivity matrices for this modification are given by*

$$\boldsymbol{B} = \widetilde{\boldsymbol{N}}\underbrace{\boldsymbol{T}\boldsymbol{C}_B^T}_{\widetilde{C}_B^T},\ \boldsymbol{S} = \widetilde{\boldsymbol{N}}\underbrace{\boldsymbol{T}\boldsymbol{C}_S^T}_{\widetilde{C}_S^T}.$$

Unnecessary bars and strings, such as the top and the bottom strings along the rim, can be removed by deleting the corresponding columns of the connectivity matrices.

E.8 Design Example

In this section, as an application of the connectivity matrix we derived, we consider a minimal mass design of a DHT cylinder subject to the equilibrium and yield stress constraints. The design problem can be described by a linear program with respect to the force densities λ_i, γ_i, Chapter 2 of [1].

E.8.1 Torsionally Loaded Cylinder

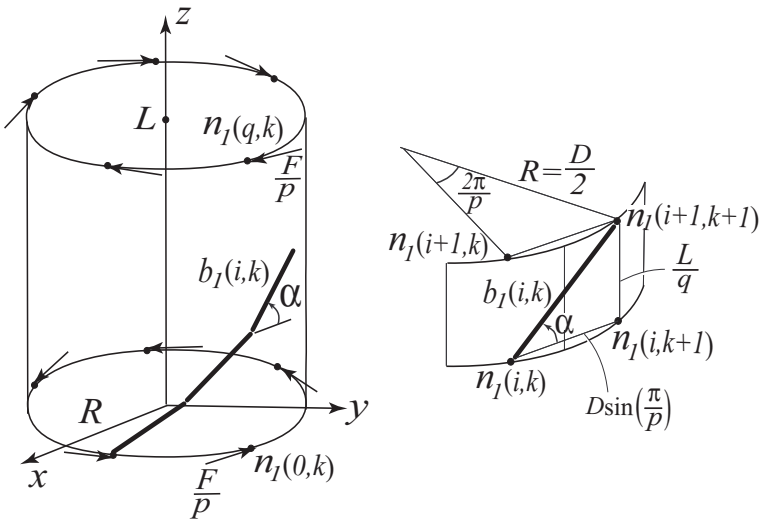

Figure E.14: Torsionally loaded cylinder

Consider a right circular cylinder formed by Corollary E.7.1, as shown in the left of Fig. E.14. The cylinder is torsionally loaded by the forces F/p, where $F = 1$ [N], along the circumference acting on the top and bottom nodes. We assume that all the bars and strings are composed of the same material.

We consider a minimal mass design problem subject to the equilibrium (force balance) and the yield stress constraints. Suppose the force densities λ_i and γ_i (member force divided by length) are positive. Then the yield stress constraint is given by

$$\lambda_i\|\boldsymbol{b}_i\| \le \sigma A_{b_i}, \quad \gamma_i\|\boldsymbol{s}_i\| \le \sigma A_{s_i}, \tag{E.84}$$

where σ is the yield stress, and A_{b_i} and A_{s_i} are cross-section areas of the bar and string. Mass of the bar and string is given by

$$m_{b_i} = \rho A_{b_i} \|\boldsymbol{b}_i\|, \quad m_{s_i} = \rho A_{s_i} \|\boldsymbol{s}_i\|, \tag{E.85}$$

where ρ is the mass density. From the minimal mass requirement, the members should be loaded at the yield stress, and the equalities of (E.84) hold. By eliminating A_{b_i} and A_{s_i} from the mass in (E.85), total mass of the structure is given by $m = \rho/\sigma J$, where

$$J = \sum_i \lambda_i \|\boldsymbol{b}_i\|^2 + \sum_i \gamma_i \|\boldsymbol{s}_i\|^2. \tag{E.86}$$

Recalling the equilibrium condition is given by (E.3), the minimal mass problem is described by

$$\min_{\lambda_i \geq 0,\ \gamma_i \geq 0} J \quad \text{subject to } (E.3). \tag{E.87}$$

From (E.87), (E.86) and (E.3), the optimization problem is a linear program with respect to λ_i, γ_i.

We can consider more realistic problems by modifying (E.87). We can consider a problem with a lower bound of the force density for robustness of the structure. We can also consider a design problem subject to the buckling constraint, and a design to sustain a variety of expected loads. However, these design issues are beyond the scope of this paper, and they will be addressed in our forthcoming papers.

In the next section, we will find the minimal mass solution calculated from (E.87) over the different complexities (p, q). Note that we can easily generate the cylinder for any (p, q) from a common computer program by using the results in the previous sections. Note also that the contour plot of J over (p, q) does not change its shape even if we choose different F because the problem is linear in F.

E.8.2 Optimization Result

Case of aspect ratio $L/D = 1$

We first consider a cylinder with $L = 1$ [m] and $D = 2R = 1$ [m] (aspect ratio $L/D = 1$). For each (p, q), we find the minimal mass structure by solving (E.87) by using the interior point method. Collecting the optimal normalized mass J for $q = 3, \cdots, 30$, $p = 2, \cdots, 10$, we have the contour plot of J shown in Fig. E.15. In the figure, we see a valley along diagonal direction. If we describe this valley by a function of (p, q), the line should be $p = 3q + 1$, shown by the dashed line. The solid line of Fig. E.16 shows the convergence of the minimal mass J along the line $p = 3q + 1$. We see rapid convergence of the mass along this line. A cylinder with the complexity $p = 7$, $q = 2$ is shown in Fig. E.17.

To get a physical insight for the above result, define the angle α between the bar $\boldsymbol{b}_1(i, k)$ and the horizontal plane as shown in the right of Fig. E.14. From the geometrical relationship, α is given by

$$\alpha = \tan^{-1}\left(\frac{L/q}{D\sin(\pi/p)}\right). \tag{E.88}$$

To see how the angle α changes with respect to (p, q), Fig. E.18 shows the contour plot of α over (p, q). We see that the line $p = 3q + 1$ almost coincides with the line for $\alpha = 45°$. If we increase

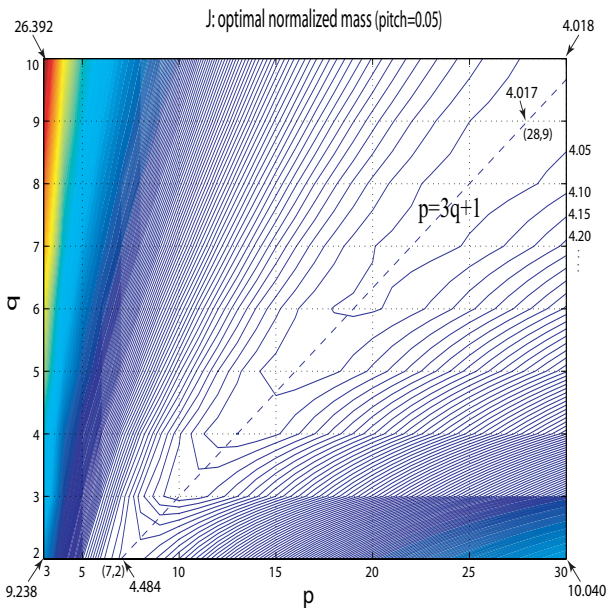

Figure E.15: Contour plot of optimal normalized mass J ($L/D = 1$)

(p, q) along this line, α approaches

$$\alpha \simeq \tan^{-1}\left(\frac{1}{\pi}\frac{L}{D}\frac{p}{q}\right)$$
$$\simeq \tan^{-1}\left(\frac{1}{\pi}\frac{3q+1}{q}\right) \simeq \tan^{-1}\left(\frac{3}{\pi}\right) \simeq 43.68^\circ.$$

Case of aspect ratio $L/D = 3$

To see dependence of the above results on the aspect ratio, we next examine the optimization for a cylinder with $L = 3$ [m] and $D = 1$ [m] ($L/D = 3$). The result is shown in Fig. E.19. From the figure, we see a valley along the different line $p = q$. To see this valley in view of α, Fig. E.20 shows the contour plot of α for $L/D = 3$. From the figure, we see that the valley in Fig. E.19 also occurs around the angle $\alpha = 45^\circ$.

From the above results, for the torsionally-loaded cylinder, we see that there are optimal relationships between the complexity in the two directions (circumferentially and vertically), namely, $p = 3q+1$ for $L/D = 1$; $p = q$ for $L/D = 3$, which come from the requirement for the angle between the bar and the horizontal plane to be around $\alpha = 45^\circ$.

E.8.3 The Impact of Manufacturing Tolerances

The above theory assumes frictionless ball-joint connections between connected bars. Furthermore we assume no lumped mass at the joints. In practice there may be some mass associated with the fabrication of a joint. If we assign some mass at each joint (node), the total mass $J+\mu n$ represented by dashed lines in Fig. E.16 has a minimum at finite (p, q), where $n = 2pq + p$ is the number of nodes (joints), and μ is the ratio of joint mass to member mass. (This number μ is dictated by the precision of the fabrication and assembly).

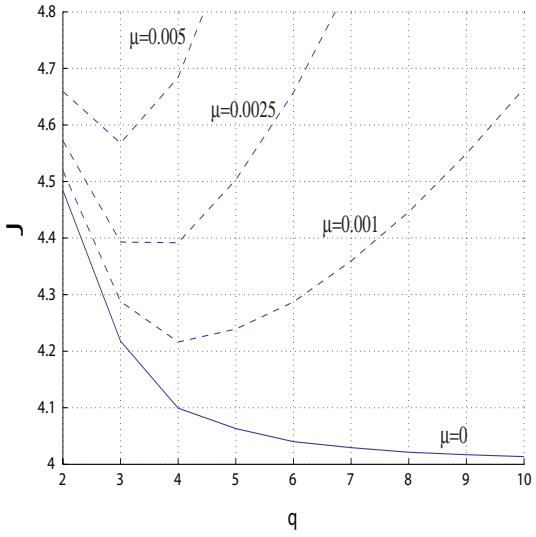

Figure E.16: Optimal mass along the valley $p = 3q + 1$

E.9 Conclusion

This paper describes a class of tensegrity systems produced from a choice of a common connectivity pattern (choice of material topology), which we call the DHT (Double Helix Tensegrity) topology. From the DHT material sheet, we can make final three-dimensional structures by specifying an enclosure rule and a node location. We first show the enclosure rule for the torus-type structures, and derive a common connectivity matrix for this type of structures. By choosing different node locations, we can form various shapes of the torus-type structures including the circular torus, elongated torus, elliptic torus, and finger ring. We next show the enclosure rule for the cylindrical-type structures, and derive a common connectivity matrix for this type of structures. Choices of the node location provide various shapes of the cylindrical-type structures including the right circular cylinder, right elliptic cylinder, paraboloid of revolution, and sphere. All the structures produced in the numerical examples are stable in the sense of positive definite stiffness matrix.

Other enclosure rules and node locations can be considered to form various types of structures. In addition, although we specifically consider the DHT type of the topology in this paper, we can easily add, delete, or exchange the members by modifying the connectivity matrix. With a choice of any number p, q of the DHT units, the connectivity matrix we derived can be used for a variety of analysis and design problems, including from-finding, optimal structure design, stiffness or stability analysis, and dynamic analysis.

As an application of the derived connectivity matrix, a minimal mass design problem for a torsionally loaded cylinder subject to the equilibrium and yield stress constraints is considered. Minimal mass calculation over the complexity (p, q), where p is the number of DHT units around the circumference and q is the number of units along the longitudinal axis, shows that there are optimal relationships, namely, $p = 3q + 1$ for the cylindrical aspect ratio $L/D = 1$; $p = q$ for $L/D = 3$, which come from the requirement for the angle α between the bars and the horizontal plane to be around $\alpha = 45°$. It is interesting to note that this result is reasonably consistent with the continuum results for a circular cylinder, where the angle of principal stress is 45° with respect to the cylinder axis.

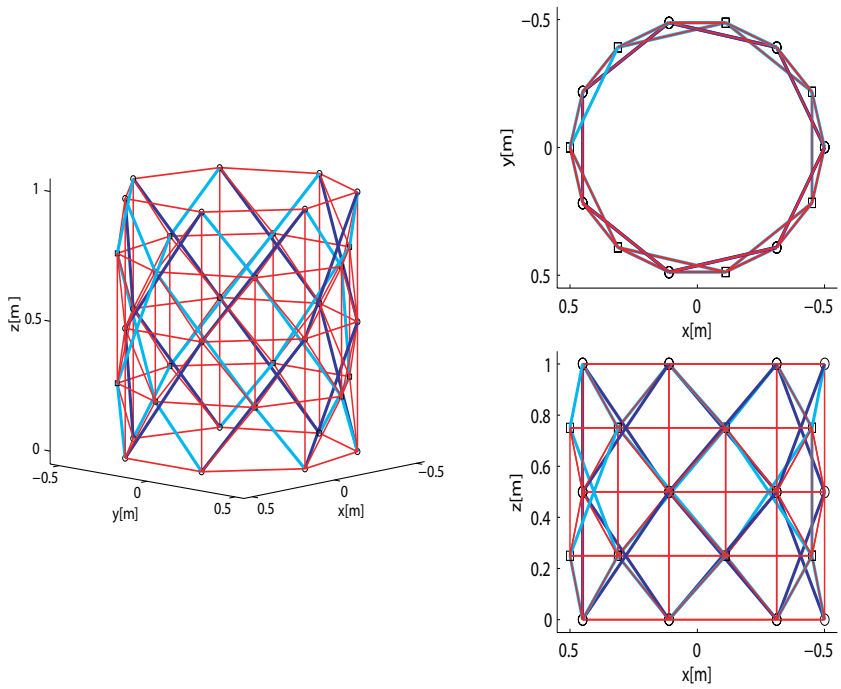

Figure E.17: Right circular cylinder with complexity $(p, q) = (7, 2)$

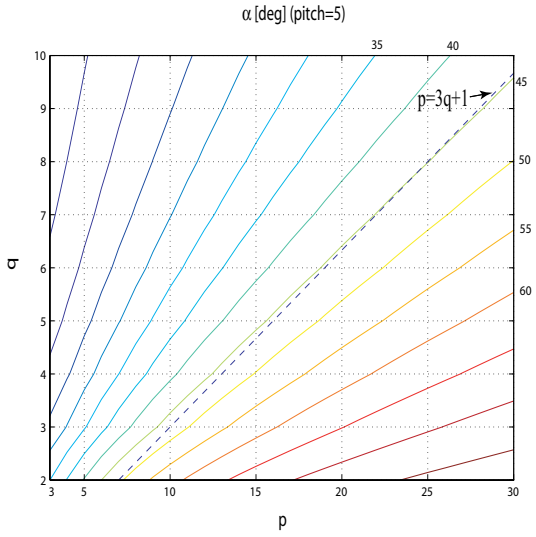

Figure E.18: Contour plot of angle of bar α [deg] $(L/D = 1)$

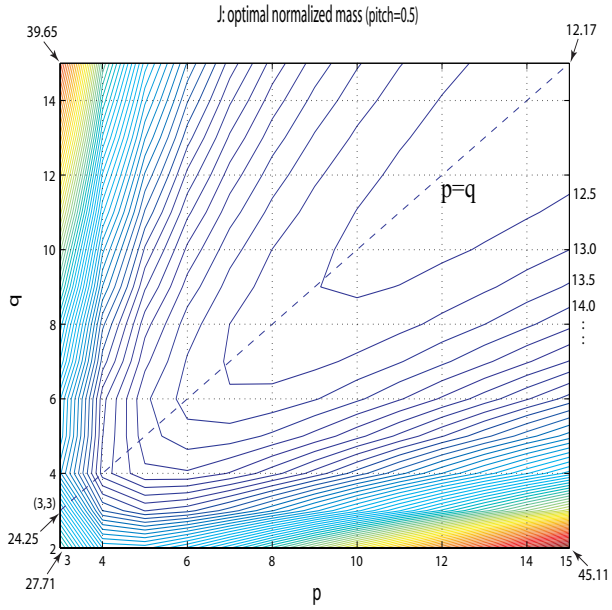

Figure E.19: Contour plot of optimal normalized mass J $(L/D = 3)$

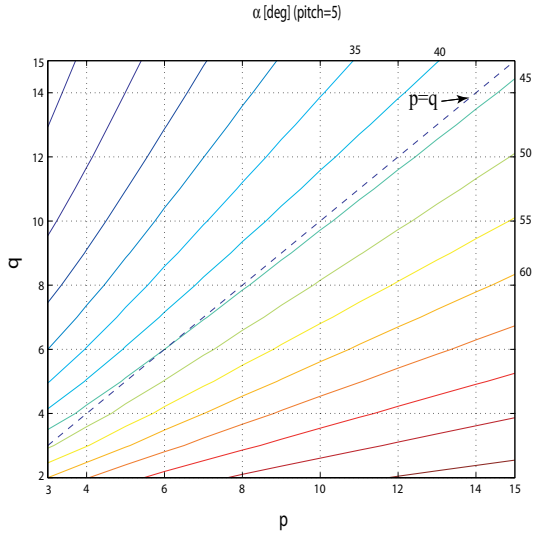

Figure E.20: Contour plot of angle of bar α [deg] $(L/D = 3)$

Appendix F

Minimal Mass Design of Tensegrity Structures

F.1 Abstract

This paper provides a unified framework for minimal mass design of tensegrity systems. For any given configuration and any given set of external forces, we design force density (member force divided by length) and cross-section area to minimize the structural mass subject to an equilibrium condition and a maximum stress constraint. The answer is provided by a linear program. Stability is assured by a positive definite stiffness matrix. This condition is described by a linear matrix inequality. Numerical examples are shown to illustrate the proposed method.

F.2 Introduction

The acronym *tensegrity* is a word coined by Buckminster Fuller [8, 9] to describe an artform created by Kenneth Snelson. Tensegrity structures are made up from axially-loaded members (bars and cables) by using frictionless ball joints. They can have very high stiffness/weight ratio, and can be easily deformable by stretching/shortening some of the members by pulleys or other kind of actuators. To design a tensegrity, one must determine the members (cables, bars), geometrical configuration, prestress pattern, and member thickness. A typical design process for tensegrity structures to determine the configuration and the prestress pattern is called form-finding [28, 29, 30, 31, 32]. Surveys on the form-finding method are found in [39, 40].

For any given configuration and any given set(s) of external forces, this paper provides a unified framework for minimal mass design of tensegrity systems of any class (class k allows k bars to touch at a node). We design force density (member force divided by length) and cross-section area to minimize the structural mass subject to an equilibrium condition and a maximum stress constraint. Self-weight or gravity force can be considered. The answer is provided by a linear program. Stability is assured by a positive definite stiffness matrix. This condition is described by a linear matrix inequality, hence the answer is provided by a convex optimization. Sometimes one must consider the behavior of the system under a variety of expected loads. This might cause a cable under tension in one load condition, while experiencing compression in another load condition. This paper also addresses a way to resolve this design issue. Numerical examples for box-type structures are shown to illustrate the proposed method.

F.3 Tensegrity Systems

F.3.1 Notation

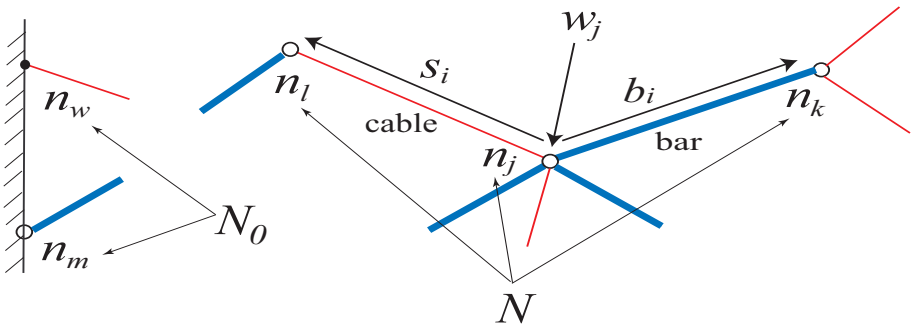

Figure F.1: Tensegrity system

Consider a network of compressible members (bars or struts) labeled by vectors $\boldsymbol{b}_i$, and tensile members (cables or strings) labeled by vectors $\boldsymbol{s}_i$, as shown in Fig. F.1. Each end of the members is connected to other members, with pins or frictionless ball joints, and the loads in all the members are directed axially.

Define a matrix $\boldsymbol{N}$ whose i^{th} column is a three-dimensional vector $\boldsymbol{n}_i \in \mathbb{R}^3$ locating the i^{th} node of the network ($\boldsymbol{N} = [\cdots, \boldsymbol{n}_i, \cdots]$). Define matrices $\boldsymbol{B}$ ($\boldsymbol{S}$) respectively such that the i^{th} columns are three-dimensional vectors $\boldsymbol{b}_i$ ($\boldsymbol{s}_i$) $\in \mathbb{R}^3$ that lie along the i^{th} bar (i^{th} cable) ($\boldsymbol{B} = [\cdots, \boldsymbol{b}_i, \cdots]$, $\boldsymbol{S} = [\cdots, \boldsymbol{s}_i, \cdots]$). Define a matrix $\boldsymbol{W}$ whose i^{th} column is an external force vector $\boldsymbol{w}_i \in \mathbb{R}^3$ acting on the node $\boldsymbol{n}_i$.

F.3.2 Equilibria of Tensegrity Systems

Define the (i, j) element of a matrix $\boldsymbol{C}_B$ to be:

$$[\boldsymbol{C}_B]_{ij} = \begin{cases} -1, & \text{if } \boldsymbol{b}_i \text{ is directed away from the node } \boldsymbol{n}_j \\ 1, & \text{if } \boldsymbol{b}_i \text{ is directed toward } \boldsymbol{n}_j \\ 0, & \text{if } \boldsymbol{b}_i \text{ does not touch } \boldsymbol{n}_j, \end{cases} \tag{F.1}$$

where $\boldsymbol{b}_i$ is the bar vector. Matrix $\boldsymbol{C}_S$ is constructed the same way from the cable vector $\boldsymbol{s}_i$. The bar and cable matrices $\boldsymbol{B}$, $\boldsymbol{S}$ are related to the node matrix $\boldsymbol{N}$ by these connectivity matrices $\boldsymbol{C}_B$, $\boldsymbol{C}_S$ as

$$\boldsymbol{B} = \boldsymbol{N}\boldsymbol{C}_B^T, \quad \boldsymbol{S} = \boldsymbol{N}\boldsymbol{C}_S^T. \tag{F.2}$$

All tensegrity equilibria satisfy [1]

$$\boldsymbol{S}\widehat{\boldsymbol{\gamma}}\boldsymbol{C}_S - \boldsymbol{B}\widehat{\boldsymbol{\lambda}}\boldsymbol{C}_B = \boldsymbol{W}, \tag{F.3}$$

where $\widehat{\boldsymbol{\gamma}}$ ($\widehat{\boldsymbol{\lambda}}$) are diagonal matrices, where $[\widehat{\boldsymbol{\gamma}}]_{ii} = \gamma_i$ is the force density [46] (member force divided by length) in the cable $\boldsymbol{s}_i$, and $[\widehat{\boldsymbol{\lambda}}]_{ii} = \lambda_i$ is the force density in the bar $\boldsymbol{b}_i$. The signs of the force densities λ_i (γ_i) are selected to be positive when they are compressed (stretched) respectively. Note that member forces in a bar and a cable are described by $\boldsymbol{t}_{b_i} = \lambda_i \boldsymbol{b}_i$ and $\boldsymbol{t}_{s_i} = \gamma_i \boldsymbol{s}_i$.

In the following analysis, we choose, without loss of generality, the node matrix to have a form $[\boldsymbol{N}\ \boldsymbol{N}_0]$, where $\boldsymbol{N}_0$ contains the nodes fixed in an inertial space by boundary conditions, and $\boldsymbol{N}$ contains all other nodes. The external force matrix is ordered $[\boldsymbol{W}\ \boldsymbol{W}_0]$ accordingly, where $\boldsymbol{W}$ and $\boldsymbol{W}_0$ are the external forces acting on $\boldsymbol{N}$ and $\boldsymbol{N}_0$. The force $\boldsymbol{W}_0$ is the reaction force from the wall or other boundaries. Partitioning the connectivity matrices according to this expression, (F.2) becomes

$$\boldsymbol{B} = [\boldsymbol{N}\ \boldsymbol{N}_0]\begin{bmatrix}\boldsymbol{C}_B^T \\ \boldsymbol{C}_{B_0}^T\end{bmatrix}, \quad \boldsymbol{S} = [\boldsymbol{N}\ \boldsymbol{N}_0]\begin{bmatrix}\boldsymbol{C}_S^T \\ \boldsymbol{C}_{S_0}^T\end{bmatrix}. \tag{F.4}$$

Numbers of the nodes in $\boldsymbol{N}$ and $\boldsymbol{N}_0$ are represented by n and n_0, and the numbers of the bars and cables are represented by n_b and n_s.

Using the expression above, the equilibrium condition (F.3) is decomposed into two components as

$$\boldsymbol{S}\widehat{\boldsymbol{\gamma}}\boldsymbol{C}_S - \boldsymbol{B}\widehat{\boldsymbol{\lambda}}\boldsymbol{C}_B = \boldsymbol{W} \tag{F.5}$$

$$\boldsymbol{S}\widehat{\boldsymbol{\gamma}}\boldsymbol{C}_{S_0} - \boldsymbol{B}\widehat{\boldsymbol{\lambda}}\boldsymbol{C}_{B_0} = \boldsymbol{W}_0. \tag{F.6}$$

Suppose the system is at an equilibrium. Then for a given external force $\boldsymbol{W}$, the force densities $\widehat{\boldsymbol{\lambda}}$, $\widehat{\boldsymbol{\gamma}}$ are given by solving (F.5). Note that (F.6) then provides the force $\boldsymbol{W}_0$ exerted by the fixed boundary of the tensegrity structure, for any given $\widehat{\boldsymbol{\lambda}}$, $\widehat{\boldsymbol{\gamma}}$, satisfying (F.5).

Because the number of the force densities $(n_s + n_b)$ are usually greater than the number of the nodes (n), the solution of (F.5) might not be unique and will have some freedom. Using this freedom, we can choose the force densities to minimize the total mass, subject to the equilibrium condition.

F.3.3 Vector Forms and Functions

The matrix form expression (F.2) can be converted to a vector form by using the Kronecker product [48] as

$$\boldsymbol{b} = \big(\boldsymbol{C}_B \otimes \boldsymbol{I}_3\big)\boldsymbol{n} \quad \boldsymbol{s} = \big(\boldsymbol{C}_S \otimes \boldsymbol{I}_3\big)\boldsymbol{n}, \tag{F.7}$$

where $\boldsymbol{b} = [\boldsymbol{b}_1^T\ \cdots\ \boldsymbol{b}_{n_b}^T]^T$, $\boldsymbol{s} = [\boldsymbol{s}_1^T\ \cdots\ \boldsymbol{s}_{n_s}^T]^T$ and $\boldsymbol{n} = [\boldsymbol{n}_1^T\ \cdots\ \boldsymbol{n}_n^T]^T$. Similarly, we will use a capital letter for a matrix form expression, and use a small letter for a vector form expression $(\boldsymbol{V} = [\boldsymbol{v}_1\ \cdots \boldsymbol{v}_n] \leftrightarrow \boldsymbol{v} = [\boldsymbol{v}_1^T\ \cdots \boldsymbol{v}_n^T]^T)$.

For a vector function $\boldsymbol{f}(\boldsymbol{x}) \in \mathbb{R}^m$ of a vector $\boldsymbol{x} \in \mathbb{R}^n$, the partial derivative $(\partial \boldsymbol{f}/\partial \boldsymbol{x})$ is a $m \times n$ matrix, whose elements are $[\partial \boldsymbol{f}/\partial \boldsymbol{x}]_{ij} = (\partial f_i/\partial x_j)$. If f is a scalar function, $(\partial f/\partial \boldsymbol{x})$ is a row vector. It follows that

$$\frac{\partial x}{\partial \boldsymbol{x}} = \frac{\boldsymbol{x}^T}{x}, \quad \frac{\partial}{\partial \boldsymbol{x}}\left(\frac{1}{x}\right) = -\frac{\boldsymbol{x}^T}{x^3}, \tag{F.8}$$

where $x = \|\boldsymbol{x}\|$. The functions $\mathrm{diag}(\cdot)$ and $\mathrm{b.d.}(\cdot)$ respectively represent a diagonal and a block diagonal matrix of the specified elements.

F.4 Mass of Members

Let A_{b_i}, A_{s_i} be the cross-section areas of a bar and a cable. Mass of the members are given by

$$m_b = \sum_{i=1}^{n_b} \rho_{b_i} A_{b_i} b_i, \quad m_s = \sum_{i=1}^{n_s} \rho_{s_i} A_{s_i} s_i, \tag{F.9}$$

where $b_i = \|\boldsymbol{b}_i\|$ and $s_i = \|\boldsymbol{s}_i\|$ are length of the members, and ρ_{b_i} and ρ_{s_i} are the mass densities.

Our design interest here is to determine A_{b_i}, A_{s_i} so as to avoid material failure (yielding or buckling) under the minimal mass requirement.

F.4.1 Member Force

As described in the previous section, the member force vectors $\boldsymbol{t}_{b_i}$, $\boldsymbol{t}_{s_i}$ are represented by the force densities λ_i, γ_i as

$$\boldsymbol{t}_{b_i} = \lambda_i \boldsymbol{b}_i, \quad \boldsymbol{t}_{s_i} = \gamma_i \boldsymbol{s}_i. \tag{F.10}$$

If the materials are Hookean, the force densities are represented by [1]

$$\lambda_i = -k_{b_i}\left(1 - \frac{L_{b_i}}{b_i}\right), \quad \gamma_i = k_{s_i}\left(1 - \frac{L_{s_i}}{s_i}\right), \tag{F.11}$$

where L_{b_i}, L_{s_i} are the rest length. The sign of (F.11) is selected so that the force densities λ_i, γ_i are positive when the bar and the cable are compressed and stretched respectively. From material properties, the spring constants k_{b_i}, k_{s_i} are given by

$$k_{b_i} = \frac{E_{b_i} A_{b_i}}{L_{b_i}}, \quad k_{s_i} = \frac{E_{s_i} A_{s_i}}{L_{s_i}}, \tag{F.12}$$

where E_{b_i}, E_{s_i} are the Young's modulus.

F.4.2 Stress Constraint

To avoid material failure, the cross-section area should be related to the member force. In the following, we assume $\gamma_i \geq 0$, $\lambda_i \geq 0$.

To avoid yielding, the member forces $t_{b_i} = \|\boldsymbol{t}_{b_i}\|$, $t_{s_i} = \|\boldsymbol{t}_{s_i}\|$ should satisfy $t_{b_i} \leq \sigma_{b_i}^Y A_{b_i}$ and $t_{s_i} \leq \sigma_{s_i}^Y A_{s_i}$,where $\sigma_{b_i}^Y$ and $\sigma_{s_i}^Y$ are the yield stress. To generalize this, we consider affine-type maximum stress constraints

$$t_{b_i} = \lambda_i\, b_i \leq \sigma_{b_i} A_{b_i} + \tau_{b_i}, \quad t_{s_i} = \gamma_i\, s_i \leq \sigma_{s_i} A_{s_i} + \tau_{s_i}, \tag{F.13}$$

where σ_{b_i}, σ_{s_i} and τ_{b_i}, τ_{s_i} are constants determined from the material properties. For yielding, we set $\sigma_{b_i} = \sigma_{b_i}^Y$, $\tau_{b_i} = 0$ and $\sigma_{s_i} = \sigma_{s_i}^Y$, $\tau_{s_i} = 0$. For buckling of bar, (F.13) can be an affine approximation of the buckling constraint as described in Appendix F.11. By A_{b_i} and A_{s_i} satisfying (F.13), total mass m is given by the sum of (F.9).

If the members are stressed at the maximum stress, we have, from (F.13),

$$A_{b_i} = \frac{\lambda_i\, b_i}{\sigma_{b_i}} - \frac{\tau_{b_i}}{\sigma_{b_i}}, \quad A_{s_i} = \frac{\gamma_i\, s_i}{\sigma_{s_i}} - \frac{\tau_{s_i}}{\sigma_{s_i}}. \tag{F.14}$$

Substituting (F.14) to (F.9), we have

$$m_b = \sum_{i=1}^{n_b} c_{b_i}\lambda_i + e_{b_i}, \quad m_s = \sum_{i=1}^{n_s} c_{s_i}\gamma_i + e_{s_i}, \tag{F.15}$$

where $c_{b_i} = \rho_{b_i} b_i^2/\sigma_{b_i}$, $c_{s_i} = \rho_{s_i} s_i^2/\sigma_{s_i}$, and $e_{b_i} = -\rho_{b_i}\tau_{b_i} b_i/\sigma_{b_i}$, $e_{s_i} = -\rho_{s_i}\tau_{s_i} s_i/\sigma_{s_i}$.

F.5 External Force

In order to consider self-weight, or gravity force, we divide the external force, into two parts: the gravity force $\boldsymbol{W}_g$ and all other external forces $\boldsymbol{W}_e$. Hence,

$$\boldsymbol{W} = \boldsymbol{W}_e + \boldsymbol{W}_g. \tag{F.16}$$

The gravity force can be modeled by lumped forces equally distributed on the member nodes. The gravity forces of $\boldsymbol{b}_i$ and $\boldsymbol{s}_i$ on the member nodes are represented by $\boldsymbol{f}_{g_{b_i}} = m_{b_i}\boldsymbol{g}/2$ and $\boldsymbol{f}_{g_{s_i}} = m_{s_i}\boldsymbol{g}/2$.

Let $\boldsymbol{n}_j$, $\boldsymbol{n}_k$ be the member nodes of $\boldsymbol{b}_i$ ($\boldsymbol{s}_i$). Recall that the elements of $\boldsymbol{C}_B$ are $[\boldsymbol{C}_B]_{ij} = \pm 1$ if $\boldsymbol{b}_i$ touches the node $\boldsymbol{n}_j$, or $[\boldsymbol{C}_B]_{ij} = 0$ otherwise. Denote $\boldsymbol{C}_B = \boldsymbol{C}_B(1,-1)$ and $\boldsymbol{C}_S = \boldsymbol{C}_S(1,-1)$ to indicate the sign of the non-zero elements. Then we have

$$\boldsymbol{W}_g = [\cdots \boldsymbol{w}_{g_j} \cdots] = \left[\cdots \boldsymbol{f}_{g_{b_i}} \cdots\right]\boldsymbol{C}_B(1,1) + \left[\cdots \boldsymbol{f}_{g_{s_i}} \cdots\right]\boldsymbol{C}_S(1,1), \tag{F.17}$$

where

$$\boldsymbol{f}_{g_{b_i}} = \frac{1}{2}\rho_{b_i} b_i A_{b_i}\boldsymbol{g},\ \ \boldsymbol{f}_{g_{s_i}} = \frac{1}{2}\rho_{s_i} s_i A_{s_i}\boldsymbol{g}, \tag{F.18}$$

and $\boldsymbol{C}_B(1,1)$, $\boldsymbol{C}_S(1,1)$ are the connectivity matrices whose all -1 entries are replaced by 1.

If the equality of (F.13) holds, (F.18) is replaced by

$$\boldsymbol{f}_{g_{b_i}} = \frac{1}{2}(c_{b_i}\lambda_i + e_{b_i})\boldsymbol{g},\ \ \boldsymbol{f}_{g_{s_i}} = \frac{1}{2}(c_{s_i}\gamma_i + e_{s_i})\boldsymbol{g} \tag{F.19}$$

from (F.15).

F.6 Minimal Mass Design

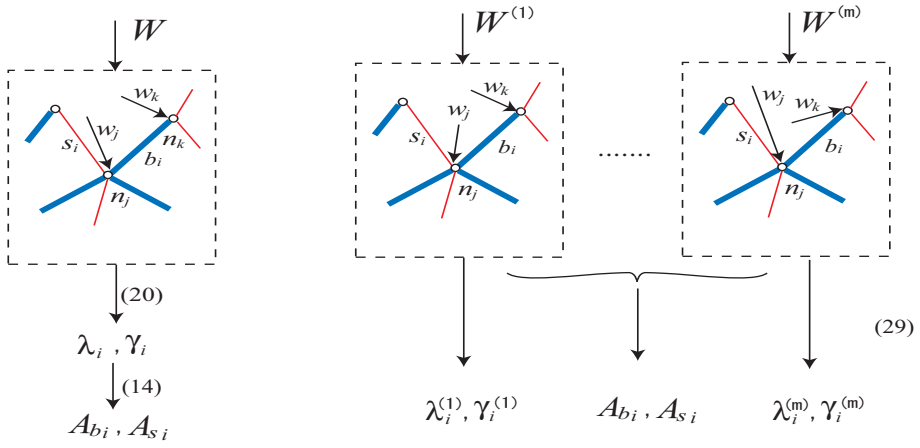

(a) Single External Force (b) Multiple External Forces

Figure F.2: Minimal mass design problems

For minimum mass design, we consider two situations shown in Fig. F.2 (a) and (b).

F.6.1 Minimal Mass Design for Single External Force

If the system is operated under one set of external forces $\boldsymbol{W}$ as shown in Fig. F.2 (a), we can always choose the cross-section area to satisfy the equality of (F.13) to minimize the mass. In this case, we can use (F.15).

From the results in the preceding sections, the minimal mass design problem can be described as follows.

Theorem F.6.1. *Consider a tensegrity system described by (F.4)-(F.6). Suppose the system is at an equilibrium in the given configuration $\boldsymbol{N}$ with an external force $\boldsymbol{W}$. The minimal mass structure under the maximum stress constraint (F.13) is given by a linear program*

$$\begin{aligned} \underset{\boldsymbol{x}}{\text{minimize}} \quad & \overline{m} = \boldsymbol{c}^T \boldsymbol{x} \\ \text{subject to} \quad & \begin{cases} \boldsymbol{A}\boldsymbol{x} = \boldsymbol{w} \\ \boldsymbol{x} \geq \boldsymbol{x}_0 \end{cases}, \end{aligned} \tag{F.20}$$

where

$$\boldsymbol{x} = [\lambda_1 \cdots \lambda_{n_b} \mid \gamma_1 \cdots \gamma_{n_s}]^T \tag{F.21}$$

$$\boldsymbol{c}^T = \begin{bmatrix} c_{b_1} \cdots c_{b_{n_b}} \mid c_{s_1} \cdots c_{s_{n_s}} \end{bmatrix} \tag{F.22}$$

$$\boldsymbol{A} = \begin{bmatrix} -(\boldsymbol{C}_B^T \otimes \boldsymbol{I}_3)\widehat{\boldsymbol{B}} & (\boldsymbol{C}_S^T \otimes \boldsymbol{I}_3)\widehat{\boldsymbol{S}} \end{bmatrix}, \tag{F.23}$$

where $c_{b_i} = \rho_{b_i} b_i^2/\sigma_{b_i}$, $c_{s_i} = \rho_{s_i} s_i^2/\sigma_{s_i}$, $\widehat{\boldsymbol{B}} = \text{b.d.}(\boldsymbol{b}_1, \cdots, \boldsymbol{b}_{n_b})$, $\widehat{\boldsymbol{S}} = \text{b.d.}(\boldsymbol{s}_1, \cdots, \boldsymbol{s}_{n_s})$, and $\boldsymbol{x}_0 \geq \boldsymbol{0}$ is a constant vector. Cross-section area of each member is given by (F.14), and the total mass m is given by the sum of (F.9).

If $\boldsymbol{W}$ is composed of the gravity force $\boldsymbol{W}_g$ and the forces $\boldsymbol{W}_e$ other than $\boldsymbol{W}_g$, then $\boldsymbol{w}$ in (F.20) is replaced by

$$\boldsymbol{w} = \boldsymbol{w}_e + \boldsymbol{w}_g. \tag{F.24}$$

The gravity force vector $\boldsymbol{w}_g$ is given by

$$\boldsymbol{w}_g = \boldsymbol{G}_x \boldsymbol{x} + \boldsymbol{w}_{g_0}, \tag{F.25}$$

where

$$\boldsymbol{G}_x = \begin{bmatrix} (\boldsymbol{C}_B^T(1,1) \otimes \boldsymbol{I}_3)\widehat{\boldsymbol{G}}_\lambda & (\boldsymbol{C}_S^T(1,1) \otimes \boldsymbol{I}_3)\widehat{\boldsymbol{G}}_\gamma \end{bmatrix} \tag{F.26}$$

$$\widehat{\boldsymbol{G}}_\lambda = \text{b.d.}\left(\frac{c_{b_1}}{2}\boldsymbol{g}, \cdots, \frac{c_{b_{n_b}}}{2}\boldsymbol{g}\right), \quad \widehat{\boldsymbol{G}}_\gamma = \text{b.d.}\left(\frac{c_{s_1}}{2}\boldsymbol{g}, \cdots, \frac{c_{s_{n_s}}}{2}\boldsymbol{g}\right) \tag{F.27}$$

$$\boldsymbol{w}_{g_0} = (\boldsymbol{C}_B(1,1)^T \otimes \boldsymbol{I}_3)\boldsymbol{g}_b + (\boldsymbol{C}_S(1,1)^T \otimes \boldsymbol{I}_3)\boldsymbol{g}_s, \tag{F.28}$$

where $\boldsymbol{C}_B(1,1)$, $\boldsymbol{C}_S(1,1)$ are the connectivity matrices whose all -1 entries are replaced by 1, and $\boldsymbol{g}_b = [(e_{b_1}\boldsymbol{g}/2)^T \cdots (e_{b_{n_b}}\boldsymbol{g}/2)^T]^T$, $\boldsymbol{g}_s = [(e_{s_1}\boldsymbol{g}/2)^T \cdots (e_{s_{n_s}}\boldsymbol{g}/2)^T]^T$, where $e_{b_i} = -\rho_{b_i}\tau_{b_i} b_i/\sigma_{b_i}$, $e_{s_i} = -\rho_{s_i}\tau_{s_i} s_i/\sigma_{s_i}$.

The first equality of the constraints in (F.20) and (F.25) respectively are rewritings of (F.5) and (F.17) with (F.19), by the Kronecker product. The vector $\boldsymbol{x}_0$ is used to specify a desired lower bound of the force density.

F.6.2 Minimal mass design for multiple external forces

Consider the case where the system is operated over multiple sets of external forces $\boldsymbol{W}^{(j)}$ $(j = 1, \cdots, m)$ as shown in Fig. F.2 (b). We can design the system in the following two ways. When any cable (bar) becomes a bar (cable) at any of the design forces, we can use a bi-directional element described in Section F.7.

Design using optimization for single external force

One simple design approach for the multiple external forces case is simply to solve the optimization problem (F.20) for each force and merge the results. The process is described as follows:

(i) Solve (F.20) for each $\boldsymbol{W}^{(j)}$, and determine $A_{b_i}^{(j)}$, $A_{s_i}^{(j)}$ by (F.14).

(ii) Choose the maximum cross-section area of each member to sustain all the forces, i.e., $A_{b_i} = \max(A_{b_i}^{(1)}, \cdots, A_{b_i}^{(m)})$, $A_{s_i} = \max(A_{s_i}^{(1)}, \cdots, A_{s_i}^{(m)})$.

Direct optimization for multiple forces

In some cases, the single force optimization design described above may produce overestimated members. We can make the cross section areas A_{b_i}, A_{s_i} as the optimization variables, and can find the minimum values over $\boldsymbol{W}^{(j)}$ directly. The minimal mass design problem for multiple sets of external forces can be described as follows.

Theorem F.6.2. *Consider a tensegrity system described by (F.4)-(F.6). Suppose the system in configuration $\boldsymbol{N}$ has an equilibrium for each external force $\boldsymbol{W}^{(j)}$ $(j = 1, \cdots, m)$. Minimal mass structure under the maximum stress constraint (F.13) is given by a linear program,*

$$\begin{aligned} &\underset{\boldsymbol{x}^{(j)}, \boldsymbol{y}}{\text{minimize}} \quad m = \boldsymbol{d}^T \boldsymbol{y} \\ &\text{subject to} \quad \begin{cases} \boldsymbol{A}\boldsymbol{x}^{(j)} = \boldsymbol{w}^{(j)} \\ \boldsymbol{C}\boldsymbol{x}^{(j)} \le \boldsymbol{D}\boldsymbol{y} + \boldsymbol{E} \\ \boldsymbol{x}^{(j)} \ge \boldsymbol{x}_0^{(j)}, \boldsymbol{y} \ge \boldsymbol{y}_0 \end{cases}, \end{aligned} \tag{F.29}$$

where $\boldsymbol{A}$ is defined by (F.23), and where

$$\boldsymbol{x}^{(j)} = [\lambda_1^{(j)} \ \cdots \ \lambda_{n_b}^{(j)} \mid \gamma_1^{(j)} \ \cdots \ \gamma_{n_s}^{(j)}]^T \tag{F.30}$$

$$\boldsymbol{y} = [A_{b_1} \ \cdots \ A_{b_{n_b}} \mid A_{s_1} \ \cdots \ A_{s_{n_s}}]^T \tag{F.31}$$

$$\boldsymbol{d}^T = [\rho_{b_i} b_i \ \cdots \rho_{b_{n_b}} b_{n_b} \mid \rho_{s_i} s_i \ \cdots \rho_{s_{n_s}} s_{n_s}] \tag{F.32}$$

$$\boldsymbol{C} = \begin{bmatrix} \mathrm{diag}(b_1, \cdots, b_{n_b}) & \boldsymbol{0} \\ \boldsymbol{0} & \mathrm{diag}(s_1, \cdots, s_{n_s}) \end{bmatrix} \tag{F.33}$$

$$\boldsymbol{D} = \begin{bmatrix} \mathrm{diag}(\sigma_{b_1}, \cdots, \sigma_{b_{n_b}}) & \boldsymbol{0} \\ \boldsymbol{0} & \mathrm{diag}(\sigma_{s_1}, \cdots, \sigma_{s_{n_s}}) \end{bmatrix}, \tag{F.34}$$

$$\boldsymbol{E} = \begin{bmatrix} \mathrm{diag}(\tau_{b_1}, \cdots, \tau_{b_{n_b}}) & \boldsymbol{0} \\ \boldsymbol{0} & \mathrm{diag}(\tau_{s_1}, \cdots, \tau_{s_{n_s}}) \end{bmatrix}, \tag{F.35}$$

and $\boldsymbol{x}_0^{(j)} \ge \boldsymbol{0}$, $\boldsymbol{y}_0 \ge \boldsymbol{0}$ are some constant vectors.

If $\boldsymbol{W}^{(j)}$ is composed of the gravity force $\boldsymbol{W}_g$ and the forces $\boldsymbol{W}_e^{(j)}$ other than $\boldsymbol{W}_g$, then $\boldsymbol{w}^{(j)}$ in (F.29) is replaced by

$$\boldsymbol{w}^{(j)} = \boldsymbol{w}_e^{(j)} + \boldsymbol{w}_g. \tag{F.36}$$

The gravity force vector $\boldsymbol{w}_g$ is given by

$$\boldsymbol{w}_g = \boldsymbol{G}_y \boldsymbol{y}, \tag{F.37}$$

where

$$\boldsymbol{G}_y = \begin{bmatrix} \left(\boldsymbol{C}_B^T(1,1) \otimes \boldsymbol{I}_3\right)\widehat{\boldsymbol{G}}_{A_b} & \left(\boldsymbol{C}_S^T(1,1) \otimes \boldsymbol{I}_3\right)\widehat{\boldsymbol{G}}_{A_s} \end{bmatrix} \tag{F.38}$$

$$\widehat{\boldsymbol{G}}_{A_b} = \text{b.d.}\left(\frac{\rho_{b_1} b_1}{2}\boldsymbol{g}, \cdots, \frac{\rho_{b_{n_b}} b_{n_b}}{2}\boldsymbol{g}\right), \ \widehat{\boldsymbol{G}}_{A_s} = \text{b.d.}\left(\frac{\rho_{s_1} s_1}{2}\boldsymbol{g}, \cdots, \frac{\rho_{s_{n_s}} s_{n_s}}{2}\boldsymbol{g}\right). \tag{F.39}$$

The second inequality of the constraints in (F.29) is equivalent to the maximum stress constraints (F.13), and (F.37) is a rewriting of (F.17) with (F.18).

F.7 Bi-directional Element

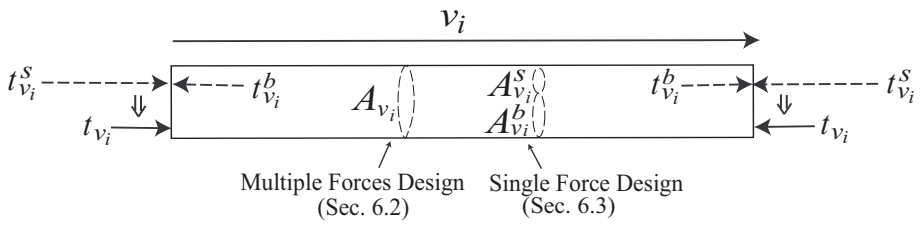

Figure F.3: Bi-directional element

In some cases, we might need a member which can produce compressive forces for some external loads, and tensile forces for other external loads. In addition, there might be some members that we do not know in a priori whether they are compressed or stretched. We can handle this generality by introducing a member whose member force is described by the sum of compressive and tensile forces.

F.7.1 Member force

Consider a member $\boldsymbol{v}_i$ whose member force is defined by the sum of compressive and tensile member forces

$$\boldsymbol{t}^b_{v_i} = \lambda_{v_i}\boldsymbol{v}_i, \quad \boldsymbol{t}^s_{v_i} = \gamma_{v_i}\boldsymbol{v}_i, \tag{F.40}$$

where $\lambda_{v_i} \geq 0$, $\gamma_{v_i} \geq 0$ (see Fig. F.3). Total member force

$$\boldsymbol{t}_{v_i} = \boldsymbol{t}^s_{v_i} - \boldsymbol{t}^b_{v_i} = \alpha_{v_i}\boldsymbol{v}_i, \tag{F.41}$$

where $\alpha_{v_i} = \gamma_{v_i} - \lambda_{v_i}$, is tensile if $\alpha_{v_i} > 0$, and compressive if $\alpha_{v_i} < 0$. Because the member forces in (F.40) have the same structure as those in (F.10), they can be readily embedded in the force balance equation (F.3).

Note that there are infinitely many choices of $\lambda_{v_i}, \gamma_{v_i}$ to produce a given (or required) α_{v_i}, however, the minimum solution for $\alpha_{v_i} = \gamma_{v_i} - \lambda_{v_i}$ is given by taking either λ_{v_i} or γ_{v_i} to be zero, i.e.

$$(\lambda_{v_i}, \gamma_{v_i}) = \begin{cases} (-\alpha_{v_i}, 0) & (\alpha_{v_i} < 0) \\ (0, \alpha_{v_i}) & (\alpha_{v_i} \geq 0) \end{cases} . \tag{F.42}$$

Mass and the maximum stress constraint of the member $\boldsymbol{v}_i$ are defined separately depending on the minimal mass problems (single or multiple external force(s)).

F.7.2 Mass for Multiple External Forces Design

For the optimization problem (F.29), consider the maximum stress constraints

$$\lambda_{v_i}\, v_i \leq \sigma^b_{v_i} A_{v_i} + \tau^b_{v_i}, \quad \gamma_{v_i}\, v_i \leq \sigma^s_{v_i} A_{v_i} + \tau^s_{v_i}, \tag{F.43}$$

where A_{v_i} is the cross-section area of the member $\boldsymbol{v}_i$, and $\sigma^b_{v_i}$, $\sigma^s_{v_i}$ and $\tau^s_{v_i}$, $\tau^b_{v_i}$ are some constants determined from the maximum stress requirement. Note that we use the same cross section area A_{v_i} for both the compressive and tensile forces constraints, as shown in Fig. F.3. Using this A_{v_i}, the mass is defined by

$$m_{v_i} = \rho_{v_i} A_{v_i} v_i, \tag{F.44}$$

where ρ_{v_i} is the mass density and $v_i = \|\boldsymbol{v}_i\|$.

The mass (F.44), the force balance equation (F.3) with (F.40) embedded, and the maximum stress constraints (F.43) can be readily implemented in the optimization problem (F.29). Note that either λ_{v_i} or γ_{v_i} is zero when the mass is minimized.

F.7.3 Mass for Single External Force Design

For the optimization problem (F.20), consider assigning both a bar and a cable at the same location $\boldsymbol{v}_i$ as shown in Fig. F.3. The maximum stress constraints are given by

$$\lambda_{v_i}\, v_i \leq \sigma^b_{v_i} A^b_{v_i} + \tau^b_{v_i}, \quad \gamma_{v_i}\, v_i \leq \sigma^s_{v_i} A^s_{v_i} + \tau^s_{v_i}, \tag{F.45}$$

where $A^b_{v_i}$ and $A^s_{v_i}$ are the cross-section areas of the bar and the cable, and $\sigma^b_{v_i}$, $\sigma^s_{v_i}$ and $\tau^b_{v_i}$, $\tau^s_{v_i}$ are some constants determined from the maximum stress requirement. Cross-section areas are minimum when the equality of (F.45) holds, i.e.,

$$A^b_{v_i} = \frac{\lambda_{v_i}\, v_i}{\sigma^b_{v_i}} - \frac{\tau^b_{b_i}}{\sigma^b_{v_i}}, \quad A^s_{v_i} = \frac{\gamma_{v_i}\, v_i}{\sigma^s_{v_i}} - \frac{\tau^s_{s_i}}{\sigma^s_{s_i}} \tag{F.46}$$

(For this purpose, we assign different cross section areas for the compressive and tensile forces constraints in (F.45)). The mass of $\boldsymbol{v}_i$ is given by the sum of the bar and cable masses

$$m^b_{v_i} = c^b_{v_i} \lambda_{v_i} + e^b_{v_i}, \quad m^s_{v_i} = c^s_{v_i} \gamma_{v_i} + e^s_{v_i}, \tag{F.47}$$

where $c^b_{v_i} = \rho_{v_i} v_i^2 / \sigma^b_{v_i}$, $c^s_{v_i} = \rho_{v_i} v_i^2 / \sigma^s_{v_i}$ and $e^b_{v_i} = -\rho_{v_i} \tau^b_{v_i} v_i / \sigma^b_{v_i}$, $e^s_{v_i} = -\rho_{v_i} \tau^s_{v_i} v_i / \sigma^s_{v_i}$, where ρ_{v_i} is the mass density.

The mass (F.47) and the force balance equation (F.3) with (F.40) embedded can be readily implemented in the optimization problem (F.20). When the mass is minimized, either λ_{v_i} or γ_{v_i} is zero, and thus only a bar or a cable is necessary at $\boldsymbol{v}_i$

F.8 Stiffness

In this section, we derive an explicit expression of the stiffness matrix by the force density and cross section area. We show that the positive definite condition of the stiffness matrix is represented by a linear matrix inequality.

In the following, we assume that the system is at an equilibrium, and all the bars and cables are loaded i.e., $b_i < L_{b_i}$ and $s_i > L_{s_i}$.

F.8.1 Stiffness Matrix for Multiple External Force Design

Suppose the system is at an equilibrium $\boldsymbol{n}_i$, $\boldsymbol{b}_i$, $\boldsymbol{s}_i$ for some external force $\boldsymbol{w}_i$. From (F.10) and (F.11), note that (F.5) is described as

$$\begin{bmatrix} \cdots & \boldsymbol{t}_{s_i}(\boldsymbol{s}_i) & \cdots \end{bmatrix}\boldsymbol{C}_S - \begin{bmatrix} \cdots & \boldsymbol{t}_{b_i}(\boldsymbol{b}_i) & \cdots \end{bmatrix}\boldsymbol{C}_B = \boldsymbol{W}. \tag{F.48}$$

Consider a small variation around the equilibrium, $\boldsymbol{n}_i + d\boldsymbol{n}_i$, $\boldsymbol{b}_i + d\boldsymbol{b}_i$, $\boldsymbol{s}_i + d\boldsymbol{s}_i$, and $\boldsymbol{w}_i + d\boldsymbol{w}_i$. Substitute these variations to (F.48), apply the Taylor expansion, and ignore the higher order terms. Then from Appendix F.12, we have

$$\boldsymbol{K}_n d\boldsymbol{n} = d\boldsymbol{w}, \tag{F.49}$$

where $d\boldsymbol{n} = [d\boldsymbol{n}_1^T, \cdots, d\boldsymbol{n}_n^T]^T$, $d\boldsymbol{w} = [d\boldsymbol{w}_1^T, \cdots, d\boldsymbol{w}_n^T]^T$, and

$$\begin{aligned}\boldsymbol{K}_n =& \big(\boldsymbol{C}_S^T \otimes \boldsymbol{I}_3\big)\text{b.d.}(\boldsymbol{K}_{s_1}, \cdots, \boldsymbol{K}_{s_{n_s}})\big(\boldsymbol{C}_S \otimes \boldsymbol{I}_3\big) \\ &- \big(\boldsymbol{C}_B^T \otimes \boldsymbol{I}_3\big)\text{b.d.}(\boldsymbol{K}_{b_1}, \cdots, \boldsymbol{K}_{b_{n_b}})\big(\boldsymbol{C}_B \otimes \boldsymbol{I}_3\big),\end{aligned} \tag{F.50}$$

where

$$\boldsymbol{K}_{b_i} = \lambda_i \boldsymbol{I}_3 - \frac{E_{b_i} A_{b_i}}{b_i^3}\boldsymbol{b}_i\boldsymbol{b}_i^T, \quad \boldsymbol{K}_{s_i} = \gamma_i \boldsymbol{I}_3 + \frac{E_{s_i} A_{s_i}}{s_i^3}\boldsymbol{s}_i\boldsymbol{s}_i^T. \tag{F.51}$$

From (F.50) and (F.51), the stiffness matrix $\boldsymbol{K}_n$ is symmetric, and it is a linear function of λ_i, γ_i and A_{b_i}, A_{s_i}.

F.8.2 Stiffness matrix for single external force design

For the optimization problem (F.20), we can use (F.14) to eliminate A_{b_i}, A_{s_i} from (F.51). In such case, $\boldsymbol{K}_{b_i}$ and $\boldsymbol{K}_{s_i}$ are given by

$$\boldsymbol{K}_{b_i} = \lambda_i \left(\boldsymbol{I}_3 - \frac{E_{b_i}}{\sigma_{b_i} b_i^2}\boldsymbol{b}_i\boldsymbol{b}_i^T\right) + \boldsymbol{K}_{b_i}^0, \quad \boldsymbol{K}_{s_i} = \gamma_i \left(\boldsymbol{I}_3 + \frac{E_{s_i}}{\sigma_{s_i} s_i^2}\boldsymbol{s}_i\boldsymbol{s}_i^T\right) - \boldsymbol{K}_{s_i}^0, \tag{F.52}$$

where $\boldsymbol{K}_{b_i}^0 = E_{b_i}\tau_{b_i}/(\sigma_{b_i} b_i^3)\boldsymbol{b}_i\boldsymbol{b}_i^T$ and $\boldsymbol{K}_{s_i}^0 = E_{s_i}\tau_{s_i}/(\sigma_{s_i} s_i^3)\boldsymbol{s}_i\boldsymbol{s}_i^T$.

F.8.3 Stability

If the work done by the force $d\boldsymbol{w}_i$ for any displacement $d\boldsymbol{n}_i$ is positive, i.e., $d\boldsymbol{w}_i^T d\boldsymbol{n}_i > 0$, the node i is stable at the equilibrium. We can extend this observation to all nodes. From (F.49), the total work $d\boldsymbol{w}^T d\boldsymbol{n}$ is positive for any $d\boldsymbol{n}$ iff $\boldsymbol{K}_n$ is positive definite, i.e., $\boldsymbol{K}_n \succ 0$. Hence the system is stable at the equilibrium if

$$\boldsymbol{K}_n \succ \varepsilon \boldsymbol{I}, \tag{F.53}$$

Table F.1: Material Properties (Steel)

yield stress [N/m^2]	$\sigma = 6.9 \times 10^8$
Young's modulus [N/m^2]	$E = 2.06 \times 10^{11}$
mass density [kg/m^3]	$\rho = 7.86 \times 10^3$

where $\varepsilon \geq 0$.

From (F.50) with (F.51) or (F.52), (F.53) is a linear matrix inequality. Hence even if we add the stiffness constraint (F.53) on the optimization problem (F.20) or (F.29), the problem is still convex [49, 50].

F.9 Design Example

F.9.1 2D box in free space (multiple external forces design)

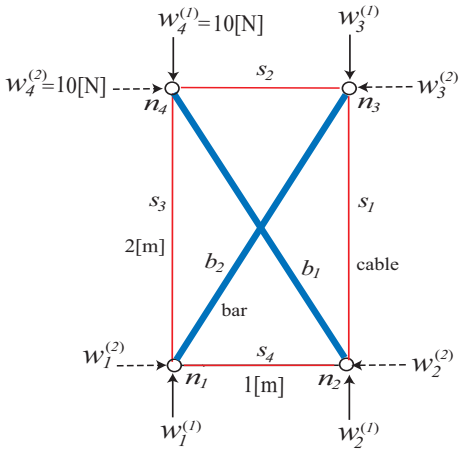

Figure F.4: 2D box structure

Consider a planar box structure [1] shown in Fig. F.4. The box has 2 diagonal bars and 4 surrounding cables. To illustrate the design for multiple sets of external forces, two sets of the external forces are considered, where $\boldsymbol{w}_i^{(1)}$ are vertical external forces and $\boldsymbol{w}_i^{(2)}$ are horizontal external forces.

To determine the total mass and the cross-section areas, the optimization problem (F.29) is solved by using the interior-point method. We assume that the bars and cables are made of steel in Table F.1 [1], and the yield stress is chosen as the maximum stress constraint for both the bar and cable ($\sigma_{b_i} = \sigma_{s_i} = \sigma$).

Optimized force densities and cross-section areas are shown in Fig. F.5 (a). From the force densities, we see that the horizontal cables support the vertical force, and the vertical cables support the horizontal force (see Fig. F.5 (b)). Note that the cross-section areas are determined to minimize the total mass over two types of external forces. Total mass is $m = 2.16 \times 10^{-3}$ [Kg].

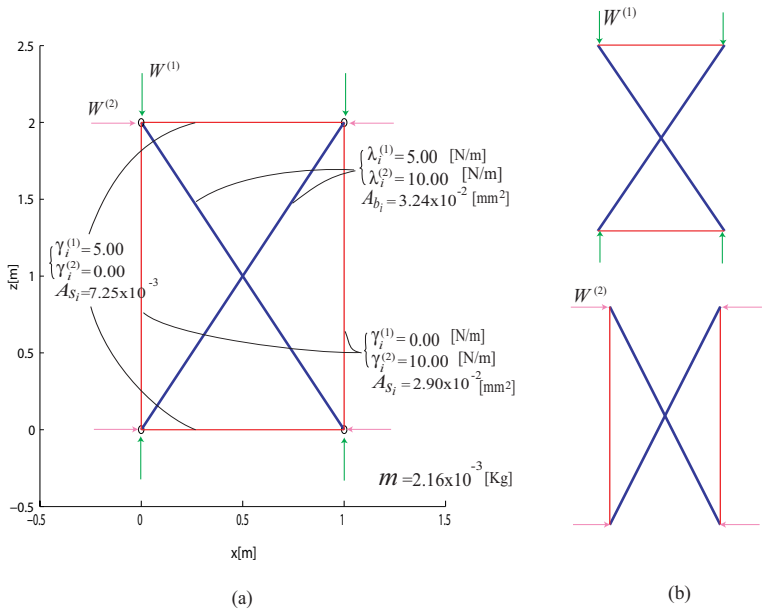

Figure F.5: Optimized 2D box structure

F.9.2 3D Box Fixed on the Ground

Consider making a 3D box by using the 2D box for each side. After merging vertical cables on each edge, we have a 3D box structure shown in Fig. F.6. The box has 8 diagonal bars and 8 horizontal and 4 vertical cables. The bottom 4 nodes are pinned on the ground ($\boldsymbol{N}_0 = [\boldsymbol{n}_1\ \boldsymbol{n}_2\ \boldsymbol{n}_5\ \boldsymbol{n}_6]$), and external forces downward vertically are acting on the top 4 nodes. For the optimization, (F.20) is solved. Material properties are shown in Table F.1.

Optimized force densities are shown in Fig. F.7 (a). (Some values are omitted because of symmetry.) From the result, the bottom and vertical cables seem to be unnecessary. In fact, we can remove these cables, and the result is shown in Fig. F.7 (b).

Total mass and the cross-section area (from (F.14)) are given by

$$\begin{aligned} m &= 1.25 \times 10^{-3}\ [\mathrm{Kg}] \\ A_{b_i} &= 8.10 \times 10^{-3} [\mathrm{mm}^2] \quad (r_{b_i} = 5.08 \times 10^{-2}\ [\mathrm{mm}]) \\ A_{s_i} &= 3.62 \times 10^{-3} [\mathrm{mm}^2] \quad (r_{s_i} = 3.40 \times 10^{-2} [\mathrm{mm}]). \end{aligned}$$

The stiffness constraint $\boldsymbol{K}_n \succ 0$ evaluated by (F.50) is satisfied, and thus the system is stable at the equilibrium.

F.10 Conclusion

The focus of this paper is to find ways to use less and less material to solve a structural design problem. For any given configuration and any given set of external forces, a minimal mass design of tensegrity structures subject to the equilibrium condition and the maximum stress constraint is provided. The method is applied to all tensegrity of any class (class k allows k bars to touch at their ends through frictionless ball joints). The method incorporates the buckling constraints as well as the yield constraints, and the gravity force can be considered. For both the single

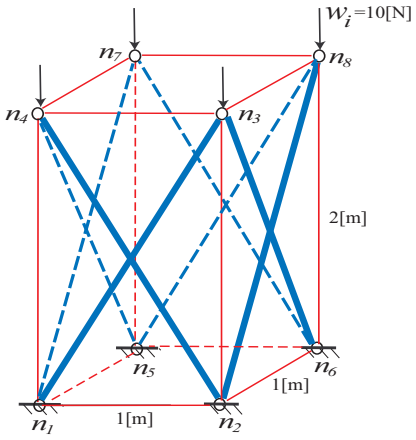

Figure F.6: 3D box structure

set and the multiple sets of external forces, the answer is provided by a linear program. Bi-directional elements can be used for the minimal mass designs where: direction of a member force (compression/tension) changes over different load conditions; and we do not know in a priori whether a member is compressed or stretched. This paper also provides formulas for the stiffness matrix. The stiffness matrix is linear in the design variables (force density, cross-section area), hence the stability is assured by adding a linear matrix inequality. Numerical examples for box-type structures are conducted to illustrate the proposed method.

F.11 Appendix: Maximum Stress Constraint of Bar

According to Euler, buckling stress of a solid bar (pinned-pinned boundary condition) is given by [1]

$$\sigma_{b_i}^B = \frac{\pi^2 E_{b_i}}{4}\left(\frac{r_{b_i}}{b_i}\right)^2 = \beta_i A_{b_i}, \tag{F.54}$$

where r_{b_i} is the radius of the bar and $\beta_i = \pi E_{b_i}/4b_i^2$. Substituting (F.54) to $t_{b_i} \le \sigma_{b_i}^B A_{b_i}$, the maximum stress constraint is given by

$$t_{b_i} = \lambda_i\, b_i \le \beta_i A_{b_i}^2, \tag{F.55}$$

which is a quadratic function of A_{b_i}. On the other hand, the yielding stress constraint is given by

$$t_{b_i} \le \sigma_{b_i}^Y A_{b_i}, \tag{F.56}$$

where $\sigma_{b_i}^Y$ is the yielding stress. The actual maximum stress constraint of the bar is given by the intersection of (F.55) and (F.56), as illustrated by the shaded area in Fig. F.8. This is obviously not a convex optimization problem, but one way to handle this constraint is to solve a convex problem, and iterate with linear updates of the nonlinear constraint space. This approach is described as follows.

Suppose we have some calculation of the member force $\bar{t}_{b_i}$, estimated from a given external force condition. Then we can choose σ_{b_i}, τ_{b_i} in (F.13) to approximate (F.55) or (F.56). From the

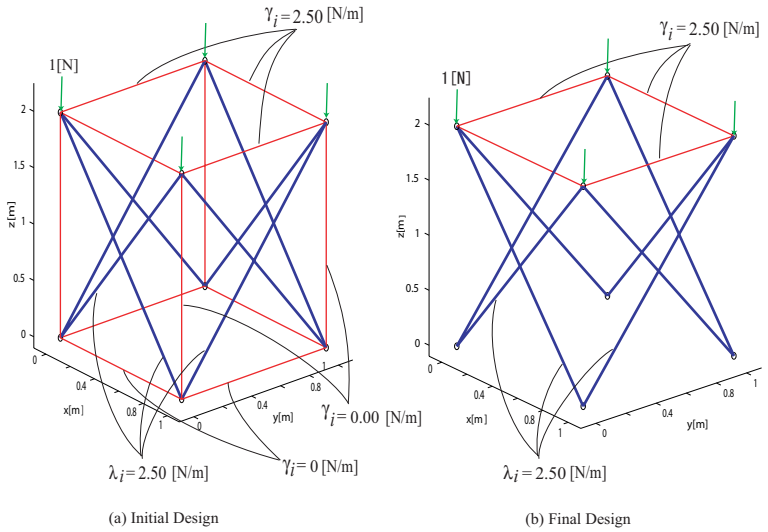

(a) Initial Design (b) Final Design

Figure F.7: Optimized 3D box structure

member force $t_{b_i} = \lambda_i b_i$ obtained from the optimization problem, the cross-section area A_{b_i} is given by

$$A_{b_i} = \begin{cases} \sqrt{t_{b_i}/\beta_i} & (t_{b_i} \le t^*_{b_i}) \\ t_{b_i}/\sigma^Y_{b_i} & (t_{b_i} > t^*_{b_i}) \end{cases}, \tag{F.57}$$

where $t^*_{b_i} = (\sigma^Y_{b_i})^2/\beta_i$ is the intersection of the line and the parabola, and the mass is given by (F.9). The above process is illustrated in Fig. F.8. If the bar is made of steel in Table F.1, $t^*_{b_i} = 2.9 \times 10^6 b_i^2$ [N].

We can iterate the above process by updating the initial guess $\bar{t}_{b_i}$ by the optimization result $\lambda_i b_i$. Similar treatment can be applied to thin wall pipes [1]

F.12 Appendix: Derivation of Stiffness Matrix

Substituting the variations $\boldsymbol{b}_i + d\boldsymbol{b}_i$, $\boldsymbol{s}_i + d\boldsymbol{s}_i$, $\boldsymbol{w}_i + d\boldsymbol{w}_i$ to (F.48), applying the Taylor expansion, and ignoring the higher order terms, we have

$$[\ \cdots\ \boldsymbol{K}_{s_i} d\boldsymbol{s}_i\ \cdots\ ]\,\boldsymbol{C}_S - [\ \cdots\ \boldsymbol{K}_{b_i} d\boldsymbol{b}_i\ \cdots\ ]\,\boldsymbol{C}_B = d\boldsymbol{W}, \tag{F.58}$$

where

$$\boldsymbol{K}_{b_i} = \frac{\partial \boldsymbol{t}_{b_i}}{\partial \boldsymbol{b}_i}, \quad \boldsymbol{K}_{s_i} = \frac{\partial \boldsymbol{t}_{s_i}}{\partial \boldsymbol{s}_i}. \tag{F.59}$$

From (F.4) and the fact that $\boldsymbol{N}_0$ is a constant vector, we have

$$d\boldsymbol{b} = \big(\boldsymbol{C}_B \otimes \boldsymbol{I}_3\big) d\boldsymbol{n}, \quad d\boldsymbol{s} = \big(\boldsymbol{C}_S \otimes \boldsymbol{I}_3\big) d\boldsymbol{n}. \tag{F.60}$$

By using the Kronecker product, (F.58) becomes (F.49) with (F.50).

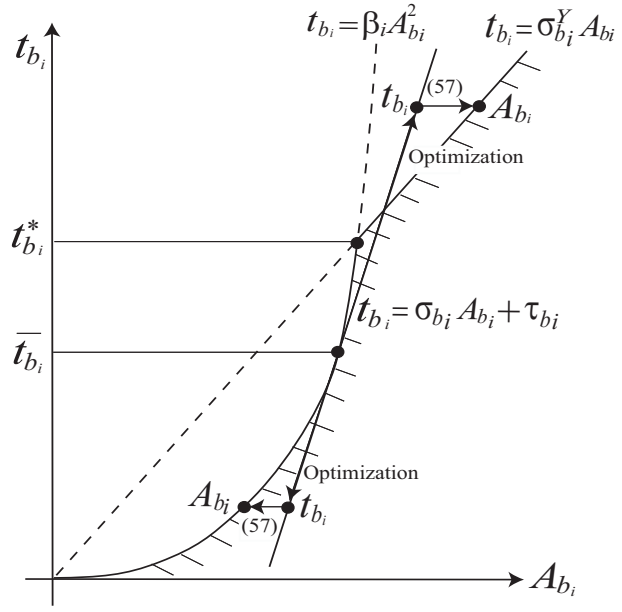

Figure F.8: Approximation of buckling constraint

Equivalence of (F.59) and (F.51) can be shown as follows. From (F.10) and (F.11), (F.59) becomes

$$\begin{aligned}\boldsymbol{K}_{b_i} &= \boldsymbol{b}_i \frac{\partial \lambda_i}{\partial \boldsymbol{b}_i} + \lambda_i \boldsymbol{I}_3 = \boldsymbol{b}_i \left(-k_{b_i} L_{b_i} \frac{\boldsymbol{b}_i^T}{b_i^3} \right) + \lambda_i \boldsymbol{I}_3 \\ &= -k_{b_i} \boldsymbol{I}_3 + \frac{k_{b_i} L_{b_i}}{b_i} \left(\boldsymbol{I}_3 - \frac{\boldsymbol{b}_i \boldsymbol{b}_i^T}{b_i^2} \right) \qquad \text{(F.61)} \\ \boldsymbol{K}_{s_i} &= k_{s_i} \boldsymbol{I}_3 - \frac{k_{s_i} L_{s_i}}{s_i} \left(\boldsymbol{I}_3 - \frac{\boldsymbol{s}_i \boldsymbol{s}_i^T}{s_i^2} \right). \qquad \text{(F.62)}\end{aligned}$$

From (F.12) and (F.11), note that

$$k_{b_i} L_{b_i} = E_{b_i} A_{b_i}, \quad k_{s_i} L_{s_i} = E_{s_i} A_{s_i} \qquad \text{(F.63)}$$

$$k_{b_i} = \frac{E_{b_i} A_{b_i}}{b_i} - \lambda_i, \quad k_{s_i} = \frac{E_{s_i} A_{s_i}}{s_i} + \gamma_i. \qquad \text{(F.64)}$$

Substituting (F.63), (F.64) to (F.61), (F.62), we get (F.51).

Appendix G

Network and Vector Forms of Tensegrity System Dynamics

G.1 Abstract

We write the equations of motion in vector form for any class k tensegrity system dynamics. The network approach yields a connectivity matrix and nodal matrix, providing the dynamics of any network of bars, pipes and cables. The class 1 (bars do not connect) dynamics are described together with a constraint added to allow bar to bar connections. The Lagrange multiplier is eliminated to yield a compact set of vector equations.

G.2 Introduction

G.2.1 Background

Tensegrity structures are mechanical trusses composed of compressive members (bars, struts, pipes) and tensile members (strings, tendons, cables). It is well known that the connectivity matrix plays a central role in static (equilibria) analysis. Typical application of the connectivity matrix is the form finding [30, 31, 32] and the minimal mass design [51, 1].

Tensegrity structure dynamics research was pioneered by Motro et al. [52]. Kanchanasaratool et al. [53] studied dynamic particle models with unitary point masses at the nodes. Sultan [54] and Sultan et al. [36] used Lagrange formulation for a class of tensegrity systems. Murakami [34] also used Lagragian formulation to model the dynamic behavior of a tensegrity structure taking into account the non-linear elasticity of the members. From a Newtonian formulation, Skelton et al. [55] derived a simple dynamic model of bars (rods), without using the conventional angular velocities for rigid bodies, by introducing non-minimal coordinates. The non-minimal matrix and network approach started with Skelton [56] for class 1 (bars do not contact) tensegrity systems using a compact matrix form representation. A survey on the tensegrity dynamics research can be found in [57].

Prior work in tensegrity dynamics [56, 1] writes non-minimal matrix equations from a network approach, but only class 1 tensegrity is treated, and the larger than necessary coordinates can causes numerical problems in simulations, without additional treatment of roundoff errors. Here we offer a vector form of the dynamics for any tensegrity system.

G.2.2 Tensegrity Systems

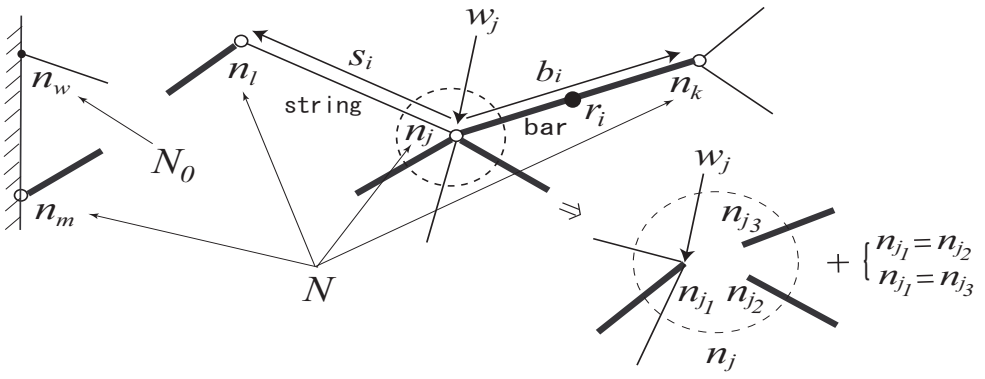

Figure G.1: Tensegrity system

A typical tensegrity structure is shown in Fig. G.1. Vectors along the i^{th} bar and string are labeled $\boldsymbol{b}_i$ and $\boldsymbol{s}_i$ respectively. Elements are connected at the nodes (end points), labeled by $\boldsymbol{n}_j$, with frictionless ball joints. Stacking these vectors in a row, we have a matrix expression of vectors [56, 1],

$$\boldsymbol{N} = [\boldsymbol{n}_1 \ \boldsymbol{n}_2 \ \cdots \ \boldsymbol{n}_n] \tag{G.1}$$

$$\boldsymbol{B} = [\boldsymbol{b}_1 \ \boldsymbol{b}_2 \ \cdots \ \boldsymbol{b}_{n_b}] \tag{G.2}$$

$$\boldsymbol{S} = [\boldsymbol{s}_1 \ \boldsymbol{s}_2 \ \cdots \ \boldsymbol{s}_{n_s}]. \tag{G.3}$$

For usual vector expressions we will use small letters, as $\boldsymbol{n} = [\boldsymbol{n}_1^T \ \boldsymbol{n}_2^T \ \cdots \ \boldsymbol{n}_n^T]^T$, $\boldsymbol{b} = [\boldsymbol{b}_1^T \ \cdots \ \boldsymbol{b}_{n_b}^T]^T$, and $\boldsymbol{s} = [\boldsymbol{s}_1^T \ \cdots \ \boldsymbol{s}_{n_s}^T]^T$. Length of vectors is represented by $b_i = \|\boldsymbol{b}_i\|$, $s_i = \|\boldsymbol{s}_i\|$.

Define the (i, j) element of a matrix $\boldsymbol{C}_B \in R^{n_b \times n}$ to be:

$$[\boldsymbol{C}_B]_{ij} = \begin{cases} -1, & \text{if } \boldsymbol{b}_i \text{ is directed away from the node } \boldsymbol{n}_j \\ 1, & \text{if } \boldsymbol{b}_i \text{ is directed toward } \boldsymbol{n}_j \\ 0, & \text{if } \boldsymbol{b}_i \text{ does not touch } \boldsymbol{n}_j. \end{cases} \tag{G.4}$$

Matrix $\boldsymbol{C}_S \in R^{n_s \times n}$ is constructed the same way, using the directed string vector $\boldsymbol{s}_i$. The bar and string matrices $\boldsymbol{B}$ and $\boldsymbol{S}$ are related to the node matrix $\boldsymbol{N}$ by these connectivity matrices $\boldsymbol{C}_B$, $\boldsymbol{C}_S$ as [1],

$$\boldsymbol{B} = \boldsymbol{N}\boldsymbol{C}_B^T, \quad \boldsymbol{S} = \boldsymbol{N}\boldsymbol{C}_S^T. \tag{G.5}$$

For the static analysis it is known that all tensegrity equilibria satisfy, [1],

$$\boldsymbol{N}\boldsymbol{K} = \boldsymbol{W}, \ \boldsymbol{K} = \boldsymbol{C}_S^T \widehat{\boldsymbol{\gamma}} \boldsymbol{C}_S - \boldsymbol{C}_B^T \widehat{\boldsymbol{\lambda}} \boldsymbol{C}_B, \tag{G.6}$$

where $\widehat{\boldsymbol{\gamma}}$ ($\widehat{\boldsymbol{\lambda}}$) are diagonal matrices where $[\widehat{\boldsymbol{\gamma}}]_{ii} = \gamma_i$ is the force density (member force divided by length) in the string $\boldsymbol{s}_i$ and $[\widehat{\boldsymbol{\lambda}}]_{ii} = \lambda_i$ is the force density in the bar $\boldsymbol{b}_i$, and the i^{th} column of the matrix $\boldsymbol{W}$ is the external force acting on the node $\boldsymbol{n}_i$.

It is useful to note that the matrix form expression (G.5) can be converted to a vector form expression by using the Kronecker product [58] as

$$\boldsymbol{b} = \big(\boldsymbol{C}_B \otimes \boldsymbol{I}_3\big)\boldsymbol{n} \quad \boldsymbol{s} = \big(\boldsymbol{C}_S \otimes \boldsymbol{I}_3\big)\boldsymbol{n}. \tag{G.7}$$

In the following analysis, we assume that the elements of the node matrix are ordered as $[\boldsymbol{N}\ \boldsymbol{N}_0]$, where $\boldsymbol{N}$ contains the nodes at which at least one bar is connected, and $\boldsymbol{N}_0$ contains the nodes at which only strings are connected (see Fig. G.1). We also assume that the nodes are assigned at every end of the bars, irrespective of whether the ends are coincident or not. If there is a node assigned to several bars, we assign a new node to each bar and add a geometrical constraint instead (see the lower right of Fig. G.1). See Appendix G.11, for the changes of the related matrices caused by this modification. If we have n_b bars, $\boldsymbol{N}$ has $2n_b$ members (columns). Partitioning the connectivity matrices according to this expression, (G.5) becomes

$$\boldsymbol{B} = [\boldsymbol{N}\ \boldsymbol{N}_0] \begin{bmatrix} \boldsymbol{C}_B^T \\ \boldsymbol{0} \end{bmatrix} = \boldsymbol{N}\boldsymbol{C}_B^T, \quad \boldsymbol{S} = [\boldsymbol{N}\ \boldsymbol{N}_0] \begin{bmatrix} \boldsymbol{C}_S^T \\ \boldsymbol{C}_{S_0}^T \end{bmatrix}. \tag{G.8}$$

In this paper, we consider the network of all the class of tensegrity systems connected as in (G.8). We will derive a closed form expression of the dynamical equation of tensegrity systems having connectivity (G.8).

G.3 Motion of Bar

For dynamics, we assume that the bars are uniform, rigid, and thin (long), and rotational motion about the longitudinal axis can be neglected.

Motion of the bar can be described by two vectors $\boldsymbol{r}_i$, $\boldsymbol{b}_i$, the gravity center and the orientation of the bar (see Fig. G.1), with the length constraint

$$h_i = b_i^2 - L_{b_i}^2 = 0, \tag{G.9}$$

where L_{b_i} is the length of the bar. The vector $\boldsymbol{r}_i$ can be also represented by the connectivity matrix as follows.

Let $\boldsymbol{n}_j$ and $\boldsymbol{n}_k$ be the nodes assigned to $\boldsymbol{b}_i$. Noting that the i^{th} column of $\boldsymbol{C}_B^T$ in (G.8) defines $\boldsymbol{b}_i$, we have

$$\boldsymbol{b}_i = \boldsymbol{n}_k - \boldsymbol{n}_j = \boldsymbol{N} \underbrace{\begin{bmatrix} \vdots \\ -1 \\ \vdots \\ 1 \\ \vdots \end{bmatrix}}_{\boldsymbol{C}_{B_i}^T(1,-1)} \begin{matrix} \\ j \\ \\ k \\ \\ \end{matrix} \tag{G.10}$$

where $\boldsymbol{C}_{B_i}^T(1,-1)(=\boldsymbol{C}_{B_i}^T)$ represents the i^{th} column of $\boldsymbol{C}_B^T$. Matrix $\boldsymbol{C}_B^T(1,+1)$ represents matrix $\boldsymbol{C}_B^T(1,-1)$ with all -1 entries replaced by $+1$.

Let $\boldsymbol{r}_i$ be the gravity center of the bar, i.e., $\boldsymbol{r}_i = (\boldsymbol{n}_j + \boldsymbol{n}_k)/2$. Observing (G.10), we see that

$$\boldsymbol{r}_i = \frac{1}{2}(\boldsymbol{n}_k + \boldsymbol{n}_j) = \frac{1}{2}\boldsymbol{N} \underbrace{\begin{bmatrix} \vdots \\ 1 \\ \vdots \\ 1 \\ \vdots \end{bmatrix}}_{\boldsymbol{C}_{B_i}^T(1,1)} \begin{matrix} \\ j \\ \\ k \\ \\ \end{matrix} \tag{G.11}$$

Let the i^{th} column of $\boldsymbol{R}$ be $\boldsymbol{r}_i$. Using the expressions (G.10) and (G.11), we have

$$\boldsymbol{R} = \frac{1}{2}\boldsymbol{N}\boldsymbol{C}_B^T(1,1), \quad \boldsymbol{B} = \boldsymbol{N}\boldsymbol{C}_B^T(1,-1), \tag{G.12}$$

where $\boldsymbol{R} = [\boldsymbol{r}_1 \cdots \boldsymbol{r}_{n_b}]$, and $\boldsymbol{C}_B^T(1,1)$ is the connectivity matrix whose -1 entries are replaced by 1.

G.4 Member Force

Forces produced by members can be also represented by the connectivity matrix. We show here two types of member forces, the string force $\boldsymbol{F}_s$ and the gravity force of bar $\boldsymbol{F}_g$. Other member forces can be handled the same way.

G.4.1 String force

Let $\boldsymbol{n}_j$, $\boldsymbol{n}_k$ be the member nodes assigned to $\boldsymbol{s}_i$, and let $\boldsymbol{t}_{s_i}$ be the string force vector produced by $\boldsymbol{s}_i$. If the material is Hookean, $\boldsymbol{t}_{s_i}$ is given by [1]

$$\boldsymbol{t}_{s_i} = \gamma_i \boldsymbol{s}_s, \quad \gamma_i = \max\Big(0, k_{s_i}(1 - L_{s_i}/s_i)\Big), \tag{G.13}$$

where k_{s_i} and L_{s_i} are the spring constant and the rest length, and γ_i is the force density (member force divided by length). Nodal forces acting on $\boldsymbol{n}_j$ (root node) and $\boldsymbol{n}_k$ (tip node) are $\boldsymbol{t}_{s_i}$ and $-\boldsymbol{t}_{s_i}$ respectively.

Let the i^{th} column of the matrix $\boldsymbol{T}_s$ be $\boldsymbol{t}_{s_i}$, and let the i^{th} column of the matrix $\boldsymbol{F}_s$ be the string force acting on $\boldsymbol{n}_i$. Recall that $[\boldsymbol{C}_B]_{ij} = -1$ if $\boldsymbol{n}_j$ is the root node, $[\boldsymbol{C}_B]_{ij} = 1$ if $\boldsymbol{n}_j$ is the tip node, and $[\boldsymbol{C}_B]_{ij} = 0$ otherwise. It follows that

$$\boldsymbol{F}_s = -\boldsymbol{T}_s \boldsymbol{C}_s(1,-1). \tag{G.14}$$

G.4.2 Gravity force

Let $\boldsymbol{n}_j$, $\boldsymbol{n}_k$ be the member nodes assigned to $\boldsymbol{b}_i$. The gravity force can be modeled by two nodal forces $\boldsymbol{t}_{g_i}$ acting on $\boldsymbol{n}_j$ and $\boldsymbol{n}_k$. where

$$\boldsymbol{t}_{g_i} = m_i \boldsymbol{g}/2, \tag{G.15}$$

where m_i and $\boldsymbol{g}$ respectively are the mass of the bar and the gravitational acceleration vector.

Let the i^{th} column of the matrix $\boldsymbol{T}_g$ be $\boldsymbol{t}_{g_i}$, and let the i^{th} column of the matrix $\boldsymbol{F}_g$ be the gravity force acting on $\boldsymbol{n}_i$. Recall that $[\boldsymbol{C}_B]_{ij} = \pm 1$ if $\boldsymbol{b}_i$ touches $\boldsymbol{n}_j$, and $[\boldsymbol{C}_B]_{ij} = 0$ otherwise. It follows that

$$\boldsymbol{F}_g = \boldsymbol{T}_g \boldsymbol{C}_B(1,1). \tag{G.16}$$

G.5 Rigid Body Connection

If we have rigid-body connections (bar-bar or bar-wall connections), we put a geometrical constraint and a constraint force to the system equation.

If the nodes $\boldsymbol{n}_j$, $\boldsymbol{n}_k$ are connected to one joint, this constraint is described by $\boldsymbol{n}_j = \boldsymbol{n}_k$. If $\boldsymbol{n}_j$ is constrained on a point $\boldsymbol{d}_j$ on the environment, possibly time varying, this constraint is described by $\boldsymbol{n}_j = \boldsymbol{d}_j$. To generalize this, we consider an affine type of constraint as

$$\boldsymbol{A}_c \boldsymbol{n} = \boldsymbol{d}_c, \tag{G.17}$$

where $\boldsymbol{A}_c \in \mathbb{R}^{n_c \times 6n_b}$ is a constant matrix and $\boldsymbol{d}_c \in \mathbb{R}^{n_c}$ is a given vector possibly time varying, where n_c is the total number of constraints. Note that we can also describe a node constrained on a line on a plane by (G.17). We assume that the constraints are independent of each other, and $\boldsymbol{A}_c$ has full row rank.

A solution of (G.17) exists if and only if $(\boldsymbol{I} - \boldsymbol{A}_c \boldsymbol{A}_c^+)\boldsymbol{d}_c = \boldsymbol{0}$, where $\boldsymbol{A}_c^+ \in \mathbb{R}^{6n_b \times n_c}$ is the pseud inverse of $\boldsymbol{A}_c$. A general solution $\boldsymbol{n}$ of (G.17) is given by

$$\boldsymbol{n} = \boldsymbol{A}_c^\perp \boldsymbol{n}_c + \boldsymbol{A}_c^+ \boldsymbol{d}_c, \tag{G.18}$$

where $\boldsymbol{A}_c^\perp \in \mathbb{R}^{6n_b \times (6n_b - n_c)}$ is a matrix whose columns span the right null space of $\boldsymbol{A}_c$ ($\boldsymbol{A}_c \boldsymbol{A}_c^+ = \boldsymbol{I}$, $\boldsymbol{A}_c \boldsymbol{A}_c^\perp = \boldsymbol{0}$). The vector $\boldsymbol{n}_c \in \mathbb{R}^{6n_b - n_c}$ is a freedom in the solution.

To keep the nodal motion to satisfy (G.17), the constraint force is added to the equation of motion. From the frictionless assumption, and the virtual work principle, the constraint force $\boldsymbol{f}_c$ acting on the nodes $\boldsymbol{n}$ should be orthogonal to the constrained motion along (G.18) ($\delta \boldsymbol{n} = \boldsymbol{A}_c^\perp \delta \boldsymbol{n}_c$). Hence we have [59]

$$\boldsymbol{f}_c = \boldsymbol{A}_c^T \boldsymbol{t}_c, \tag{G.19}$$

where $\boldsymbol{t}_c \in \mathbb{R}^{n_c}$ is the Lagrange multiplier.

G.6 Dynamics of Bar

Let $\boldsymbol{n}_j$, $\boldsymbol{n}_k$ be the member nodes of the bar $\boldsymbol{b}_i$, and let $\boldsymbol{f}_j$, $\boldsymbol{f}_k$ be the nodal forces acting on these nodes. Equations of motion of the bar are derived from the force balance of the translational motion $\boldsymbol{r}_i$ and the rotational motion $\boldsymbol{b}_i$ combined with the acceleration of the length constraint (G.9), i.e.,

$$\ddot{h}_i/2 = \boldsymbol{b}_i^T \ddot{\boldsymbol{b}}_i + \|\dot{\boldsymbol{b}}\|^2 = 0. \tag{G.20}$$

From the discussion in Appendix G.12, the equations of motion are given by [1]

$$m_i \ddot{\boldsymbol{r}}_i = \boldsymbol{f}_{r_i} \tag{G.21}$$

$$J_i \ddot{\boldsymbol{b}}_i + \kappa_i \boldsymbol{b}_i = \boldsymbol{H}_i \boldsymbol{f}_{b_i}, \tag{G.22}$$

where $\boldsymbol{f}_{r_i} = \boldsymbol{f}_k + \boldsymbol{f}_j$ and $\boldsymbol{f}_{b_i} = (\boldsymbol{f}_k - \boldsymbol{f}_j)/2$, and where

$$J_i = \frac{m_i}{12}, \quad \kappa_i = \frac{J_i}{b_i^2}\|\dot{\boldsymbol{b}}_i\|^2, \quad \boldsymbol{H}_i = \boldsymbol{I}_3 - \frac{\boldsymbol{b}_i \boldsymbol{b}_i^T}{b_i^2}. \tag{G.23}$$

Note that the term κ_i comes from the second term of the acceleration of the bar length constraint (G.20). For numerical simulation, we can add a stabilization factor to κ_i to avoid numerical instability in integration of the constraint (see Sec. E.8). Equations (G.21) and (G.22) have a simple form of dynamics with constant mass/inertia, without trigonometric functions (no angles).

Let the i^{th} column of the matrix $\boldsymbol{F}$ be the nodal force $\boldsymbol{f}_i$ acting on $\boldsymbol{n}_i$, and let the i^{th} columns of the matrices $\boldsymbol{F}_r$ and $\boldsymbol{F}_b$ be $\boldsymbol{f}_{r_i}$ and $\boldsymbol{f}_{b_i}$ respectively. From a discussion similar to Sec. G.3, we have

$$\boldsymbol{F}_r = \boldsymbol{F}\boldsymbol{C}_B^T(1,1), \quad \boldsymbol{F}_b = \frac{1}{2}\boldsymbol{F}\boldsymbol{C}_B^T(1,-1). \tag{G.24}$$

Similar to (G.7), (G.12) and (G.24) can be converted to a vector form

$$\begin{bmatrix}\boldsymbol{r}\\ \boldsymbol{b}\end{bmatrix} = \text{b.d.}\left(\frac{1}{2}\boldsymbol{I}, \boldsymbol{I}\right)\overline{\boldsymbol{C}}_B\boldsymbol{n}, \quad \begin{bmatrix}\boldsymbol{f}_r\\ \boldsymbol{f}_b\end{bmatrix} = \text{b.d.}\left(\boldsymbol{I}, \frac{1}{2}\boldsymbol{I}\right)\overline{\boldsymbol{C}}_B\boldsymbol{f}, \tag{G.25}$$

where b.d.$(\cdot)$ represents a block diagonal matrix and

$$\overline{\boldsymbol{C}}_B = \begin{bmatrix}\boldsymbol{C}_B(1,1)\otimes\boldsymbol{I}_3\\ \boldsymbol{C}_B(1,-1)\otimes\boldsymbol{I}_3\end{bmatrix}. \tag{G.26}$$

The matrix b.d. $\left(\boldsymbol{I}, \frac{1}{2}\boldsymbol{I}\right)\overline{\boldsymbol{C}}_B$ is non-singular because the inverse of the mapping from $\boldsymbol{n}$ to $(\boldsymbol{r}, \boldsymbol{b})$ should exist from the geometrical relationship.

Collecting (G.21) and (G.22) for all the bars, and using (G.25), we have the next theorem.

Theorem G.6.1. *Consider a tensegrity system represented by (G.8). Let $\boldsymbol{n}_k$ and $\boldsymbol{n}_j$ be the member nodes of $\boldsymbol{b}_i$. Let $\boldsymbol{f}_k$ and $\boldsymbol{f}_j$ be the nodal forces acting on $\boldsymbol{n}_k$ and $\boldsymbol{n}_j$. Equation of motion of the bars with respect to the node $\boldsymbol{n}$ is given by*

$$\boldsymbol{M}\overline{\boldsymbol{C}}_B\ddot{\boldsymbol{n}} + \boldsymbol{K}\overline{\boldsymbol{C}}_B\boldsymbol{n} = \boldsymbol{H}\overline{\boldsymbol{C}}_B\boldsymbol{f}, \tag{G.27}$$

where $\overline{\boldsymbol{C}}_B$ is defined by (G.26), and where

$$\boldsymbol{M} = \begin{bmatrix}\text{diag}(m_1,\cdots,m_{n_b})\otimes\boldsymbol{I}_3 & \boldsymbol{0}\\ \boldsymbol{0} & \text{diag}(J_1,\cdots,J_{n_b})\otimes\boldsymbol{I}_3\end{bmatrix} \tag{G.28}$$

$$\boldsymbol{K} = \begin{bmatrix}\boldsymbol{0} & \boldsymbol{0}\\ \boldsymbol{0} & \text{diag}(\kappa_1,\cdots,\kappa_{n_b})\otimes\boldsymbol{I}_3\end{bmatrix} \tag{G.29}$$

$$\boldsymbol{H} = \begin{bmatrix}2\boldsymbol{I}_{3n_b} & \boldsymbol{0}\\ \boldsymbol{0} & \frac{1}{2}\text{b.d.}(\boldsymbol{H}_1,\cdots,\boldsymbol{H}_{n_b})\end{bmatrix}, \tag{G.30}$$

where J_i, κ_i, and $\boldsymbol{H}_i$ are defined by (G.23), where m_i and L_{b_i} be the mass and length of the bar $\boldsymbol{b}_i$. Functions diag$(\cdot)$ *and* b.d.$(\cdot)$ *represent diagonal and block diagonal matrices.* □

G.7 Total Dynamics

Total dynamics of the system is given by substituting the constrained motion (G.18) to (G.27), and adding the constraint force (G.19) to $\boldsymbol{f}$ in (G.27).

Theorem G.7.1. *Consider a tensegrity system represented by (G.8). Suppose the system has rigid body connections represented by (G.17). Let $\boldsymbol{n}_c$ and $\boldsymbol{t}_c$ respectively be the freedom of the nodal motion and the Lagrange multiplier of the constraint force corresponding to (G.17). Let $\boldsymbol{f}_{n_c}$ be the nodal force other than the constraint force $\boldsymbol{f}_c$, i.e., $\boldsymbol{f} = \boldsymbol{f}_c + \boldsymbol{f}_{n_c}$. Using (G.18) and Lagrange multiplier $\boldsymbol{t}_c$, the equations in the variable $\boldsymbol{n}_c$ obey*

$$\boldsymbol{M}_c\ddot{\boldsymbol{n}}_c + \boldsymbol{K}_c\boldsymbol{n}_c = \boldsymbol{B}_c\boldsymbol{t}_c + \boldsymbol{H}\overline{\boldsymbol{C}}_B\boldsymbol{f}_{n_c} - \boldsymbol{N}_d, \tag{G.31}$$

where

$$\boldsymbol{M}_c = \boldsymbol{M}\overline{\boldsymbol{C}}_B\boldsymbol{A_c}^{\perp}, \quad \boldsymbol{K}_c = \boldsymbol{K}\overline{\boldsymbol{C}}_B\boldsymbol{A_c}^{\perp} \tag{G.32}$$

$$\boldsymbol{B}_c = \boldsymbol{H}\overline{\boldsymbol{C}}_B\boldsymbol{A}_c^T \tag{G.33}$$

$$\boldsymbol{N}_d = \boldsymbol{M}\overline{\boldsymbol{C}}_B\boldsymbol{A}_c^{+}\ddot{\boldsymbol{d}}_c + \boldsymbol{K}\overline{\boldsymbol{C}}_B\boldsymbol{A}_c^{+}\boldsymbol{d}_c, \tag{G.34}$$

where $\boldsymbol{M}$, $\boldsymbol{K}$, $\boldsymbol{H}$ and $\overline{\boldsymbol{C}}_B$ are defined by (G.28)-(G.30) and (G.26), and $\boldsymbol{A}_c^{+}$ and $\boldsymbol{A}_c^{\perp}$ are the pseudo inverse of $\boldsymbol{A}_c$ and a matrix whose columns span the right null space of $\boldsymbol{A}_c$ ($\boldsymbol{A}_c\boldsymbol{A}_c^{+} = \boldsymbol{I}$, $\boldsymbol{A}_c\boldsymbol{A}_c^{\perp} = \boldsymbol{0}$).

If the nodal force $\boldsymbol{f}_{n_c}$ is given by the sum of the external force $\boldsymbol{w}$, the string force $\boldsymbol{f}_s$, and the gravity force $\boldsymbol{f}_g$, then $\boldsymbol{f}_{n_c}$ in (G.31) is given by

$$\boldsymbol{f}_{n_c} = \boldsymbol{w} + \boldsymbol{f}_s + \boldsymbol{f}_g \tag{G.35}$$

where

$$\boldsymbol{f}_s = -\big(\boldsymbol{C}_S^T(1,-1)\otimes\boldsymbol{I}_3\big)\boldsymbol{t}_s \tag{G.36}$$

$$\boldsymbol{f}_g = \big(\boldsymbol{C}_B^T(1,1)\otimes\boldsymbol{I}_3\big)\boldsymbol{t}_g, \tag{G.37}$$

where the i^{th} block of the vectors $\boldsymbol{t}_s$ and $\boldsymbol{t}_g$ are given by (G.13) and (G.15). □

Proof. (*outline*) *Equation (G.31) is derived by substituting (G.18) and (G.19) to (G.27). Equations (G.36) and (G.37) are rewritings of (G.14) and (G.16) by using the Kronecker product.* □

Equation (G.31) is $6n_b$ equations with unknowns $\ddot{\boldsymbol{n}}_c \in \mathbb{R}^{6n_b-n_c}$, $\boldsymbol{t}_c \in \mathbb{R}^{n_c}$, where n_b and n_c are the numbers of the bars and the constraints. The solution $\ddot{\boldsymbol{n}}_c$ is given explicitly by the next corollary.

Corollary G.7.1. *Consider a tensegrity system given by (G.8) with a rigid body connection (G.17). Suppose $[\boldsymbol{M}_c\ -\boldsymbol{B}_c]$ is non-singular. Under the same assumption in Theorem G.7.1, the system trajectory $\ddot{\boldsymbol{n}}_c$ is given by*

$$\ddot{\boldsymbol{n}}_c = \boldsymbol{M}_c^T(\boldsymbol{M}_c\boldsymbol{M}_c^T + \boldsymbol{B}_c\boldsymbol{B}_c^T)^{-1}\big(\boldsymbol{H}\overline{\boldsymbol{C}}_B\boldsymbol{f}_{n_c} - \boldsymbol{N}_d - \boldsymbol{K}_c\boldsymbol{n}_c\big). \tag{G.38}$$

Proof. From (G.31), it is obvious

$$\begin{bmatrix}\ddot{\boldsymbol{n}}_c\\ \boldsymbol{t}_c\end{bmatrix} = [\boldsymbol{M}_c\ -\boldsymbol{B}_c]^{-1}\left(\boldsymbol{H}\overline{\boldsymbol{C}}_B\boldsymbol{f}_{n_c} - \boldsymbol{N}_d - \boldsymbol{K}_c\boldsymbol{n}_c\right). \tag{G.39}$$

Note that the pseudo inverse of a full row rank matrix $\boldsymbol{A}$ is given by $\boldsymbol{A}^{+} = \boldsymbol{A}^T(\boldsymbol{A}\boldsymbol{A}^T)^{-1}$, and $\boldsymbol{A}^{-1} = \boldsymbol{A}^{+}$ if $\boldsymbol{A}$ is square in addition. Hence

$$[\boldsymbol{M}_c\ -\boldsymbol{B}_c]^{-1} = \begin{bmatrix}\boldsymbol{M}_c^T\\ -\boldsymbol{B}_c^T\end{bmatrix}\left([\boldsymbol{M}_c\ -\boldsymbol{B}_c]\begin{bmatrix}\boldsymbol{M}_c^T\\ -\boldsymbol{B}_c^T\end{bmatrix}\right)^{-1}. \tag{G.40}$$

Substituting (G.40) to (G.39), we get (G.38). □

Using $\boldsymbol{n}_c$ obtained from (G.38), the nodal position $\boldsymbol{n}$ is given by (G.18). We can determine the Lagrange multiplier $\boldsymbol{t}_c$ by using the lower block of (G.40). The constraint force $\boldsymbol{f}_c$ is given by (G.19).

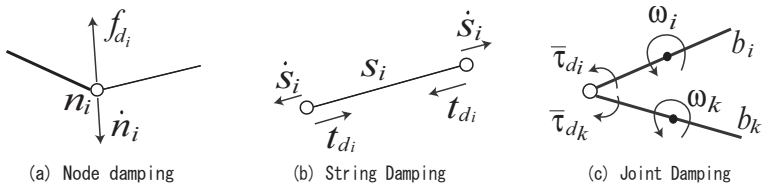

Figure G.2: Damping forces

G.8 Damping

In the preceding sections, we ignore the system damping. Damping effect is easily implemented by adding a term to (G.31).

G.8.1 Damping Force

Damping of this mechanical system has several sources. A string or cable attached to a node might be attached by wrapping the cable around the node, or running the cable inside the hollow compressive member. In either case, the stretching of the cable under load rubs against the hard surface of the joint, creating damping force. This case can be approximated by adding a term $\boldsymbol{f}_d$ to $\boldsymbol{f}_{n_c}$ in (G.35).

One convenient but crude approximation of this damping is viscous damping related to the node velocity, i.e.,

$$\boldsymbol{f}_{d_i} = -c_i \dot{\boldsymbol{n}}_i \tag{G.41}$$

(see Fig. G.2 (a)), where c_i is the damping coefficient. The i^{th} block of $\boldsymbol{f}_d$ is defined by (G.41).

Another typical approximation of the damping is related to expansion/contraction velocity of the string, as shown in Fig. G.2 (b). Similar to (G.13), the member force produced by the string can be described by

$$\boldsymbol{t}_{d_i} = \gamma_{d_i} \boldsymbol{s}_i, \quad \gamma_{d_i} = \begin{cases} c_i \dot{s}_i / s_i & (s_i \geq L_{s_i}) \\ 0 & (s_i < L_{s_i}) \end{cases}, \tag{G.42}$$

where c_i is the damping coefficient. The damping force $\boldsymbol{f}_d$ is given the same way as (G.14) (in matrix form) .

G.8.2 Damping Torque

In the case of class k tensegrity joints, for $k > 1$, two bars connect with frictionless ball joints in theory, but the relative angular motion between ball and bar create friction and hence damping torque (see Fig. G.2 (c)). This case can be approximated by adding a term $[\boldsymbol{0}_{1\times 3n_b}^T \ \boldsymbol{\tau}_d^T]^T$ to the right hand side of (G.31), where $\boldsymbol{\tau}_d \in \mathbb{R}^{3n_b}$ represents the torque acting on the rotational motion $\boldsymbol{b}_i$ of bar.

Let $\boldsymbol{b}_i$, $\boldsymbol{b}_k$ be the bars connected to a joint. From the discussion in Appendix G.13, the angular velocity $\boldsymbol{\omega}_i$ of the bar $\boldsymbol{b}_i$ is given by (G.59). Damping torque on $\boldsymbol{b}_i$ produced by this joint damping is given by

$$\overline{\boldsymbol{\tau}}_{d_i} = -c_i(\boldsymbol{\omega}_i - \boldsymbol{\omega}_k), \tag{G.43}$$

where c_i is the damping coefficient. If there are other joint dampings acting on $\boldsymbol{b}_i$, the damping torque $\overline{\boldsymbol{\tau}}_{d_i}$ is the sum of them.

From the derivation process of (G.22) described in Appendix G.12, we see that the i^{th} block of $\boldsymbol{\tau}_d$ is given by $\boldsymbol{\tau}_{d_i} = -(\widetilde{\boldsymbol{b}}_i/b_i^2)\overline{\boldsymbol{\tau}}_{d_i}$.

G.9 Numerical Example

G.9.1 Rotating boom

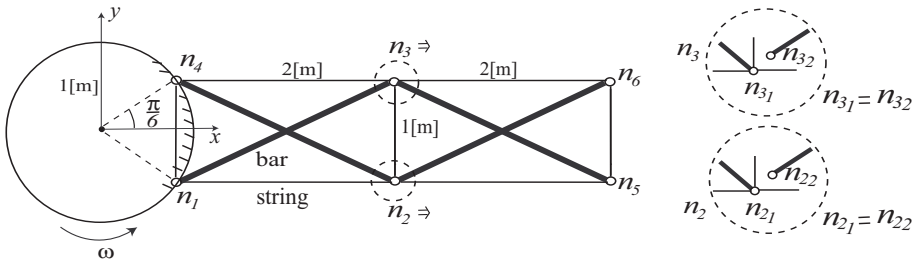

Figure G.3: Rotating boom

Consider a planar column structure shown in Fig. G.3. The structure has 4 bars and 7 strings. The left nodes $\boldsymbol{n}_1$, $\boldsymbol{n}_4$ are pinned to the circular base, and the base is rotated counterclockwise with the angular velocity ω [rad/sec]. For the bar-bar connections at $\boldsymbol{n}_2$ and $\boldsymbol{n}_3$, we assign new nodes on each bar and add the geometrical constraints.

Physical parameters are chosen as $m_i = 0.5$ [Kg], $k_{s_i} = 10^6$ [N/m], and the joint damping (G.43) with $c_i = 25$ [Nms/rad] is considered. Strings are at rest at the initial configuration. From the initial configuration shown in Fig. G.3, the base is rotated with the angular velocity

$$\omega = \begin{cases} 0 & (t < 0) \\ \pi/2 & (0 \le t \le 0.5) \\ 0 & (t > 0.5) \end{cases} .$$

To avoid numerical instability to integrate the acceleration constraint (G.20), we introduce the constraint stabilization imposed by a choice of $\zeta_i > 0$, $\omega_i > 0$ such that [60, 61], $\ddot{h}_i + 2\zeta_i\omega_i\dot{h}_i + \omega_i^2 h_i = 0$, where $\zeta_i > 0$, $\omega_i > 0$. The term κ_i in (G.23) is replaced by $\kappa_i' = \kappa_i + J_i e_i/b_i^2$, where $e_i = \zeta_i\omega_i\dot{h}_i + \omega_i^2 h_i/2 = 2\zeta_i\omega_i\boldsymbol{b}_i^T\dot{\boldsymbol{b}}_i + \omega_i^2(b_i^2 - L_{b_i}^2)/2$. In this example, we set $\zeta_i = 1$ and $\omega_i = 500$.

G.9.2 Simulation Result

Results are shown in Figs. G.4-G.5. Figure G.4 shows transition of the configuration at $t =$ 0, 0.25, 0.5. From the initial configuration, the base is rotated by $\pi/4$, and the structural dynamics follow this motion. To see vibration properties of the structure, Fig. G.5 shows residual vibration after $t = 0.5$ at the tip nodes along the tangent direction of the structure (y' direction in Fig. G.4 (c)). Vibration caused by the abrupt stop of the base is attenuated gradually by the joint damping.

G.10 Conclusion

Under the assumptions of rigid bars (compressive members) and massless string, the non-minimal dynamics of class k tensegrity structures are given in vector form, where the bar length constraints

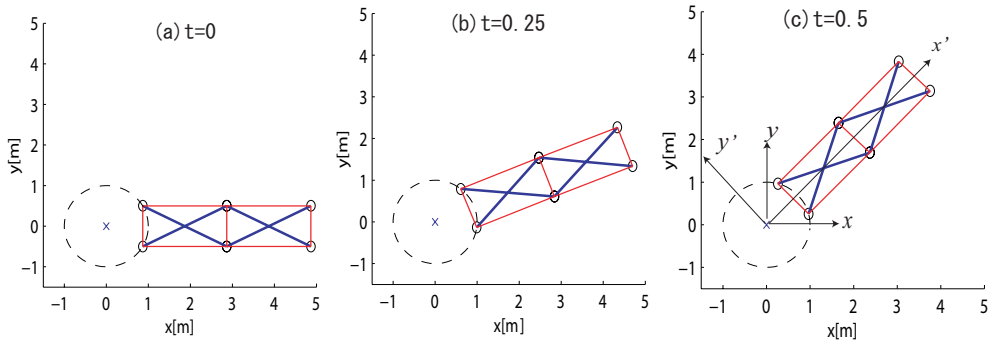

Figure G.4: Transition of configuration

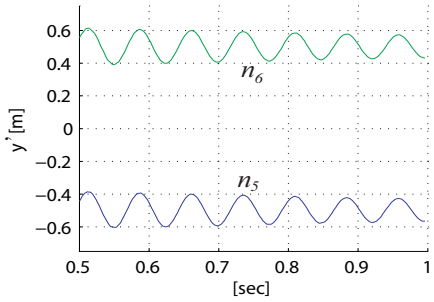

Figure G.5: Residual vibration of tip nodes

are stabilized by adding an auxiliary term. Our network approach to the formulation of the dynamic forces allows these equations to be used for any tensegrity structure, with damping of several types included as options, as well as gravity. The key to generality is the use of connectivity matrices that contain all the information about bar-to-bar or bar-to-string connections. Lagrange multipliers are used to handle the class k constraints, where bar-to-bar connections are made. The Lagrange multipliers are eliminated analytically to reduce the number of equations. System configurations (number of members, member location, string connection, rigid body connection (class k, connection to environment), etc.) can be easily changed without essential modification. Tensegrity solutions are now being sought for important engineering applications. It has been shown in previous work that tensegrity provides the solution for minimal mass approaches to static and dynamic structures. This paper provides an important extension to the analytical tools that are available for this growing class of solutions to engineering problems.

G.11 Appendix: Node settings for dynamical analysis

If the node $\boldsymbol{n}_j$ is assigned to more than one bar in the original formulation, we assign a node for each bar and add a geometrical constraint instead (see Fig. G.1). Corresponding changes in the connectivity matrix and the geometrical constraints are discussed in the following.

Let $\boldsymbol{C}_{B_j}^T$ and $\boldsymbol{C}_{S_j}^T$ be the j^{th} row of $\boldsymbol{C}_B^T$ and $\boldsymbol{C}_S^T$, i.e.,

$$\boldsymbol{B} = [\ \cdots\ \boldsymbol{n}_j\ \cdots\ ] \begin{bmatrix} \vdots \\ \boldsymbol{C}_{B_j}^T \\ \vdots \end{bmatrix}, \quad \boldsymbol{S} = [\ \cdots\ \boldsymbol{n}_j\ \cdots\ ] \begin{bmatrix} \vdots \\ \boldsymbol{C}_{S_j}^T \\ \vdots \end{bmatrix}. \tag{G.44}$$

If $\boldsymbol{n}_j$ is assigned to n_j (≥ 2) bars, $\boldsymbol{C}_{B_j}^T$ has n_j non-zero elements as

$$\boldsymbol{C}_{B_j}^T = \underbrace{[\ \cdots 1\ \cdots\ -1\ \cdots\cdots\ 1 \cdots]}_{\boldsymbol{C}_{B_j}^T(1,-1,\cdots,1)}. \tag{G.45}$$

If we assign new nodes to each bar as in Fig. G.1, the node matrix and the external force matrix are modified as

$$\boldsymbol{N} \to [\boldsymbol{n}_1 \cdots \boldsymbol{n}_{j-1} \mid \underbrace{\boldsymbol{n}_{j_1}\ \boldsymbol{n}_{j_2}\ \cdots\ \boldsymbol{n}_{j_{n_j}}}_{\boldsymbol{n}_j} \mid \boldsymbol{n}_{j+1} \cdots \boldsymbol{n}_n] \tag{G.46}$$

$$\boldsymbol{W} \to [\boldsymbol{w}_1 \cdots \boldsymbol{w}_{j-1} \mid \boldsymbol{w}_j\ \ \mathbf{0}\ \ \cdots\ \ \mathbf{0}\ \ \mid \boldsymbol{w}_{j+1} \cdots \boldsymbol{w}_n], \tag{G.47}$$

and the connectivity matrices are modified as

$$\boldsymbol{C}_B^T \to \begin{bmatrix} \boldsymbol{C}_{B_1}^T \\ \vdots \\ \boldsymbol{C}_{B_{j-1}}^T \\ \hline \boldsymbol{C}_{B_j}^T(1,0,\cdots,0) \\ \boldsymbol{C}_{B_j}^T(0,-1,\cdots,0) \\ \vdots \\ \boldsymbol{C}_{B_j}^T(0,0,\cdots,1) \\ \hline \boldsymbol{C}_{B_{j+1}}^T \\ \vdots \\ \boldsymbol{C}_{B_{n_b}}^T \end{bmatrix}, \qquad \boldsymbol{C}_S^T \to \begin{bmatrix} \boldsymbol{C}_{S_1}^T \\ \vdots \\ \boldsymbol{C}_{S_{j-1}}^T \\ \hline \boldsymbol{C}_{S_j}^T \\ \mathbf{0} \\ \vdots \\ \mathbf{0} \\ \hline \boldsymbol{C}_{S_{j+1}}^T \\ \vdots \\ \boldsymbol{C}_{S_{n_s}}^T \end{bmatrix}. \tag{G.48}$$

To see the change in the constraint matrix in (G.17), divide $\boldsymbol{A}_c$ according to each node as

$$[\cdots \boldsymbol{A}_{c_j} \cdots] \begin{bmatrix} \vdots \\ \boldsymbol{n}_j \\ \vdots \end{bmatrix} = \boldsymbol{d}_c \tag{G.49}$$

Because we add the new nodes $\boldsymbol{n}_{j_1}, \cdots, \boldsymbol{n}_{j_{n_j}}$ at $\boldsymbol{n}_j$, we add the geometrical constraints $\boldsymbol{n}_{j_1} = \boldsymbol{n}_{j_2}, \cdots, \boldsymbol{n}_{j_1} = \boldsymbol{n}_{j_{n_j}}$ instead, or equivalently,

$$\boldsymbol{E}_{c_j} \begin{bmatrix} \boldsymbol{n}_{j_1} \\ \boldsymbol{n}_{j_2} \\ \vdots \\ \boldsymbol{n}_{j_{n_j}} \end{bmatrix} = \mathbf{0}, \qquad \boldsymbol{E}_{c_j} = \begin{bmatrix} \boldsymbol{I}_3 & -\boldsymbol{I}_3 & \mathbf{0} & \cdots & \cdots & \mathbf{0} \\ \boldsymbol{I}_3 & \mathbf{0} & -\boldsymbol{I}_3 & \ddots & \ddots & \vdots \\ \boldsymbol{I}_3 & \mathbf{0} & \mathbf{0} & \ddots & \ddots & \mathbf{0} \\ \vdots & \vdots & \ddots & \ddots & \ddots & \mathbf{0} \\ \boldsymbol{I}_3 & \mathbf{0} & \cdots & \mathbf{0} & \mathbf{0} & -\boldsymbol{I}_3 \end{bmatrix}. \tag{G.50}$$

Adding this constraint to the bottom of (G.17), the resultant constraint matrices for the new node (G.46) is given by

$$\boldsymbol{A}_c \to \left[\begin{array}{c|c|c} \cdots \boldsymbol{A}_{c_{j-1}} & \boldsymbol{A}_{c_j}\ \boldsymbol{0}\cdots\boldsymbol{0} & \boldsymbol{A}_{c_{j+1}}\cdots \\ \hline \boldsymbol{0} & \boldsymbol{E}_{c_j} & \boldsymbol{0} \end{array}\right], \quad \boldsymbol{d}_c \to \left[\begin{array}{c} \boldsymbol{d}_c \\ \hline \boldsymbol{0} \end{array}\right]. \tag{G.51}$$

G.12 Appendix: Derivation of (G.21) and (G.22)

Equation (G.21) is obvious from the translational motion of the gravity center.

To derive (G.22), note that angular momentum of the bar is given by (G.54) in Appendix G.13. From the rotational motion of the bar, we have

$$J_i \boldsymbol{b}_i \times \ddot{\boldsymbol{b}}_i = \frac{1}{2}\boldsymbol{b}_i \times (\boldsymbol{f}_k - \boldsymbol{f}_j) + \boldsymbol{b}_i \tau_{c_i}. \tag{G.52}$$

The last term of (G.52) represents the constraint force of (G.9), which is orthogonal to the constrained motion $\boldsymbol{b}_i^T \delta \boldsymbol{b}_i = 0$.

Collecting (G.52) and (G.20), we have

$$\begin{bmatrix} \widetilde{\boldsymbol{b}}_i \\ \boldsymbol{b}_i^T \end{bmatrix} \ddot{\boldsymbol{b}}_i = \begin{bmatrix} \dfrac{1}{2J_i}\widetilde{\boldsymbol{b}}_i(\boldsymbol{f}_k - \boldsymbol{f}_j) + \dfrac{1}{J_i}\boldsymbol{b}_i\tau_{c_i} \\ -\|\dot{\boldsymbol{b}}_i\|^2 \end{bmatrix}, \tag{G.53}$$

where $\widetilde{\boldsymbol{b}}_i$ is a skew symmetric matrix equivalent to the map of the vector product $\boldsymbol{b}_i\times$. Note that $\widetilde{\boldsymbol{b}}_i^T\widetilde{\boldsymbol{b}}_i = b_i^2\boldsymbol{I}_3 - \boldsymbol{b}_i\boldsymbol{b}_i^T$. Multiplying the pseudo inverse $\begin{bmatrix} \widetilde{\boldsymbol{b}}_i \\ \boldsymbol{b}_i^T \end{bmatrix}^+ = \dfrac{1}{b_i^2}\begin{bmatrix} \widetilde{\boldsymbol{b}}_i^T & \boldsymbol{b}_i \end{bmatrix}$ of the coefficient matrix from the left, and noting $\widetilde{\boldsymbol{b}}_i^T\boldsymbol{b}_i = \boldsymbol{0}$, we have (G.22).

G.13 Appendix: Angular momentum and angular velocity of bar

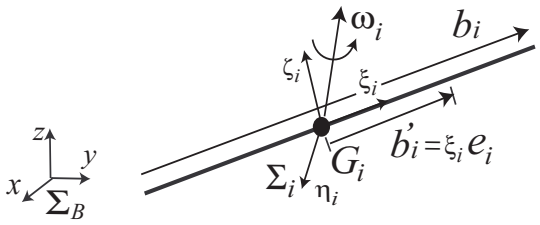

Figure G.6: Angular momentum and angular velocity

Consider a uniform bar shown in Fig. G.6. The gravity center G_i is located at the midpoint, and define $\boldsymbol{b}_i' = \xi_i \boldsymbol{e}_i$, where $\boldsymbol{e}_i = \boldsymbol{b}_i/b_i$ is the unit vector along the bar. Note that the bar length b_i is constant. Let Σ_B and Σ_i be the base frame and a frame fixed on the bar respectively. We choose the direction of the axis ξ_i of Σ_i to coincide with $\boldsymbol{b}_i$. Let $\boldsymbol{\omega}_i$ be the angular velocity of Σ_i with respect to Σ_B.

From the definition, the angular momentum about G_i is given by

$$\begin{aligned}\boldsymbol{L}_{G_i} &= \int \boldsymbol{b}_i' \times \dot{\boldsymbol{b}}_i' dm_i = \int_{-\frac{b_i}{2}}^{\frac{b_i}{2}} (\xi_i \boldsymbol{e}_i) \times (\xi_i \dot{\boldsymbol{e}}_i) \frac{m_i}{b_i} d\xi_i \\ &= \frac{m_i}{b_i^3} \int_{-\frac{b_i}{2}}^{\frac{b_i}{2}} \xi_i^2 d\xi_i \cdot \boldsymbol{b}_i \times \dot{\boldsymbol{b}}_i = J_i \boldsymbol{b}_i \times \dot{\boldsymbol{b}}_i, \end{aligned} \tag{G.54}$$

where $J_i = m_i/12$.

Because the length of $\boldsymbol{b}_i'$ is constant, it follows that $\dot{\boldsymbol{b}}_i' = \boldsymbol{\omega}_i \times \boldsymbol{b}_i'$ [62]. Hence

$$\boldsymbol{b}_i' \times \dot{\boldsymbol{b}}_i' = \boldsymbol{b}_i' \times (\boldsymbol{\omega}_i \times \boldsymbol{b}_i'). \tag{G.55}$$

By using the Σ_i coordinate, the right hand side of (G.55) becomes

$${}^i\boldsymbol{b}_i' \times ({}^i\boldsymbol{\omega}_i \times {}^i\boldsymbol{b}_i') = \begin{bmatrix} \xi_i \\ 0 \\ 0 \end{bmatrix} \times \left(\begin{bmatrix} 0 \\ \omega_{\eta_i} \\ \omega_{\zeta_i} \end{bmatrix} \times \begin{bmatrix} \xi_i \\ 0 \\ 0 \end{bmatrix} \right) = \xi_i^2 \, {}^i\boldsymbol{\omega}_i. \tag{G.56}$$

Multiply $d\xi_i$ on the both sides of (G.55), and take the integral over the length. Then the left hand side of the equation becomes

$$\int_{-\frac{b_i}{2}}^{\frac{b_i}{2}} \boldsymbol{b}_i' \times \dot{\boldsymbol{b}}_i' d\xi_i = \frac{1}{b_i^2} \int_{-\frac{b_i}{2}}^{\frac{b_i}{2}} \xi_i^2 d\xi_i \cdot \boldsymbol{b}_i \times \dot{\boldsymbol{b}}_i. \tag{G.57}$$

By using the expression (G.56), the right hand side of the equation becomes

$$\int_{-\frac{b_i}{2}}^{\frac{b_i}{2}} {}^i\boldsymbol{b}_i' \times ({}^i\boldsymbol{\omega}_i \times {}^i\boldsymbol{b}_i') d\xi_i = \int_{-\frac{b_i}{2}}^{\frac{b_i}{2}} \xi_i^2 d\xi_i \cdot {}^i\boldsymbol{\omega}_i. \tag{G.58}$$

Observing the vector in (G.58) in the base frame Σ_B, and equating (G.58) to (G.57), we get

$$\boldsymbol{\omega}_i = \frac{1}{b_i^2} \boldsymbol{b}_i \times \dot{\boldsymbol{b}}_i. \tag{G.59}$$